In-situ X-ray Study of the Initial Electrochemical Corrosion of $Cu_3Au(111)$

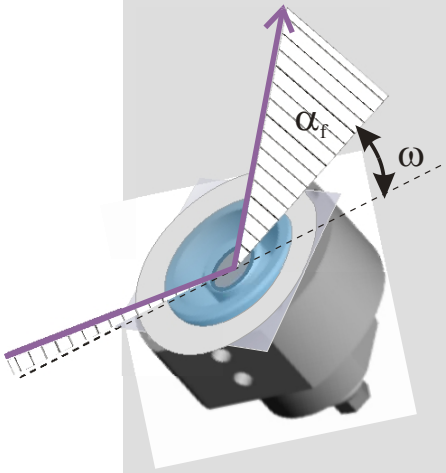

Frank Uwe Renner

Stuttgart, June 2004

European Synchrotron
Radiation Facility
in Grenoble

Max-Planck-Institut für
Metallforschung
in Stuttgart

Institut für Theoretische
und Angewandte Physik
der Universität Stuttgart

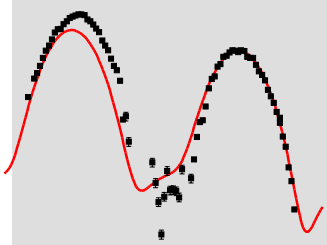

In-situ X-ray Study of the Initial Electrochemical Corrosion of $Cu_3Au(111)$

Von der Fakultät für Mathematik und Physik
der Universität Stuttgart
zur Erlangung der Würde eines
Doktors der Naturwissenschaften (Dr.rer.nat.)
genehmigte Abhandlung

Vorgelegt von
Frank Uwe Renner
aus Künzelsau

Hauptberichter Prof.Dr.H.Dosch
Mitberichter Prof.Dr.C.Bechinger
Vorgelegt am 17.06.2004
Tag der mündlichen Prüfung: 19.11.2004

Institut für Theoretische und Angewandte Physik
der Universität Stuttgart

2004

Contents

Chapter 1

Zusammenfassung in deutscher Sprache

1.1 Einleitung

Der wesentliche Teil einer Wechselwirkung eines Materials mit der Umgebung findet an der Grenzfläche statt. Dies gilt für die heterogene Katalyse ebenso wie für Korrosionsprozesse, die an der Oberfäche des Werkstoffes beginnen. Der Fortschritt der Oberflächenphysik als neue Disziplin war von mehreren Entwicklungen beeinflusst. Zum einen war die Vakuumtechnik eine Bedingung um reproduzierbare und definierte experimentelle Bedingungen zu erhalten und mit der Nutzung eines Elektronenstrahls wichtige oberfächensensitive Techniken zu entwickeln. Ein weiterer wesentlicher Schritt lag auf der methodischen Seite. Durch die Verwendung von möglichst einfachen Modelsystemen konnten die Randbedingungen verringert und die Interpretation der experimentellen Ergebnisse erleichtert werden. Im wesentlichen wurde dies durch die Verwendung von in immer besserer Qualität zu erhaltenden Einkristalloberflächen erreicht. Die Entwicklung des Rastertunnelmikroskops (STM) hat hier das Zeitalter der direkten Abbildung eingeläutet. Unabdingbare komplementäre Methoden beinhalten die Nutzung von Synchrotronstrahlung und damit auch die hier hauptsächlich verwendete oberflächensensitive Röntgenbeugung. Die experimentellen Methoden mit atomarer Auflösung sind somit nun ein wesentlicher Bestandteil der Oberfächenphysik und unabdingbar für ein grundlegendes Verständniss von Prozessen wie Schicht- oder Kristallwachstum, chemischen Reaktionen auf Oberfächen und heterogener Katalyse, wie auch der Korrosion. Die zuletztgenannten experimentellen Techniken sind auch unter realen Prozessbedingungen anwendbar, also auch außerhalb des Ultrahochvakuums (UHV). Mit der Verwendung von Modelsystemen mit definierten Ausgangsbedingun-

gen, wird versucht, die in Vakuum gewonnenen Ergebnisse auf reale Prozessbedingungen zu übertragen.

Korrosion verursacht einen enormen volkswirtschaftlichen Schaden, der sich auf ca. 3-6% eines nationalen Bruttosozialproduktes beläuft. Eine Erweiterung des grundlegenden Verständnisses von Korrosionsprozessen und der Bildung von korrosionshemmenden Passivierungsschichten ist somit überaus wünschenswert. Im wesentlichen ist Korrosion ein elektrochemischer Vorgang. Mit der Wahl der Einkristalloberfläche $Cu_3Au(111)$ wurde als Modelsystem eine zweikomponentige Edelmetalllegierung im sauren Elektrolyten potentialabhängig und bei Normaldruck untersucht. Der Vorteil des Legierungssystems Cu-Au liegt in der relativen chemischen Inertheit beider Komponenten und einer großen Differenz der Gleichgewichtsspannungen (Nernstpotentiale). Mit anodischem Potential kommt es zur selektiven Auflösung nur des Kupfers , unterhalb eines kritischen Potentials E_c jedoch passiviert die Oberfläche. Erst oberhalb des kritischen Potentials E_c kommt es zu einer massiven Auflösung des Kupfers und zur Bildung poröser Goldschichten (Dealloying). Neben einigen ex-situ AFM Aufnahmen wurde für diese Problemstellung hauptsächlich in-situ Röntgenbeugung mit Synchrotronstrahlung angewandt. Mit Hilfe der Röntgenbeugung lassen sich vor allem kristalline Materialien charakterisieren und für die Korrosion wichtige Fragen beantworten: Wie dick sind entstehende passivierende Deckschichten und welche Zusammensetzung, welche Ausdehnung und welche kristallographische Orientierung haben sie? Die Antwort beinhaltet die Dichte und Art von Kristalldefekten oder von Korn- oder Inselgrenzen auf der Oberfläche, die wesentlich für ein Fortschreiten der Korrosion sind. Auf welcher Zeitskala bilden sich Passivierungsschichten und bei welchem Potential gibt es Veränderungen? Zusätzlich wurden mit ex-situ AFM Aufnahmen ein direktes Abbild der realen Oberflächen gewonnen. Die Ergebnisse werden in dieser Arbeit vorgestellt.

1.2 Röntgenbeugung als wichtige in-situ Methode

Seit ihrer ersten Beobachtung durch W.C. Röntgen im Jahr 1895 und der Verleihung des ersten Nobelpreises für Physik für ihre Entdeckung (1901) haben sich Röntgenstrahlen einen wichtigen Platz in der Materialforschung erschlossen. Röntgenstrahlen durchdringen Materie, aber die geringe Wechselwirkung ist noch groß genug um vermessen zu werden. Wegen der geringen Wechselwirkung können kompliziertere Prozesse, wie etwa eine Mehrfachstreuung, oft vernachlässigt werden und die Experimente können mit Hilfe der sog. kinematischen Theorie interpretiert werden. Das Braggsche Gesetz gibt eine eingängliche Interpretation der Beugung an Kristallen als Interferenzerscheinung von den an Atome-

benen im Material reflektierten einfallenden Strahlen (Abb. 1.1). Wird das Braggsche Gesetz für den Einfallswinkel ϑ erfüllt entsteht ein Reflex, der durch sogenannte Miller Indizes beschrieben wird. Die Miller Indizes beschreiben Atomebenen und damit Punkte des reziproken Raumes. Kristall-Defekte und Materialverspannungen oder auch das Vor-

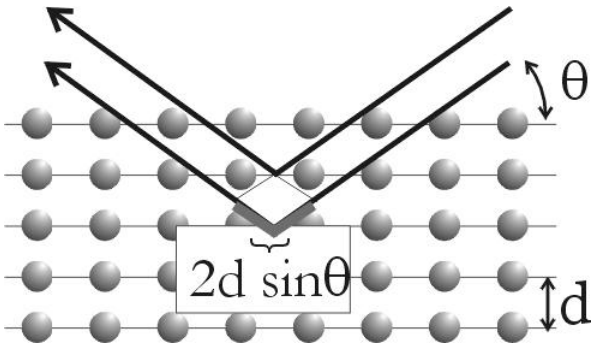

Figure 1.1: 2d sinθ=nλ. Das Braggsche Gesetz ist eines der grundlegenden Gleichungen der Rntgenbeugung. Es erklärt den gebeugten Röntgenstarhl als Interferenzerscheinung der an den Atomebenen reflektierten Strahlen.

handensein einer definierten Oberfläche, führen zu gebeugter Intensität auch an Stellen des reziproken Raumes an denen das Braggsche Gesetz für einen idealen Volumen-Kristall nicht erfüllt ist. Ausgehend von einem starken Kristallreflex erzeugt eine Oberfläche gebeugte Intensität entlang der Oberflächennormalen, die allerdings sehr schnell abfällt. Jedoch wird an modernen Elektronenspeicherringen die sog. Synchrotronstrahlung erzeugt, deren Röntgenstrahlen enorm intensiv sind, so dass diese Oberflächen-Effekte oft leicht zu messen sind. Bei gut ausgerichteten, niedrig-indizierten Einkristalloberflächen sind diese abfallenden Intensitäten zwischen Braggreflexen entlang der Oberflächennormalen verbunden. Die so entstandenen reziproken Gitterstäbe (englisch: CTR) können mit Synchrotronstrahlung gemessen werden und mit kinematischen Modellrechnungen verglichen werden. So lassen sich Strukturmodelle für Oberflächen erhalten. Mit intensiver Röntgenstrahlung aus Synchrotronquellen lassen sich selbst Braggreflexe von einzelnen Atomlagen noch messen. Die Intensität lässt sich oft unter Verwendung von streifendem Einfall der Röntgenstrahlen erhöhen (GID). Und mit Röntgenstrahlung höherer Energie (10-100 keV) lassen sich Studien an vergrabenen Grenzflächen, u.a. also Oberflächen in Kontakt mit Flüssigkeit oder einer Elektrolytlösung durchführen. Zur Beobachtung kristalliner Strukturen bietet sich daher die Röntgenbeugung als hervorragende in-situ Methode an.

1.3 Experimentelle Technik

Die Untersuchungen dieser Arbeit wurden an einkristallinen $Cu_3Au(111)$ Proben durchgeführt. Dabei wurden zwei verschiedene Arten von Proben verwandt. Zum einen wurden am Max-Planck-Institut für Metallforschung dünne epitaktische $Al_2O_3(11\bar{2}0)/Nb(111)/Cu_3Au(111)$

Filme mit Cu_3Au Schichtdicken von ca. 100 nm hergestellt. Diese Filme weisen zwei Arten von Domänen mit einer relativen Drehung um 60° (oder 180°) und mit einer Mosaikverteilung von etwas unter 1° auf. Die $L1_2$ Überstrukturordnung wurde durch eine langsame Abkühlung mit einer Temperaturrampe über 12 Stunden erreicht. Die Überstruktur-Reflexe waren danach ca. 1.5° (Rockingkurve) breit. Die Messung von CTR Intensität wurde mit diesen Proben nicht durchgeführt. Das Al_2O_3 Substrat wurde auch auf der Rückseite beschichtet um eine elektrische Kontaktierung in der Messzelle zu ermöglichen. Zum anderen wurden Cu_3Au Volumen-Einkristalle verwendet, deren (111) Oberfläche zuerst mechanisch poliert wurde. Diese Proben wurden vor den Experimenten im UHV mit den üblichen Methoden (sputter-annealing) präpariert. Für die Strukturbestimmung im Vakuum und für die Messungen der reziproken Gitterstäbe (CTR) in der Elektrolytlösung wurde der Kristall, mit der besten kristallinen Ordnung (mit einer Mosaikverteilung von etwas unter 0.1°) verwendet. Die $L1_2$ Überstrukturordnung wurde in einer mobilen Röntgen-Messkammer durchgeführt. Hier ließsich die Ordnungsübergangstemperatur T_c durch die Verfolgung eines $L1_2$ Überstruktur-Beugungsreflexes genau bestimmen und eine Reflexbreite von ca. 0.2° erhalten werden. So ließen sich sowohl Fundamental- als auch Überstruktur-CTR's durchgängig vermessen.

Für die in-situ Röntgenbeugung wurde eine elektrochemische Röntgen-Messzelle konstruiert, ähnlich zu Vorlagen aus der Literatur [fl87]. Diese sogenannte Dünnschicht-Zelle verwendet eine flexible dünne Folie (Mylar, 6μm) vor der Probenoberfläche um, zum einen, während der Änderung des Potentials eine ausreichend dicke Elektrolytschicht über der Probe zu ermöglichen. Zum anderen wird die Folie während der Röntgenmessungen auf die Probenoberfläche abgesenkt. Ein sehr dünner (ca. 10μm) Elektrolytfilm gewährleistet dann eine Potentialkontrolle an der Kristall-Elektrolyt Grenzfläche und gleichzeitig eine geringe Absorption der einfallenden Röntgenstrahlung. In der Zelle sind Anschlüsse für die üblichen Gegen- und Referenzelektroden, sowie Einlass und Auslass des Elektrolyten integriert. Die Zelle kann für Röntgenbeugungs-Experimente auf üblichen Diffraktometern befestigt werden.

Die Röntgenbeugungs-Experimente wurden an der europäischen Synchrotronstrahlungsquelle (ESRF) in Grenoble (ID32 und ID03), am Hamburger Synchrotronstrahlungs-Labor (HASYLAB) und an der Strahllinie des Max-Planck-Institutes für Metallforschung an der Ångstøm-Quelle Karlsruhe (ANKA) durchgeführt. Dort standen Diffraktometer zur Verfügung mit denen Beugung unter streifendem Einfall durchgeführt werden konnte.

Herkömmliche elektrochemische Experimente konnten im Elektrochemie Labor an der ESRF durchgeführt werden. An der ESRF konnte auch ein AFM (Molecular Imaging (MI) Dimension 3100) benutzt werden. Mit diesem Gerät wurden die AFM Aufnahmen

angefertigt.

1.4 Experimentelle Ergebnisse

Vor der Beschreibung der Ergebnisse sollen hier kurz die verwendeten reziproken Koordinaten eingefürt werden. Die Gitterkonstante von Cu_3Au beträgt a_0=0.3753 nm. Zur Beschreibung der Reflexe verwenden wir nicht die üblichen kubischen Miller Indizes, sondern auf die (111) Oberflache angepasste Koordinaten, mit zwei in-plane Vektoren mit 120° Winkel. Die in-plane Positionen H=1 oder K=1 entsprechen dann $2\pi/5.308\,\text{Å}$, bzw. der kubischen $(1\bar{1}0)$ Position. L=1 entspricht $2\pi/6.5\,\text{Å} = 2\pi/3\times 2.167\,\text{Å}$ in Richtung der Oberflächennormalen; wobei Cu_3Au {111} Atom-Lagen einen Abstand von 2.167 Å haben. Die Oberflächenkoordinaten werden durch den Index 's' gekennzeichnet.

1.4.1 Test Experimente

Da die experimentelle Ausrüstung für elektrochemische Experimente neu an einer Synchrotronstrahlungsquelle der dritten Generation mit einem sehr intensiven Röntgenstrahl aufgebaut wurden, entschieden wir uns Testexperimente an einem reproduzierbaren und leicht vorzubereitenden elektrochemischen System durchzuführen. Goldkristalle eigenen sich hierfür hervorragend, da ihre Oberfläche durch Tempern in einer Flame an Luft gereinigt und eine (thermisch) rekonstruierte Oberfläche mit atomar glatten Terrassen erhalten werden kann. Alle Untersuchungen an Au Oberflächen wurden in reiner 0.1 M H_2SO_4 Elektrolytlösung durchgeführt.

Oberflächenrekonstruktion von Au(111)

Die $\sqrt{3}\times$ 23 Oberflächenrekonstruktion von Au(111) ist im Elektrolyten bei kathodischen Potentialen stabil. Aus der Literatur ist bekannt, dass sich diese Rekonstruktion (sogenannte „herringbone" Rekonstruktion) reproduzierbar durch verändern des Potentials aufgehoben und wiedergebildet werden kann [oc90][et97][ma90]. Die durch die Domänen der Rekonstruktion erzeugten sechs Seiten-Maxima um die zentralen Bragg-Reflexe konnten in unserer Messzelle nachgewiesen werden. Jedoch zeigte sich, dass die Intensität der Seiten-Maxima geringer war als in der Literatur berichtet und die Periode war dazu größer als für die eingestellten Potentialen berichtet (normalerweise kommt es erst kurz vor der Aufhebung der Rekonstruktion zu einer Vergrößerung der Periode). Die Wiederbildung nach einer Aufhebung der Rekonstruktion (durch Erniedrigung des Potentials) war nicht

möglich. Eine Erklärung für diese Beobachtung ist eine mögliche Rest-Verunreinigung, etwa durch den starken Röntgenstrahl auf der Mylar-Folie, oder eine zu schlechte Wasserqualität, da zu dieser Zeit nur eine Filter-Anlage mit einem TOC-Wert von 15 ppb benutzt wurde.

Oberflächenrekonstruktion von Au(001)

Nach Erwerb einer Filter-Anlage mit einem TOC-Wert von 2 ppb konnten wir die reine Au(001) Oberfläche untersuchen. Hier existiert eine stabile hexagonale Rekonstruktion auf der kubischen (001) Oberfläche. Die thermisch rekonstruierte Oberfläche (nach dem Flammen-Tempern) wird durch einen einzigen Rekonstruktions-Beugungsreflex bei (1.2 1.2 0) im reziproken Raum (in üblichen kubischen Koordinaten) angezeigt. Bei einer im Elektrolyten gebildeten Rekonstruktion ist dieser Reflex zweifach aufgespalten. Die thermisch gebildete Rekonstruktion konnte erst nach Erwerb der reineren Filter-Anlage beobachtet werden, vorher war stets nur der aufgespaltene Reflex zu sehen.

1.4.2 Saubere $Cu_3Au(111)$ Oberfläche

An der Strahllinie des Max-Planck-Institutes für Metallforschung an der Ångstømquelle Karlsruhe ANKA konnte mit Hilfe einer mobilen Röntgen-UHV-Kammer die reine $Cu_3Au(111)$ Oberfläche im UHV studiert werden. Die Ordnung der $L1_2$ Überstruktur des Kristalles in der Kammer wurde mit Hilfe eines Überstruktur-Beugungsreflex überprüft und die Ordnungstemperatur optimiert. Mit einer Energie des Röntgenstrahls und eines durch die Kammer auf 54° begrenzten Ausfallwinkels des gebeugten Strahles konnten die reziproken Gitterstäbe $(22L)_s$, $(02L)_s$, $(11L)_s$ und $(10L)_s$ bis L=3.8 Å^{-1} vermessen werden (L=4 rlu). Mit Hilfe des Programes ANAROD [vl00] wurde ein Model für die Oberflächenstruktur ermittelt. Im wesentlichen enthält dieses Model einen verringerten obersten {111} Lagenabstand und eine nur zu 70% besetzte oberste Atomlage. Die Parameter sind in Tabelle 10.2 angegeben. Die {111} Lagen sind bis zur obersten Lage stöchiometrisch, es wurde also keine Segregation festgestellt.

1.4.3 Wachstum eines Passivierungsfilms

Die $Cu_3Au(111)$ Proben wurden für die Korrosionsexperimente aus dem UHV an Luft in die elektrochemische Röntgenzelle transferiert, wo sie dann unter angelegtem kathodischem Potential (ca. -100 mV vs. Ag/AgCl) mit der wässrigen 0.1 M H_2SO_4 Elektrolytlösung in

Kontakt gebracht wurden. Nach erreichen einer Überspannung für die Kupferauflösung reichert sich mit der selektiven Kupferauflösung Gold an der Oberfläche an.

Niedrige Überspannung

In-plane und out-of-plane Beugung zeigte ab einem Potential von ca. +100 mV die Entstehung einer ultra-dünnen epitaktischen kfz-artigen und goldreichen Au_xCu_{1-x} Schicht mit einer in-plane Gitterkonstante mit Werten zwischen denen für Cu_3Au und Au an. Bei geringen Überspannungen von weniger als 350 mV ist diese Schicht letztlich stabil. Die laterale Ausdehnung wurde aus den Reflex-Breiten auf ca. 15-20 nm abgeschätzt. Anhand der out-of-plane Messungen konnte die genaue epitaktische Beziehung und die sehr kleine Dicke der Schicht erkannt werden (ultra-dünne Oberflächenschicht). Die (111) Schicht-Normale ist dabei entlang der $Cu_3Au(111)$ Oberflächennormalen ausgerichtet und die Rotations-Orientierung der Schicht ist genau anti-parallel zum Substrat, d.h. die $(\bar{1}10)$-Richtung der Schicht zeigt in die $(1\bar{1}0)$ Substrat-Richtung. Möglicherweise sind für eine solche exakte Orientierungs-Beziehung der beiden kristallinen Strukturen (Schicht und Substrat) übernächste Nachbar-Wechselwirkungen der Atome verantwortlich. Nötige theoretische Rechnungen sind jedoch, nach unserer Kenntnis, noch nicht durchgeführt.

Die an einer Stelle durchgeführten CTR Messungen an der ultra-dünnen Schicht konnten durch ein einfaches krz Modell im wesentlichen beschrieben werden, ohne jedoch auf die Zusammensetzung (Au oder Cu) sensitiv zu sein. Dabei sind zwei Atom-Lagen voll besetzt und zwei weitere, mit 45% und mit 5%, nur teilweise. Demnach sind keine Beiträge von etwaigen Zwillingsinseln oder möglichen hexagonalen Inseln vorhanden. Die Beugungsmessungen zeigen jedoch auch, dass Abweichungen von einem kfz Model vorliegen, da die, von unterschiedlichen Braggreflexen abgeleiteten, Gitterkonstanten nicht übereinstimmen. Speziell die Reflexe entlang der $(0\ 1.9\ L)_s$ und der $(1.9\ 0\ L)_s$ (CTR) Stäbe ergeben unterschiedliche Werte, die jedoch mit größerem L-Wert näher zusammenrücken. So konnte ein extrapolierter Wert bestimmt werden. Die Werte der so aus den Beugungsmessungen abgeleiteten Atomebenenabstände, stimmen nicht mit den Werten für Volumenkristalle aus Gold oder Mischungen aus Gold mit Kupfer überein. Die Abweichungen für die ultra-dünne Schicht werden auf Kristall-Defekte zurückgeführt, die bei dem Wachstum bei Raumtemperatur wahrscheinlich vorhandenen sind. Unter Anwendung der elastischen Konstanten (für Volumenkristalle) können die Messwerte als verspanntes und reines, oder nahezu reines, Gold verstanden werden. Die Gitterkonstanten der stabilen ultra-dünnen Schicht liegen interessanterweise sehr nahe bei für eine freistehende ultra-dünne reine Goldschicht berechneten Werten [wo91]. Das elastische Verhalten ultra-dünner Filme ist jedoch noch wenig

untersucht. Anomale (Energie-abhängige) Messungen haben für eine ultra-dünne Schicht einen Kupfer-Anteil von 40% ergeben (Siehe Kapitel 1.4.5).

Erhöhte Überspannung

Bei größeren anodischen Potetialen (Erhöhte Überspannung) wurde die Entstehung von ca. 3 nm dicken Gold-Deckschichten beobachtet, mit Gitterparametern, die der Volumenstruktur entsprechen (dünne Goldfilme). Gleichzeitig verschwanden die Reflexe der ultra-dünnen Schicht. Wurde das Potential langsam bis zu erhöhten Überspannungen vergrößert, zeigten sich sofort Reflexe an der Au Position, während sich bei bei schneller Erhöhung (innerhalb einer Stunde) der in-plane Reflex kontinuierlich verschob. Die Schicht besteht, im Einklang mit ex-situ AFM Bildern, aus Inseln von ca. 20 nm im Durchmesser und einer Dicke von ca. 3 nm. Die Ausdehnung der Inseln ist also nur wenig größer als im Fall der ultra-dünnen Schicht. Die epitaktische Orientierung der monokristallinen Inseln war hauptsächlich wie bei den ultra-dünnen Inseln anti-parallel ausgerichtet. Jedoch war ein kleiner Beitrag der parallelen Zwillingsinseln vorhanden. Dieser Beitrag wurde mit erhöhtem Potential etwas höher.

1.4.4 Grenzflächen-Aufrauhung

Durch eine Oberflächenrauhigkeit kommt es zu einem Abfall der Intensität entlang eines entsprechenden reziproken Oberfächenstabes. Nach dem Transfer nach der Präperation aus dem Vakuum durch Luft in die elektrochemische Zelle konnten wir eine stark erhöhte Rauhigkeit nachweisen. Der Intensitätsabfall war hauptsächlich durch diese Rauhigkeit gegeben ($\beta \approx 0.56$) und die Messungen waren wenig sensitiv auf sonstige strukturelle Veränderungen. Es zeigte sich, dass die Rauigkeit sich während der ersten Kupferauflösung bei niedrigen, und anfänglich auch bei erhöhten, Potentialen nicht mehr anstieg. Erst mit der Bildung einer deckenden dünnen Goldschicht bei erhöhten Potentialen wurde eine wesentliche weitere Erhöhung der Rauhigkeit beobachtet ($\beta = 0.9$). Der anfängliche Auflösungsprozess verläuft ohne Erhöhung der Oberfächenrauhigkeit.

1.4.5 Anomale Streuung

An einer Absorptionskante eines Elements muss der Atom-Formfaktor um die sogenannten Dispersionsterme f' und f" korrigiert werden. Der Formfaktor zeigt dadurch einen charakteristischen Abfall an der entsprechenden Kante. Wird die Intensität eines Bragg-Reflexes um die Energie dieser Kante herum vermessen, lässt sich der Anteil des entsprechenden

Elements in der streuenden Struktur bestimmen (DAFS). Die etwas dickeren Goldinseln, die bei erhöhter Überspannung entstanden, zeigten bei anomalen Streuexperimenten an entsprehenden Beugungsreflex keine Abhängigkeit der Intensität im Bereich der Kupfer-Absorptionskante bei 8.975 keV. Der Kupferanteil des Cu_3Au Substrates konnte gut reproduziert werden. Oben wurde die Interpretation der Gitterparameter der ultra-dünnen Schicht als eventuell verspannte, jedoch reine Au Schicht vorgestellt. Im Gegensatz zu dieser Interpretation haben anomale Streuexperimente an einem entsprechenden Beugungsreflex einer ultra-dünnen Schicht einen Kupfer-Anteil von 40% ergeben. Die Messung zeigte einen deutlichen Abfall der Bragg Intensität an der K-Kante des Kupfers.

1.4.6 Zusätzliche Informationen

Zusätzliche Informationen konnten von der Charakterisierung von Proben nach einem Verlust der Potentialkontrolle gewonnen werden. Hier ist zwar das genaue Potential unbekannt, doch kann aus der Schichtdicke der meist entstandenen Au Passivierungsschicht auf die geflossene Ladungsmenge geschlossen werden. Die beobachteten Dicken lagen in derselben Größenordnung, wie bei den bei höheren Potentialen entstandenen dickeren passivierenden Au Inseln. Diese Ladung floss jedoch bei einem Verlust der Potentialkontrolle wesentlich schneller. Als Ergebniss lassen sich zum einen das Auftreten eines diffusen Untergrundes am Substrat Bragg-Reflex und entlang des CTR's beobachten und zum anderen eine unterschiedliche Epitaxie-Orientierung. Während bei Potential-kontroliertem langsamen Wachstum hauptsächlich nur die invertierte Stapelfolge verwirklicht ist (erst bei höheren Potentialen lässt sich ein kleiner Anteil mit paralleler Orientierung beobachten), sind bei einem Verlust der Potentialkontrolle bis zu 50% der gleich orientierten Inseln (im Vergleich zum Substrat) zu sehen. Die Schicht-Normalen sind in allen Fällen entlang der Substratoberflächen-Normalen ausgerichtet. Für die Orientierung der Schicht stehen dann zwei Möglichkeiten offen: eine Schicht mit der (bevorzugten) umgekehrten Stapelfolge im Vergleich zum Cu_3Au Substrat und eine Schicht mit derselben Stapelfolge.

1.4.7 Cl^--haltiger Elektrolyt

Bei Zusatz von 5 mM HCl zur 0.1 M H_2SO_4 Elektrolytlösung wurden im wesentlichen die gleichen Strukturen beobachtet, wie im Fall der Cl^--freien, reinen 0.1 M H_2SO_4 Elektrolytlösung. Jedoch trat der Übergang zu den entsprechenden reinen und relaxierten Au Inseln schon bei +250 mV auf, also ca. 150-200 mV unterhalb des Übergangspotentials in reiner 0.1 M H_2SO_4 Elektrolytlösung. Ein um einen solchen Betrag veringerten Wert wurde

auch für das kritische Potential in Cl^--haltigem Elektrolyten beobachtet [mo91].

1.4.8 Ex-situ AFM Bilder

Ex-situ AFM Aufnahmen an Luft zeigten bei Proben, die vorher im Elektrolyten einer Spannung von 250 mV (niedrige Überspannung) ausgesetzt waren, das Entstehen von korrelierten Inseln an. Die Autokorrelations-Funktion (HHCF) ergab Seitenmaxima (mittlerer Inselabstand) bei einem Abstand von 24 nm. Bei erhöhter Überspannung waren eine gleichmäßige Bedeckung der Substratoberfläche deutlich zu erkennen. Die Autokorrelations-Funktion (HHCF) ergab Seitenmaxima bei einem Abstand von ca. 40 nm. In der entsprechenden zweidimensionalen (2D) Berechnung waren deutlich eine sogar hexagonale Anordnung von Seitenmaxima zu erkennen. Auch in der Fouriertransformierten der HHCF (power spectral density, PSD) war ein mittlerer Abstand als Ringstruktur sichtbar. Bei Proben die während der Röntgenbeugungs-Messungen lange Zeit (länger als ein Tag) bei erhöhten Potentialen im Elektrolyten eingetaucht waren, liessen sich in den AFM Aufnahmen zusätzlich zu den dichtgepackten Inseln, poröse Bereiche erkennen. Interesanterweise zeigten die 2D Autokorrelation und die PSD ähnliche Muster, wie für die ursprüglichen dichtgepackten Inseln, jedoch mit einem sehr viel größeren mittleren Abstand von dann ca. 100-140 nm. Eine Erklärung für diese Ordnung der Inseln, bzw. der porösen Struktur, kann im Moment noch nicht angeboten werden. Um den Entstehungsmechanismus und die zeitliche Entwicklung deutlicher zu beobachten schlagen wir eine in-situ AFM Studie vor.

1.5 Ausblick

Mit in-situ Röntgenbeugung an potential-kontrolierten $Cu_3Au(111)$ Oberflächen in wässriger 0.1 M H_2SO_4 Lösung (teilweise unter Zusatz von 5 mM HCl) konnten strukturelle Veränderungen der Oberfläche und Veränderungen der chemischen Zusammensetzung beobachtet werden. Dabei zeigte sich, dass der Spannungsbereich unterhalb des kritischen Potentials E_c zwei unterschiedliche Oberflächen-Morphologien aufwies. Bei Zugabe von Cl^--Ionen war das Übergangspotential deutlich kathodisch verschoben (Im Einklang mit einer ähnlichen Verschiebung des kritischen Potentials). Begleitende ex-situ AFM Studien bestätigten die Ergebnisse der Röntgenbeugung und zeigten auch interessante zusätzliche Ordnungsstrukturen. Aus den Ergebnissen ergeben sich weitere interessante Fragestellungen:

- Besonders zeitabhängige Messungen versprechen zusätzliche interessante Ergebnisse.

- In-situ elektrochemische AFM Studien können das zeitliche Verhalten der Inselbildung und der weitergehenden Bildung der porösen Strukturen verfolgen und Entstehungsmechanismen zuordnen.
- Die Untersuchung der strukturellen Veränderungen im unterkritischen Potentialbereich unter Zugabe von Additiven, besonders von Inhibitoren wie etwa Thiolen, verspricht weitere interessante Ergebnisse.
- Die Ausdehnung entsprechender vergleichender Untersuchungen auf andere Oberflächenorientierungen und weitere Edelmetalllegierungen verspricht eine Erweiterung des Verständnisses der Legierungskorrosion.
- In-situ FTIR in wässriger 0.1 M H_2SO_4 Lösung kann das potential-abhängige Absorptionsverhalten von Sulfationen bestimmen.

Chapter 2

Introduction

The development of human civilization is closely related to the use of ever advanced materials. Gold and copper are the first metals used in human history, and only as early as 7000 years ago. Bronze is one of the first examples for improving material characteristics by alloying. Since these times corrosion is a known problem. The word corrosion has its origin in the Latin word „corrodere“, meaning „to eat away“. This observed degradation is caused by chemistry in the natural surrounding. The oxygen of the air, the chlorides of the salty sea water, nowadays the sulfur dioxide in the atmosphere. They all offer reaction partners to form the mineral products of corrosion, the apparent rusty surfaces. Corrosion is affecting the stability of bridges, the lifetime of cars and the reliability of electrical connections in microelectronics. Studies claim that the cost of corrosion is six percent of a nation's gross domestic product (GDP). It is though needless to state, that any progress in understanding corrosion and improving corrosion protection for technically used metals is highly desirable.

The basic processes of corrosion are chemical reactions that are also employed for the tailored production of respective structures. Dealloying produces nano-porous layers with possible applications in sensor systems [er01] and thin or ultra-thin oxide layers are used e.g. as templates for model catalysts [fr99] or as barrier layers in magnetic structures (Tunneling Magneto-Resistance, TMR). Also the use of metal alloys as catalysts rises knowledge of the alloy stability in various (reactive) environments. Corrosion research is thus embedded in a more general context and has impacts on various fields of modern technologies.

Corrosion can be defined as unwanted material degradation that starts from the surface by a chemical reaction with ambient reaction partners. Thermodynamically nearly all metals are less stable than their mineral compound. The reactions can be activated by high

temperatures, although in practice, most corrosion processes are electrochemical in nature. Due to our humid atmosphere liquid layers can form on the materials and create what is called a local electrochemical corrosion cell. The corrosion is then driven by potential differences e.g. formed by contact potentials. Nevertheless, fast corrosion rates are mostly overcome by the reaction products themselves. These form very often dense layers on the surface, that effectively hinder further reactions and are passivating the metal surfaces. Prominent example for such passivation layers is the clearly visible patina formation on copper or bronze statues or roofs.

Corrosion and corrosion resistance has mainly been a subject of largely empirical, trial and error engineering study in the last century. Basic research contributions were rare, because the explanation of corrosion phenomena is not at all straightforward. This is especially true for alloy corrosion. Corrosion science is interdisciplinary, including physics, chemistry, biology, metallurgy and surface science. Surface sensitive techniques were mainly developed in the second half of the last century. M.Faraday already introduced the idea of the passivating role of thin reaction product layers, but their existence was controversial. U.Evans could isolate for the first time thin passivating layers, also in cases where they have not been visible before [evn60].

Metals are mainly used in the form of alloys, because mixing certain specific components is improving the desired material properties. Stainless steel contains small amounts of chromium and other metals to improve hardness, lower brittleness and improve corrosion resistance. „The more elements, the merrier“[sh03]. Some binary alloys are better catalysts than their pure „parents“[mar01]. chemical surrounding and for a specific study one has to focus on a specific condition. Anodic dissolution is of basic importance not only for corrosion processes but also in many technologies, like electropolishing and electrowinnining of metals, battery electrodes, anodes for electrocatalysis, and the like. In the case of alloys two cases have to be considered. In the case where the equilibrium potentials of the alloy components is similar, the dissolution proceeds in a simultaneous way, with dissolution rates proportional to the composition. If on the other hand the equilibrium potentials are different the dissolution rates will differ from the proportional behavior. This can lead to passivation by selective dissolution of the less noble component and accumulation of the more noble one on the surface. At higher potentials this passivation is usual breaking down e.g. an onset of a large increasing current is observed in current-potential curves. This potential is called the critical potential and porous microstructures develop, assuring the contact of the solution with the reaction interface [pi63][ka86] [er01].

In low melting point samples like SnIn also bulk diffusion plays an important role in the restructuring of the surface during selective dissolution at subcritical potentials

and therefore rather thick passivation layers can be formed [[ka89]]. In contrast, for high melting point metals at ambient temperature, selective dissolution will rather result in very thin passivation layers; bulk diffusion plays here supposingly a minor role. Model systems studied for the case of high melting point selective dissolution and dealloying comprise noble metal binary alloys with a big difference of equilibrium potential of the components. These systems include e.g. CuPd, AgAu and CuAu alloys.

Anodic dissolution proceeds often from defect sites, like kink positions at mono-atomic steps, present on flat surfaces [ma00]. It also depends on the orientation of the surface in the case of single crystal experiments. In the case of the mentioned high melting point alloys the passivation layers forming in the passive region are often only monolayers thick. It is therefore obvious that experiments able to give information on an atomic scale will be highly beneficial for the improvement of understanding of alloy dissolution and corrosion. Two prominent examples for new techniques are scanning probe methods, including scanning tunnelling microscopy (STM) and atomic force microscopy (AFM), and surface sensitive x-ray diffraction with synchrotron radiation. The STM was invented by G.Binnig and H.Rohrer in 1982 and earned them the Nobel prize in the year 1986. Later the AFM followed. These techniques are nondestructive and able to give images of the topography of surfaces with atomic resolution and can be performed in electrochemical environment, thus enabling in situ experiments. The same is true for synchrotron radiation. With the large intensities offered from modern synchrotron radiation facilities, it is now possible to study surface effects in-situ in liquids and to obtain detailed structural information of the surface and below the surface, i.e. the entire surface-near region. Studies with synchrotron radiation are costly methods and the spot size in diffraction experiments is typically in the order of one millimeter and therefore integrating over a large size. Scanning probe methods are local and therefore complementary to (averaging) synchrotron experiments. There have been already some scanning probe studies on high melting point alloys in the last decade[ec01][op91]. This thesis is one of the first synchrotron radiation studies using single-crystal diffraction of electrochemical corrosion of binary alloys.

With the study of $Cu_3Au(111)$ in 0.1 M H_2SO_4 electrolyte solution (pH=1) we focus on structural changes during the selective dissolution of the less noble component Cu. In this acidic environment no Cu-oxide is stable and Cu will dissolve as Cu-ions in the electrolyte solution. Au is rather inert and will accumulate on the surface. Below the critical potential E_c of $Cu_3Au(111)$ this leads to a passivation effect. X-ray diffraction performed at modern synchrotron radiation facilities like the European Synchrotron Radiation Facility (ESRF) in Grenoble, France, provides an excellent tool for in-situ structural studies of surfaces of crystalline materials. The results of this thesis are presented in the following.

Chapter 3

Electrochemistry and Corrosion

3.1 Electrochemistry

Chemistry is the science of substances - how and of what they are made up, and also of the reactions that change them into other substances. Electro-chemical reactions involve always the transfer of one or more electrons from one of the reaction partners to the other one. Oxidation is the process through which an atom or a molecule looses electrons; reduction is the (reversed) process of gaining electrons. A neutral atom or molecule is often attributed an oxidation number of zero. Gaining one electron enlarges the oxidation number by one, while loosing one electron diminishes it by one.

$$\text{Reduced State} \quad \overset{-ne^-}{\underset{+ne^-}{\rightleftharpoons}} \quad \text{Oxidised State}$$

Historically, the observation of a physiological reaction of a frog leg to electrical charging by L.Galvani in 1785, led A.Volta to his discovery of the first battery, the Volta-pile. Such piles, and a better version invented by J.F. Daniell, were also used by M. Faraday to discover the laws of electrolysis. Nowadays electrochemical processes are widespread in use. Examples are electro-winning and refining of metals, e.g. the reduction of aluminum from the ore (Eq. 3.1), electrolysis, e.g. of sodium and chlorine from rock salt melts or of hydrogen and oxygen from water (Eq.3.2) and also electrodeposition of metals and battery technology (Eq.3.3). Reaction 3.3 is the basic reaction of the Daniell element.

$$2Al_2O_3(s)^1 + 3C \rightarrow 4Al(s) + 3CO_2 \tag{3.1}$$

$$2H_2O \rightarrow 2H_2 + O_2 \tag{3.2}$$

$$Zn_{solid} + Cu^{2+} \rightarrow Zn^{2+} + Cu_{solid} \tag{3.3}$$

In reverse direction, Reaction 3.2 is the basis for electrical energy conversion in a com-

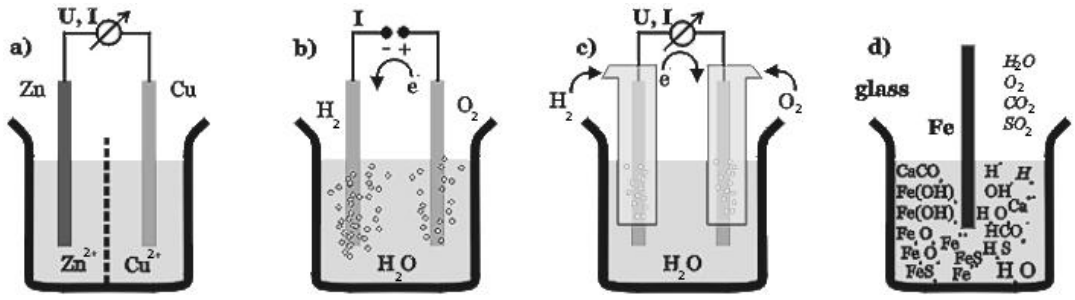

Figure 3.1: Some electrochemical systems: (a)the Daniell element, (b) water electrolysis, (c) hydrogen fuel cell reaction and (d) a simple Fe rod in town water.

bustion or fuel cell, with hydrogen as fuel. Further examples of modern electrochemical processes include magnetic layer deposition for computer storage hard discs, deposition of metal interconnects in semiconductor industry, as well as applications as sensors or in analytics.

3.1.1 Redox Reactions and Interface Structure

One of the important features of electrochemical reactions is that the partial reactions can be separated by the creation of two cells, which are electrically contacted. As an example we can take the mentioned Daniell element. The overall reaction is $Zn_{solid} + Cu^{2+} \rightarrow Zn^{2+} + Cu_{solid}$, which is Eq.3.3. Two electrons are transferred from a Cu atom to a Zn ion. In the setup of a Daniell element two cells containing an electrode of each metal and the solution of a respective metal salt are connected by a salt bridge. An electrode serves in general as source or drain of electrons. As this setup is only useful with both cells, a single cell alone is sometimes called "half cell". The two partial reactions, also referred to as electrode reactions, are then:

$$\begin{aligned} Cu^{2+} + 2e^- &\rightarrow Cu(s) \\ Zn(s) &\rightarrow Zn^{2+} + 2e^- \\ \hline Zn_{solid} + Cu^{2+} &\rightarrow Zn^{2+} + Cu_{solid} \end{aligned}$$

[1] in my notation, (s) means a substance in the solid state

To introduce some other basic definitions and formulas, we consider the half cell reaction $Cu^{2+} + 2e^- \rightarrow Cu(s)$. A Cu electrode is immersed in a aqueous solution of a Cu salt, e.g. $CuSO_4$. Water molecules, hydronium ions (H_3O^+), hydroxide ions (OH^-), sulfuric ions and Cu ions are thus in contact with a solid Cu surface. Similar to surfaces in contact with gas phases, adsorption of atoms and ions is taking place. But, as in aqueous solutions the ions are hydrated, we can distinguish two cases: first an approaching with no structural change of the hydration shell and second a stronger bonding to the surface, with the result of a at least partial stripping of the hydration shell and a closer approach of the ion to the surface. Some of the Cu ions will deposit on the surface and finally being incorporated in the crystal lattice by taking up two electrons (Reduction). And some Cu atoms from the solid Cu lattice will dissolve by going into solution as a Cu^{2+} ions, giving two electrons to the crystal lattice (Oxidation). As a result of these processes a mostly charged interface is built up, the so called "electrochemical double layer". Helmholtz, Gouy-Chapman, and Stern developed models for the structure of this double layer. The simplest approach, which holds to good approximation for high ionic concentrations in the electrolyte, is the Helmholtz model 3.1.1. If we do not allow for specific adsorption, i.e. all ions keep their hydration shell, all adsorbed ions will approach the surface up to a distance $\frac{1}{2}d$, which is determined by the extension d of the hydration shell. As can be seen in Figure 3.1.1, the situation is similar to a plate condensator, with one plane being the charged surface of the metal (or semiconductor) and the other plane being the layer of adsorbed hydrated ions. Gouy and Chapman introduced a model, where ions are not adsorbed, but are concentrated at the interface in a more extended diffuse layer. This is similar to the space charge region in semiconductor contacts. Because of insufficient screening owing to a much smaller concentration of charge carriers compared to metals, an extended 'space' charge region is formed, while on metals only 'surface' charges are observed. Finally, Stern combined the two existing models for the electrochemical double layer structure and also introduced the so called "Inner Helmholtz Layer" due to (mainly anionic) specific adsorption of ions at the electrode surface 3.1.1, b. The double layer is comparable to a capacitor and the capacitance depends on both, the chosen electrolyte and the surface structure of the electrode at a given potential. Indeed capacitance measurements are one electrochemical method to learn about the double layer structure at the electrode/electrolyte interface.

The driving force for the formation of the space charge or electrical double layer is the chemical potential of the freely moving particles, i.e. electrons in metals and semiconductors or ions in electrolyte solutions, so that at equilibrium the chemical potential has the same value everywhere. In general the chemical potential μ_n of a species n is defined via the molar free enthalpy G (or Gibbs energy) of the system. For a system with electrically

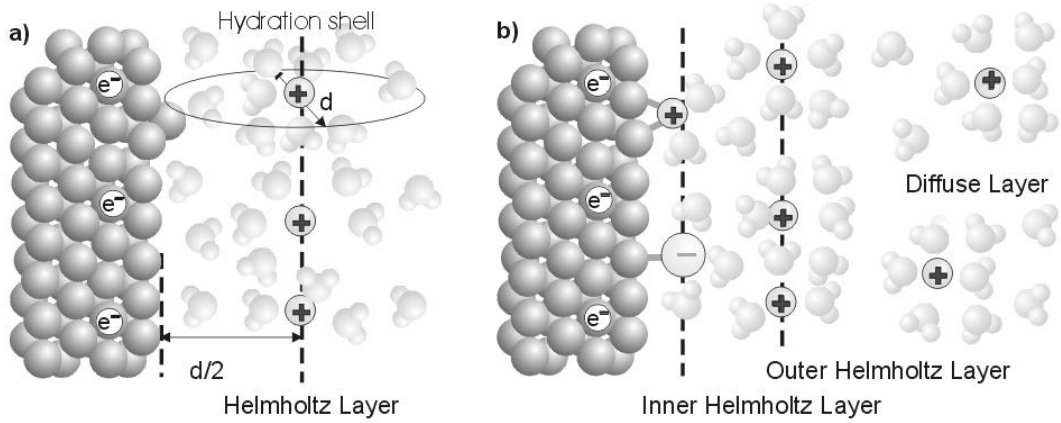

Figure 3.2: (a) The Helmholtz model of the double layer is essentially equal to a condensator and the potential drop is linear between the surface and the Helmholtz layer. (b) In the Stern model the linear potential drops at the two Helmholtz layers is followed by an exponential drop over the diffuse double layer region

neutral components n we can write:

$$G = \sum_n \mu_n N \qquad \text{N is the number of mols of the component } n$$

The equilibrium condition for a chemical reaction, with stoichiometric coefficients ν_n is, as known from standard thermodynamic text books:

$$\sum_n \nu_n \mu_n = 0 \tag{3.4}$$

For charged particles, G includes the energy due to the electrical potential at the site of the particle. We can assign an inner potential φ_i (or 'Galvani potential') to the sites of constant potential in the electrode and in the electrolyte. Since only potential differences can be measured, and the choice of φ_i (but not of $\Delta\varphi_i$!) is arbitrary. We can write the electrochemical potential $\tilde{\mu_n}$ as the sum of the chemical potential μ_n (without electrical field) and a term reflecting the electrical energy:

$$\tilde{\mu_n} = \mu_n + zF\varphi_i \tag{3.5}$$

In this equation, z is the charge of the particle and F is the Faraday constant.The chemical potential itself will be dependent on the actual concentration of the species in e.g. the electrolyte. Making use of the concept of activity in chemistry, where concentration and effects like solvation/hydration are taken into account, we can write:

$$\tilde{\mu_n} = \tilde{\mu_n^0} + RT \ln a_n \tag{3.6}$$

where μ_n^0 is a standard chemical potential defined by the condition of activity $a_n = 1$, R is the usual gas constant and T the temperature. If we combine Eq. 3.4, 3.5 and 3.6 for the case of the Cu partial reaction in Eq.3.3, we get for the equilibrium condition at an electrochemical interface of a solid electrode s and an electrolyte solution 'el':

$$\begin{aligned} \mu^0_{Cu(s)} + RT \ln a_{Cu(s)} &= \mu^0_{Cu^{2+}} + RT \ln a_{Cu^{2+}} + 2F\varphi_{el} \\ &\quad + \mu^0_{e^-} + 2RT \ln a_{e^-} - 2F\varphi_s \end{aligned}$$

The activity constants of Cu, $a_{Cu(s)}$, and of the electrons in the metal, a_{e^-}, will be effectively equal and we can therefore write:

$$\begin{aligned} \Delta\varphi &\equiv \varphi_s - \varphi_{el} \\ &= \frac{\mu^0_{Cu^{2+}} + \mu^0_{e^-} - \mu^0_{Cu(s)}}{2F} + \frac{RT}{2F} \ln a_{Cu^{2+}} \\ &= \Delta\varphi_0 + \left(\frac{RT}{2F}\right) \ln a_{Cu^{2+}} \end{aligned} \tag{3.7}$$

$\Delta\varphi$ is called the Galvani potential difference. As our considerations until now involved only a half cell or one electrode, $\Delta\varphi$ can not be measured as it is. Therefore we have to introduce a second electrode into the solution. This will be treated in the next section.

3.1.2 Electrochemical Cells and Standard Potentials

Because of there definition, 'absolute' potentials, cannot be measured, but only potential differences. In order to evaluate electrode potentials we have to create an electrochemical cell with two electrodes and not with one only. Ideally the additional electrode should be immersed in the same electrolyte to avoid liquid junctions and therefore additional potential drops. If we consider such an ideal second electrode we can then measure the potential difference ΔE between electrode 1 and electrode 2: $\Delta E = \Delta\phi(1) - \Delta\phi(2)$, and if the second electrode is surrounded by solution of activity $a_2 = 1$ we can write Equation 3.7 for the general case of a metal species with a corresponding ion of oxidation number z:

$$\Delta E = E^0 + \left(\frac{RT}{zF}\right) \ln \frac{a_{Me^{z+}}}{a_{Me(s)}} = E^0 + \frac{59mV}{z} \log a_{M^{z+}} \tag{3.8}$$

This formula is the Nernst equation for a metal electrode in contact with an electrolyte solution of its ions M^{z+}. We can set the activity a_{Me} equal to one. The potential E_0 can be in principle arbitrarily chosen, although it is convention to use the Standard Hydrogen

Electrode (SHE) as a reference for tabulated values as in Table 3.1. The SHE electrode uses the equilibrium that is attained when bubbling H_2 gas of 1 bar pressure over a platinum electrode immersed in an aqueous electrolyte with hydronium activity $a_{H_3O^+}$=1. This electrode has the advantage of reproducibly delivering a constant potential and was therefore used as a reference for measurements of the potential differences between two half cells. The overall reaction is catalyzed by the platinum surface (where atomic hydrogen is adsorbed) and is written as:

$$2H_3O^+ + 2e^- \rightleftharpoons 2H_2O + H_2$$

To describe the setup of electrochemical cells a convention was developed. The electrode and the respective active ion or redox pair are separated by a vertical line, as are different electrolytes. For our example of the Cu/Cu^{2+} electrode, the electrochemical cell can be written as:

$$Pt|H_2|H_2SO_4|Cu^{2+}|Cu.$$

If a salt bridge is used to connect two different electrolytes, a double line ‖is used.
A particularly important case is if one of the two half cells is the one studied, while the other serves simply to provide the opposite electrode (counter electrode, CE). In order to get easier interpretable results one is obliged to use an counter electrode with a rather high surface area (compared to the electrode under study). Diffusion and chemical reactions involved can give rise to saturation phenomena, which are avoided at the counter electrode, if the counter electrode area is rather high. This will be discussed in chapter 3.1.4.

3.1.3 Under-Potential Deposition

Within a pure metal/metal-ion electrolyte system of a specific metal the onset of deposition (or dissolution) is well defined by the respective Nernst equilibrium potential. However, for metal deposition on a foreign metal substrate, we have to consider the interaction of the substrate atoms Me_{sub} with the deposited adlayer Me_{ad}. When the interaction of Me_{sub}-Me_{ad} is stronger than the Me_{ad}-Me_{ad} interaction the first adlayer (in some cases also a double layer) is already deposited at potentials positive of the Nernst potential, i.e before the pure metal equilibrium potential is reached. This effect can be used as a single monolayer deposition technique and is called underpotential deposition (UPD) [ko78]. Not only different metals show UPD, but also hydrogen adsorption, e.g. on Pt surfaces [cl80]. Cu UPD on Au(111) in sulfuric acid solution is one thoroughly studied system [ma91][to95][it98]. This process is depicted in Figure 3.1.3 and serves here as an

Table 3.1: Table Standard Equilibrium Potentials for a Selection of Different Elements

Half Cell	Electrode Process			E_0, in Volt
$Au\|Au^+$	$Au^+ + e^-$	$\rightleftharpoons$	Au	$+1.420$
$Pt\|Pt^{2+}$	$Pt^{2+} + 2\,e^-$	$\rightleftharpoons$	Pt	$+1.188$
$Pd\|Pd^{2+}$	$Pd^{2+} + 2\,e^-$	$\rightleftharpoons$	Pd	$ca. + 0.900$
$Ag\|Ag^+$	$Ag^+ + e^-$	$\rightleftharpoons$	Ag	$+0.799$
$Hg\|Hg_2SO_4\|SO_4^{2-}$	$Hg_2SO_4 + 2\,e^-$	$\rightleftharpoons$	$SO_4^{2-} + 2\,Hg$	$+0.616$
$Cu\|Cu^{2+}$	$Cu^{2+} + 2\,e^-$	$\rightleftharpoons$	Cu	$+0.340$
$Pt\|Hg—Hg_2Cl_2 \mid Cl^-$	$Hg_2Cl_2 + 2\,e^-$	$\rightleftharpoons$	$2Cl^- + 2\,Hg$	$+0.268$
$Ag\|AgCl\|Cl^-$	$AgCl + e^-$	$\rightleftharpoons$	$Ag + Cl^-$	$+0.223$
$Pb\|Pb^{2+}$	$Pb^{2+} + 2\,e^-$	$\rightleftharpoons$	Pb	-0.126
$Ni\|Ni^{2+}$	$Ni^{2+} + 2\,e^-$	$\rightleftharpoons$	Ni	-0.230
$Pb\|PbSO_4\|SO_4^{2-}$	$PbSO_4 + 2e^-$	$\rightleftharpoons$	$Pb + SO_4^{2-}$	-0.276
$Co\|Co^{2+}$	$Co^{2+} + 2\,e^-$	$\rightleftharpoons$	Co	-0.277
$Fe\|Fe^{2+}$	$Fe^{2+} + 2\,e^-$	$\rightleftharpoons$	Fe	-0.409
$Zn\|Zn^{2+}$	$Zn^{2+} + 2\,e^-$	$\rightleftharpoons$	Zn	-0.763
$Al\|Al^{3+}$	$Al^{3+} + 3\,e^-$	$\rightleftharpoons$	Al	-1.706
$Na\|Na^+$	$Na^+ + e^-$	$\rightleftharpoons$	Na	-2.711
$Li\|Li^+$	$Li^+ + e^-$	$\rightleftharpoons$	Li	-3.045

example. Shown is a current-potential curve, also called voltammogram, which is described in the next chapter in more detail. At a potential marked as I, first a clean 1×1 Au(111) surface is observed and the Cu^{2+} ions are in solution. At potential close to II Cu^{2+} ions start to deposit, but only until a 2/3-coverage honey comb arrangement is formed (In a LEED image such an arrangement causes reflections at a distance of $1/\sqrt{3}$ times the original unit vector and rotated by 30°; it is therefore called a $(\sqrt{3} \times \sqrt{3})$R30° structure). This step is causing a first peak II in a current-potential measurement shown in Figure 3.1.3 due to the process $Cu^{2+} + 2\,e^- \rightarrow Cu$. Between the potentials a and b this $\sqrt{3} \times \sqrt{3}$ structure is stable and can be observed with STM [ma91] or X-ray diffraction [to95]. Interesting to note is that also the {111}-layers in Cu_3Au contain hexagons of Cu atoms (and with

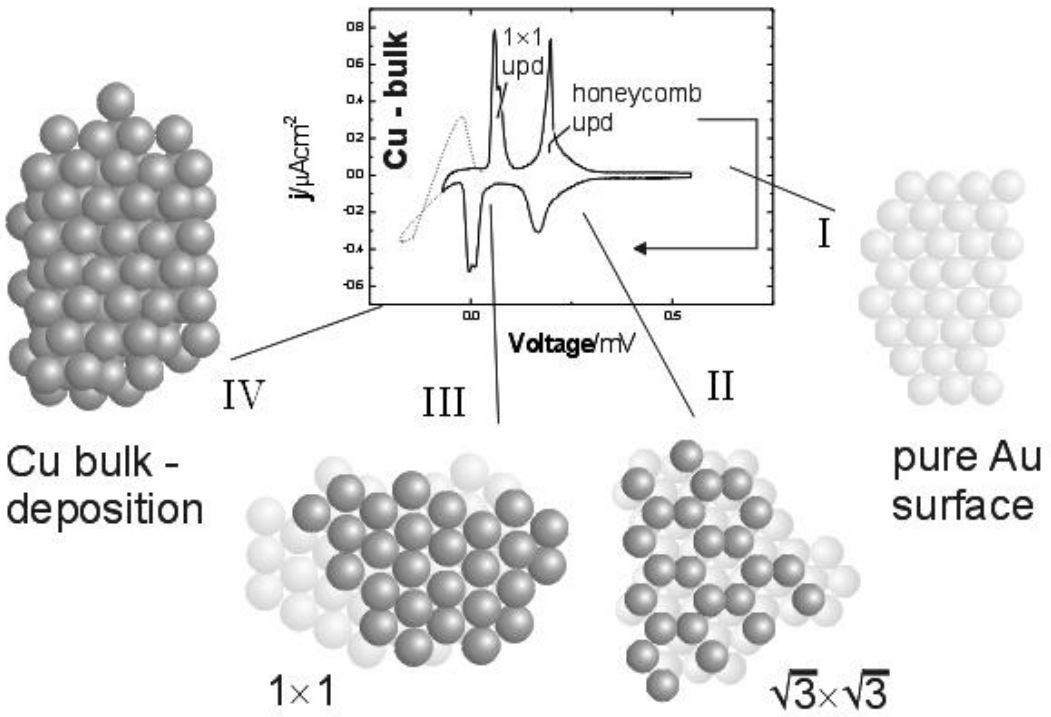

Figure 3.3: Monolayer deposition, which is also called underpotential deposition (UPD) is using favored hetero-metal bondings. The first monolayer is thus deposited at potentials before the respective bulk Nernst potential. Here as an example the Cu/Au(111) process is shown.

a Au atom in the middle), but the overall arrangement is different (see Figure B.1 to compare). At more negative potentials then a full 1×1 monolayer is completed (III), before the actual Cu bulk deposition starts at potentials negative of the Nernst potentials (IV). Although the interactions between different metals is well understood and can be estimated by considering for example the occurrence or not of mixed alloys, UPD is more complicated and other processes as solvation and pre-adsorbed species in different electrolytes have to be considered. Many studies examine the influence of specifically adsorbed anions on different UPD processes [gew97][it98]. The adlayer structure is not always pseudomorphic and the adlayer lattice constant can be dependent on the actual applied potential. This is referred to as electro-compressibility [ch97]. To conclude, UPD provides a unique method of a controlled, often exactly one monolayer, metal deposition on a foreign substrate in a small potential window before the onset of bulk deposition. The possibility of UPD layers has to be considered in special conditions of electrochemical reactions.

3.1.4 Overpotential and Electrode Kinetics

Until here we were considering equilibrium potentials. But in many cases we have to deal with non-equilibrium conditions, when either a current is forced through the electrochemical cell (galvanic mode) or a potential, different from the equilibrium conditions, is applied (potentiostatic mode). For nearly all chemical reactions, to proceed from reactants to products, an activation barrier E_a has to be passed (Figure 3.4 a).

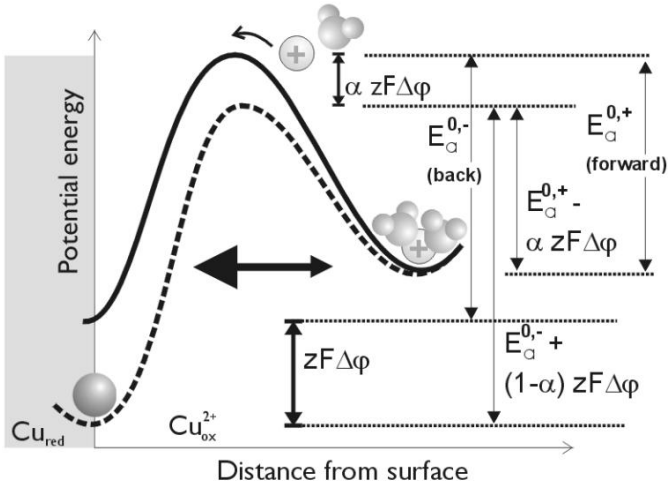

Figure 3.4: In the Arrhenius model the reactions are kinetically hindered by activation barriers. The rates (expressed by the Bultler-Volmer equation) for the reaction currents dependent on an applied potential can be derived.

In general the barrier height that has to be overcome depends on the direction of the reaction. In Figure 3.4 we consider the deposition of Cu on a Cu substrate. $E_a^{0,+}$ and $E_a^{0,-}$ are the forward and backward activation barrier heights at equilibrium. They can be changed by applying an external potential, different from the equilibrium potential, across the interface. For an additional applied potential difference $\Delta\varphi$ the energy difference of the reduced and oxidized state change by a factor of $\Delta E = zF \cdot \Delta\varphi$. The activation barrier occurs because the intermediate states between the initial and the final state are higher in energy. The influence of an applied potential on the intermediate states, i.e. the actual barrier height, is not straightforward to determine. Nevertheless one can introduce a phenomenological constant α, called asymmetry parameter, to describe the considered reaction barrier behavior. The asymmetry parameter has to be determined for each reaction, but has in many cases a value close to 0.5. The activation barriers will change according to this parameter, as shown in Figure 3.4

S.Arrhenius discovered in 1889 that chemical reaction rates depend on the activation barrier E_a, via a Boltzmann factor, known from statistical thermodynamics. This energy barrier occurs because the intermediate states between the original and the final state are associated with higher energies. The rate will also depend on the concentration c or

the activity a of the reactants and a specific rate constant k. This result can be used for expressing the electrochemical interface current. For our reaction $Me^{z+} + ze^- \rightarrow Me$ we can define a 'forward' current j^+ and a backward current j^-. We write η for the difference between the applied and the equilibrium potential. This difference η, is referred to as the applied "overpotential". If the rate of the entire reaction is determined by additional steps involved, then not the entire overpotential is entering in the occurring current, expressed by the Butler-Volmer equation as presented in the following. Since the externally applied potential changes the electrochemical potential, all contributing reaction steps (diffusion, additional chemical reactions, ...) have their proper partial overpotential (diffusion overpotential, reaction overpotential,...) in addition to the electron transfer overpotential, that is determining the bi-directional current through the electrochemical interface, expressed by $j^+$and j^- respectively. As a result we get:

$$j^+(\eta) = +j_0 \cdot \exp\{+\frac{\boldsymbol{\alpha} zF\eta}{RT}\} \tag{3.9}$$

$$j^-(\eta) = -j_0 \cdot \exp\{-\frac{(1-\alpha)zF\eta}{RT}\} \tag{3.10}$$

$$\text{with} \quad j_0 = zFc_{ox}k_0^+ \cdot \exp\{-\frac{(E_a^{0,+}}{RT}\}$$

$$= zFc_{red}k_0^- \cdot \exp\{-\frac{(E_a^{0,-}}{RT}\}c_{red}k_0^+ \tag{3.11}$$

The total current passing through the interface is the sum of the forward current and the backward current. This expression is also known as the Butler-Volmer equation:

$$j = j^+ + j^- = j_0 \cdot \left[\exp\{+\frac{\alpha zF\eta}{RT}\} - \exp\{-\frac{(1-\alpha)zF\eta}{RT}\}\right] \tag{3.12}$$

The Butler-Volmer equation predicts an exponentially rising current, when a higher overpotential is applied. The current in the opposite direction can be neglected. For small overpotentials, i.e. close to the equilibrium potential ($\eta = 0$), the forward and the backward currents become equal in size. Depending on the original rate constants k_0^+ and k_0^-, and on the concentrations c_{ox} and c_{red} at the equilibrium potential, the system is in a dynamic equilibrium and the exchange current j_0 can be calculated with equation 3.11. Further, it should be mentioned that a graphical semi-logarithmic representation of the measured currents against the potential, known as Tafel plot, yields the values for α and j_0 as slopes in the different regimes of low and high overpotential.

The Butler-Volmer equation does not completely describe kinetic processes at the electrochemical interface, but gives a first quantitative approximation. Important additional effects are diffusion of reaction partners or chemical reactions involved. If the electron

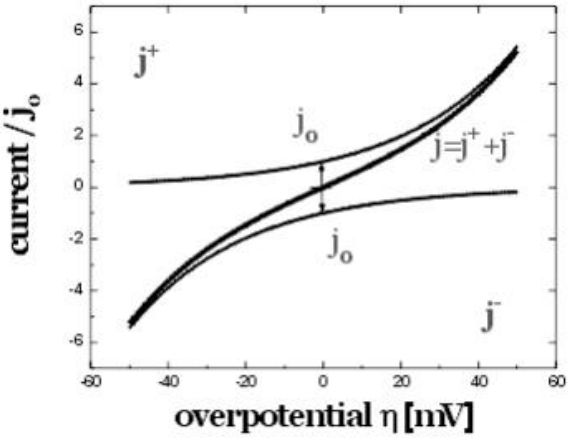

Figure 3.5: Electrical currents through an electrochemical interface as calculated by the Bultler-Volmer equation (asymmetry parameter α =0.5). At the equilibrium potential we observe an exchange current j_0. For $\alpha \neq 0.5$ the resulting curve becomes asymmetric and approaches j^+ (or j^-).

transfer through the electrode surface is not the rate limiting step, the concept of overpotential gets more complicated. In the current-overpotential curve this is reflected by a deviation from the described Butler-Volmer model. If the electrochemical reaction is limited by diffusion, at higher currents the current-potential curve will deviate from the exponential form and saturate, giving smaller current values.

3.1.5 Voltammetry as an Electrochemical Method

An important electrochemical method, called voltammetry (derived from $Volt - Am$pere $- M$easurement), relies on changing the applied potential and measuring the resulting currents. Information in such obtained current-potential curves is interpreted considering different electrochemical processes. This includes rising currents due to reached equilibrium potentials of certain processes as well as simple charging of the double layer capacitor, with in general changing capacity. For reversible systems the potential can be cycled between two values and the resulting current-potential curves can in many cases serve as fingerprints of ongoing processes. The voltammogram for the Cu UPD process described in Figure 3.1.3is an example. The method is then called Cyclic Voltammetry (CV) and the obtained curves are referred to as cyclic voltammograms (CV). Their shape is determined by external parameters like cycling speed or concentrations and mobility of involved species. For a quantitative evaluation of voltammetry data, appropriate correction procedures have to be applied. Currents other than these caused by interface capacitor charging are referred to as Faraday currents. Faraday currents occur, because specific processes, such as adsorption, desorption, deposition, dissolution, or redox reactions take place and involve a charge

transfer through the interface.

3.1.6 Practical Reference Electrodes

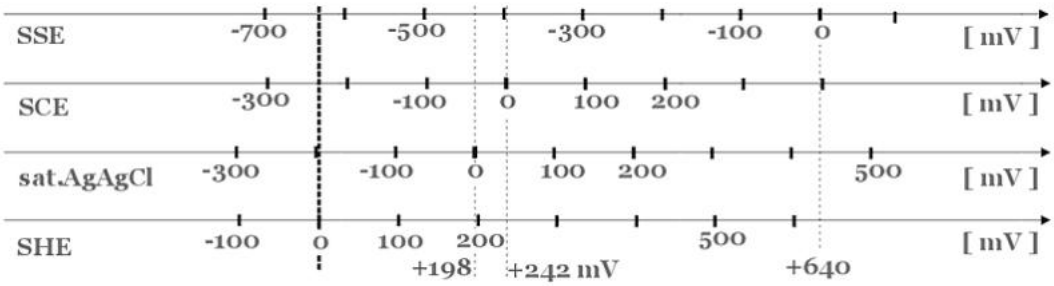

Figure 3.6: Graphical comparison of the most frequently used reference electrodes. Saturated Mercury Sulfate Electrode (SSE), Saturated Calomel Electrode (SCE), and the Saturated Silver Silver Chloride (Ag/AgCl). The Saturated Hydrogen Electrode (SHE) is used as reference in the literature.

In day to day laboratory work there is a strong demand for easy-to-use reference electrodes. From this point of view the hydrogen-platinum half cell has some disadvantages. The platinum has to be freshly prepared to avoid poisoning. Also the purity of electrolyte and hydrogen gas has to be guaranteed to obtain reproducible potentials. Instead, mainly used in laboratories are the so-called electrodes of the second kind. In addition to the electrode and the solution containing the active metal-ion, a salt of this metal-ion with low solubility is present in the system. So the activity of the metal ion is mainly dependent of the solubility product of the salt. The activity of the anion is influencing the final potential as well, but less than the activity of the active cation. Widely used electrodes of the second kind are the saturated silver silver chloride electrode (sat.Ag/AgCl) and the Saturated Calomel Electrode (SCE). The Ag/AgCl electrode can be also manufactured in form of very small micro reference electrodes.

Table 3.2: Common reference electrode systems of the second kind, taken from [ha98]

Half Cell	Solution	Electrode Process	E_0, in Volt
silver-	a_{Cl^-}=1		+0.223
silver (Ag/AgCl)	saturated KCL	AgCl + $e^- \rightleftharpoons Ag + Cl^-$	+0.198
chloride	KCl(c = 1M)	Half cell: Ag|AgCl|Cl^-	+0.237
electrode	KCl(c = 0.1M)		+0.289
	a_{Cl^-}=1		+0.268
Calomel (SCE)	saturated KCL	Hg_2Cl_2+ 2 $e^- \rightleftharpoons$ 2Cl^-+2 Hg	+0.242
electrode	$KCl(c = 1M)$	Half cell: Hg|Hg_2Cl_2|Cl^-	+0.281
	KCl(c = 0.1M)		+0.334
Mercury	$a_{SO_4^{2-}}$=1		+0.616
Sulphate (SSE)	saturated K_2SO_4	Hg_2SO_4+ 2 $e^- \rightleftharpoons$ SO_4^{2-}+ 2 Hg	+0.640
Electrode		Half cell:Hg|Hg_2SO_4|SO_4^{2-}	
Lead	$a_{SO_4^{2-}}$=1		−0.276
Sulphate		$PbSO_4$+ 2 $e^- \rightleftharpoons$ Pb + SO_4^{2-}	
Electrode		Half cell:Pb|$PbSO_4$|SO_4^{2-}	

3.2 Corrosion

Chemically rather inert metals are referred to as noble metals. An electrochemical definition of the term 'noble' uses the series of standard potentials, which have positive values for noble metals. Historically, these were the metals that were found in their elementary state on earth. All other metals had to be reduced from their ores, since these ores are in ambient atmosphere thermodynamically more stable than the respective pure metal. Our atmosphere offers, at least at the surface of the earth, the necessary reaction partners. Gold is the only metal that is also thermodynamically stable in our ambient conditions. Nevertheless has the use of metals as materials revolutionized the human life. The reason why we can make reliable tools or construction materials from metals is that through the reaction with oxygen, sulfur species or halogenoids, the surface is covered with a structurally different layer. This often very complex layer is protecting the metal underneath. The corrosion reaction is kinetically hindered through this passivating layer.

But corrosion failure is nevertheless accompanying the application of metals. Immense costs are arising to protect metallic materials from corrosion. Painting, special surface treatments, replacement of affected parts, and also associated material failure and

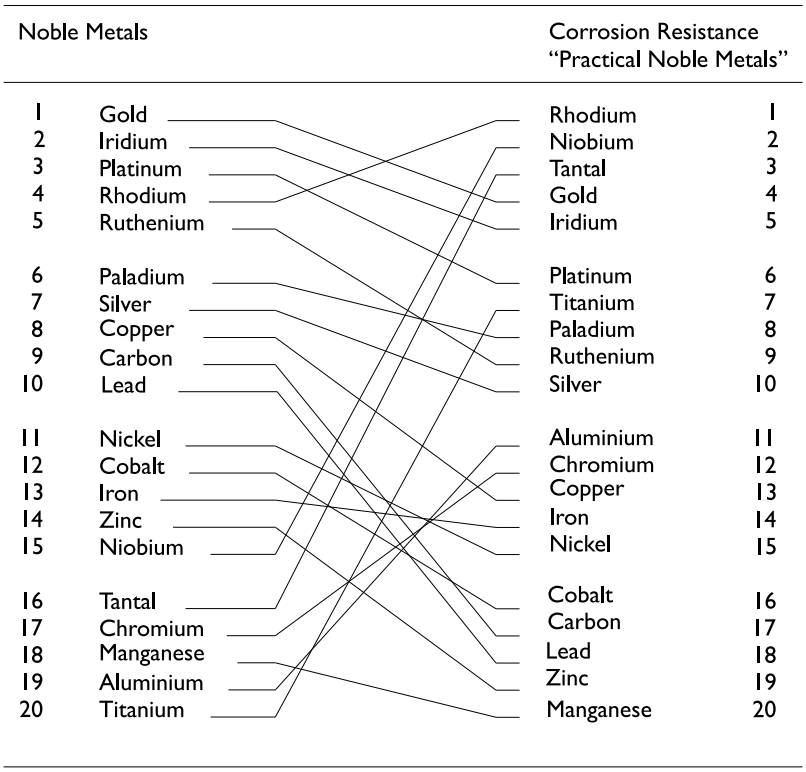

Figure 3.7: If the noble metals (sorted by standard potential) are listed with respect to their practical corrosion resistance the order is changing. Often more reactive metals form oxide layers with less structural defects and are thus better passivated and less susceptible to pitting and high diffusion rates than comparatively less reactive metals. The structural details of the passivation layer play an important part in corrosion resistance.

accidents- a society is spending 3-6% of its GDP because of corrosion [corr]. Improvement of our knowledge of the mechanisms of corrosion and improvement of corrosion protection is highly desirable. Figure 3.2 is showing the influence of formed protecting or passivating layers on the applicability of metals. We see that often thermodynamically less stable metals are nevertheless practically more useful. The better a particular metal is resisting to corrosion, the longer is its lifetime in possible applications. For different applications in various fields, e.g. food storage, petrochemical industry, high temperature turbines, ... specific materials are chosen. Special alloys are developed and in widespread use. Stainless steel has replaced the silver spoon at the table, and Ni based superalloys find their domain in aircraft turbines.

3.2.1 Dry Oxidation Theory

Although we study in this work electrochemical interfaces in aqueous solutions, a very short overview of the main aspects in dry oxidation is given here. Oxide formation is by far more studied than the formation of sulfide or chloride layers. The basic models for oxidation are thus dealing with a homogeneous oxide layer formed at the surface of the metal substrate [we86] [fro76]. After an initial growth all the surface is covered with an oxide layer and the growth of its thickness with temperature and time is the topic of many studies. For further oxide growth after completion of a closed layer the following basic processes can contribute to the overall oxide growth rate:

- Electron or hole tunnelling through the oxide layer. The tunnelling process is especially important for very thin layers.
- Diffusion of metal ions towards the surface and oxygen ions towards the metal-oxide interface. Diffusion is enhanced by defects, so structural properties are important.
- Electron thermoemission into the oxide conduction band and subsequent diffusion to the surface. Thermoemission plays an important role for high temperatures.

For oxidation to proceed, at least the diffusion of one ion or atom species is necessary. Oxygen and metal atoms have to meet to further form an oxide. This can happen either at the surface or at the interface. In order to be able to derive an explicit formula for the growth rate one of the basic processes is considered as the rate determining step. In reality often many processes occur at the same time. C. Wagner developed already in 1938 a formula to describe the growth of already rather thick oxide layers [wa33]. In his theory the thickness increases with a parabolic time dependence and can be expressed with the parabolic rate constant k_p:

$$L(t) = k_p\sqrt{t}$$

For thin layers (from nm up to $1\mu m$) much higher rates are observed [at85]. Important at room temperature are the electron tunnelling process, and diffusion, enhanced by defect rich thin oxide layers. Within certain assumptions one can get to growth laws which depend logarithmically on the time.

$$L(t) \sim \log(t)$$

At ambient temperatures the logarithmic growth effectively stops after reaching a certain thickness. In cases where only the metal ion diffuses often voids are produced, often directly in the neighborhood of vertical defect lines serving as diffusion channels. Structural details and morphology of the surface near region are coupled to the practical corrosion resistance.

3.2.2 Electrochemical Corrosion

Most corrosion reactions are electrochemical in nature, driven by e.g. contact potentials between dissimilar metal regions. In section 3.1.2 we introduced the Nernst Equation, expressing the equilibrium potential depending on concentrations of the reaction partners (in electrochemistry the activity is frequently set equal to the concentration, in case dilute electrolytes of low concentration are used) . In aqueous electrolytes often the hydronium ion H_3O^+ is participating in the reaction. The cathodic (hydrogen evolution) and anodic (oxygen evolution) partial reactions are:

$$2\,H_3O^+ + 2e^- \rightarrow H_2 + 2\,H_2O \tag{3.13}$$

$$2H_2O \rightarrow O_2 + 4H^+ + 4e^- \tag{3.14}$$

For metals in aqueous solutions, the metal ions in the solution are in equilibrium with the solid state:

$$Me(s) + zH_3O^+ \rightarrow Me^{z+} + \frac{z}{2}H_2O \tag{3.15}$$

With the hydronium ion participating in the reaction, the pH value is entering in many calculations for the equilibrium potential. The basic metallic corrosion reaction is the oxidation of a metal atom in a solid state. The associated redox pair of the process is thus the metal/metal ion pair M/M^{z+}. Using Eq. 3.8 we can write for the pH-dependent equilibrium potential:

$$E = E^0_{M/M^{z+}} + \left(\frac{RT}{F}\right) \ln c_{H_3O^+} = E^0_{M/M^{z+}} - 0.059V \cdot pH$$

with the definition of pH, as $\mathrm{pH} = -\log \mathrm{c}_{H_3O^+}$ and the relation $\ln(\mathrm{x}) = 2.3\log(\mathrm{x})$ included. The dependance of the equilibrium potential on the metal ion concentrations is contained in $E^0_{M/M^{z+}}$. This equation holds also for the electrolysis reactions of water itself (Eq. 3.13 and 3.14). With the hydronium ion participating the process in Eq. 3.15 is also called acid corrosion; the partial reaction of the metal dissolution, $\mathrm{Me} \rightarrow \mathrm{Me}^{z+} + 2\ \mathrm{e}^-$ is coupled with the hydrogen evolution reaction Eq. 3.13. If oxygen is dissolved in the solution the metal dissolution is coupled with the reduction of oxygen, $\mathrm{O}_2 + 2\,\mathrm{H}_2\mathrm{O} + 2\mathrm{e}^- \rightarrow 4\,\mathrm{OH}^-$. This later reaction has a more positive equilibrium potential compared to the hydrogen evolution reaction and, what is then called oxygen corrosion, is therefore more favorable to occur. With oxygen dissolved in the electrolyte the metal oxydation (corrosion) rates are in general higher.

3.2.3 Pourbaix Diagrams

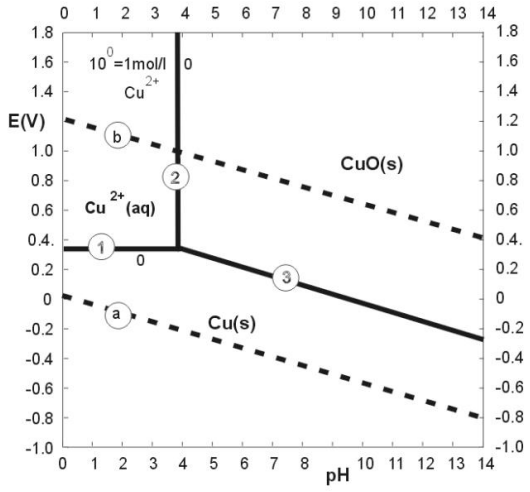

Figure 3.8: A Pourbaix diagram for Cu in aqueous solution, considering only Cu, Cu^{2+} and CuO. A Pourbaix diagram is the graphical representation of the pH dependent equilibrium potentials of the considered reactions (Equations 3.16). The lines a and b limit the stability region of water.

We saw above that the equilibrium potential E of such reaction depends on the pH value, giving for example a slope of -0.059 V/pH in a potential-pH diagram for a reaction with two hydrogen ions and two electrons involved. Such potential-pH diagrams are the graphical representations of the pH-dependent equilibrium potentials and are referred to as 'Pourbaix' diagrams [po63]. The lines for each considered reaction are plotted and for reactions involving hydronium or hydroxide ions, the slope depends on the number of transferred electrons and of the number of participating hydronium ions. In Figure 3.8 five reactions are considered. The drawn broken lines (a) and (b) enclose the stability range of water, limited on the cathodic and the anodic side by the onset of equations (also 3.13 and 3.14). Beyond this regime a large quantity of gas will be produced, i.e. the partial pressure of H_2 or O_2 will exceed the ambient pressure, so that a gas phase can form. (1),(2) and (3) correspond to reactions with Cu atoms involved.

$$
\begin{array}{lrcll}
\text{(a)} & H_2 & \rightleftharpoons & 2H^+ + 2e^- & E_0{=}0.00\,\text{V}- 0.059\,\text{V}\cdot\text{pH} \\
\text{(b)} & 2H_2O & \rightleftharpoons & O_2{+}4H^+ + 4e^- & E_0{=}1.23\,\text{V} - 0.059\,V\cdot\text{pH} \\
\text{(1)} & Cu(s) & \rightleftharpoons & Cu^{2+} + 2e^- & E_0{=}0.337\ \text{V} \\
\text{(2)} & Cu^{2+}{+}\ H_2O & \rightleftharpoons & CuO(s){+}\ 2H^+ & \log Cu^{2+}{=}7.89 - \text{x}\cdot\text{pH} \\
\text{(3)} & Cu(s){+}\ H_2O & \rightleftharpoons & CuO(s){+}2H^+{+}2e^- & E_0{=}0.570\text{V}-0.059\,\text{V}\cdot\text{pH}
\end{array}
\tag{3.16}
$$

The dependence on the metal ion concentration of the systems represented in a Pourbaix diagram is included by plotting several (parallel) lines, representative for the different concentrations and normally labeled by the exponent of the concentration. In the Figures 3.8 and 3.2.3 the lines correspond to a fixed concentration of Me^{z+} of 10^{-6} mol/l and of 1 mol/l respectively.

With this background in mind, we can define three corrosion regimes. First, the potential-pH regions where the elementary metal is stable is called immunity. Further, the regions where the corrosion reaction (i.e. metal oxidation) is thermodynamically possible are separated in a second regime called passivation regime and a third one called corrosion regime. In the passivation regime the growing layer is protecting or screening the metal from further contact with the oxidizing species. Like that, the corrosion rates are slowed down, often by many orders of magnitude. Crossing the line from a passivated regime to an inert or immune regime is also referred to as 'activation' of the metal. The passivating layer is then dissolved and the metal is the in direct contact with the solution. Especially in heterogeneous catalysis this activation can be of crucial importance. In the corrosion regime the corrosion product layer is often formed with a porous structure and the surface is not protected, allowing ongoing high corrosion or dissolution rates. There is no clear separation between the passivation regime and the corrosion regime. Figure 3.2.3 is showing simplified Pourbaix diagrams for different metals with indication of the three regimes.

3.2.4 Corrosion of Binary Alloys

In fact, most of the technically used metals are alloys. By varying the specific composition superior material properties can be achieved. These properties include mechanical strength, elastic properties, and corrosion resistance in many different specific environments.
Up to here we have considered the electrochemical behavior of pure elements. To use this knowledge for composite materials we have to be careful. One of the most significant electrochemical values of a certain metal is the Nernst or equilibrium potential E°. As a first approximation, we can consider an alloy AB as a mixed crystal with the respective atoms A and B obeying the equilibrium potential of the pure metal i.e. taking the Nernst potential values for the elements. Only the case when no product layer is stable is taken into consideration (i.e. we consider pure dissolution, as with the formation of additional overlayers the situation gets even more complicated). Supposing now that the activity of the metal atom in the surface is not equal to 1 and will be related to the actual composition fractions c_A and c_B=(1-c_A) for the binary alloy via an activity coefficient, $a_{A,B}$=$f_{A,B} \cdot c_{A,B}$,

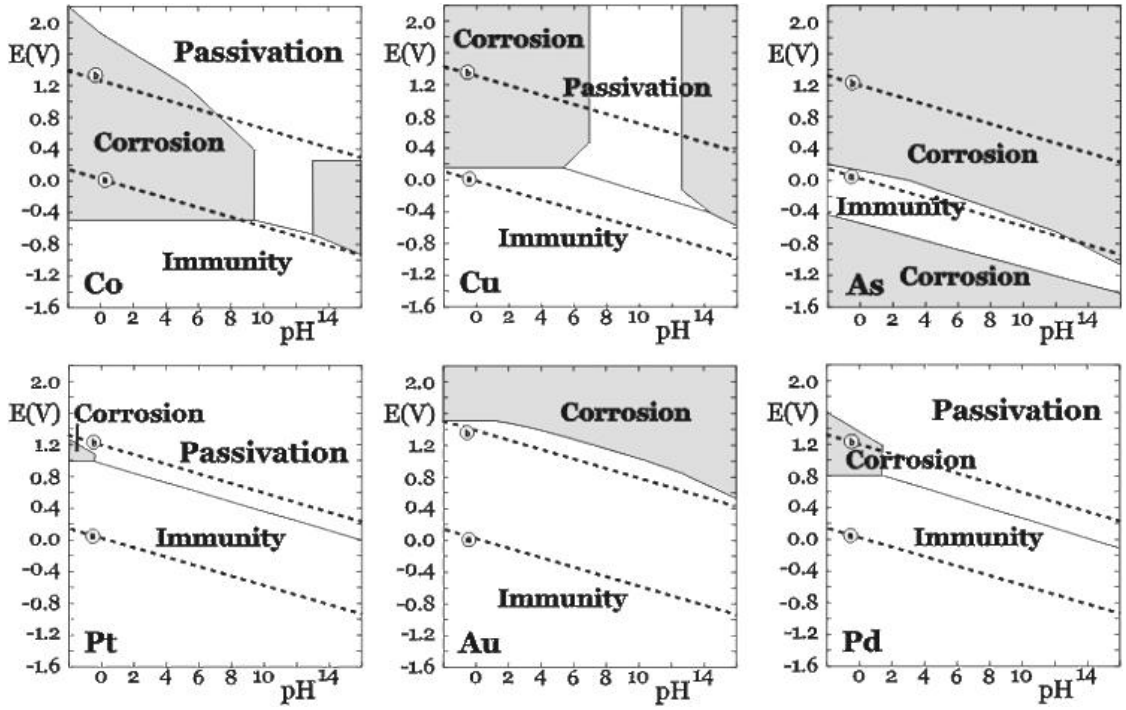

Figure 3.9: Corrosion diagrams for several metals in aqueous electrolytes. To plot these diagrams the concentration of metal ion in solution has been assumed to be 10^{-6} mol/l. In the region of immunity the metal is thermodynamically stable, while in the passivation region a oxidation product layer is covering the surface. In the corrosion regime high oxidation rates are maintained. Plots are from [po63]

we can write for the two elements:

$$E_A = E_A^0 + \left(\frac{RT}{zF}\right) \ln \frac{a_{A^{z+}}}{a_A} \quad \text{and} \quad E_B = E_B^0 + \left(\frac{RT}{zF}\right) \ln \frac{a_{B^{z+}}}{a_B} \tag{3.17}$$

Putting these two relations together with the equilibrium condition E_A=E_B for a mixed system of both elements, will yield:

$$\frac{a_B^{z+} + a_A}{a_A^{z+} + a_B} = \exp\left((E_A^0 - E_B^0)\frac{F}{RT}\right). \tag{3.18}$$

We see from this equation, that in case of a difference in Nernst potentials also a difference in the activities of the two metals has to be established to reach equilibrium. This implies that the open circuit potential (OCP) of the mixed electrode will lie in between the two elementary potentials. Alloy behavior for dissolution will vanish if the two elements, A and B, possess very similar Nernst potentials. The difference should be not larger than the thermal energy at room temperature, i.e. $\Delta\mathrm{E}^0 = \mathrm{E}_A^0 - \mathrm{E}_B^0 \leq \frac{RT}{F}$. In this case the

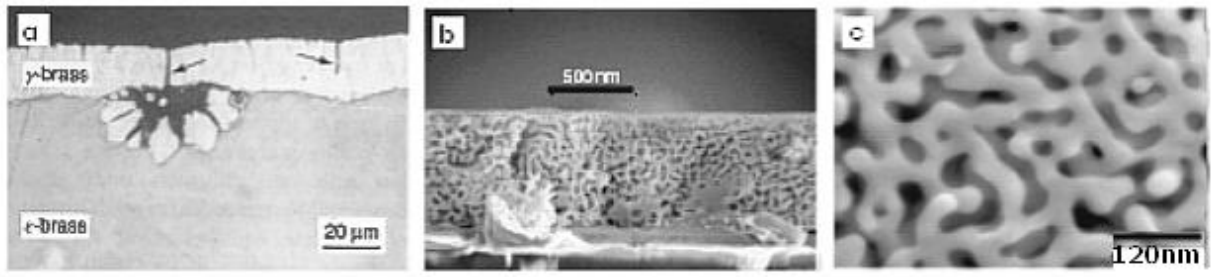

Figure 3.10: The developing morphology of the surface is important for the passivation of corroding materials. An attempt to classify different materials is to distinguish according to their melting temperature T_M, because it is related to the diffusion constants at room temperature. Low melting temperature materials (a shows brass as an example [ka03]) develop often thick passivation layers and cracks play a major role in their corrosion. For high melting point materials the low diffusion rate prevents the formation of thick passivation layers and a porous microstructure is evolving with ongoing corrosion. These might find application in sensors or catalysis [er01]

two elements will dissolve simultaneously and small deviations in Nernst potential will be controlled by small changes in activity, i.e. concentrations of the Elements A and B.
More difficult to treat is the case of a big difference in Nernst potentials of the components A and B, $\Delta E^0 \gg \frac{RT}{F}$. In this case selective dissolution will occur.

Low-Melting-Point Alloys: Volume Diffusion

In-Sn, Zn-Cu (brass), Zn-Fe and Zn-Ni alloys, among others, are low melting point alloys. In their case volume diffusion plays an important role, due to their higher diffusion coefficients, related to their relative low melting point [ka89] [ka03]. Selective dissolution results for these materials in rather thick depleted layers at the surface (Fig. 3.2.4a). The composition of the dissolved component is increasing with depth towards the bulk values. The observed depletion often induces phase transformations. For In-Sn, the involved phase have very similar specific volumes and therefore no obvious porous structure is developed during dissolution of In and a rather smooth interface develops. The process is controlled completely by volume diffusion and is described by a parabolic rate law, like in the advanced (thick layer) dry oxidation. For the Zn alloys the situation is different: as the involved phases are different in specific volume, stress is accumulated in the product layers and finally released by formation of cracks. A porous crack-structure is thus evolving and the cracks are opening or facilitating direct access of the solution to the interface. As can

be seen in Figure 3.2.4 diffusion models fail after the growth of a first coherent layer, with a thickness in the order of μm, and the material deterioration by corrosion proceeds faster.

High-Melting-Point Alloys

Selective dissolution produces a passivating behavior at intermediate potentials and results close to or above the so-called critical potential in porous structures. The porous 'backbone' consists of nearly only the nobler component of the alloy. The term 'dealloying ' is referring to this fact.

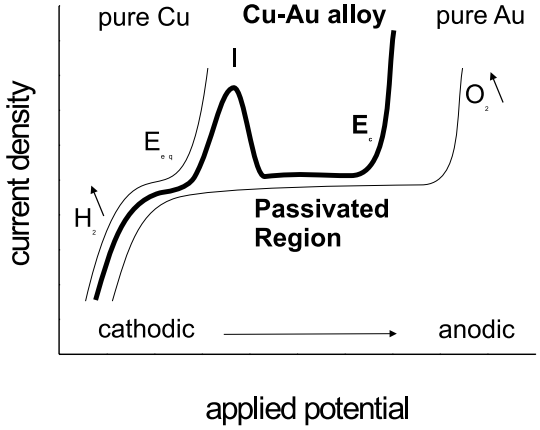

Figure 3.11: Schematic description of the selective dissolution of Cu from Cu-Au alloys. Initial selective dissolution of Cu from Cu-Au alloys creates an Au-rich layer, which is passivating the surface and prevents further dealloying. Reaching E_c the onset of (massive) dealloying is observed, together with the formation of a porous Au layer

Two differences compared to the low-melting-point alloys are most obvious. First, dealloying occurs only, if a certain concentration limit is surpassed. This limit is called "parting limit" in the literature and was first described by Tammann in 1919 [tam19]. Below the parting limit the less noble species will not reach the surface after an initial dealloying and the electrode will behave like an electrode made of the noble constituent. Second, as with lower diffusion coefficients much less material is transported via bulk diffusion to the dissolution interface, high melting-point alloys develop often a pronounced porous microstructure with advanced dissolution. The question of the influence of the initial surface structure has not been answered yet. The element with the higher equilibrium potential (i.e. the more noble element) will accumulate on the surface and bloc further dissolution of the less noble element. This blocking behavior is called passivation of the surface, like in the case of product layers (oxides,...). The involved thickness is reported to be in the monolayer up to nm range. For the selective dissolution process of binary alloys this passivation holds until a more elevated potential is reached and the dissolution current largely rises. This point is called the critical potential. Still under question is the nature

of the critical potential. At the critical potential, and above, a change in morphology is observed, and often the development of porous layers on the surface. This porous structure was reported to change and coarsen with long time scales [ne94]. But already below the critical potential a pit formation was observed [str01] and in this work we observe a porous surface forming on long lime scales (days)and as well below the critical potential.

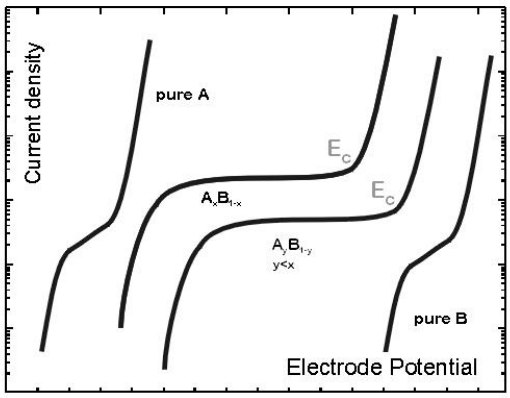

Figure 3.12: Sketch of the general alloy behavior. The alloy composition influences the critical potential. The currents in the passive regions are higher for lower contents of the less noble element. The origin of the higher passive current is unclear.

In the passive region of the current-potential behavior a modified surface structure or composition is preventing higher dissolution rates. This modified layer can be very thin. In the literature often one single monolayer is mentioned for high melting point alloys at room temperature. In contrast for low melting point alloys, thicker layers are reported. The difficulty of selective alloy dissolution is the unknown mechanism, how the altered surface region influences the dissolution kinetics. In Figure 3.2.4 current potential curves for a general alloy system are shown. The alloy composition influences the critical potential. The currents in the passive regions are higher for lower contents of the less noble element. The origin of the higher passive current is unclear. Very similar characteristics have been observed for CuPd samples by Kabius et al. [ka03] and it might be a common characteristic for high melting point alloys.

Chapter 4

X-ray Scattering

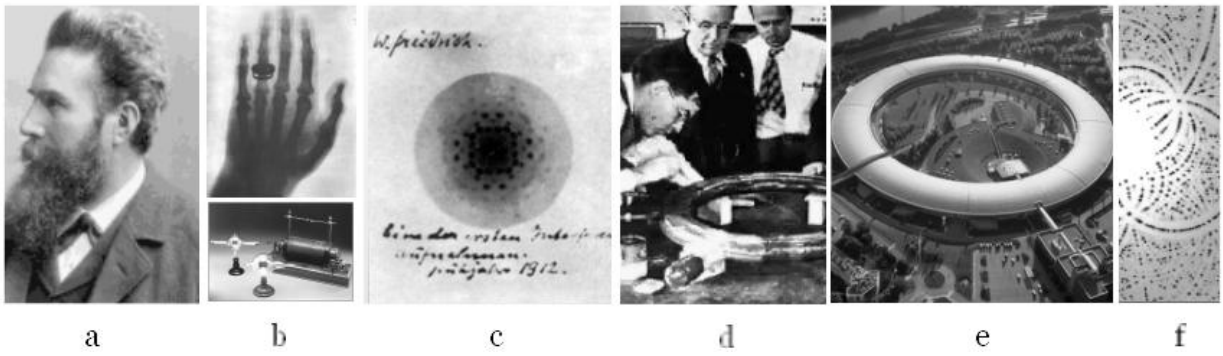

Figure 4.1: (a)Röntgen discovered in 1895 the X-Radiation and demonstrated by an image of his wife's hand its immense possibilities of the new technique (b). Also shown is an early X-ray apparatus and one of the first diffraction images obtained by Friedrich et al.(c). In 1947 synchrotron radiation was observed for the first time at General Electric, USA (d) and today's light sources (e shows the ESRF, France) deliver many new results in science (like in structural biology, (f) shows part of a diffraction pattern obtained from a protein crystal)

In 1895 Wilhelm C. Röntgen[1] discovered a new type of radiation occurring inside his vacuum tube in his laboratory at the Würzburg University, Germany. Röntgen himself called this new type of radiation „X-Radiation“ and also demonstrated, by taking a famous first X-ray image of the hand of his wife, its immense new possibilities in medical diagnosis. In 1912 Friedrich, Knipping und Laue[2] demonstrated with the first x-ray diffraction experiment the electromagnetic nature of the X-radiation, and revealed at the same time

[1]Wilhelm Conrad Röntgen, 1845-1923. He won the first Nobel price for physics in history (1901)
[2]Max von Laue 1879-1960, Nobel Price 1914

the atomic structure of crystals [fri13]. With X-ray diffraction a powerful method has been found to make distances of atoms in condensed matter directly „visible “. Since then many important observations have been made with X-rays, e.g. the double helix structure of DNA.

Some unique features make X-ray methods suitable for investigating many scientific problems on length scales down to atomic dimensions.

- The X-ray wavelength is on an atomic scale and diffraction of X-rays therefore reveals information on inter-atomic distances.
- X-ray diffraction is one of the few methods applicable for in-situ investigations of solid-liquid and other buried interfaces. The penetration of high energy X-rays in matter is relative large due to a small scattering cross section.
- Due to a small scattering cross section, the analysis of many problems is relatively straightforward, within the so-called kinematical approximation.
- The high X-ray photon flux offered by synchrotron light sources is sufficient to get signal from the extremely small quantity of atoms that form a surface (compared to the 3D bulk).
- X-rays methods are mostly non-destructive (within certain limitations concerning problems with beam damage e.g. in organic crystals).

4.1 Refractive Effects and X-ray Reflectivity

Like visible light, X radiation is of electromagnetic nature. The laws of optics apply also for X-rays. The trace of electromagnetic waves can be calculated, once we know the refractive index of the materials in the pathway. Since the refractive index for X-rays is smaller than unity total reflection will occur on the way from the optically denser vacuum or air side (with larger n) to the less dense sample. The complex refractive index for X-rays can be written:

$$n \;=\; 1 - \frac{\lambda^2}{2\pi} r_0 \rho_e - i \frac{\lambda}{4\pi} \mu_x = 1 - \delta - i\beta \tag{4.1}$$

Here λ is the wavelength of the radiation, r_0 is the classical electron radius, ρ_e the electron density and μ_x is the linear absorption coefficient of the material. β describes the absorption. Snells[3] law is valid also in the X-ray regime. To describe reflectivity of x-rays, the

[3] In France Snells law is known as Descartes' law

angles are measured normally relative to the surface.

$$n_1 \cdot \cos\alpha_1 = n_2 \cdot \cos\alpha_2 \tag{4.2}$$

with α_1 (α_2) being the angles between the incident (reflected) beam and the surface. With $n_1 = 1$ for vacuum/air, $n_2 < 1$ for X-rays in the material and $\beta = 0$ in Eq. 4.1, we can calculate the critical angle α_c:

$$\alpha_c = \sqrt{2\delta} \tag{4.3}$$

δ and β are both very small numbers in the order of 10^{-6} to 10^{-5} and the deviation of n from unity is consequently very small. The critical angle α_c is for hard X-rays (with energies around 10 keV) in the range of a few times 0.1 degrees. For X-ray energies close to an absorption edge of an illuminated crystal, dispersion corrections have to be considered. If in 4.1, $\rho_e = \rho_{atom} \cdot Z$, with the density of atoms ρ_e and atom number Z (number of electrons), we can include the dispersion correction by replacing the number of electrons by an effective number $Z = Z_0 + f' + if''$ (anomaleous Scattering). Values for f' und f" are tabulated [xtab]. There is a strong variation with energy, especially close to an absorption edge, while the variation with the scattering angle is quite small and can be neglected in first approximation. Several keV away from the edge f' and f" can still be sizeable (Compare Fig. 4.5).

The reflectivity can be calculated with the equations known from optics [bw]. Starting from Maxwells equations and the appropriate boundary conditions at the interfaces the transmitted and the reflected intensity of an incoming electromagnetic beam can be determined. A more complicated situation results if we have to deal with a sample with more than one interface (e.g. a thin metal layer on a substrate plus a very thin natural oxide on top). Parrat introduced an iterative procedure [par55], which is followed by most of the existing programs to calculate reflectivity curves. In a reflectivity measurement the incident and the exit angle are equal and the scattering vector $\vec{q}$ is therefore perpendicular to the surface, i.e. the scattering is sensitive to the electron density projected on the axis along the surface normal (the z-axis in surface science nomenclature). Due to the interference of the various reflected beams the reflectivity curve will show an oscillation pattern that reveals the internal composition of the film. Roughness of the surfaces and the interfaces will damp out the occurring oscillations.

4.2 X-ray Diffraction

Like visible light is diffracted at periodic macroscopic gratings, the periodicity of the atomic arrangement in crystals gives rise to sharp diffracted spots when X-rays, with wavelengths in the order of the atomic distances, are used. X-ray Diffraction (XRD) thus became an important method in material science. The first synchrotron radiation X-ray diffraction experiment was conducted by Rosenbaum et al. at DESY in Hamburg [ros71]. X-ray diffraction from surfaces would hardly be possible without the intense flux and the high brilliance of high energy synchrotron radiation. In addition the ability of hard X-rays to penetrate in matter, enables us to study buried interface structures on an atomic length scale.

4.2.1 X-ray Scattering from a Single Atom

X-ray scattering by an atom is the coherent sum (i.e. the squared sum of wave amplitudes)of the scattering events by the electrons of the atomic shells. If the x-ray photon energy is far away from certain values of the binding energy of electrons in the atom, the basic scattering event of an incoming photon with an electron can be described by Thomson's formula for the differential scattering cross section valid for a single free electron [jack] [al00]:

$$\frac{d\sigma}{d\Omega} = r_0^2 \cdot P \tag{4.4}$$

With r_0 being the classical electron radius (also called the Thompson scattering length) and P the polarization factor. For a linearly polarized beam, P is equal to $\cos 2\vartheta$ for all scattering vectors at an angle 2ϑ towards the polarization direction. An un-polarized beam can be described by the superposition of two polarization vectors and we get P=1/2(1+cos 2ϑ). The synchrotron beam which we will apply is highly polarized (p $\approx$1). The total scattered Intensity I_{scatt} detected in an solid angle $\Delta\Omega$ (e.g. the detector acceptance) that emerges from a single electron seeing an incoming Intensity I_0 will be:

$$I_{scatt} = I_0 \cdot \Delta\Omega \cdot \left(\frac{d\sigma}{d\Omega}\right). \tag{4.5}$$

Far away from absorption edges, the Thompson scattering cross section is valid for electromagnetic radiation of all wavelengths and is independent of the energy of the radiation.

If we consider now an atom, there are more electrons within the coherence length of the incoming x-ray beam, and we have to add all scattered waves coherently, i.e. to get

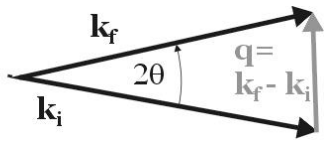

Figure 4.2: The scattering triangle shows the basic definitions for photon scattering. The difference of the initial and final wave vectors is called the scattering vector $\vec{q}$.

the intensity we have first to add the amplitudes. Two coherently and elastically scattered waves from two electron sites $\vec{r}$ in the atom, separated by $\vec{r'}$ will then have a phase shift of $(\vec{k_0} - \vec{k_f})\vec{r'} = \vec{q} \cdot \vec{r'}$, if $\vec{k_i}$ and $\vec{k_f}$ are the wave vectors of the incoming and scattered radiation (compare with Figure 4.2. The wave vector is related to the wavelength by $k = 2\pi/\lambda$ and points in direction of the energy flux of the wave. The modulus of q is therefore q=$4\pi \sin\theta/\lambda$. For an atom the sum of all electrons can be described by a continuous electron density n($\vec{r}$). Then the coherent sum of all wave amplitudes originating from all the electrons in the atom, can be replaced by the following integral:

$$f_{atom}(\vec{q}) = \int_{atom} d^3\vec{r'} n(\vec{r'}) e^{i\vec{q}\cdot\vec{r'}}. \tag{4.6}$$

This integral takes into consideration all the phase shifts originating from the scattering at the different sites of the electrons in the atom (orbitals). To finally obtain the scattered intensity of the atom the factor f_{atom} has to be squared and multiplied with the intensity given by Thomson's formula for a single electron (Eq. 4.5). f_{atom} is also called the atomic form factor. In the case of scattering in forward direction, i.e. $q = 0$, all the phase shifts become zero and the integral for an atom with Z_0 electrons reaches $f_{atom} = Z_0$. Values for the atomic scattering factor are calculated by using atomic or crystal wave functions and are tabulated in the literature [xtab]. These values can be approximated by an analytic expression with 9 parameters which are also tabulated [xtab]:

$$f(\sin\theta/\lambda) = \sum_{i=1}^{4} a_i \exp(b_i \sin^2\theta/\lambda^2) \; + c. \tag{4.7}$$

This analytic expression gives an excellent fit to the calculated values and is used in many computer calculations, as these parameters are a convenient form to enter into computer programs. In Figure 4.2.1 the scattering angle dependent atomic form factors as calculated by this expression are plotted for several elements (with parameter values from [xtab]). At $\sin\theta/\lambda = 0$ f^0_{atom} is equal to the atomic number. For elements with close Z numbers the shape is similar, as shown for Pd and In^{3+}. As the incoming intensity is often unknown, the actual amplitude of the form factor is usually not important because it can be scaled. In (b) Au and Cu are normalized to each other. The difference in f is biggest for $\sin\theta/\lambda = 0.8$ and this can eventually used to perform optimized experiments if one wants to distinguish in a fitting procedure between Cu and Au.

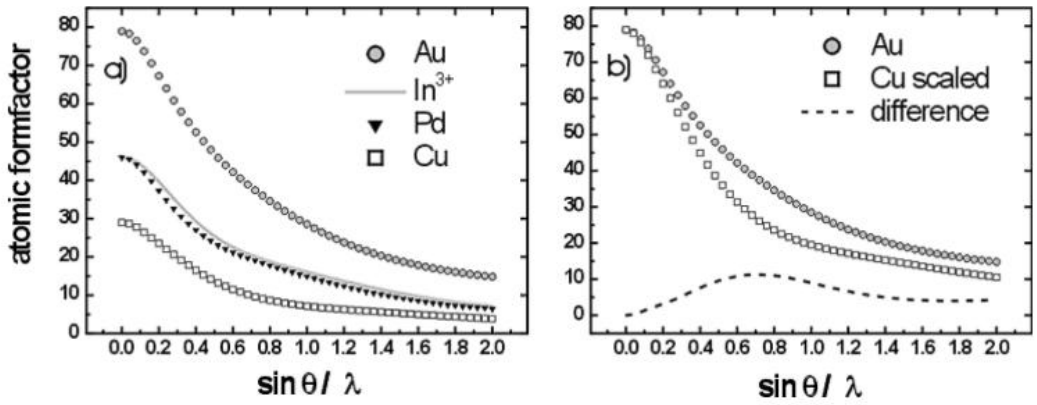

Figure 4.3: The atomic form factor f_{atom} is shown for several elements as calculated by an often used analytical function [xtab]. For $\sin\theta/\lambda = 0$ and far from absorption edges, f^0_{atom} is equal to the atomic number. For elements with close Z numbers the shape is similar, as shown for Pd and In^{3+}. In (b) Au and Cu are normalized to each other. The difference in f is biggest for $\sin\theta/\lambda = 0.8$.

4.2.2 Scattering from a crystal: Diffraction

Kinematical Approximation

As we have seen, X-ray scattering can be deduced starting from the scattering of an incoming plane wave on a single electron. The cross section, i.e. the probability, for this process is, on the other hand, very small. In what is called the kinematical approximation, absorption, extinction, and refractive effects are neglected. Also multiple scattering effects are not considered. The advantage of this approximation is that, if we now consider scattering from a crystal, we can add all scattered amplitudes originating from all electrons with the same weight, keeping the calculation easy and straightforward. In many cases this approximation is able to describe a scattering experiment in sufficient detail. Considerable deviation and insufficient description is mainly occurring in scattering experiments from perfect crystals, like e.g. silicon. In these cases all the neglected effects have to be considered and the theory is then called a dynamic theory. In this sense an intermediate theory is the *D*istorted *W*ave *B*orn *A*pproximation (DWBA) where the refractive effects at the interface are taken into account by treating the incident wave exact, but multiple scattering events, extinction and absorption are still neglected. For most metal single crystals the kinematical approximation gives a good description of the scattered intensity and will be considered here exclusively.

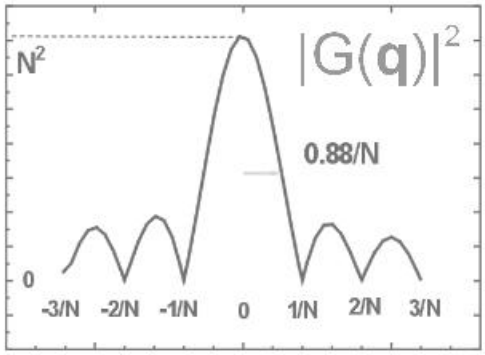

Figure 4.4: The modulus squared of the interference function. The minima are separated by 1/N and the central peak has a height of N^2. The half width at half maximum (HWHM) is 0.88 N. We see that for increasing N the peak height is increasing and the width is decreasing.

Diffracted Intensity

A complete description within the kinematical approach could be obtained by integrating equation 4.6 over the entire crystal. This would give the scattering amplitude A (also called scattering factor or crystal form factor F) directly:

$$A(\vec{q}) = \int_{crystal} d^3\ \vec{r'} n(\vec{r'}) e^{i\vec{q}\vec{r'}} \tag{4.8}$$

The calculation becomes simpler when the crystal symmetry is taken into account. Taking Equation 4.6 as a description of one atom in the crystal, we now have to consider the effect of adding the atoms on the positions of the crystal. The atomic form factors are tabulated [xtab] and can be to good approximation used in any crystal. A crystal is defined by having translational symmetry and can be described within one of the 14 Bravais lattices of the seven existing lattice systems. On each of the lattice points of these systems an identical basis is placed. This basis can consist of one atom for simple systems or, as in macromolecular protein crystals, up to many thousands of atoms. In a perfect crystal the knowledge of the crystal lattice (i.e. its unit cell) and the basis (i.e. the atoms contained in the unit cell) is sufficient to calculate the diffracted intensity with the tabulated atomic form factors. Therefore we have to consider first the atoms in the basis. The sum of the scattering amplitudes of the basis is called the 'structure factor'. The summation of the structure factor over the whole crystal lattice gives the scattering amplitude A. The scattered intensity is proportional to the square of the scattering amplitude ($I \propto A^2$). The actual value for the scattered intensity is obtained by multiplying the Thomson Intensity for a single electron (Eq. 4.5).
For a crystal having the shape of a parallelepiped, with n_1, n_2 and n_3 unit cells in the three

respective directions and a basis containing M atoms, we can write:

$$\begin{aligned} A(\vec{q}) &= \sum_{n_1}\sum_{n_2}\sum_{n_3}\sum_{j=1}^{M} f_j e^{i\vec{q}\ (\vec{r_j}+n_1 a+n_2 b+n_3 c)} \cdot e^{-B_j q^2} \\ &= \sum_{n_1}\sum_{n_2}\sum_{n_3} e^{i\vec{q}(n_1 a+n_2 b+n_3 c)} \times \sum_{j=1}^{M} f_j e^{i\vec{q}\vec{r_j}} \cdot e^{-B_j q^2} \\ &= G(\vec{q}) \times F(\vec{q}) \end{aligned} \tag{4.9}$$

G(q) is the lattice sum and F(q) is the structure factor (calculated for one lattice unit cell). Note, that even if G(q) is non-zero, F(q) can be zero.

We can further consider additional effects: the thermal vibration, and also static disorder that is averaged over the diffracting part of the crystal, is taken into account by introducing the 'temperature' or 'Debye-Waller factor' $e^{B_j q^2}$ [xtab] for the atom j. It has been recommended to use the expression 'atomic displacement parameter' (ADP) instead of the term 'Debye-Waller factor' to emphasize that not only temperature effects but also static displacements are considered by using such a factor [Tru96]. In first approximation an isotropic ADP factor can be chosen. For a further refinement normally anisotropic factors, i.e. tensor descriptions, have to be considered. Also a limited penetration depth of the X-ray beam into the crystal due to absorption can be included in the above summation. The first part in the sum in Equation 4.9, $G(\vec{q})$, is in fact the well known geometrical series. After some calculation we can write:

$$G(\vec{q}) = \frac{\sin(\frac{1}{2}n_1\vec{q}\vec{a})}{sin(\frac{1}{2}\vec{q}\vec{a})} \cdot \frac{\sin(\frac{1}{2}n_2\vec{q}\vec{b})}{sin(\frac{1}{2}\vec{q}\vec{b})} \cdot \frac{\sin(\frac{1}{2}n_3\vec{q}\vec{c})}{sin(\frac{1}{2}\vec{q}\vec{c})} \tag{4.10}$$

We can recognize here Laue's conditions for a non-zero scattering amplitude:

$$\vec{q}\cdot\vec{a} = 2\pi h \qquad \vec{q}\cdot\vec{b} = 2\pi k \qquad \vec{q}\cdot\vec{c} = 2\pi l \tag{4.11}$$

If all three of these conditions are fulfilled all contributions to Equation 4.10 will add up constructively (i.e. with a phase shift of an integer multiple of 2π) and a diffracted beam can be observed. If we only take the sum over a finite number of unit cells n_i, we obtain the so-called interference function known from optics [bw] and producing intensity oscillations with changing scattering vector. For X-ray diffraction this interference function is called Laue function. The Laue oscillations can be observed for example in the case of thin epitaxial layers, where $n_1, n_2 \to \infty$ and n_3 finite, with $n_3 \cdot a_0$ in the range from 1 to 1000

nm for hard X-rays (a_0 being the size of the unit cell in that direction). The more unit cells contribute to the diffracted intensity, the narrower becomes the central peak. We can, on the other side, measure the width of a diffracted peak and estimate the width of the coherently scattering parts (in the direction of the measurement). For polycrystalline samples the Debye-Scherrer formula is derived with these arguments [war] [gu94].

As an example we consider now the structure factor F for the unit cell of a Cu_3Au crystal. This crystal will be described later in more detail (Chapter 6). It shows atomic ordering, with a so-called $L1_2$ structure, below a order-disorder transition temperature T_c of 390°C. The $L1_2$ structure is basically a fcc lattice, but with the different elements Cu and Au occupying the four (before equivalent) fcc positions. The Au atoms occupy e.g. the corner of a cube at the position 000, while the Cu atoms the occupy the three face centered positions of the unit cell at $0\frac{1}{2}\frac{1}{2}$, $\frac{1}{2}0\frac{1}{2}$ and $\frac{1}{2}\frac{1}{2}0$.With the Au and Cu atoms at this positions (fully ordered crystal), we get for the structure factor F for the Cu_3Au crystal:

$$F(\vec{q}) = \sum_{j=1}^{M} f_j e^{i\vec{q}\vec{r_j}} = f(Au) + f(Cu) \cdot (e^{\pi i(h+k)} + e^{\pi i(h+l)} + e^{\pi i(k+l)}). \tag{4.12}$$

From Equation 4.12 we can distinguish two cases. If all Miller indices hkl are unmixed (so-called fundamental reflection) we obtain F(q)=f(Au)+3·f(Cu) and in the case of mixed indices F(q)=f(Au)-f(Cu). The latter reflection can only be observed if the crystal is ordered and is, therefore, called a superstructure reflection. Note that f is q-dependent (Equation 4.7).

The Reciprocal Lattice and Miller Indices

The phenomenon of diffraction has its origin in the regular arrangement of atoms in a crystal. In this way, we can built up for example a simple cubic crystal by layers of atoms in a squared arrangement, with atoms in succeeding layers sitting on top of each other. These layers, also called 'lattice planes' and imagined to build up the 3D crystal, can be labeled by three indices h, k and l. The distance of the considered layers in the crystal is d_{hkl}. The indices h,k and l are called Miller indices and determine exactly the family of equivalent lattice planes in consideration. To describe such a family we consider the origin of the unit cell in one atom of one layer of this family at position '0' in all three axis of the 3D unit cell, i.e. at position (0,0,0). The next plane of this family is then intersecting the unit cell by cutting the three unit axis at well-defined points. The Miller indices are then the reciprocal of the intersection point distance from the origin in units of the unit vectors, h along $\vec{a}$, k along $\vec{b}$ and l along $\vec{c}$. If we think of a bcc crystal the base centered atoms

form a plane that is cutting one of the cubic unit vectors at $\frac{1}{2}$ and the others at infinity. We can so describe this additional plane as a {2 0 0}, {0 2 0} or {0 0 2} plane. For a given family of planes each layer will have the same density of lattice points and the individual layers will be equidistantly. For example for a cubic lattice with the lattice parameter a_0 the layer distance of hkl-planes will be:

$$d_{hkl} = \frac{a_0}{\sqrt{h^2 + k^2 + l^2}} \tag{4.13}$$

Bragg's law[4] can be viewed as reflection of the incoming beam at atomic layers (or atomic planes) in the crystal and is equivalent to the Laue conditions (Eq.4.11), but more intuitive. Within the Bragg formulation the condition for an observable reflection is that the path difference of the reflected beams of two subsequent layers is equal to λ or an integer value n times λ, so that the two beams (and all the others) interfere constructively (i.e. add up with their full modulus). Constructive interference is then possible for all integer values of n, where n is called the order of the reflection, and Bragg's law writes:

$$2d_{hkl}sin\theta = n\lambda \tag{4.14}$$

Higher order reflections are obtained by thinking additional lattice planes; diffraction peaks are thus labeled with the Miller indices hkl of the planes they originate from in the Bragg picture.

In fact, in the Bragg formulation, each diffracted beam is a reflection with equal incoming and out-going angle θ with respect to the reflecting plane. The scattering vector $\vec{q}$ for such a reflection is pointing along the normal to the atomic plane. The observed diffracted (reflected) beams can be described by a new space, called reciprocal space, linked to the real space of the 3D periodic crystal. The scattering vector $\vec{q}$ of a Bragg reflection fulfills the Laue conditions (Eq. 4.11) and is represented in this reciprocal space by a point at distance |q|.

The reciprocal unit vectors $v_i^\star$ are linked to the unit vectors of the lattice by $\vec{v}_i \cdot \vec{v}_i^\star = 2\pi$ and $\vec{v}_i \cdot \vec{v}_j^\star = 0$ for $i \neq j$. A point with strong intensity in this reciprocal space is called a reflex. The $\vec{v}_i^\star$ obeying above requirements are defined by:

$$\vec{v}_i^\star = 2\pi \times \frac{\vec{v}_j \times \vec{v}_k}{\vec{v}_i \cdot (\vec{v}_j \times \vec{v}_k)} \tag{4.15}$$

4.2.3 Resonant Scattering from a crystal

Resonance occurs when the energy of the impinging X-ray photons is close to an adsorption edge of an element. Anomalous scattering is for purely historic reasons called 'anomalous',

[4]Bragg, father and son, received the Nobel Prize in 1915 for their X-ray spectrometer

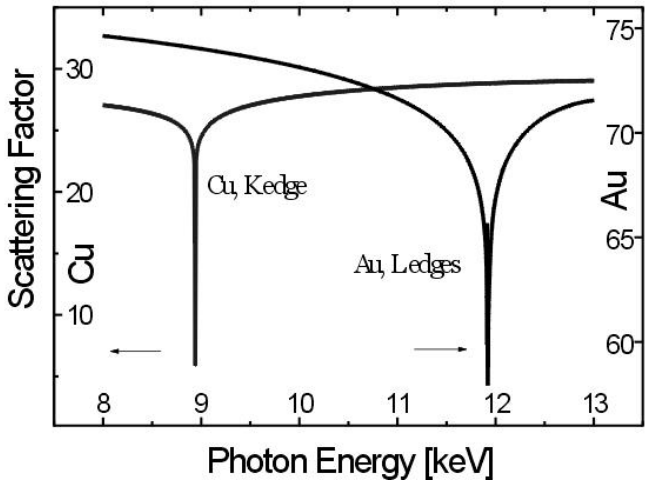

Figure 4.5: Anomalous scattering factors (real part) for Cu and Au in the energy range from 8 to 13 keV. Considerable deviations from f^0 occur close to absorption edges.

even if nowadays nobody perceives anything anomalous with resonant behavior. With some assumptions on the inner structure (e.g. discrete energy levels) resonant behavior can even be understood in a classical treatment of a forced oscillation of the electrons in an atom [al00]. The main effect of the resonance is, that we have to replace the number of electrons Z in the respective formulas by an effective electron number $Z_{eff} = Z_0 + f' + if''$ with the so-called real and imaginary dispersion corrections f' and f". For example in the formula for the structure factor (Eq. 4.9); or for the critical angle (Eq. 4.3) Z (in ρ_e) has to be replaced by Z_{eff}. Note that the correction is, although largest close to the absorption edge, still considerably large several keV away from the edge.

The dispersion correction depend in general on the energy $E = \hbar\omega$ and on the scattering angle or scattering vector. The dependence on the scattering vector is nevertheless normally neglected. The imaginary part f"(ω) of the dispersion corrections is directly related to the absorption cross section $\sigma(\omega)$ through:

$$f''(\omega) = -\left(\frac{\omega}{4\pi r_0 c}\right)\sigma(\omega), \tag{4.16}$$

and can thus be obtained by measuring the energy dependent absorption. The dispersion factors f'(ω) and f"(ω) are related to each other through a Kramers-Kronig transformation. The tabulated values are obtained by calculations, assuming free atoms. As in a solid interference effects change the absorption behavior considerably (e.g. EXAFS or NEXAFS features), the direct measurement of f' (f" follows the from a Kramers-Kronig transformation) might be in many cases the appropriate approach [al00][sc03]. For more details the interested reader is referred to the literature [al00].

In many cases where the relative size of the atomic scattering factor matters (e.g. for contrast in ordered alloys or in multilayers) the anomalous behavior provides means to

perform an optimized experiment, e.g. by chosing an energy with maximum contrast of two elements. Furthermore, with measuring energy dependent diffraction intensities, anomalous measurements offer the possibility to separate contributions of different elements. The method is called Diffraction Anomalous Fine Structure (DAFS).

4.3 Surface Sensitive X-ray Diffraction (SXRD)

For $n = 1 - \frac{\lambda^2}{2\pi} r_0 \rho_e = 1 - \delta$ with $\beta = 0$ we get for the refracted beam inside a material: $k'_z = k_0\sqrt{sin^2\alpha_i - 2\delta}$. And because of the continuity of the electromagnetic field at the interface $k_{xy} = k'_{xy}$. The dashed values are inside the material. For small angles $\alpha_i < \alpha_c = \sqrt{2\delta}$ is k'_z purely imaginary. The impinging X-ray beam is totally reflected. Consequently there is no transmitted wave. The transmissivity, which is defined as the energy flux through the surface, is thus zero. Nevertheless the reflected beam enters the material at the surface, as imposed by the condition of continuity of the electromagnetic field at the interface. On the surface of the material we have an electromagnetic wave penetrating a little into the material; the field intensity is quickly vanishing with distance to the surface. This wave is called evanescent wave and the penetration depth is usually a few nm and dependent on the incident angle.

$$E(r) = E_0 e^{i\vec{k'}\vec{r}} = E_0 e^{i\vec{k'_{xy}}\vec{r}} e^{i\vec{k'_z}\vec{r}} = E_0 e^{i\vec{k'_{xy}}\vec{r}} e^{-\frac{z}{2\Lambda_p}}$$

with the penetration depth Λ_p for $\alpha_i < \alpha_c$:

$$\Lambda_p = \frac{1}{2\vec{k'_z}} = \frac{1}{2k_0\sqrt{sin^2\alpha_i - 2\delta}} \tag{4.17}$$

For angles bigger than the critical angle α_c the penetration depth is determined then by the absorption coefficient μ of the material. The transmissivity is approaching quickly unity. The wave vector of the evanescent wave lies exactly in the surface. Diffraction using this evanescent wave is called „in-plane“-diffraction or *G*razing *I*ncidence X-Ray *D*iffraction (GID). The respective diffraction planes are perpendicular to the surface plane (see Fig. 4.3). For the transmission function to adopt non-zero values α_i and α_f have to be bigger than zero. Within the framework of the „Distorted Wave Born Approximation“ (DWBA), we can calculate the diffracted in-plane intensity as a function of the in-coming and outgoing transmission functions $T_{i,f}$ and an actual scattering function S(q) (e.g. the squared structure factor for a crystalline sample)[do92][do86][do87] [fe85]:

$$I(q) \propto \mid T_i \mid^2 \cdot \mid T_f \mid^2 \cdot S(q) \tag{4.18}$$

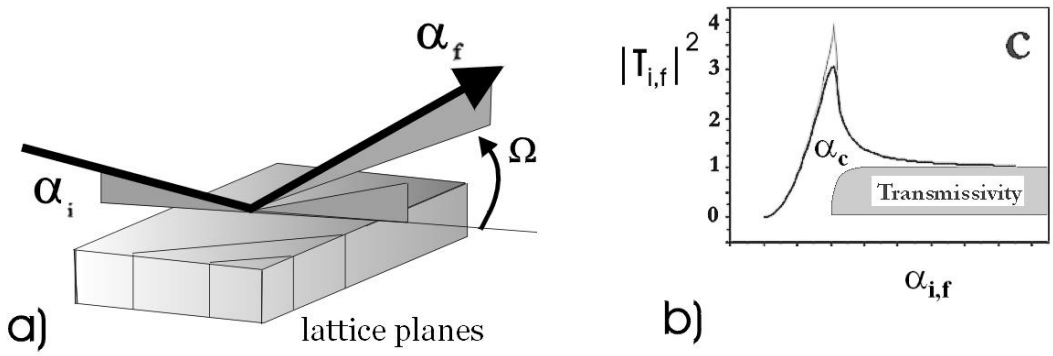

Figure 4.6: Scattering geometry for a grazing angle diffraction experiment (a) and the transmission function $T^* \cdot T$ for $\beta = 0$ and a flat surface (b). Below the critical angle the transmitted energy (transmissivity) is zero and the incoming beam is totally reflected.

4.4 Crystal Truncation Rods (CTR)

The intensity along a Crystal Truncation Rod (CTR) is sometimes also called asymptotic Bragg diffraction, as it was first observed in vicinity to Bragg peaks. Due to the presence of the surface, the otherwise sharp Bragg points are smeared out in the direction of the surface normal. M. v. Laue explained in 1936 such observations made with electron diffraction[5] [la36]. Even if his theory includes X-ray diffraction as well, the techniques available at that time didn't allow for experimental verification. With the intense X-ray beams of today's third generation synchrotron light sources we can follow this originally observed 'streaked' intensity the whole region in between two successive Bragg peaks.

A quantitative analysis of the intensity profile is within the kinematic approach quite straightforward. We know the expression for the structure factor F_{hkl}:

$$F_{hkl} = \sum_j f_j e^{2\pi i(hx_j+ky_j+lz_j)^2} \cdot e^{-B_j Q^2/(4\pi)^2}$$

with f_j being the atomic scattering factor of atom j, B_j is the Debye-Waller factor, hkl are the Miller indices and $(xyz)_j$ the position of atom j in the unit cell. Programs available to calculate CTRS intensity, e.g. ROD of Elias Vlieg [vl00], do calculate this sum. The intensity between two Bragg peaks varies over many orders of magnitude [rob86][fe85]. For a simply truncated surface, i.e. without any relaxation or reconstruction of the surface,

[5]He concludes: „Satz VII: Hat der Kristall eine ebene Grenzfläche, so hat sein Intensitätsbereich einen stachelartigen Auswuchs in der zu ihr senkrechten Richtung.“, translated: If the crystal has a flat surface plane, the shape of the intensity will show a streak

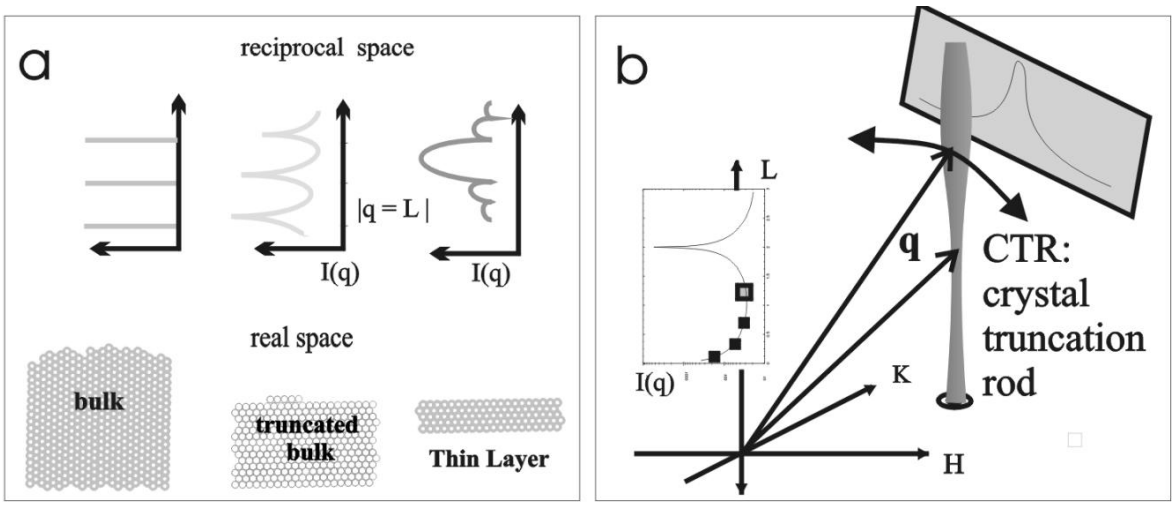

Figure 4.7: Scattering along a Crystal Truncation Rod (CTR) originates in the fact that a sharp interface is introduced in the summation of the single atomic contributions. While the complete summation in 3D results for an infinitely extended crystal in points of intensity (δ functions), the truncated crystal gives rise to scattered intensity in between Bragg peaks, perpendicular to the introduced surface. Measurements are normally performed as a succession of rocking scans along the L-coordinate, with the L-direction chosen to be along the z direction, i.e. perpendicular to the surface.

we can mathematically introduce a truncation by multiplying a step function $\theta(z)$ in one direction of an otherwise infinite crystal. Using the Fourier transform for θ (z) : H(q)= $\frac{i}{2\pi q} - \frac{1}{2}\delta(q)$ (e.g. [ab]) an intensity drop proportional to $\frac{1}{q_z^2}$ [do92]. For a truncated surface the intensity or the scattering factor is thus symmetrically connecting the Bragg reflections lying along the direction of the surface normal. In the case where the surface normal is not aligned with one of the high symmetry directions, e.g. in case of a preparation miscut or a vicinal surface, the intensity must not necessarily connect and we will observe intensity tails originating from each Bragg reflection in the direction of the surface normal. Real crystal surfaces are in general different from a simple bulk truncated surface and by model calculations and fitting its parameters to a measured CTR, we can learn about exact atomic positions and the composition at the surface (surface crystallography).

Crystal truncation rods are normally recorded by successive transversal rocking scans at different L-positions. The slits should be open in order to collect all the intensity of the peak, i.e. broad CTR's are difficult to measure. The corrected integrated intensity or the square root of it (scattering amplitude) is then plotted against the L-position. Compared to a simple line-scan (L-scan), recording a CTR is more time consuming. But this procedure

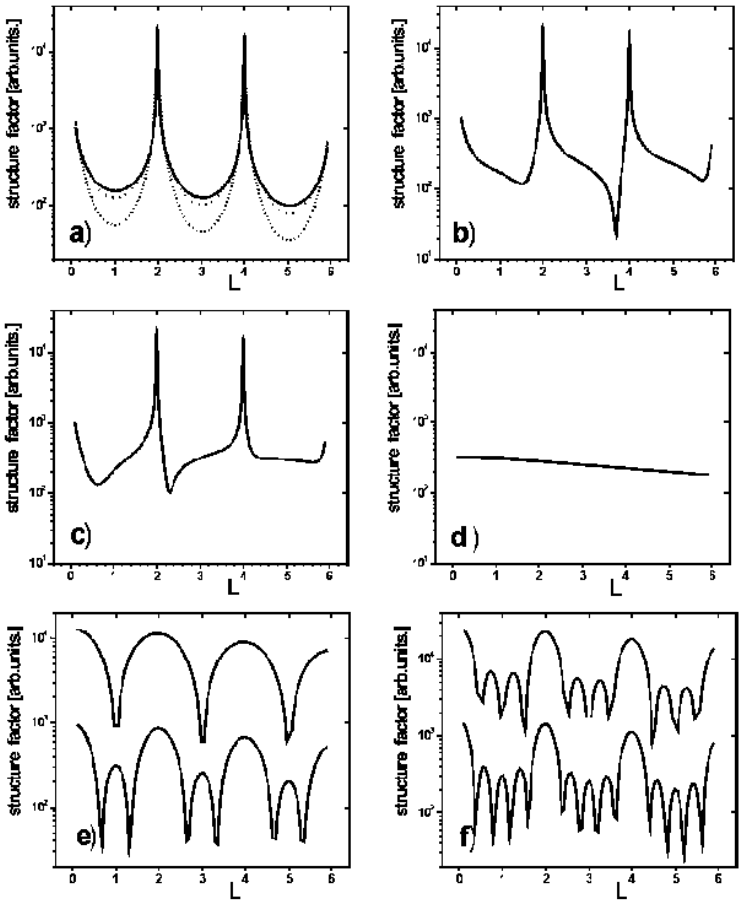

Figure 4.8: With the program ROD of Elias Vlieg [vl00] calculated structure factors for different model of Au(001) surfaces: (a) bulk terminated with different roughness factors (β model), (b) Au(001) with the topmost layer 5% relaxed in the outward direction, (c) Au(001) with the topmost layer 5% relaxed in the inward direction. For relaxations of the surface, i.e. deviations from the bulk layer spacing, we get asymmetric CTR profiles, with the minimum shifted towards smaller (higher) values of L for outward (inward) relaxations. (d-e) are over-layer rods and can be observed when the lattice constants are different from the bulk: (d) a single Au(001) layer, (e) only two (top) and three single Au(001) layers and (f) only four (top) and five single Au(001) layers. In (e) and (f) we see Laue oscillations, if we take a high number of layers we would get the CTR in (a).

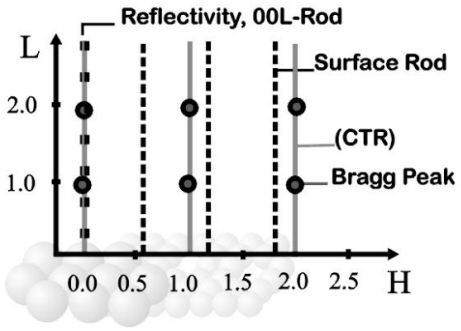

Figure 4.9: Scattering from only the overlayer can be observed when the inplane lattice constant is different from the bulk. In this case the CTR and the overlayer rod are separated.

has advantages, firstly the background intensity can be more accurately corrected for, and secondly, the relative intensity along the rod is correctly measured, even if the peak width is changing along the rod. This is often the case, because the intensity close to a Bragg peak is originating from the whole illuminated (bulk) crystal, while in-between two Bragg peaks at the rod minimum (sometimes called anti-Bragg position) the intensity comes solely from the topmost layer. In the first case, the domain or mosaic block size determines the peak profile, while at the rod minimum the surface structure, e.g. the mean terrace size, is most important. In general both are different in size.

4.5 Synchrotron Radiation

The main part of this work was conducted at the European Synchrotron Radiation Facility (ESRF) at the beamline ID32, that will be described later. The ESRF is the world's first third generation synchrotron radiation source. It had its first user experiment in 1993. The first synchrotron radiation ever was observed as blue visible light in 1947 at General Electric in the USA. (For a short historic Review, see [dat]). The first X-ray diffraction experiments with hard X-ray synchrotron radiation were conducted 1971 at the 7.5 GeV high energy ring DESY in Hamburg by molecular biologists [ros71].The intensity or flux offered in a small solid angle element by synchrotron radiation is many orders of magnitudes higher than for the most powerful rotating anode set-up in an usual laboratory. The most important parameters for a synchrotron radiation light source are the flux, the brilliance, and the emittance:

$$\begin{aligned}
\text{flux} &= \frac{\text{photons per second}}{\text{mrad}^2 \cdot 0.1\%\ \text{bandwidth}} \\
\text{brilliance} &= \frac{\text{photons per second}}{\text{mrad}^2 \cdot (\text{source area in mm}^2) \cdot 0.1\%\ \text{bandwidth}} \\
\text{emittance} &= \frac{\text{photons per second}}{\text{mrad}^2 \cdot (\text{electron ring current in mA}) \cdot 0.1\%\ \text{bandwidth}}
\end{aligned}$$

With the high flux new kind of experiments emerged, from which material science, surface science and structural biology benefit.

That accelerated electrons emit electromagnetic radiation was already confirmed by H. Hertz in 1888. The relativistic electrons (or positrons) in modern storage rings (the first 'synchrotron' radiation was observed with a synchrotron, but modern light are sources based on the concept of an electron storage ring) are forced on a circular trace by bending magnets. The bending, due to the centripetal acceleration, causes the emittance of photons with a continuous spectrum dependent on the energy of the ring electrons. Because of the relativistic speed of the electrons (e.g. E=6 GeV for the ESRF, i.e. appproximatly 10^4 times the electron rest mass m_e of 511 keV), the calculations for the characteristics of the emitted spectrum have therefore to be based on the Lorentz transformations known from Einsteins special theory of relativity [schw49]. Besides the radiation from simple bending magnets one can obtain higher flux and much higher brilliance with insertion devices, i.e. wigglers and undulators, that contain a periodic array of magnets. For a wiggler the intensity is multiplied by the number of periods N. This is different in an undulator, where the design parameters are chosen so that the emission of new photons from each 'wiggle' of the electrons occurs in phase with the emerging photon beam. As a result a peaked,

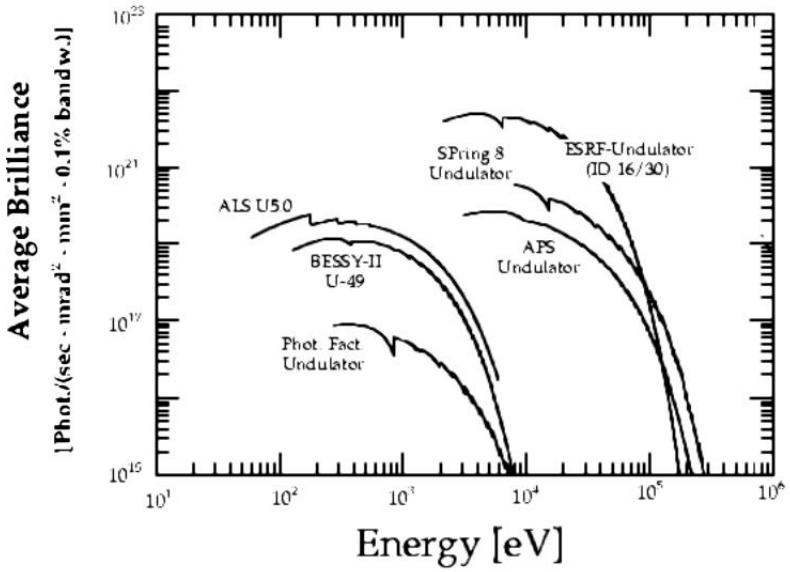

Figure 4.10: The flux of synchrotron radiation light sources is many orders of magnitude higher than the most intense available laboratory X-ray sources (in this figure they would be at values close to 10^8). The cut-off energy depends on the original electron energy of the used storage ring and on the insertion device used.

N^2-times higher, intensity is observed. Third generation light sources use also the light from bending magnets (BM Beamlines) which are built to curve the electron beam, but primarily from more powerful insertion devices (ID beamlines) placed within the straight sections of the electron path. With the higher flux, surface science experiments with X-rays (SXRD, CTRS, Surface XSW and more) can be conducted, that would not be possible otherwise. Plans for even more powerful Free Electron Lasers (FEL) in the X-ray regime may become reality, which would further boost advances in science, due to further new experimental possibility.

Chapter 5

Experimental Methods and Setups

5.1 In-Vacuum Preparation

Many surface science techniques use electron beams and require therefore an in-vacuum sample environment. Because of their limited penetration depth, electrons allow extreme surface sensitive experimental methods. The field of surface science began to grow substantially with the development of ultra-high vacuum (UHV) conditions, where prepared samples could be kept free of contaminants for the duration of the experiment.

One requirement to obtain a good signal to noise ratio of X-rays diffracted from surfaces, is to achieve smooth surfaces and a surface crystalline quality characterized by large domains. For crystal surfaces a combination of mechanical polishing, UHV surface cleaning by ion bombardment (sputtering) and annealing at high temperatures (to enhance surface mobility of adatoms and defects) results in sufficient surface quality. For electrochemical experiments (i.e. experiments at ambient pressure), Claviler developed a method to prepare some noble metals like Au, Pt,... by flame annealing of mechanically polished surfaces [cl80]. For these metals in ambient pressure inert atmospheres even at high temperatures no remarkable oxidation of the surface occurs. But in general high temperatures applied to annealing surfaces is only possible under UHV conditions.
It is also possible to prepare the surface by electrochemical polishing and etching, but the results are often hard to reproduce and very often an unfavorable surface crystalline quality and morphology is obtained. The sample preparation method of choice for the experiments of this work was therefore UHV annealing. In addition to the use of single crystals one set of MBE grown epitaxial Cu_3Au films have been produced.

The UHV Systems

The cleaning and annealing procedures, together with convenient characterization tools offered, make UHV techniques a good choice for surface preparation. Different experiments are usually installed in different chambers of the entire UHV system and connected by means of a transfer mechanism. The single chambers can then be separated for maintenance by the use of UHV valves. All necessary parts are commercially available.

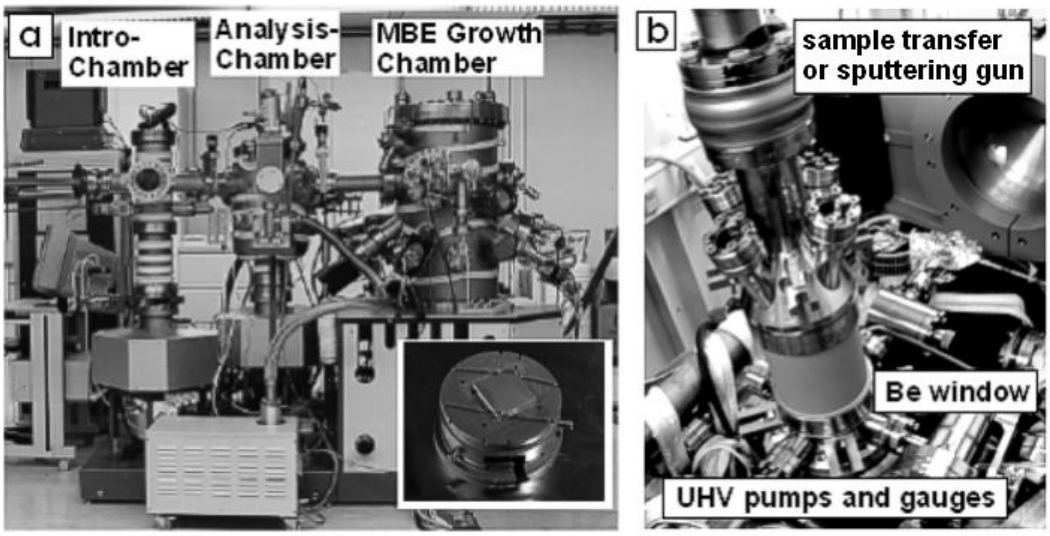

Figure 5.1: (a) An image of the UHV/MBE system at the MPI-MF in Stuttgart. (b) The portable X-ray diffraction chamber that can be connected to the MBE system.

The Stuttgart UHV System and Diffraction Chamber

At the Max-Planck-Institute for Metal Research (MPI-MF) in Stuttgart we have prepared samples for the experiments at HASYLAB and ANKA and for one experiment at the ESRF. In addition, epitaxial $Cu_3Au(111)$ thin films have been produced. Figure 5.1 shows the UHV system with the different inter-connected parts of the chamber and a typical sample mounted on the RIBER sample holder system. In the introduction chamber (Intro-Chamber, base pressure $1\times10^{-}8$mbar) an additional heating station is mounted. The sample can be warmed up during pumping in order to eventually desorb existing adsorbates like e.g. water molecules. The analysis chamber contains a sputter gun and a combined LEED and AES set-up. The base pressure in this part of the chamber is $1\times10^{-}9$mbar. Here the sample can be cleaned by ion bombardment (sputtering with Argon gas) and the surface can be annealed. At the time of the experiments a radiative

heating station with a filament close to the sample backside was installed; this gave the possibility to heat the sample up to a temperature of approximately 800K. Higher temperatures can be reached with this heating station by using a thinner and longer filament, but this design is more susceptible to failure. In the MBE growth chamber, nevertheless, such a heating station was installed to reach the necessary high temperatures for the deposition. Also installed in the MBE chamber was a RHEED set-up. For the deposition of epitaxial films the chamber offered Knudsen-type and electron beam evaporator cells (these two methods will be shortly described in the next paragraph). A free port at the analysis chamber allowed a **portable X-ray diffraction chamber** to be connected. This chamber is shown in Figure 5.1 b. A Be cylinder with 2mm wall thickness is surrounding the sample, so that for in-plane diffraction no restrictions for the incoming or out-going beam occurs. On top of the cylinder a gauge allows the sample transfer from the Analysis Chamber into the portable chamber and all necessary pumps are below the sample surface plane. The exit angle towards the sample surface can be as high as 54°. In addition to this portable X-ray diffraction chamber a simple UHV transport chamber was also available.

The **Molecular Beam Epitaxy (MBE) Chamber** (a RIBER EVA32 MBE Chamber) offers three Knudsen-type cells and two electron beam evaporator cells. With this techniques Cu_3Au films on $Nb(110)/Al_2O_3(1120)$ have been produced with growth parameters optimized before [ern00][ern01]. Knudsen-type cells consist of crucibles, where the material placed inside can be melted by a surrounding filament, if the melting temperature is not higher than 1400°C. The vapor pressure inside the UHV chamber is in this case increasing sufficiently to actually evaporate the material. Due to the elongated shape of the crucibles an atomic or molecular beam is created. On a sample in this beam the material is subsequently deposited. Depending on the vapor pressure (i.e. the temperature of the crucible) growth rates in the order of 0.01 to 0.1 nm/s can be used. For niobium (Nb), with its much higher melting temperature, this technique is not suitable for evaporating enough material to deposit a layer on a substrate. Nb is thus evaporated with the help of an electron beam evaporator. An energetic electron beam (5-20 keV) is focused on the material and is producing enough heat to melt the part around the impinging electron beam.
The MBE growth chamber is equipped with a Quarz microbalance to measure growth rates of the different elements. As the position and view angle of the microbalance probe and the growth substrate surface are not exactly the same, a so-called tooling factor has to be determined for each element separately. This is done by ex-situ thickness measurements by X-ray reflectometry of individual calibration samples.

The Grenoble ESRF ID32 UHV Systems

Two separate UHV systems are associated to ID32 beamline at the ESRF in Grenoble (Laboratory 01.0.07/08). The smaller system is equipped with a load lock, a sputtering and annealing station and a LEED set-up, using the same sample position, and an Omicron STM in a second chamber.

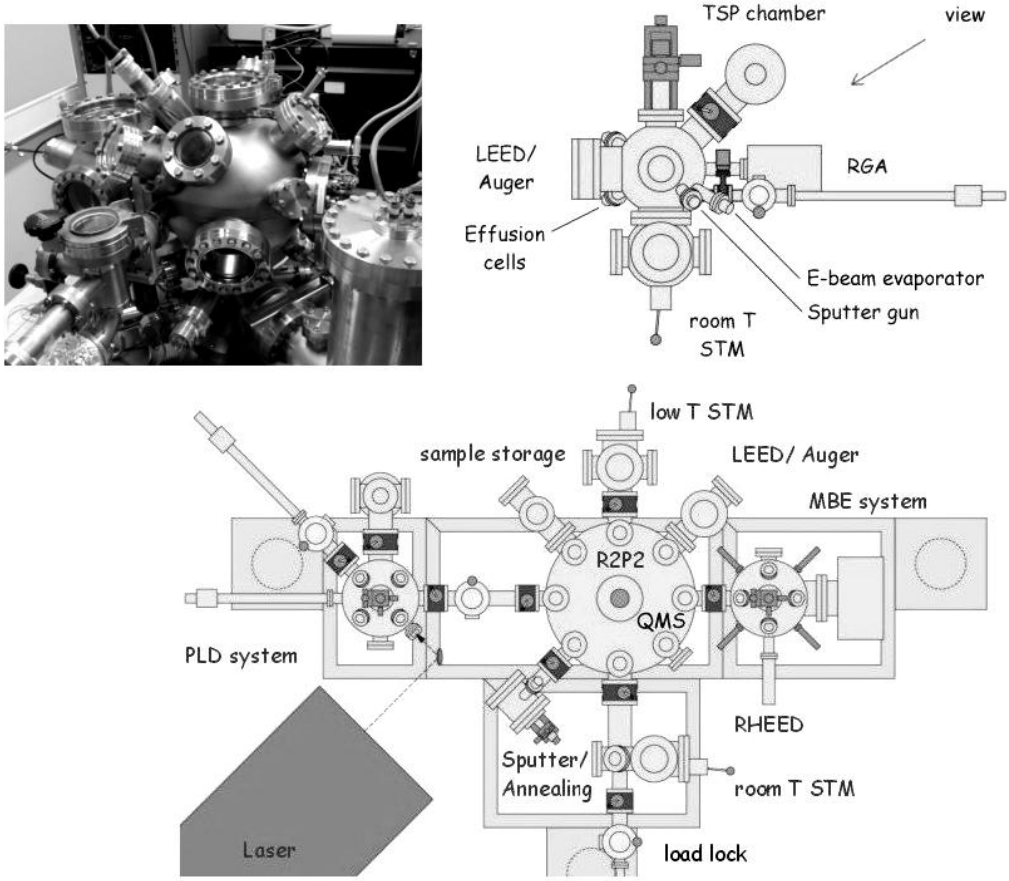

Figure 5.2: An image of the UHV systems of ID32/SCL at the ESRF. Top: image and sketch of the small system (STM and LEED). Bottom: sketch of the big system, with STM, LEED, AES and MBE and PLD chamber.

The bigger UHV system consists of multiple connected side chambers This system is shown in Figure 5.1 b. It offers a chamber for Molecular Beam Epitaxy (MBE) with a heating sample stage, a Pulsed Laser Deposition chamber (PLD), a sputtering and annealing side chamber, that can be separated from the main vacuum ,a chamber with an OMICRON μ-STM, a combined LEED and AES optics and means for loading samples and STM tips. In addition a baby chamber can be connected to be used for the crystallography of surfaces in UHV in X-ray experiments at the ID32 beamline diffractometer. Also a simpler sam-

ple transfer chamber can be used to transfer samples under UHV conditions to the ID32 beamline UHV chamber.

UHV Electron Techniques

Auger Electron Spectroscopy (AES)

During his PhD work in 1925 P. Auger observed traces of electrons on photo plates which were exposed to hard x-ray radiation [aug26]. He interpreted the occurrence of these electrons as being the result of a radiationless transition in atoms excited by the primary X-ray photons. The emission of an electron competes with the emission of characteristic X-ray radiation. These "Auger" electrons have since been the subject of extensive theoretical and experimental investigations and *A*uger *E*lectron *S*pectroscopy (AES) has become a standard tool in surface science (for further information see [ert85]). Even without thorough analysis, an AES scan is often used as a indication for the quality of a sample preparation in UHV, e.g. as a test for still present surface impurities after ion bombardment cleaning. With the very limited penetration depth of electrons in matter, in the order of nm for 1 keV electrons, AES is an inherently surface sensitive technique. An important step toward the widespread use of this method was the work of Tharp and Scheibner who demonstrated that the ordinary electron optics for LEED experiments could be used as a retarding field energy analyzer for the detection of Auger electrons [tha67]. In AES mode, the energy of the arriving electrons is detected by applying a retarding field on a first grid, that can only be passed by electrons with sufficient energy. The passing electrons are then accelerated in a field produced by a second grid and detected with the help of a third one. (With the addition of a fourth grid to a commercial 3-grid LEED optics by Palmberg a better resolution of the Auger spectrometer could be achieved [pa68].)

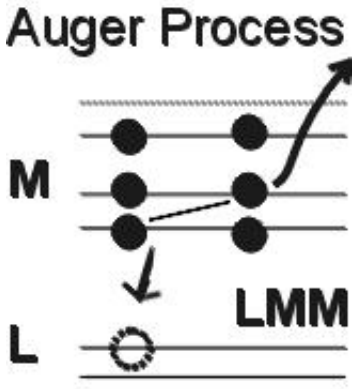

Figure 5.3: The energy of Auger electrons is determined by the difference in energy of the initial and final states of a relaxing inner-atomic electron. The nomination of the Auger lines reflects the respective energy levels of the initial core hole and the origin of the two participating electrons.

Combined LEED and AES optics are frequently used in most laboratory's UHV systems

as a first characterization method for sample preparation. The basic set-up is shown in Fig. 5.1a: the electron gun and the four grids, in front of the phosphorous screen used for LEED images. The primary electron beam has usually energies of 3000eV to 5000eV. Since the small Auger peaks must be distinguished from a large secondary electron background, originating from the excitation with an electron beam, it is only by the use of a Lock-In amplifier that it becomes possible to achieve a surface sensitivity down to the submonolayer region with small primary beam currents. Spectra are usually shown as the differentiated curve of the detected number of Auger electrons, dependent on the retarded energy. Because of different atomic energy levels for electrons, all elements are related to specific spectra, with peaks reflecting the difference of inner atomic levels. The values are tabulated in literature (e.g. Auger Atlas [aug]).

The Auger process is depicted in Fig. 5.3 for a LMM transition as an example. A core hole, caused by an ionizing electron beam, is filled by an electron of the atom. The energy is used by another electron to escape the atom with a certain kinetic energy (a non-radiative process in competition to florescence, where a photon is emitted). In this notation the first letter L is the final state and M the initial state of the relaxing electron. The level of the finally escaping Auger electron is noted by the last letter. The energy equation for this three particle process of an Auger electron can be written for a solid as follows:

$$E_{WXY} = E_W - E_X - (E_y + e\varphi) + R - F(X,Y) \tag{5.1}$$

where φ denotes the work function of the solid, R the electrostatic screening term for the core hole and $F(X,Y)$ is the two electron interaction energy describing the coupling of the two final state holes in the remaining, double ionized atom after the Auger transition [shi73][aug].

Low Energy Electron Diffraction

The technique of *L*ow *E*nergy *E*lectron *D*iffraction (LEED) has nowadays become one of the most common methods in surface science to study the structure of surfaces [ert85], [de96] and it was one of the first techniques used in this field [la36]. The discovery of interference phenomena of electrons is closely related to the development of quantum mechanics. L. de Broglie postulated the wave-like nature of matter in 1924. This was experimentally confirmed in 1927 by Davisson[1] and Germer with the demonstration of diffracted electrons obtained with a Ni crystal. A flux of particles with velocity v and mass m and a momentum p=mv is correlated with a de Broglie wavelength $\lambda = h/p$, h being Planck's constant.

[1] C. Davisson, Nobel price 1937

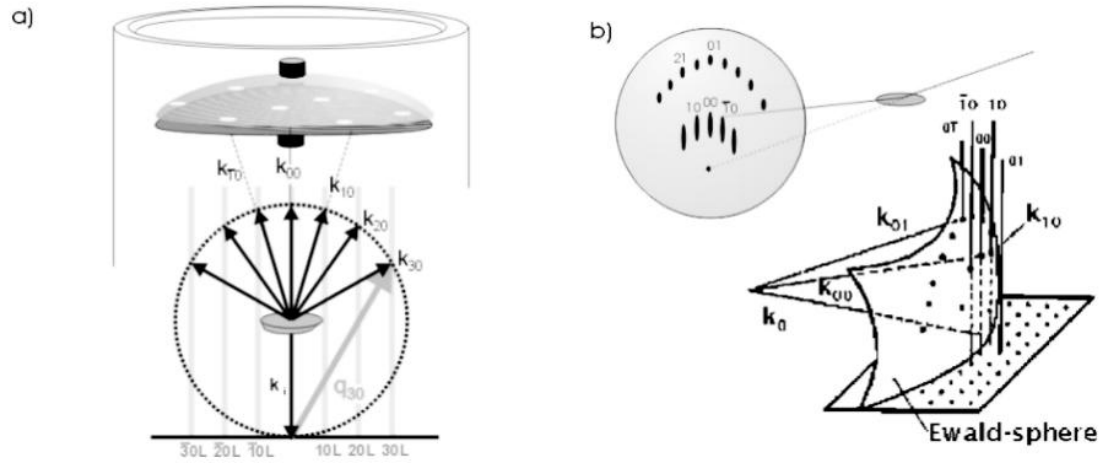

Figure 5.4: Comparison of LEED and RHEED

For electrons accelerated by an applied electrical potential difference ΔV we can write for its momentum p=$\sqrt{2m_e e\Delta \mathrm{V}}$ and we obtain for the de Broglie wavelength of such electrons as λ=12.285Å/$\sqrt{\Delta \mathrm{V}}$. It follows immediately from this equation that the wavelength for 100 eV electrons is about 1.23 Å, so that interference effects of particles with energies around 100eV is to be expected at periodic crystal lattices, just as X-rays with similar wavelength are diffracted. Besides an atomic scale structure analysis of surfaces within the framework of the dynamical scattering theory [cow95], [ov98], valuable information about the long-range order and defect arrangements of periodic surface structures can already be derived by a mere optical inspection of the LEED pattern. These interpretations of the spot positions and spot shapes in a LEED pattern use the much simpler kinematical scattering theory [ert85]. A LEED image can be thus used as a reciprocal map for X-ray diffraction experiments.

A sketch of an ordinary 4-grid LEED optics is shown in Figure 5.1 together with the Ewald sphere and a rough scheme of the reciprocal space. The electron gun is pointing normal to the surface of the sample. The grids are used for screening secondary electrons and to accelerate the diffracted electrons on the phosphorous screen. As the penetration depth of low energy electrons is only in the order of a few atomic diameters, the intensity variation along a crystal truncation rod (CTR) is not extremely big (compare Fig.4.7 b,e,f). Independent of the incident energy most diffraction spots can be observed, but their relative intensity might change. Like in the case of X-rays a detailed analysis of the L-dependent CTR intensity reveals structural details of the surface. But the analysis has to be based on dynamical theory, because the strong interaction of electrons with matter means that multiple scattering events can not be neglected anymore.

In this work LEED has only been used to check for a successful UHV cleaning and annealing procedure. Typical primary energies in a LEED experiment range from 25 to 200 eV and the current density is about 1 μA/mm^2. Switching between an AES and LEED mode in these combined set-ups requires a change in voltages applied to the electron gun, the grids and the LEED screen.

Reflection High Energy Electron Diffraction

In both, the Stuttgart and the Grenoble MBE chamber a RHEED system is included. The main advantage of using electrons with high energies (in the range of 10 000 to 30 000eV) is that it allows for the sample to be placed further away from the screen. Reflection High Energy Electron Diffraction (RHEED) is often applied in growth chambers, where the area around the sample is exposed to material (metal) deposition, and complicated electrical grid arrangements would become prone to failure. Visualization of the RHEED image does not require further accelerating fields (as in the case of LEED). As reflection with small angles is used, the penetration depth is limited and the resulting scattering vectors are small (comparable to LEED). The Ewald sphere of the RHEED method is sketched in Fig.5.1b. As the Ewald sphere is cutting the reciprocal intensity rods with shallow angles often extended streaks are seen instead of sharp reflections. These streaks have their origin in non-ideal surface structures that broaden the intensity rod (like a stepped surface or a mosaic structure, with slightly different surface normal vectors, for example)

5.2 Beamlines and Diffractometers

Surface X-ray diffraction (SXRD) and scattering from surfaces would hardly be possible without the intense flux of high energy synchrotron radiation. In addition, the ability of hard X-rays to penetrate in matter enables us to study buried interface structures on an atomic length scale.

Due to the high radiation exposure of the surrounding of the X-ray beam, the experiment is usually setup inside of radiation screened hutches. The experiment is then remote controlled from an experiment control room. The control software used depends on the experimental station. At BW2 in Hamburg 'tascom' is used, which was developed at RisøResearch Laboratory, Denmark. At ANKA and ESRF the program SPEC, a widely distributed code for diffractometer control, is used. X-ray measurements for this thesis work were conducted at three different synchrotron light sources: ESRF in Grenoble (beamlines ID3 and ID32), HASYLAB in Hamburg (beamline BW2) and ANKA (MPI

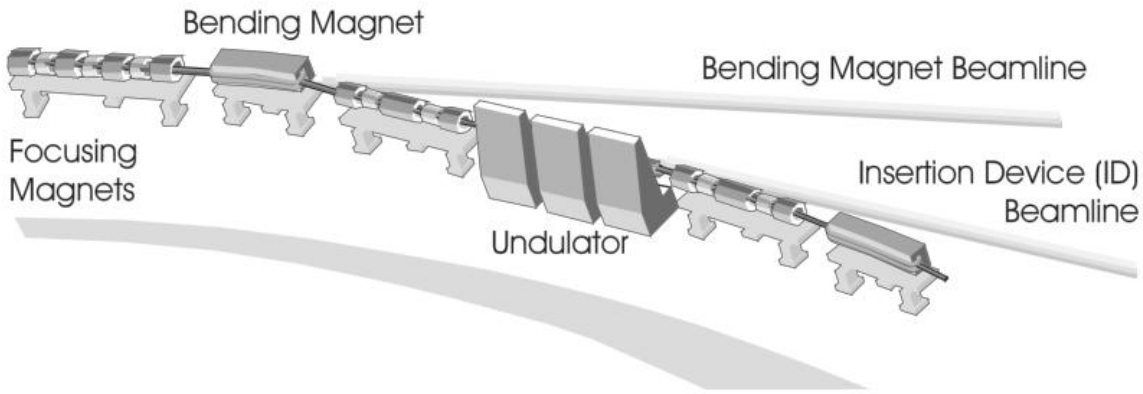

Figure 5.5: A general sketch of a section of a synchrotron light source. The beamlines are distributed around the ring and the actual spectrum is dependent on the specific setup. Bending magnets, one or more wigglers or undulators are determining the spectrum.

Diffraction Beamline) in Karlsruhe. The used beamlines are shortly introduced in the following sections.

ID32, ESRF

Source and Beamline Characteristics

The ESRF is a third generation synchrotron light source with a 6 GeV electron storage ring. The cut-off energy is about 20keV at bending magnet beamlines (compare Fig. 4.5). ID32 is installed at a high β section,i.e. the beam has a low angular divergence. As optical elements after a liquid nitrogen cooled primary silicon monochromator, which can be used between 2 and 30 KeV, a mirror for harmonic energy photon rejection or a high resolution post-monochromator can be employed. The mirror contains three stripes of different materials with different cut-off energies for a fixed angle of incidence (using the different critical angle for different energies): SiO_2, Cr and Pt. The beamline has been described in the literature [co95]

Experimental Endstation

ESRF ID32 is a surface and interface science beamline offering a X-ray UHV chamber with an installed PHI hemispherical electron analyzer and, separately, a 6-circle Kappa diffractometer, which was received in the beginning of 2003. For this work only the dif-

Figure 5.6: The image on the left shows the ESRF ID32 diffractometer with a mounted tower to run in six circle mode, in the middle the HASYLAB BW2 Risøz-axis diffractometer, on the right the ANKA MPI diffractometer. All machines allow the mounting of relative heavy sample environments.

fractometer was used. During this thesis work the original W21V (2 × 2) machine was replaced by this new Huber Kappa diffractometer, with the possibility to use a sample tower instead of the Kappa set-up. With the sample tower the diffractometer can be run in 6-circle mode, but with incident angles not larger than 1° (or 0.66° if the mirror is used). In this way the new diffractometer was used for measurements in this work.

BW2, HASYLAB

BW2 (from Bending Wiggler 2) is a wiggler beamline at the DORIS III, 4.5 GeV positron storage ring. DORIS was originally a high energy physics accelerator, that was last upgraded for the use as a first generation ('$1\frac{1}{2}$ generation source') synchrotron radiation light source in 1993.
The optics of the BW2 beamline includes a first mirror and a bend second monochromator crystal for vertical and horizontal (sagitally) focusing of the beam. At the end of the beamline optics an additional mirror can be introduced for rejection of photons with higher harmonic energies. For this work a Au mirror with a cut-off at 11.92 keV photon energy was used.
The diffractometer at BW2 is a so-called 6-circle z-axis diffractometer, which is basically a 2×2 diffractometer plus two motors (cradles) to align the sample surface normal horizontally. 2×2 means two degrees of freedom for the detector and 2 for the sample, after alignment. The diffractometer is controlled by 'tascom', a control language developed at RisøResearch Laboratory.

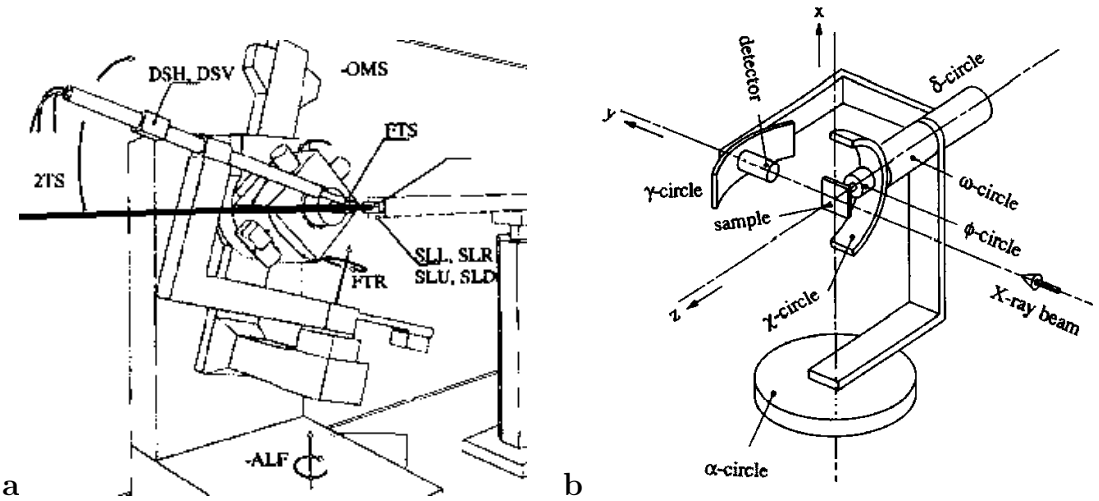

Figure 5.7: This sketch of the BW2 diffractometer shows the main motor names and directions. The motors are controlled by the software 'tascom'. The BW2 diffractometer is a 6-circle z-axis diffractometer and the according correction factors for comparing calculated F^2 intensity with the measured integrated intensity has been calculated by Elias Vlieg [vl97].

MPI-MF, ANKA

On the site of the Research Center Karlsruhe (FZK) a new member in the world wide family of synchrotron light sources was inaugurated in 2001. The Angström Quelle Karlsruhe (ANKA) is a third-generation style electron storage ring with an energy of 1.9 and 2.5 GeV. The lower energy is better suited for X-ray Lithography (LIGA), the higher energy yields a higher flux at smaller wavelengths, i.e. also at the wavelengths used for this work. The heavy load 2×3 diffractometer installed at the dedicated MPI-MF Diffraction beamline is shown in the right image of Figure 5.2

5.3 The Atomic Force Microscope (AFM)

The Scanning Tunnelling Microscope (STM), presented for the first time 1981 by Gerd Binnig and Heinrich Rohrer ([bi82]), was the first of a kind of experimental techniques, that is more generally called Scanning Probe Microscopes (SPM). It was again G.Binnig who was involved in the development of Atomic Force Microscopy (AFM) ([bi99]). After that, several additional SPM techniques emerged. They all differ in the way the distance between tip and sample is detected or in the physical origin of the force causing deflection of a probing tip. SPMs are a family of instruments used for studying surface properties of materials from the atomic to the micron level. They are imaging tools with a vast dynamic

range, spanning the realms of optical and electron microscopes. It is also a profiler with unprecedented 3-D resolution. In some cases, SPM's can measure physical properties such as surface conductivity, static charge distribution, localized friction, magnetic fields, and elastic modulus. As a result, the applications of SPMs are very diverse. The STM was first applied in UHV, because clean contaminant free surfaces are required for a sufficient image quality. Nowadays SPMs work in environments ranging from UHV to high pressure,

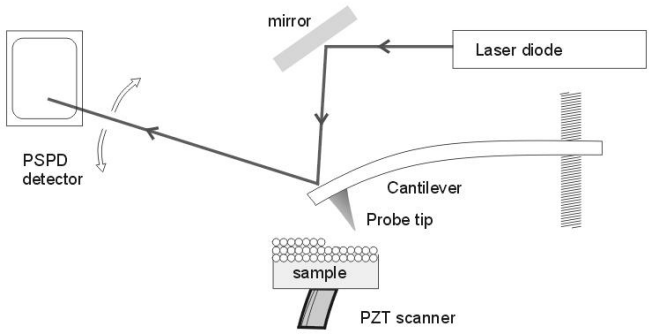

Figure 5.8: Scheme for the most common set-up of an AFM.

including liquids and easy to use ambient air pressure set-ups.

In this work an in-air atomic force microscope (AFM) in non-contact tapping mode was used (Molecular Imaging (MI) Dimension 3100), mainly because images on the μm scale are less sensitive to traces of contaminants residing from the x-ray cell measurements and from transfer through air. The AFM can also better cope with a rough surface morphology generated by the dealloying process compared to e.g. a STM. Although STM's give better resolution on the atomic scale, they also require clean and flat surfaces on the scale of the image. The AFM probes the surface of a sample with a sharp tip, a couple of micrometers long and often less than 10 nm in diameter. The tip is located at a free end of a cantilever that is 100 to 200 μm long. Forces between the tip and the sample surface cause the cantilever to bend, or deflect. A detector measures the cantilever deflection as the tip is scanned over the sample, or the sample is scanned under the tip. The measured cantilever deflections allow a computer to generate a map of surface topography. AFMs can be used to study insulators and semiconductors as well as electrical conductors, which is an advantage compared to the STM, which requires sufficient conductance of the sample.

Several forces typically contribute to the deflection of an AFM cantilever. The force most commonly associated with basic non-contact AFM technique is an inter-atomic force

called the Van der Waals force. The dependence of the van der Waals force upon the distance between the tip and the sample is shown in Figure 5.9. Two distance regimes are labeled: 1) the contact regime; and 2)the non-contact regime. In the contact regime, the cantilever is held less than a few tens of a nm (several Angstroms) from the sample surface, and the inter-atomic force between the cantilever and the sample is repulsive (mainly as a result of repulsive Coulomb interaction of the electrons in tip and surface). In the non-contact regime, the cantilever is held one to ten nm from the sample surface, and the inter-atomic force between the cantilever and the sample is attractive. This is a result of the long-range van der Waals interactions. Mainly because of the expected contaminants and the expected surface roughness after dealloying in electrolyte, for this work the non-contact regime was chosen and will be described more in detail in the following.

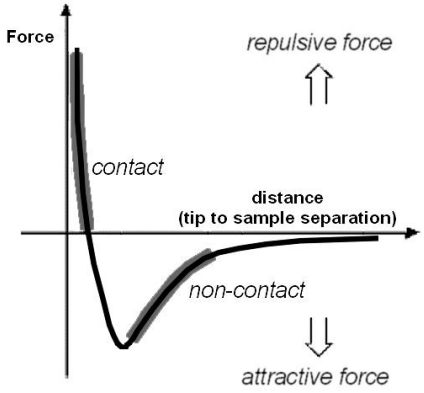

Figure 5.9: Different regimes that are used for atomic force microscopy (AFM). The attractive forces for larger distances are mainly due to van der Walls forces. At a distance of about the scale of atomic bonds (i.e. in contact) the repelling Coulomb interaction dominates.

Most AFMs currently on the market detect the position of the cantilever with optical techniques. In the most common scheme, (Fig. 5.8) a laser beam bounces off the back of the cantilever onto a position-sensitive photodetector (PSPD). As the cantilever bends, the position of the laser beam on the detector shifts. A PSPD can measure displacements of light as small as 1 nm. And as the ratio of the path length between the cantilever and the detector and the length of the cantilever itself produces an amplification of the movements on the detector site, the system can detect sub-nanometer vertical movement of the cantilever tip. Non-contact tapping mode AFM is using a vibrating cantilever, which is hold close to the sample surface in the non-contact regime of 5.9. The advantage of the tapping mode is that it provides means for scanning the sample topography with no or little contact between the tip and the sample and does not suffer from tip or sample degradation effects sometimes observed after performing several contact AFM scans. The total force between the tip and the sample is very small, generally about 10^{-12} N. This

small force it is more difficult to measure, than in the contact AFM regime, where forces are several orders of magnitudes greater. To avoid the tip being pulled towards contact with the surface, NC-AFM tips are made stiffer than those made for contact AFM. The small force values in the non-contact AFM regime and the greater stiffness of the cantilevers used are both factors that make the NC-AFM signal small, and therefore difficult to measure. Thus, a sensitive, AC detection scheme is used for NC-AFM operation. In non-contact mode, the system vibrates a stiff cantilever near its resonant frequency (typically from 100 to 400 kHz) with an amplitude of a few tens to hundreds of angstroms. Then, it detects changes in the resonant frequency or vibration amplitude as the tip vibrates close to the surface of the sample. This change has it origin in the different force gradient on the van der Waals curve at different distances to the sample surface. The resonant frequency varies via the spring constant of the whole system depending on the force gradient experienced by the cantilever. While scanning the sample surface the resonant frequency (and so the sample-tip distance, if the elastic properties of the sample do not change laterally) is kept constant with the aid of a feedback system that moves the scanner up and down. Finally, the motion of the scanner (besides other values like phase or amplitude) can be used to generate the data set or image.

5.4 In-Situ X-Ray Electrochemical Cell

Understanding surface structures is important, since it is mostly the surface where a material interacts with its surrounding. This fact is of upmost relevance for processes like deposition (nucleation), heterogeneous catalysis or corrosion. In the technically important

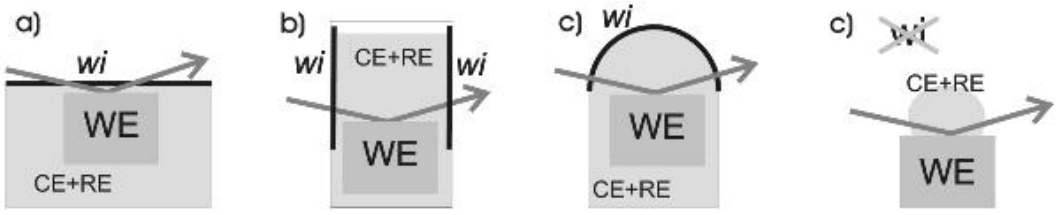

Figure 5.10: Different types of in-situ X-ray cell designs. (a) the thin-layer cell can be used with x-rays in the 10 keV range, but has limitations for kinetic measurements, due to a big resistive potential drop, when a current is passed. The thick-layer designs (b-c) have the advantage of better control over the applied potentials and are less questionable for impurity accumulation. X-ray energies above 20 keV have to be used in order to pass the electrolyte reservoir. (d) The droplet cell is not in contact with a window and the sample holder.

case of electrochemistry an extended knowledge has been obtained with ex-situ structural

methods, like LEED, after transfer from electrolyte solutions into vacuum chambers. Nevertheless ex-situ experiments always cause a rest of doubt about the effects of the change of environment or the loss of potential control within electrochemical studies. With the availability of custom access to synchrotron radiation facilities also electrochemical experiments are increasingly conducted, since X-rays offer in many cases the only possibility for 3D-structural studies at buried interfaces (i.e. in solution in the case of electrochemistry). Many different designs for in-situ X-ray experiments have been reported (Fig.5.4), adapted for Diffraction (XRD)[fl87][oc90][ze98][ze98b] [rob86][na02], x-ray standing waves (XSW)[mat87], Reflectivity[na02], or X-ray Absorption Spectroscopy (XAS).

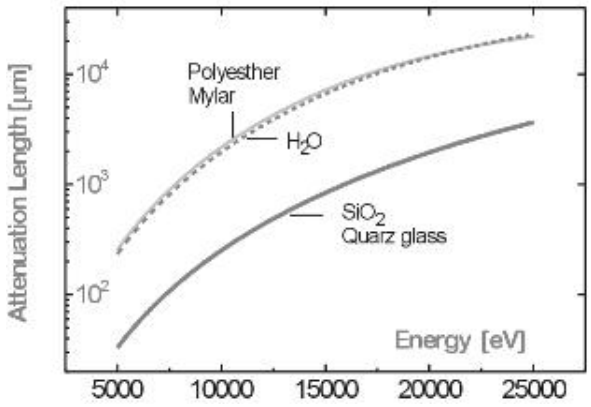

Figure 5.11: Attenuation lengths of the main materials in the pathway of X-rays in electrochemical cells: Quartz can be used for windows, but mylar is the most common window material. Water (H_2O) is the main part of dilute electrolytes.

The choice of cell design and the used materials have to be considered for each experiment. The geometry and the X-ray energy influences the amount of produced side products in the beam path. It is anticipated that for example water electrolysis will take place and peroxide and hydrogen is produced in the beam. Also organic impurities can be cracked and radicals formed. Especially at third generation synchrotron light sources this are factors have to be considered, while at second generation sources no such limitations have been reported. Etgens et al. reported Cu dissolution under the beam at otherwise stable conditions and holes punctured by the beam in the polypropylene or mylar membrane are a common nuisance. A general feature of electrochemical cells is the use of chemically very inert materials, due to the need of ultra-clean conditions and the therefore applied heavy cleaning procedures. For this purpose the use of a Teflon/Kapton sandwich membrane [na02] would be ideal, but was not tested here. Quarz glass (SiO_2) is mainly used in common electrochemistry. For specialized cell designs plastic materials can often not be avoided. Table 5.1 gives a list with the cell materials we have used.

For all measurements in this work the thin film in-situ X-ray cell was used. Additional cells were designed and partially tested, and are ready for a first use. In the following,

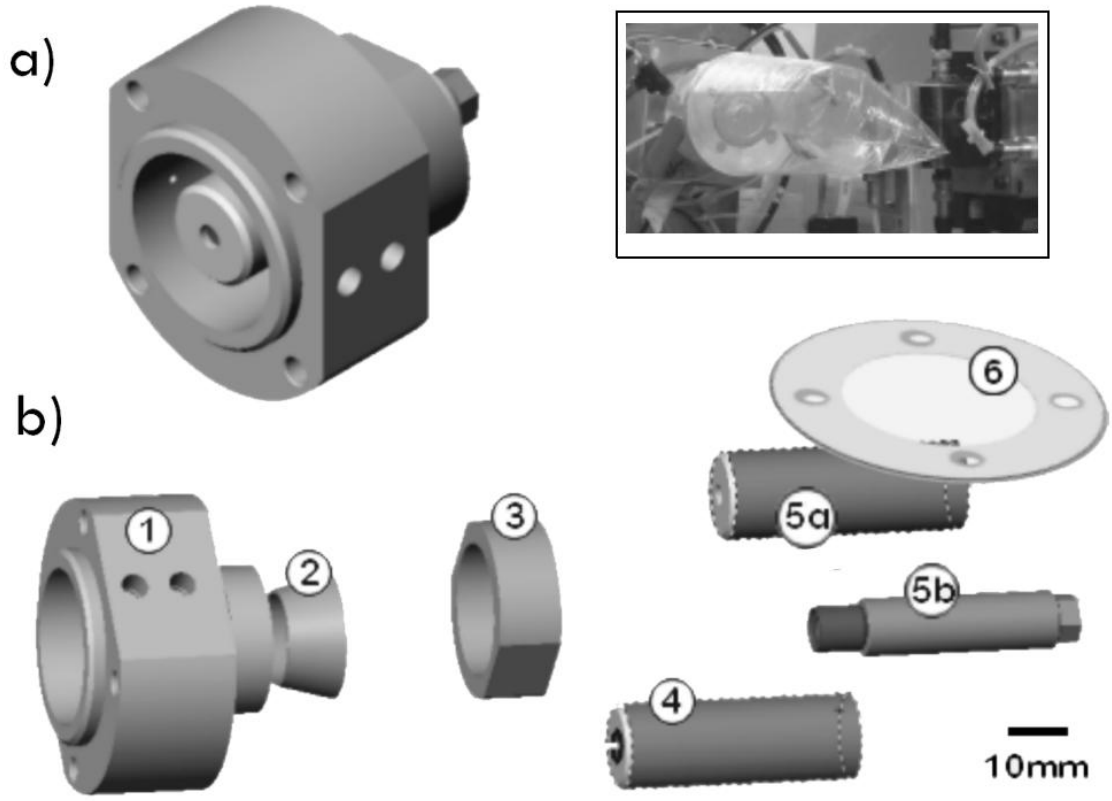

Figure 5.12: The thin-layer in-situ X-ray cell was designed in collaboration with INFM-OGG in Grenoble. (a) The assembled cell, without sample and polyethylene foil. (b) The parts of the cell: (1)Cell body, PCTFE, with four connections for electrolyte inlet and outlet, reference and counter electrode. (2)Sealing Ring, Teflon or Kel-F. (3)Nut to fix the sample holder, Teflon. (4)Vacuum nozzle sample holder, PCTFE and o-ring, Kalrez. (5a) and (5b)Sample holder, PCTFE, for hat-shape samples with metal bolt to fix and press the sample from the backside (6)stainless steel ring to fix the polyethylene foil and the bag for the inert atmosphere in front of the sample.

mainly the thin film cell will be described and the other cells shortly mentioned.

5.4.1 Thin Layer Cell

The penetration of X-rays into matter is large if compared with the penetration of electrons. But strong absorption of the radiation occurs, if we have to pass material on the length scale of mm. Figure 5.4 shows the transmission of water, which is the main constituent of aqueous electrolyte solution. Due to this reduced transmission of X-rays in the energy range of 10 keV, the first electrochemical experiments at second generation synchrotron

light sources were conducted with thin-layer designs, were the path through the electrolyte is minimized. At third generation hard X-ray machines like the ESRF the flux would be sufficient even at higher energies to work with a thick-layer or transmission design. Such experiments have been conducted [et97][ze98]. Nevertheless, if experiments are aimed to be performed at lower energies the thin-layer design is the favorite set-up. This is the case if energies below absorption edges are chosen, or for experiments using anomalous scattering, if the used absorption edges are at lower energy (e.g. the Cu K edge at 8.98 keV).

In order to sustain the strong oxidative acid (Caro's acid, also called piranha-acid, see below) used for the thorough cleaning procedure, all parts, with exception of the polyethylene foil, were made from PCTFE or Teflon (PTFE). Different sample holder designs can be used for our in-situ cell; the common feature is a sample-holder-rod diameter of 18mm. For the experiments we mainly used the vacuum holder, together with a roughing pump and a liquid trap, which prevents the electrolyte solution from entering the pump in case of leakage. A sample holder for hat-shaped samples, which is especially important for X-ray Standing Wave (XSW) experiments (because strain in the sample is a problem for the necessary sharp Bragg peak width and the sample will be much less strained if fixed at the hat edge) is also available and was used by several external user groups. The construction with the fixing from the backside has two advantages: the mounting is very quick and the clean parts inside the cell don't have to be touched when mounting a new sample.

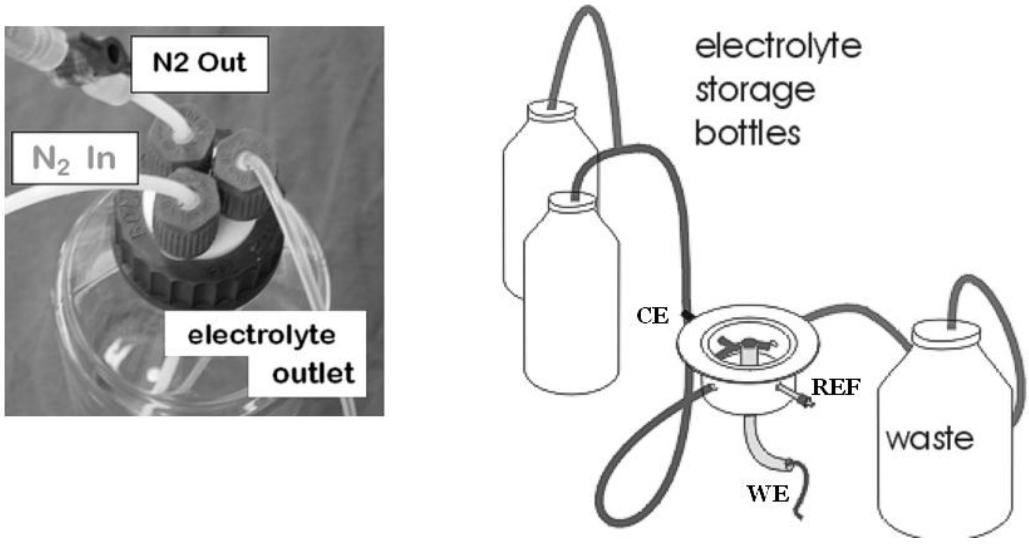

Figure 5.13: The in-situ cell is connected to an electrolyte storage bottle and to a waste bottle. The storage bottle can be purged with various inert gases, e.g. Argon or Nitrogen

The main body of the cell has four additional openings with 1/4"-28 threads, which are used also in high pressure liquid chromatography (HPLC). This has the advantage that the connectors to the Teflon or PFA tubing are commercially available in Teflon. Two of these connections are used to insert the Pt counter electrode and the used Ag/AgCl micro reference electrode (diameter 1.5 to 2mm). Here, commercially available micro-reference electrodes were used, either the model DRI-REF purchased from World Precition Instruments(WPI), or the model EE009 from Cypress Systems, Inc. The two remaining openings are connected to the electrolyte inlet and outlet tubing. A schematic drawing of the connected setup is shown in Figure 5.13. This scheme is the same for all used cells, i.e. the other cells that will be presented below are connected in the same way.

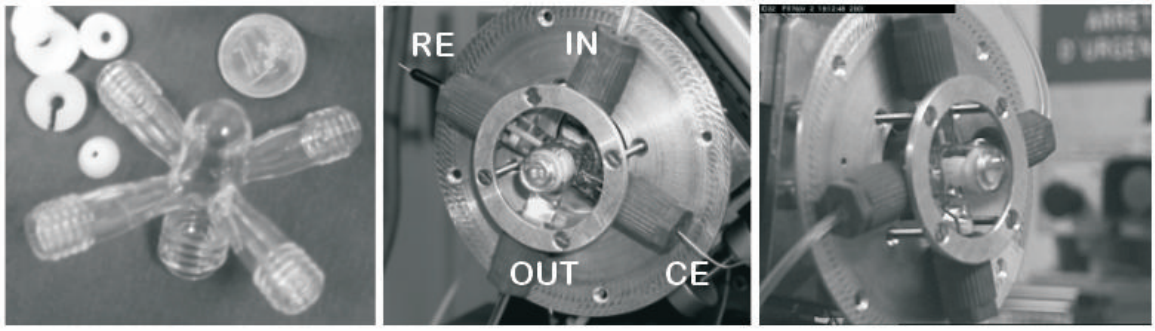

Figure 5.14: A transmission design: The electrochemical glass dome X-ray cell.

5.4.2 Transmission Cells

Transmission cells, also called thick-layer cells, have the advantage of good electrochemical conditions for dynamic interface processes. A big reservoir volume of electrolyte is above the sample, allowing a homogeneous electrical field even with current flowing in the system.

The drawback of these cells is that a long pathway of the X-rays through the electrolyte can not be avoided. This implies that a higher energy should be used in an experiment to diminish the absorption and to obtain a good signal to noise ratio. As can be seen in Figure 5.4 the attenuation length increases with higher X-ray energies. To contain the electrolyte solution and as a window for the radiation a Quartz dome has been used. Strong background intensity emerging from scattering at the Quartz glass has to be screened out by the usage of well adjusted slits. All parts that are exposed to electrolyte solution are made from Quartz, Teflon, Kel-F or Kalrez. They can all be cleaned with Caro's acid to achieve clean experimental conditions. During experiments an accumulation of gaseous

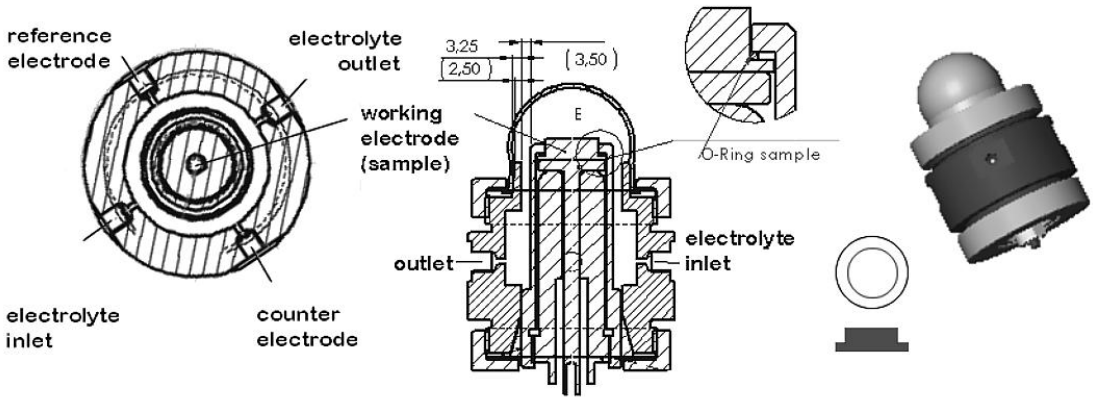

Figure 5.15: The large electrochemical glass dome X-ray cell for high energy radiation (e.g. 70keV).

products has to be avoided, as this would influence the total absorption along the pathway of the X-rays and a normalization of intensity might become impossible.

Material	**Full Name**	**Chemical Formula**	**Comments**
PTFE Teflon^{TM}	polytetra-flouro-ethylene	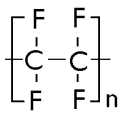	resistance to strong oxidizing acids
Teflon FEP (tubing)			similar to PTFE transparent
PCTFE Kel-F^{TM}	polychlor-triflouro-ethylene	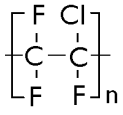	resistance to strong oxidizing acids, good hardness for machining
ETFE Tefzel^{TM}	ethylene-tetraflouro-ethylene	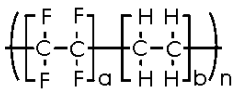	less resistant to strong oxidizing acids
Viton^{TM}		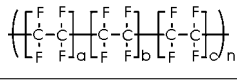	resistant only to weak acids (1 M H_2SO_4)
PEEK	polytether-etherketone		not resistant to weak acids
Polyesther Mylar^{TM}			Used as X-ray Window breaks after exposure

Table 5.1: Table of the used materials

5.5 Electrochemical Measurements

Chemicals and Cleaning Procedures

Conclusive surface science experiments are hardly possible without clean surfaces. For electrochemical experiments this means some prerequisites are necessary: ultra-pure glassware, chemicals and an ultra-pure water supply. In the Electrochemistry Laboratory (ID32 and INFM-OGG) standart electrochemical equipement is available (Fig. 5.16). Glassware and instruments in contact with the electrolyte solutions have to be thoroughly cleaned. For the **cleaning procedure** we chose to use Caro's acid, which is a mixture of concentrated H_2SO_4 and hydrogen peroxide H_2O_2 at a ratio of 3:1, respectively. In this mixture the highly oxidative SO_5^{3-} ion is forming. Caro's acid is a strong oxidizing acid and has to be handled with care. All parts, that will be in contact with the solution during or before the experiments and that are chemically resisting are soaked overnight into Caro's acid. Afterwards all parts have to be rinsed with ultrapure water and are subsequently immersed into a cleaned beaker filled with ultraclean water and heated close to the boiling temperature. This last cycle is then repeated three times.

Figure 5.16: The Electrochemisty Laboratory offers the possibility to perform standart electrochemical measurements.

As an **ultrapure water supply** an ELGA Maxima system was installed in our laboratory. This filter machine uses the illumination of the water with UV light before passing the final filter and low contamination levels are reached. The water supply for the ELGA Maxima could be demineralized water from the store, but we used an Millipore Direct-Q as supply, which delivered already pure water of higher TOC values. The purity is measured in values of the total organic content (TOC). The Millipore Direct-Q delivered water with a TOC of 10-15 ppb and the ELGA system (with UV treatment) reached values <2ppb.

Name	Producer	Comments
H_2SO_4 96%	Merck suprapur	for electrolyte solution
$HClO_4$ 96%	Merck suprapur	for electrolyte solution
HCl 30%	Merck suprapur	for electrolyte solution
H_2SO_4 96%	Merck p.a.	for Caro's acid
H_2SO_4 96%	Fluka p.a.	for Caro's acid
H_2O_2 30%	Aldrich p.a.	for Caro's acid
HCl 30%	Merck	for Au electropolishing process
H_2O	millipore and USF	Water Filter Systems (TOC$\leq$ 2ppb)

Table 5.2: Chemicals used for the Experiments

To check the experimental setup, including the water quality, we used voltammetry of single crystal Au(111). Clavilier developed the so-called **flame-annealing** for Pt samples, but the technique is today used for many other noble metals, including Au. In the case of Au single crystal surfaces, flame-annealing produces reliably clean, flat and reconstructed surfaces, simply by heating the crystal in the flame of a Bunsen or laboratory burner. Figure 5.17 shows an image taken in our laboratory. To avoid melting, the temperature is

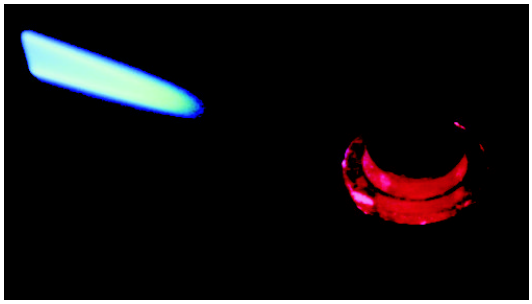

Figure 5.17: Flame annealing is a very powerful technique frequently used to prepare noble metal crystals for electrochemical experiments.

judged by the onset of a red glowing color in a darkened room. After several seconds the surface is already reconstructed, but, to remove residual surface contaminations, it is kept hot for a few minutes by moving it calm and regularly through the flame. The crystal is then let cool down, possibly in a slow nitrogen stream, and finally covered with a droplet of ultra-clean water.

Electrochemical Measurements: Voltammetry

Voltammetry is one of the most frequent techniques in electrochemistry. A quick overview of reactions taking place can be obtained. The method can also serve as a fingerprint of the sample status, because changes in morphology (i.e. more defects on a rougher surface)

or in solution or surface purity will change the response to a potential scan. In Figure 3.1.3 the UPD process of Cu on Au(111) was shown, together with the voltammogram shown also in the inset of Figure 5.18.

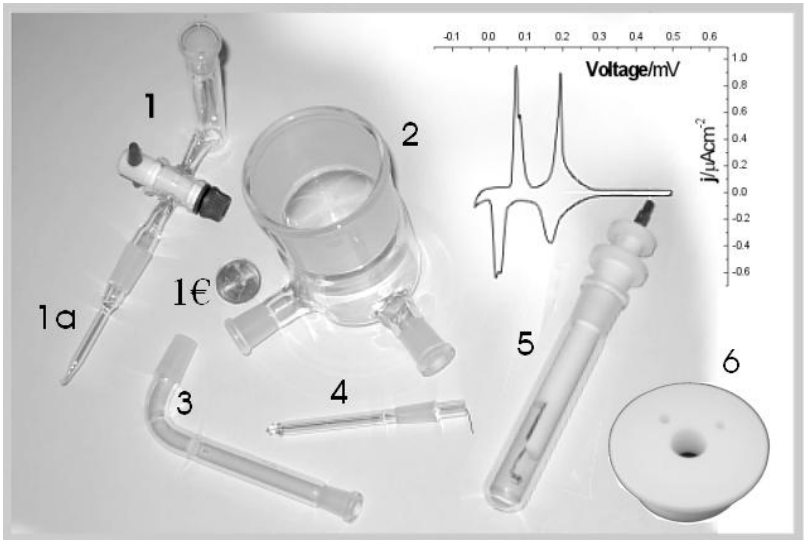

Figure 5.18: Parts of the glass cell. The common setup includes a Luggin capillary (1a) for the reference electrode (1) and the main cell (2). The counter electrode is separated from the main electrolyte by a ceramic frit (3) and is made with a Pt wire twisted around a glass rod (4). The sample is fixed on a sample holder (5) by a Au wire, so that only the sample surface can be brought in contact with the electrolyte (dipping technique). The cover (6) is made from Teflon and has openings for nitrogen purge and the sample.

In a common **setup for voltammetry measurements** a glass cell is used, because glass can be cleaned easily and withstands most aggressive chemicals (HF is an important exception). In the design we used in our electrochemical laboratory, the reference electrode is introduced with a Haber-Luggin capillary and is separated from the main cell by a Teflon valve. The valve consists of a conical Teflon bolt with a passage in one direction. The bolt can be turned inside a glass surrounding. If the Teflon valve is turned in the filled cell, a thin electrolyte layer will wet the thin space between Teflon bolt and glass, which is already enough to maintain an electrical connection with the main cell (i.e. even for a closed valve). This inhibits diffusion of eventually introduced contaminations from the reference electrode towards the main cell. In Figure 5.18 the Luggin capillary ($1a$) at the reference electrode holder (1) is shown. The counter electrode is behind a ceramic frit to separate reaction products of the counter electrode from the working electrode. The

sample is fixed on a sample holder (5) by a Au wire, so that only the sample surface can be brought in contact with the electrolyte (dipping technique). The cover (6) is made from Teflon and has openings for nitrogen purge and the sample holder. The voltammetry experiments in the electrochemistry laboratory were conducted inside a Faraday cage (a metal box). At the beamline (with a lead covered hutch) a faraday cage was not necessary.

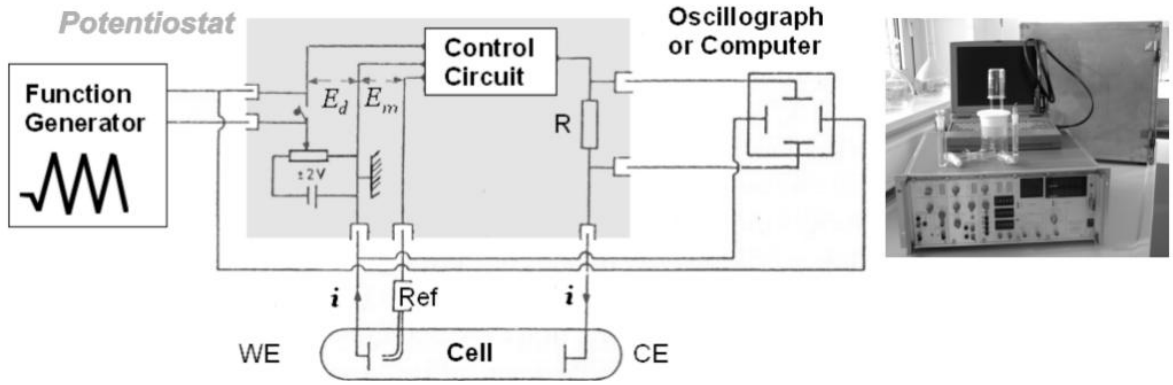

Figure 5.19: Schematic drawing of a potentiostat. For accurate electrochemical experiment a three electrode setup is necessary. A potentiostat is controlling the potential difference between a (ideally current free) reference electrode and the working electrode.

We have seen in Chapter 3.1.4 that an electrical current passing through an electrode is also causing potential drops, i.e. process overpotentials and ohmic drops in the electrolyte. In accurate electrochemical measurements therefore a three electrode setup is used, with a reference electrode (Ref) a working (WE) and a counter (CE) electrode. The experiment, i.e. the applied potential, is then controlled by a potentiostat (Fig. 5.5). The reference electrode is connected with a high input impedance on the potentiostat and is essentially current free. The potentiostat is regulating the applied potential between counter and working electrode such that the (measured) potential drop between the reference and the working electrode E_m will be equal to a desired (e.g. given by a function generator) voltage E_d. The current in the electrochemical cell is passing through the working electrode and the counter electrode. We used a potentiostat built at the Fritz-Haber-Institute in Berlin, which was on loan from the Department of Electrochemistry (University of Ulm).

Chapter 6

The System Cu-Au

Because of their noble character, Au and Cu can be found naturally and belong to the earliest metals ever used in the human history. Depletion gilding for Au-Ag-Cu, for example, alloys is an early electrochemical technique, that was used already by high cultures in Andean South America [le84]. Nowadays Cu-Au is an important model alloy; ordering phenomena of the bulk crystal and the surface having attracted most attention, but also aspects of corrosion, like studies of stress corrosion cracking (SSC) and dealloying.

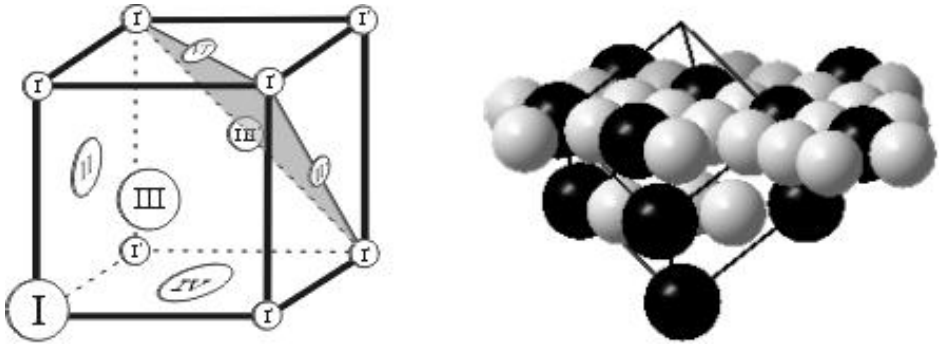

Figure 6.1: Cu_3Au is the most prominent example for the $L1_2$ structure, which consists of a base fcc lattice with the two alloy atoms occupying different cubic sub-lattices. Viewed in different directions, the $L1_2$ superlattice consists of a stacking with specific layer compositions. In the [100] direction, a pure Cu {100} layer follows on a 50%-Cu and 50%-Au layer. The same is true for the [110] direction. The succeeding layers in the [111] direction consist of equal and stoichiometrically occupied planes. Cu_3Au has an order-disorder transition at T_c= 390°C. In the disordered temperature region ($T > T_c$) each of the sublattices is statistically occupied by Cu and Au atoms, with a probability according to their stoichiometry (A2 structure type).

Above 410°C Cu and Au are miscible over the whole range of composition. The Cu-Au system phase diagram is shown in Figure 6. We recognize the three ordered phases

Au_3Cu, CuAu and Cu_3Au. The structure of ordered Cu_3Au (as for Au_3Cu) below T_c is referred to as $L1_2$ superlattice structure. AuCu is of the $L1_0$ type. A fcc crystal, like e.g. pure Au, is made of four equivalent cubic sub-lattices (I to IV in Figure 6) In the Cu_3Au-$L1_2$ structure a fcc lattice is the basis for the alloy crystal, with the Au atoms sitting on one and the Cu atoms occupying the three other sub-lattices. Above the ordering transition temperature all sites are statistically occupied with a probability according to the stoichiometry (A2 structure-type). Cu_3Au has at T=390°C an order-disorder phase transition, which was extensively studied in the past, in bulk materials and at surfaces [war] [do91][re96] [bo96][mc90].

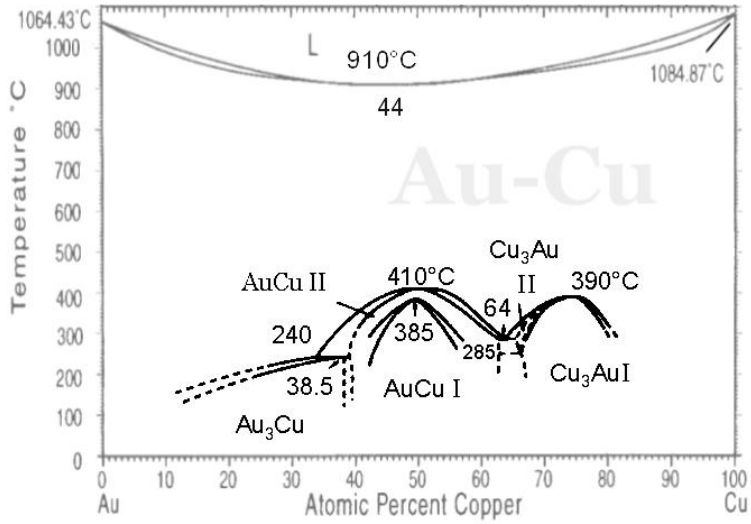

Figure 6.2: Phase diagram of the Cu-Au system. Above 410°C Cu and Au are completely miscible. The Cu_3Au I structure below 390°C is of the $L1_2$ superstructure type.

The process of ordering has been studied (Compare literature in [mc90]). An ordered crystal contains anti-phase boundaries between different ordered domains, which are often separated in [100] direction by a fully with Cu occupied {100} plane. If the translation vector for the Au sub-lattice change lies within the respective domain wall, it does not include any change of the nearest neighbor coordination and is therefore of low domain wall energy (Type I domain walls). In the other cases there is an accumulation of Cu (a second pure Cu layer)[la92]. Ordering can be approximately considered as annealing-out of domain walls. After a temperature step from above to just below T_c, a time of roughly one day is required to obtain a substantially ordered crystal.

6.1 Studies on Cu_3Au-Alloys in UHV

6.1.1 Order-Disorder Transition

Cu_3Au is a classical model for order-disorder transition. The ordering phase transition temperature is $T_c = 390°C$ or 663K, where the structure is changing from the ordered $L1_2$ type to the (disordered) A2 type. In the three dimensional (3D) $L1_2$ binary alloy crystal the order parameter and the crystal composition can be represented as a four dimensional parameter $\eta = (\eta_x, \eta_y, \eta_z, \eta_4,)$, which depend on the four Au occupancy numbers c_1, c_2, c_3 and c_4 in the four sub-lattices, see e.g. [do00]. The behavior of the bulk order parameter was studied by Keating and Warren [ke51] experimentally and by Cowley [cow50] theoretically. A good review on these early studies is given in Warrens book [war]. Also the behavior at the surface of different orientations was studied [mc90][do00]. For the ordered structure far below T_c the composition is oscillating between Au contents of 0 and 0.5 and the crystal is terminated with the Au-rich plane. Using X-ray CTR measurements for studies close to T_c, Reichert [re96] observed for $Cu_3Au(001)$ an exponentially decreasing oscillating composition at temperatures even much higher than T_c, together with surface induced (in-plane) disorder below T_c. Similar surface-induced disorder below T_c was found for $Cu_3Au(111)$ [bo96][ern01]. Schweika computed simulations of the (111) surface order, which was also vanishing already below T_c [sch96]. Such surface induced disorder was measured by Ern et al. for thin $Cu_3Au(111)$ epitaxial layers [ern00] and the onset temperature for the disorder was determined to be $T_c-160K=230°$, i.e. at room temperature the (111) surface is expected to be well ordered up to the topmost layer.

6.1.2 Surfaces at Room Temperature

Much less work was done to characterize Cu_3Au at room temperature. The order-disorder transition temperature T_c is at T=663K. The thermodynamically stable bulk structure of Cu_3Au at room temperature is the $L1_2$ type. The pure $Cu_3Au(001)$ and $Cu_3Au(110)$ surfaces (read [ni02] for a review) and also $Cu_3Au(111)$ have been studied at room temperature. The (111) surface was imaged by Eckstein with UHV-STM [ec01] and shows the (2×2) superstructure expected for bulk-like termination. The $Cu_3Au(001)$ and $Cu_3Au(110)$-2×1 (stable at elevated temperatures below T_c) surfaces, are terminated by the 50%Cu-50%Au layer followed by the pure Cu layer. These two layers are then repeated (stacked) to form the bulk crystal. The fact that the gold rich layer occurs at the top was explained by the lower surface energy of pure Au in comparison with pure Cu [ov97](1550 mJ/cm^2 for Au and 1850mJ/cm^2 for Cu [mi79]). Indications for additional Au segregation have been also

observed in the second layer of the (110) surface [ov97]. The $Cu_3Au(110)$ surface develops, as the thermodynamically stable termination at room temperature, in a (4×1) reconstruction by formation of Cu double rows in the surface. In contrast to the single rows of the bulk terminated (2×1) surface, which is stable at elevated temperatures below T_c [ov97][ba96]. It seems that these Cu single or double rows determine the reactivity of the $Cu_3Au(110)$ surface. Morgenstern et al. exposed oxygen and nitrogen on the (110) surface and the oxygen dissociated already at room temperature and the induced reconstruction contains extra Cu rows segregated to form -Cu-O-Cu- chains on the surface. The subsequent layers are bulk-like. The nitrogen had to be dissociated by other means, before it adsorbed on the (110) surface. This behavior is similar to the one found on pure Cu(110) [cou90]. On $Cu_3Au(100)$ surfaces, neither nitrogen nor oxygen adsorbed readily at room temperature [ach93], but after offering atomic species the adsorbate layer is sticking to a topmost pure Cu layer. Altogether one can conclude, that the $Cu_3Au(110)$ surface behaves rather like pure Cu and the (100) and (111) surfaces like pure Au. With chemical treatment (i.e. offering atomic oxygen or nitrogen) an adsorption can be provoked, with one layer of Cu segregated to the top layer.

6.2 Corrosion of Cu-Au Alloys

In corrosion studies the Cu-Au system is, together with Ag-Au alloys, one of the most studied systems for dealloying and selective dissolution. It provides a very large ΔE^0 and a relative large difference of lattice parameters of the elements. Cu-Au alloys are, as expected for noble metal alloys, chemically relative inert.
Difficult to interpret though, is the influence of the elemental order in the samples. Controversial statements about the value of the critical potential in ordered species have been made [pa89] [mo91] [rei92], but good ordering is difficult to obtain. In addition most studies up to now have been made with poly-crystalline samples exposing all different orientations at the surface. Eckstein though revealed a pronounced dependence of the electrochemical activity on the crystal orientation [ec01].

6.2.1 Pourbaix Diagrams: Cu and Au

In the Figure 6.3 and 6.4 the potential-pH stability diagrams (Pourbaix Diagrams) for Cu and Au in aqueous electrolytes is shown. In these Figures the lines represent different electrochemical reactions between the reaction partners indicated, at different concentrations of the soluble species in the solution, e.g. 10^{-2}mol/l, 10^{-4}mol/l, 10^{-6}mol/l, etc. Within

the stability regime of water only the elemental state of Au is stable. In the absence of complex formers Au is stable over the whole range of practically accessible potentials and no dissolution takes place.

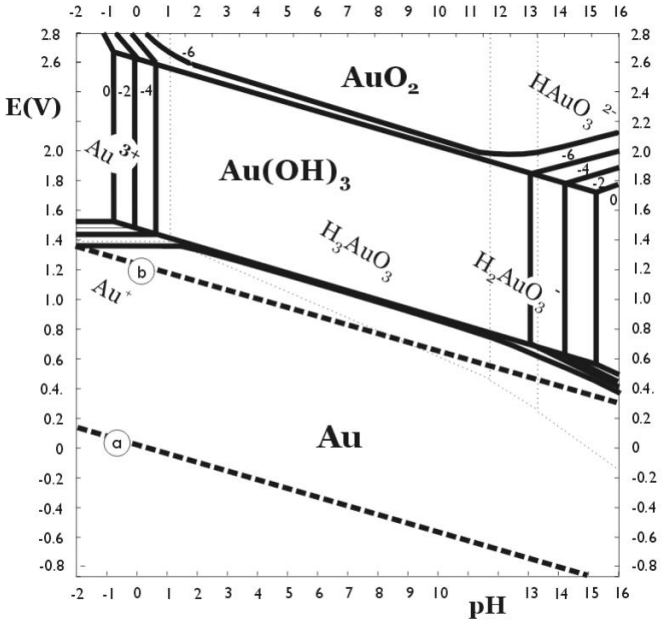

Figure 6.3: Pourbaix diagram for Au in aqueous systems without complex formers. In the whole range of the stability of water between the lines a and b, Au is stable (inert). The pointed lines separate the regions of the dominant dissolved species. The diagram is taken from [po63]

The situation is different for the element Cu. For certain pH values, the formation of oxides is observed. As the regimes of CuO and $Cu(OH)_2$ overlap, two diagrams are plotted, each considering one of them. Oxide layers will have a passivating effect and so the detailed formation of these oxide layers is a result of parameters like defect densities, diffusion constants and diffusion mechanisms. Only in acidic (ph < 4) or basic environments no Cu oxide is stable and Cu is directly dissolved predominantly as hydrated Cu^{2+} ions. Being just a representation of the considered bulk phases and dissolved species, the diagram does not include a possible UPD layer in the system Cu^{2+}/Cu_3Au or $Cu^{2+}/Au/Cu_3Au$.

6.2.2 Polycrystalline Cu-Au Alloys

Cu dissolution from Cu-Au alloys above the critical potential has been studied for a long time. Graf as early as 1932 examined the dealloying of Cu-Au species performing X-ray measurements [gr32]. He found after chemical etching in different oxidizing solutions the occurrence of pure Au powder peaks, but also very broad powder rings indicating intermediate lattice constants, i.e. the formation of not fully depleted Cu-Au regions. Gerischer addressed stress corrosion with the study of current transients emerging from

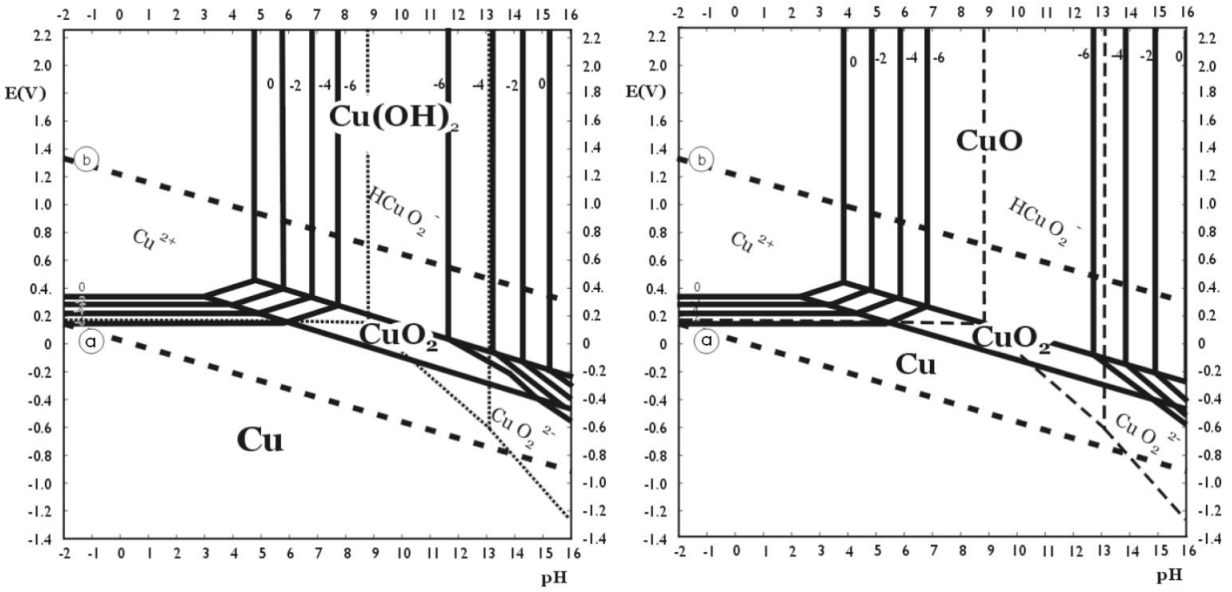

Figure 6.4: Pourbaix diagrams for Cu in aqueous systems without complex formers. In the left diagram $Cu(OH)_2$ is considered and no CuO. In the right diagram CuO is considered and no $Cu(OH)_2$. The pointed lines separate the regions of the dominant dissolved species.

a Cu-Au wire under load with an applied potential in the passive region. He explained occurring passivation by the protective influence of pure Au adlayers and current spikes with the exposure of fresh uncorroded regions after a gliding of slip planes under stress [ge55]. He also found a dependance of the critical potential of the composition of the Cu-Au alloy, like it was later published also by Pickering and by Kaiser (Fig. 6.2.2) [pi71][ka86]. Pickering and Swann observed in 1963 the spongy-like appearance of the reacted layers in 1N H_2SO_4 solution [pi63]. Using X-ray diffraction, Pickering [pi67] found later, similar to observations of Graf, diffraction peaks in between Cu_3Au and Au positions. In this study the method of defined anodic treatment (i.e. electrochemical dissolution of Cu from $Cu_{0.9}Au_{0.1}$ polycrystalline samples) was used: while in 1N H_2SO_4 solution the diffraction pattern showed quickly only additional pure Au peaks, in buffered 1N NaCl solution the intermediate peaks stayed more pronounced. And in NaCl solution electron microscopy showed, rather than a porous microstructure, cracks and elevated corrosion along inter- and transgranular pits, slightly extending into the unreacted substrate. Electron microscopy was employed by Swann and observations of Cu_3Au exposed to ferric chloride solutions (a known embritteling solution) showed an accumulation of pure Au particles within corrosion tunnels and an seemingly unattact surrounding. No evidence was found for intermediate lattice parameters in this solution [sw69].

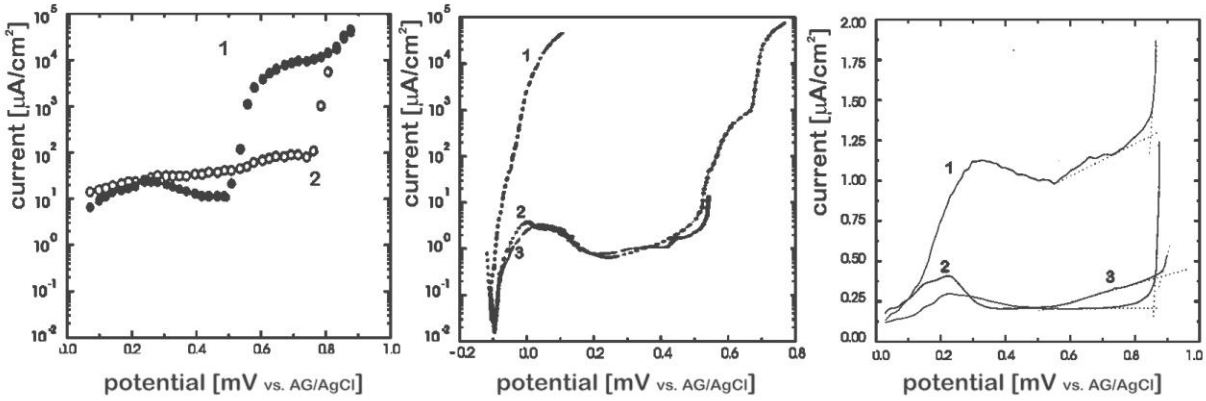

Figure 6.5: CV's from publications of different authors. Parks [pa89] (left) observed a difference in the value of E_c for ordered (2) and disordered (1) polycrystalline Cu_3Au samples, Moffat et al. [mo91] (middle) could not reproduce this result but Reining [rei92] did. Eckstein [ec01] (right) studied different single crystal Cu_3Au(hkl) surfaces(*1*:(111), *2*:(001) and *3*:(110)).

The influence of ordering towards the value of the critical potential of Cu_3Au was discussed. Parks et al. observed a pronounced difference for ordered and disordered samples. In Figure 6.2.2*a* the curve *1* for disordered Cu_3Au rises 250 mV before the ordered sample, *2*. In an experiment performed by Moffat [mo91] this difference could not be observed (In Fig. 6.2.2*b* *1* shows the dissolution curve for pur Cu, *2* and *3* for ordered and disordered samples). Reining [rei92] later published results similar to Parks. Moffat performed an in-situ STM study on polycrystalline samples and observed Au clustering and subsequent surface smoothing (aging). But the results are hard to interpret due to the low resolution and the already rough starting surface resulting from an in air preparation. Their electrochemical results showed the influence of adsorbates: while for 1M Cl^- containing electrolytes the critical potential was shifted 250 mV to lower values an derivatization with alkylthiols caused a positive shift of 150 mV (more anodic). These results were interpreted as a sign for the enhanced or inhibited surface mobility of Au [mo91].

Stress Corrosion Cracking (SSC) is of utmost relevance for construction materials under stress (e.g. loaded construction materials or welding connections). Basic research on alloy SSC has been performed with polycrystalline Cu-Au samples [chj93]. The basic mechanisms of SSC are, due to the manifold contributing parameters, poorly understood, but it seems that in the case of noble metal alloys the dealloyed layer brittleness and the often coherent or epitaxial interface to the unattacked substrate are of major importance. [new95]

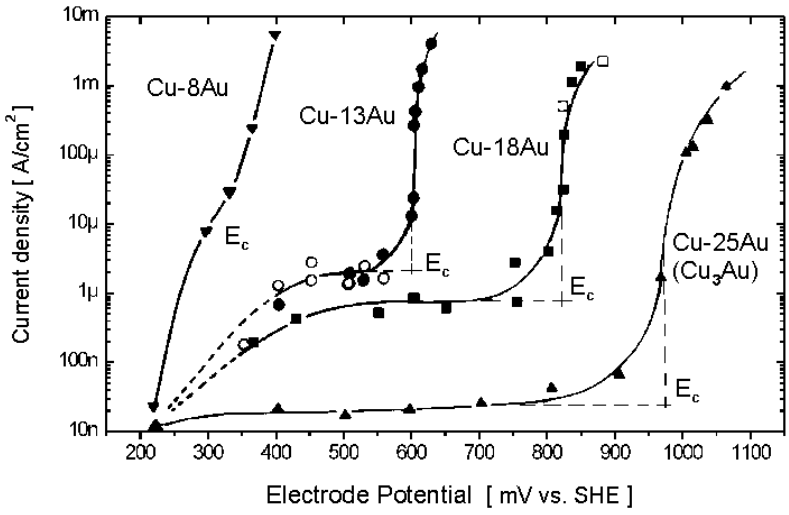

Figure 6.6: The Cu-Au Alloy composition influences the critical potential. Studies were done with polycrystalline alloys. The currents in the passive regions are higher for lower contents of the less noble element. The origin of the higher passive current is unclear. (From [ka93])

6.2.3 Single Crystal Studies: Low Index Surfaces

The lack of coherence of the existing models for explaining the critical potential, emphasized the need for single crystal studies with well defined and controllable experimental conditions. The emerging STM technique offered an in-situ tool [so86] to study also the passive region with its often atomically smooth structures. Due to the lack of experimental techniques to resolve the structural changes on the atomic length scale, the sub-critical region was rarely addressed in corrosion studies. Early studies include dissolution from Ag-Au alloys [op91] and Au_3Cu [chs93]. Eckstein studied selective Cu dissolution from Cu-Au low-index single crystal surfaces in the passive region with in-situ EC-STM and could show a dependance of the surface morphology and dissolution currents on the orientation [ec01]. All authors report atomic monolayer deep vacancy clusters and restructuring phenomena on the surface pointing to an important contribution of surface diffusion to explain the critical potential. Eckstein could show, that a deeper, pitting type of attack occurs already below the critical potential on surfaces including $Cu_3Au(111)$ [str01].

Chapter 7

In-Vacuum Sample Preparation

For the electrochemical corrosion experiments, described later, two different types of samples have been used. The main part of this work was carried out with bulk single crystals. Two of the crystals were delivered by MaTecK GmbH, Jülich and one by the Crystal Growth Laboratory at the Max-Planck-Institute in Stuttgart. In addition to the bulk single crystals, one batch of MBE grown $Cu_3Au(111)/Nb(110)/Al_2O_3$ epitaxial thin films were used. They were fabricated in the MBE chamber at the Max-Planck-Institute for Metal Research in Stuttgart. Two of this films had a thickness of 100nm, several others were between 15 and 30 nm thick.

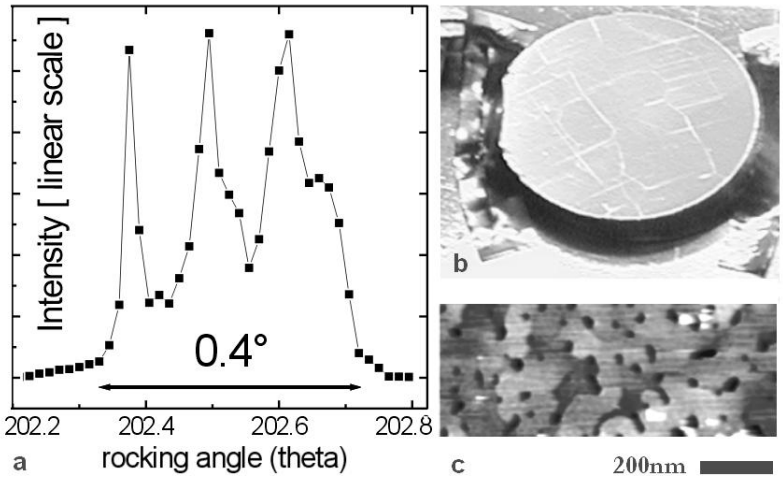

Figure 7.1: Some examples of the difficulties with finding a good sample. (a) The MaTecK crystals showed several grains in an X-ray rocking scan. (b) The MPI crystals were composed of big grains. Only one grain surface is oriented in the desired (111) direction. (d=10mm) (c) The 15-30nm thick epitaxial films did not have a continuous layer as revealed by AFM.

Cu-Au crystals are difficult to produce. The used crystals were not ideal single crystals. The MaTecK crystals showed a distribution of mosaicity with some sharp Bragg reflections originating from isolated larger grains with an overall spread in mosaicity below 1° (Fig.7.1). The MPI crystals had fewer and bigger grains, but only one of these grains was oriented in the desired (111) direction, while the others showed huge misalignment. A rocking scan of a MaTecK crystal is shown in Figure 7.1, together with an image of a MPI crystal with many visible (large angle) grain boundaries. The (111) oriented grain of this crystal was too small for an easy alignment of the sample for the X-ray experiments. From the MPI crystals only one specimen had a sufficiently large and well oriented region, which was then used for the measurements.
From the MBE grown samples we used only the two thickest films (100nm) for the X-ray experiments. The thinner films were not continuous, as the AFM image after growth shows(Fig. 7.1c). All these discontinuous samples were not used for the corrosion experiments.

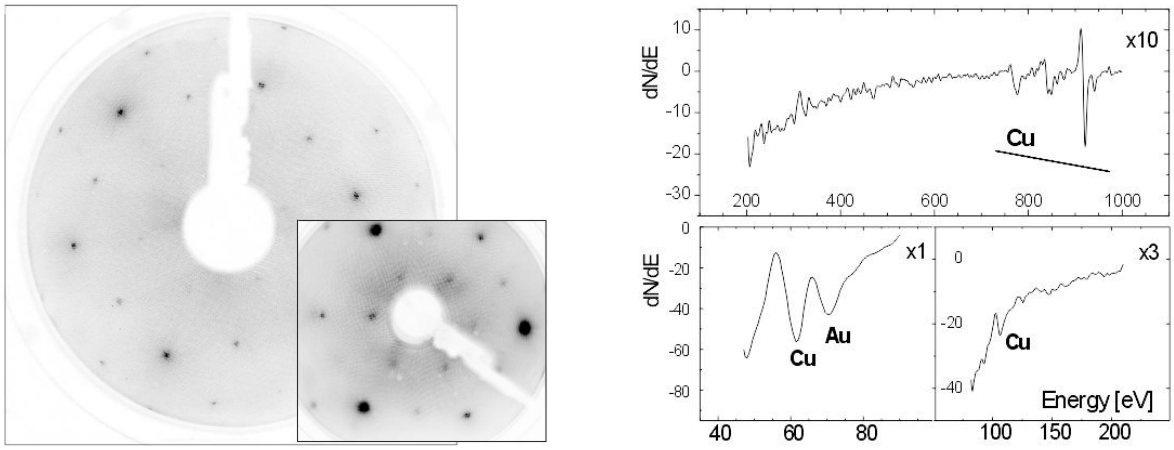

Figure 7.2: (a)LEED image of $Cu_3Au(111)$ recorded at 129 eV after an initial ordering at only approximately the ideal ordering temperature. (b) AES spectra of $Cu_3Au(111)$ recorded after the same conditions than (a).

The preparation of the Cu_3Au crystal surfaces for the experiments was carried out in ultra high vacuum (UHV) by sputtering with Ar^+ at 500-1000 V and subsequent annealing. Several sputter-annealing cycles were applied before a final ordering of the $L1_2$ superstructure just below the order transition temperature T_c. The time determining step in the ordering process is the ripening of nucleated ordered domains, which are at first separated by anti-phase domain walls. The surface quality was, in-between the sputter-annealing cycles, characterized with AES and LEED. Examples for an Auger spectrum of a typical

clean surface and a typical LEED image of the ordered single crystal surface are given in Figure 7.2. Three of the fundamental LEED spots are stronger -the single crystal consists of only one of the possible fcc (111) stacking sequences, i.e. the crystal is free of twin domains. The ABC-like stacking sequence can be distinguished from CBA, because part of the Bragg peak positions are different. For the (111) surface these are the Bragg peak positions along the CTR's with no in-plane Bragg peak, e.g. the $(20L)_s$, $(10L)_s$, etc. (A description of the used adopted surface coordinates is found in Appendix B). The epitaxial thin films show both of the possible twin domains, because both are energetically equal for the first nucleation on the flat Nb(110) buffer layer.

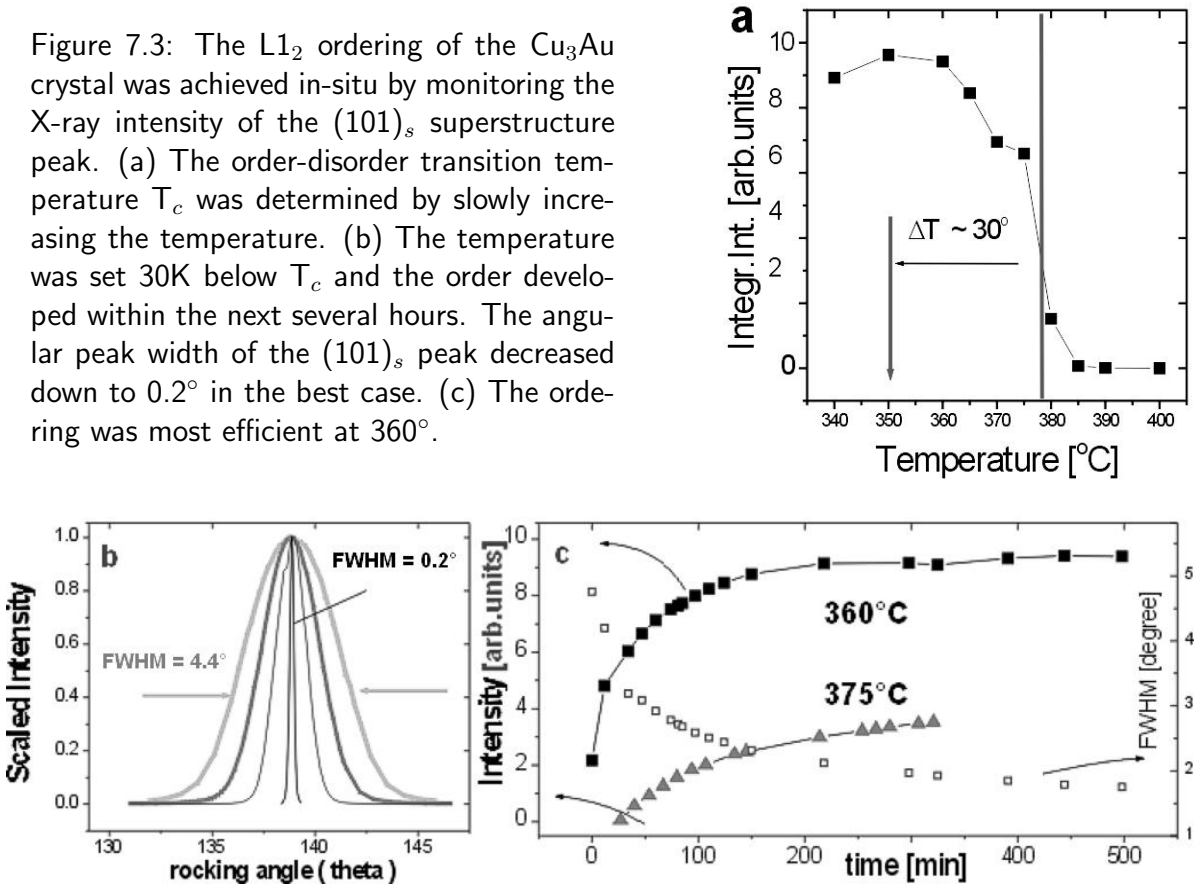

Figure 7.3: The $L1_2$ ordering of the Cu_3Au crystal was achieved in-situ by monitoring the X-ray intensity of the $(101)_s$ superstructure peak. (a) The order-disorder transition temperature T_c was determined by slowly increasing the temperature. (b) The temperature was set 30K below T_c and the order developed within the next several hours. The angular peak width of the $(101)_s$ peak decreased down to 0.2° in the best case. (c) The ordering was most efficient at 360°.

For pronounced $L1_2$ ordering, it turned out that the temperature has to be carefully controlled to be at 20-30K below T_c=660 K for many hours. An optimal ordering temperature of 360°C was already given by Nagy [nag62]. However, it is difficult to measure the absolute temperature in UHV. The temperature determination by pyrometers depends on the emissivity and thermocouples are often not directly installed at the sample surface,

making it often difficult to determine dependably the sample temperature due to existing large temperature gradients. This is especially true for this work where different UHV chambers with different sample holders have been used for the respective experiments and, in addition, the shape of each of the crystals was different. A well established order results in large domains, giving rise to sharp superstructure Bragg peaks in X-ray diffraction. We achieved the best results by using X-rays to determine the order phase transition temperature T_c. Therefore, we followed the intensity of a $L1_2$ superstructure peak in a UHV diffraction chamber; and after observing the sharp drop in the superstructure peak intensity at T_c we set the current for the sample heating station to a value giving a by 30 K lower temperature. This was the only way to obtain a well ordered Cu_3Au sample in a controlled way. LEED could not be used for this purpose, because the $Cu_3Au(111)$ surface is already disordered well below the disorder transition T_c for the bulk crystal (Chapter 6.1.1 [**?**][bo96]). At the ID32 beamline a superstructure peak width of an angular rocking scan of 0.2° was measured after an X-ray monitored ordering of the crystal in the Stuttgart laboratory. Without the determination of the accurate T_c with the help of X-ray diffraction the best value obtained was 0.8° (but often larger than 1°).

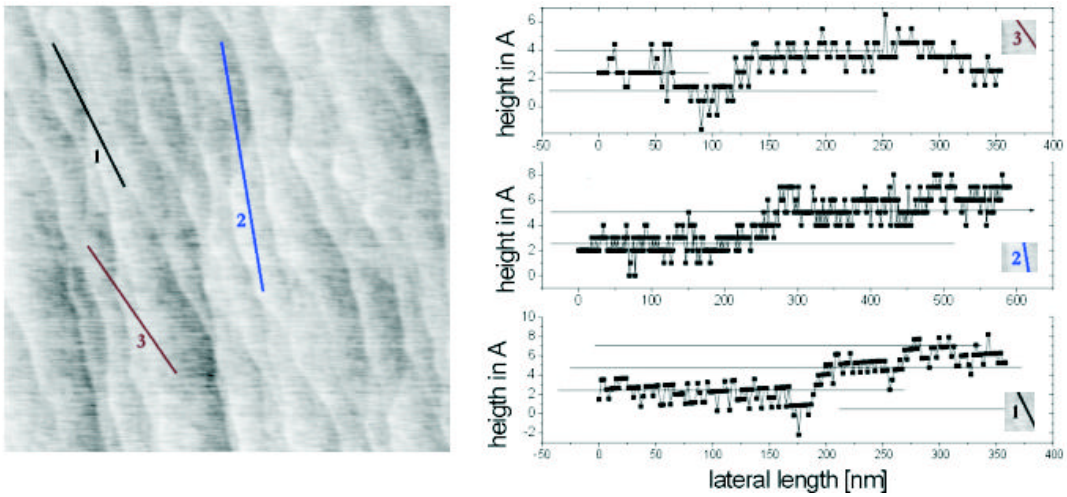

Figure 7.4: AFM image of the $Cu_3Au(111)$ surface in air after several sputter and annealing cycles in UHV. Steps are clearly visible and the corresponding height agrees well with the value of 0.2167 nm for a monoatomic step of $Cu_3Au(111)$.

In the course of an ex-situ AFM study of the corrosion process of $Cu_3Au(111)$ in electrolyte we also imaged the clean Cu_3Au surface directly after treatment in UHV, as was described above. One of the AFM images is shown in Figure 7.4. The step structure of the surface is clearly visible and the measured step height corresponds, within the error

of the measurement, well with the expected 0.2167 nm

The MBE growth chamber was described in Chapter 5.1. To produce the $Cu_3Au(111)$/ $Nb(110)$/ $Al_2O_3(11\bar{2}0)$ epitaxial thin films we used the same growth parameters as Ern [ern01] in the same chamber and which had been originally developed by Zhu [zhu88]. First we compared growth rates for the respective independent Cu and the Au (Knudsen-type) crucibles as determined by the Quartz Crystal Microbalance (QCM, Growth Rate Monitor) and independently by ex-situ thickness measurements of deposited Cu and Au films ('calibration' samples) obtained by X-ray reflectometry. These additional tests are necessary, because the Quartz oscillator is not measuring exactly at the sample position. The resulting calibration factors are the so-called 'tooling' factors, they were 0.6 for the Cu cell and 0.465 for Au. With the first grown epitaxial alloy films we adopted the individual growth rates (for Cu and Au respectively) in order to obtain the ratio of the measured Auger peaks at 60 eV and 69 eV as shown in Figure 7.2. The film deposition included finally several steps. The (A-plane) sapphire substrates have been high temperature annealed at ambient pressure for several hours. The 30-50nm Nb(110) buffer layer was then deposited in the MBE growth chamber at a substrate temperature of 800°C (maximum of the installed heater) with a growth rate of 0.01nm/min (using the electron beam evaporator). Afterwards, the $Cu_3Au(111)$ alloy film was deposited at a substrate temperature of 350°C with growth rates of 0.03nm/min for the 15-30nm samples and 0.1nm/min for the 100nm samples. After growth the film was annealed during 1 hour above T_c at 450°C and then slowly cooled down at a rate of 25K/hour. This cooling procedure resulted in ordered, but rather small domains and broad superstructure diffraction peaks. Along the specular (00L) rod the Nb and Cu_3Au Bragg peaks show thickness, or so-called Laue oscillations. No Laue oscillation along the film CTR's could be observed. The Cu_3Au film consists of two kinds of fcc domains, distinguished by the stacking sequence (ABC and CBA). Within our films both domains give rise to equal intensity on their separated Bragg peaks, respectively. Each domain occupies thus an area of 50%. (By a surface miscut of the $Al_2O_3(11\bar{2}0)$ substrate this ratio can be changed). The angular (rocking) width was for e.g. the $(220)_s$ fundamental peak 1° and for a $L1_2$ superstructure peak 1.5° to 2°.

Table 7.1: List of the main X-ray experiments performed at different Synchrotron Radiation Sources for this thesis work.

Experiment	Sample Preparation Notes	Aim, Problems and Results
In-house research ID32, ESRF July 2001	Au(111) with flame annealing	test of equipment and electrochemistry at the beamline
Proposal SI-789 ID32 September 2001	Au(001) with flame annealing	test of equipment and electrochemistry at the beamline
In-house research ID32, ESRF February 2002	Stuttgart MBE grown samples transferred in air; layer thickness 1000Å, broad superstructure peaks	observation of new structure and moving position of diffraction peak
In-house research ID32, ESRF June 2002	Crystals, UHV preparation with help of LEED and AES in SCL results in broad superstructure peaks	Grainy crystals caused surface miscut (wrong alignment before polishing)
In-house research ID32, ESRF July 2002	LEED and AES in SCL, broad superstructure peaks, measurement on 'good' grain	Fast potential increase, peak position moved to Au position
In-house research ID3, ESRF July 2002	LEED and AES in SCL, X-ray ordering and measurement of UHV clean surface. Study of ordering kinetics.	Samples had too poor crystalline quality to record CTR of clean surface
MPI-MF Beamline, ANKA October 2002	LEED and AES in Stuttgart. Sputter-annealing and ordering in X-ray chamber	CTR measurement in UHV of clean surface
Proposal SI-861 ID32, ESRF November 2002	LEED, AES and X-ray ordering in Stuttgart, UHV transport, Cell only with thin electrolyte film because of fragile mylar	CTR and new layer rod, detailed in-plane and out-of-plane position
BW2, HASYLAB December 2002	LEED, AES and X-ray ordering in Stuttgart, UHV transport, thick electrolyte layer while changing potentials	study of further growth at higher corrosion potentials
BW2, HASYLAB February 2003	LEED, AES and X-ray ordering in Stuttgart, UHV transport, thick electrolyte layer while changing potentials	study of CTR and further growth at higher corrosion potentials
Proposal SI-913 ID32, ESRF June 2003	LEED and AES in SCL	Anomalous Diffraction and Cl^- containing electrolyte

Chapter 8

First In-Situ Measurements and Test of the Experimental Set-Up: Surface Reconstructions on Au

Setting up new equipment in a new environment requires reliable testing systems to verify the functionality of the set-up. For electrochemistry the choice of gold single crystals is best fulfilling this requirements. The gold surface is easily prepared by flame-annealing in air and the voltammetry shows features of surface processes, that are easily distinguished and can serve as a benchmark for sufficient cleanliness. Therefore, Au provided a perfect system to study, in order to check the functioning of the equipment and the whole set-up at the ID32 beamline. An user-friendly electrochemical (EC) in-situ X-ray cell has been designed and built and was meanwhile also used by external groups. In this chapter we shortly describe the first in-situ experiments on Au surfaces with the new set-up, which proves that electrochemistry and X-ray measurements are working well with our set-up.

For the X-ray measurements of the (001) surface of Au, we used the usual cubic reciprocal unit cell deduced from the cubic crystal unit cell (fcc coordinates). For the (111) surface, a surface unit cell was adopted, which allowed the reciprocal space L-direction to point along the surface normal. This is usually done in surface studies to more easily distinguishing in-plane and out-of-plane directions. In the latter case, the real space crystal unit cell was spanned by two vectors lying in the surface plane at an angle of 120°, equal e.g. to the cubic $\langle 1\bar{1}0\rangle$ and cubic $\langle 0\bar{1}1\rangle$ crystal lattice vectors, and a vector perpendicular to the surface equal to the cubic-$\langle 1/3,\ 1/3,\ 1/3\rangle$ vector. This way the reciprocal cubic (111) position corresponds to the $(003)_{s,Au}$ position in our surface adopted coordinates. The cubic $(\bar{4}22)$ position corresponds to the $(300)_{s,Au}$ position in surface reciprocal coordinates.

The Bragg peaks along one CTR of the (111) surface are separated by ΔL=3.

8.1 Lifting of the Au(111) Reconstruction

On Au(111) the $\sqrt{3}\times 23$, known as „herringbone"reconstruction, is the thermodynamically stable surface structure and has been extensively studied, in UHV [tan81][har85][sa91][tar02] [ba90], as well as in electrolyte solution [oc90][ma92] [ko96]. Figure 8.1 shows two electrochemical (EC) STM images (a, c; from [kl]) of the Au(111) surface in 0.1M H_2SO_4 electrolyte solution, together with its voltammogram (b). Image (a) is taken at a potential region labelled (I) in the voltammogram. The features labelled (II) and (III) in the voltammogram are generally interpreted as the charge flow due to the lifting of the reconstruction towards the 1×1 surface (feature II). With a restructuring of the surface, the potential-of-zero-charge (pzc) and the capacity C of the interface are changing and this change is causing a current flow. The broad peak (III) originates from the adsorption of one monolayer of sulfate ions from the solution. This monolayer undergoes a phase transition from a disordered adlayer to a $\sqrt{3} \times \sqrt{7}$ surface reconstruction [ma91][ed94][it98]. Due to the high mobility of the sulfate ions the 1×1 substrate is seen with the EC-STM in the potential region of the disordered sulfate adlayer. The phase transition is seen as a sharp current spike in the voltammogram (IV). As a consequence of the $(\sqrt{3} \times 23 \rightarrow 1 \times 1)$ phase transition additional Au is released and forms monoatomic high islands on around 4% of the surface area on the 1×1 Au(111) surface (see inset of Fig.8.1c). These structural changes are completely reversible. The observation of the Au(111) reconstruction in 0.1M H_2SO_4 was a good sign for a clean environment, when working with the glass cell in the electrochemistry laboratory. The corresponding voltammogram is shown here to describe the following measurements.

After flame-annealing, the Au(111) crystal was immersed in 0.1M H_2SO_4 solution in our in-situ X-ray cell. Starting with a reconstructed Au(111) surface at -250 mV (vs.Ag/AgCl), the potential is gradually increased. The superstructure/reconstruction side maximums of the main in-plane Au $(100)_{s,Au}$ peak were recorded by performing rocking scans. In Figure 8.1 the main results are presented. The initial reconstruction side peak maximums corresponds to a period of 29. Figure 8.1b is a 2D contour plot of the data in a. With increasing potential the side maximums are shifting towards the main peak, i.e. indicating an increasing reconstruction period. While the intensity of the side peak is vanishing with the appearance of the unreconstructed 1×1 Au(111) surface, the main peak intensity is rising sharply by a factor of 5. Setting our detector on the maximum of the main peak,

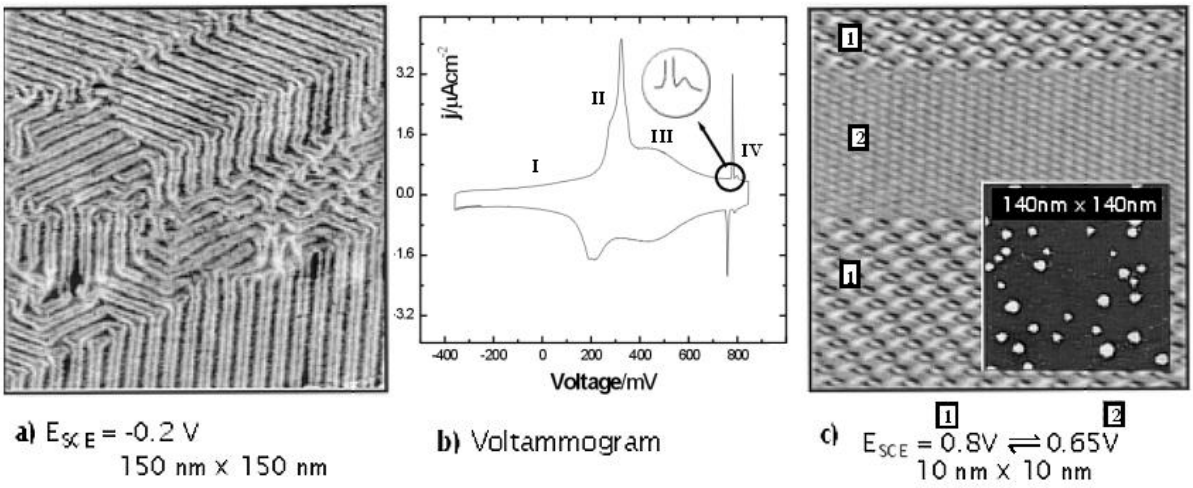

Figure 8.1: Two EC-STM images showing the Au(111) surface in electrolyte solution at potentials in region I for image (a) and III/IV for image (c) of the voltammogram. The voltammogram (b) is explained in more detail in the text. EC-STM images are from [kl].

we could follow the in-plane Au peak intensity while scanning the applied potential from -300 mV to 900 mV and back with a scan rate of 5 mV/s.

In hexagonal coordinates the reconstruction period p and the reciprocal distance Δq of a side peak are related by p=($\sqrt{3}/2$)/Δq. The initial maximum of the reconstruction side peak corresponds to a period p=29 , and is thus larger than the reported 22-23 in the literature. Approaching the potential of the lifting of the Au(111) reconstruction, this longer period is increasing, before the 1×1 surface is obtained (p=∞). With this shift of the period additional Au must be released as adatoms from the reconstructed layer onto the surface to adopt for the new superstructure period. This might lead to an increased roughness, diminishing the intensity of the main diffraction peak. With parts of the intensity being scattered into the side peaks, the main peak is smaller, than for a unreconstructed surface and will thus increase, when the reconstruction is lifted. As our experiment shows, the point of the steepest slope of the resulting change in intensity of the Au $(100)_{s,Au}$ central peak is correlated not directly with the reconstruction-lifting peak in the voltammogram, but with the maximum of the presumed sulfate adsorption peak.

Compared to a recent study in salt solutions [oc90] and in 0.1M H_2SO_4 [et99], our reconstruction peak was smaller. In addition, it was not fully recovered after lifting it under beam exposure (while before the X-ray measurement the potential has been cycled over the lifting potential and back several times) and finally it was not stable even at potentials negative of the pzc during X-ray exposure. This behavior was probably a sign

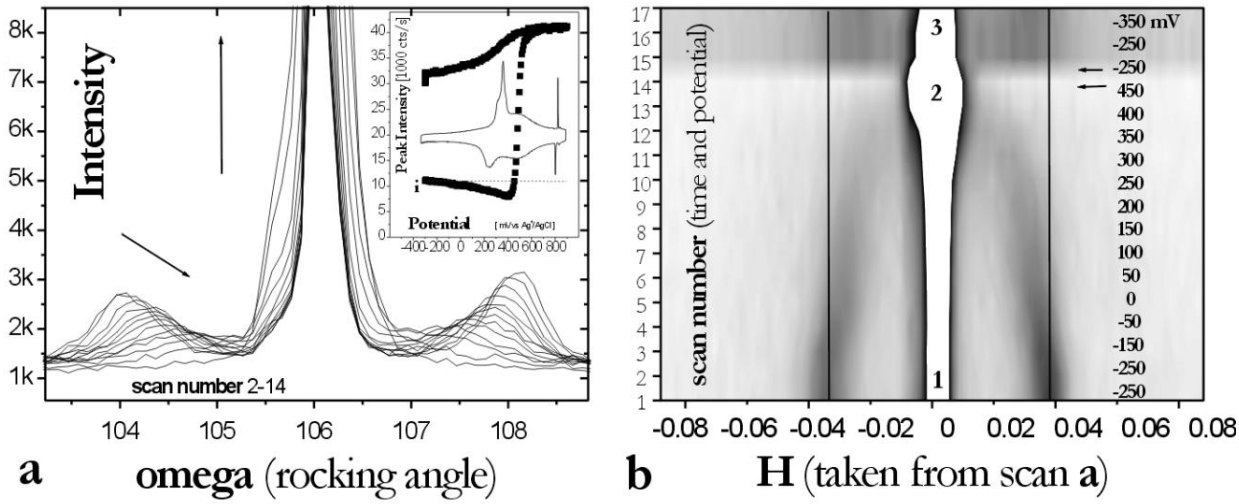

Figure 8.2: Measurements of the Au(111) $\sqrt{3} \times 23$ reconstruction. (a) shows rocking scans including the main in-plane Au peak (fcc- $\frac{1}{2}(2\,\overline{2}4)$) and the side maximums due to the Au(111) reconstruction. The initial reconstruction side peak corresponds to a period of 28. The inset shows the intensity obtained from the main in-plane Au peak $(100)_{s,Au}$ while scanning the potential. The sharp rise in the peak intensity correlates with the maximum of the SO_4^{2-} adsorption peak of the voltammogram. (b) A 2D contour plot of the data in (a). Even if clearly visible the side maxima are much smaller, the corresponding initial period is larger than expected and the reconstruction is not reformed after beam exposure. The results are thus pointing to a present surface contamination, probably coming from the water we used.

of a contamination/beam damage effect. At the time of the measurement, we used a water filter system without UV-light treatment and accordingly a higher total organic content (TOC was measured >15 ppb). Due to the used thin film EC X-ray cell and the energy of 8.5 keV, together with the high flux at ID32, ESRF, an effect of a contamination of the ultra-clean water might be amplified. For the next experiment (on Au(001)) a water filter setup with UV-light treatment was used, supplying ultra-clean water with a TOC of <2 ppb.

8.2 Reconstruction of Au(001)

On Au(001) a hexagonal reconstruction is observed after thermally annealing the surface (e.g. by flame-annealing for electrochemical or by heating in UHV for in-vacuum studies), or by applying an appropriate potential in electrolyte at ambient temperature. For a thermally (high temperature) annealed crystal the surface gives rise to a single diffraction peak for each of the two main domain orientations of the top hexagonal Au layer on the

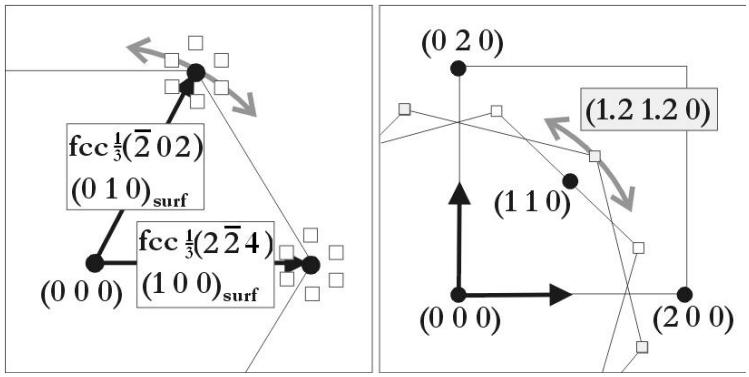

Figure 8.3: Parts of the reciprocal maps for the ($\sqrt{3} \times 23$)-Au(111) [a] and (hex)-Au(001)[b] reconstructions. The region of the Au(111) reconstruction spots for the (expected) 23-fold period of is enlarged.

cubic Au(001) crystal surface. The potential induced reconstruction shows a peak doublet due to two slightly rotated hexagonal domains. These rotated domains are also observed for a thermally treated crystal surface, annealed at a too low temperature. Due to this different behavior, it becomes possible to judge, if the thermally induced Au(001) reconstruction was stable during an immersion into electrolyte solution at potentials favorable for the reconstruction. Within beamtime dedicated to the study of Ethanethiol on Au(001) (SI-789, ESRF) we could check the behavior of the reconstruction on clean Au(001). In a first test experiment, using the less pure water, we could only observe the potential induced reconstruction, showing the peak doublet. For the main experiment we then used ultra-clean water with a TOC value of <2 ppb. The result was that we could reliably observe the single diffraction peak of the thermal induced reconstruction after flame-annealing and immersion of the crystal surface in 0.1 M H_2SO_4 electrolyte solution.

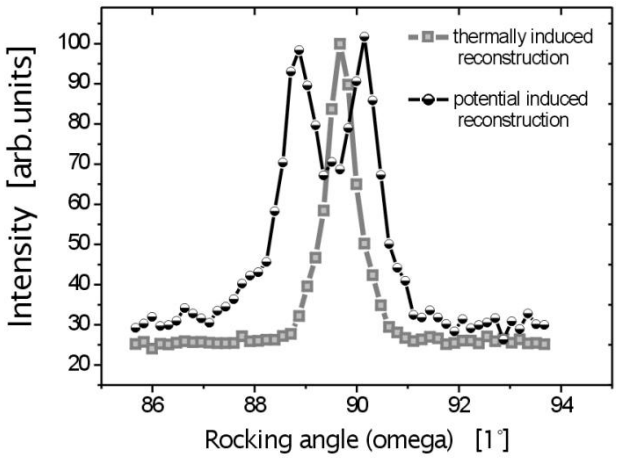

Figure 8.4: Using ultra-pure water (TOC<2ppb), we could observe the thermally induced hexagonal reconstructed Au(001) surface in electrolyte, with one single central diffraction peak. The crystal was flame-annealed and immersed in electrolyte under potential control. The potential induced reconstruction shows a double peak structure [oc90].

8.3 Experiments on Au surfaces: Conclusions

The experimental infrastructure for electrochemical experiments has been completed and first successful experiments have been conducted, which were documented in this Chapter. The Au experiments, meant to check the set-up, showed the necessity of using ultra-pure water, at least for experiments using a X-ray energy in the range of 8 to 12 keV. Only when using ultra-clean water (TOC of <2ppb) we could reliably observe the expected electrochemical behavior in the case of the Au(001) reconstruction. Therefore, two main conclusions were drawn after the experiments described in this Chapter. Firstly, the quality of the water is crucial, especially for X-ray experiments (that often take several hours to be completed due to sample alignment and time consuming motor scans). Secondly, possible beam interaction with impurities, as well as beam damage, have to be considered. Working at the highest possible energy is in our opinion preferable (because of the lower cross section for interaction events of the impurity molecules of the X-ray photons with the electrolyte).

Chapter 9

Current-Potential-Curves of $Cu_3Au(111)$

Voltammetry as an electrochemical method was described in Chapter 5.5. Current-potential curves from alloys are difficult to obtain, because they are in general not reversible. Moreover it is more difficult to prepare an initial favorable (smooth) surface structure and the desired (bulk) composition, since e.g. segregation or partial oxidation can occur. The selective dissolution of Cu from Cu_3Au is an irreversible process and a reversible cyclic voltammogram can thus be expected only if a stable passivated surface is obtained after an initial Cu dissolution. For cyclic voltammetry one is therefore restricted to potential values below the critical potential E_c. By a pre-polarization just below the critical potential of polycrystalline Cu_3Au samples in electrolyte containing SO_4^{2-} ions, Moffat obtained a stationary cyclic voltammogram showing a behavior very similar to the Cu-UPD on Au(111) [mo91]. They concluded , that in the passive region pure Au is formed on the surface. The dependence of the critical potential of Cu-Au samples on the Cu content, as well as the influence of different anions and other electrolyte additives (e.g. corrosion inhibitors) have been frequently studied.

To verify the electrochemical behavior of our samples we measured current-potential curves in a range of potentials including also the critical potential. But, as at potentials above the critical potential the formation of porous layers in depth is reported, we applied only cycles of the potential with (fast) potential sweep rates, i.e. values typical for cyclic voltammetry (potentiodynamic scans, v>5mV/s) and not extending far in the critical range. The time interval of an applied potential in the critical range was so kept short, on the order of several seconds only. In this way we avoided either a severe change of our polished single crystal surface or an untypical behavior due to the limited film thickness of

our MBE grown samples. The single crystal surfaces have been prepared for the voltammetry measurement in UHV by sputter-annealing cycles, before they were transferred to air and mounted to the sample holder of the standard electrochemical glass cell. Prior to the alloy voltammetry a cyclic voltammogram of a pure Au(111) crystal in the 0.1M H_2SO_4 solution was recorded in order to check the cleanness of the solutions, the set-up and the absence of oxygen after deaerating the solution by purging with nitrogen. An example of a typical Au(111) voltammogram in 0.1M H_2SO_4 electrolyte solution as it was obtained in our electrochemistry laboratory at the ESRF in Grenoble is shown in Figure 9.1.

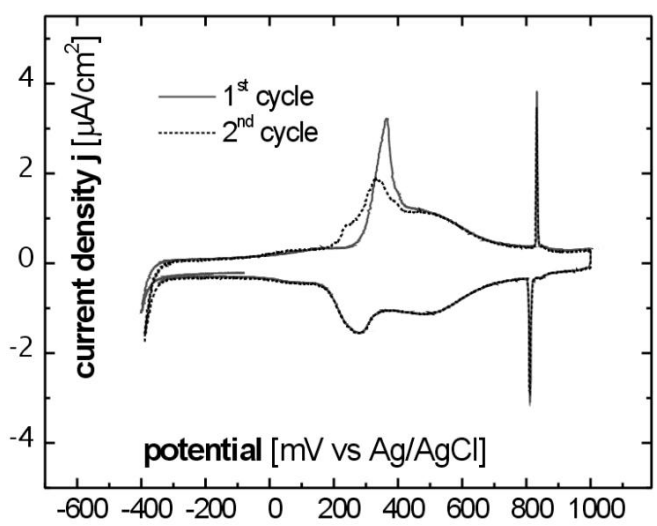

Figure 9.1: A (cyclic) voltammogram of Au(111) in the 0.1M H_2SO_4 solution subsequently used for the Cu_3Au alloy current-potential curves, showed the cleanness of the system after assembling the electrochemical glass cell.

For two MBE-grown, thin, epitaxial Cu_3Au-films the respective voltammograms are shown in Figure 9.2. In the anodic scan direction, starting in the region of the beginning hydrogen evolution at -100 mV (I), the current reached a maximum at a potential close to the Standard equilibrium potential of Cu (II). We have to note though, that the equilibrium potential is, due to the initially Cu-free electrolyte, dependent on the actual concentration of Cu close to the interface during the dissolution process and is thus not well defined. In the passive region (III) the current is nearly constant until the critical potential E_c is reached and the current rises quickly (Fig.9.2 a, IV). In a second cycle, limited to potential values below E_c, the peak (II) has nearly vanished, but a small contribution remains, together with a small peak in the cathodic scan direction. The (negative) rise of current for the hydrogen evolution reaction begins at slightly more negative potentials than in the initial first cycle. The situation is very similar for a second thin film sample in Figure 9.2 b. For this second sample we restricted the potential to sub-critical values, between -200 mV and 600 mV. The scan rate in a and b was 5 mV/s for the initial curve. After

a short sweep to the critical potential we observed a pair of small redox peaks (IIb and IIb'), which shifted in position for higher potential sweeping rates. A $Cu_3Au(111)$ surface has $16.4 \cdot 10^{14}$ atoms per cm^2 and the selective dissolution and oxidation of Cu to Cu^{2+} consumes a charge of $394\mu C$ per atomic layer. The integrated charge in peak IIa and IIb of Figure 9.2 is approximately the charge needed for dissolving the Cu from one layer of Cu_3Au (0.77 and 0.89 monolayers respectively). The small redox peaks (IIb and IIb') are thus associated with processes involving much less than one monolayer. Note that in Figure 9.2 b the cyclic voltammograms are reproducible (several curves shown) for each potential-sweep velocity.

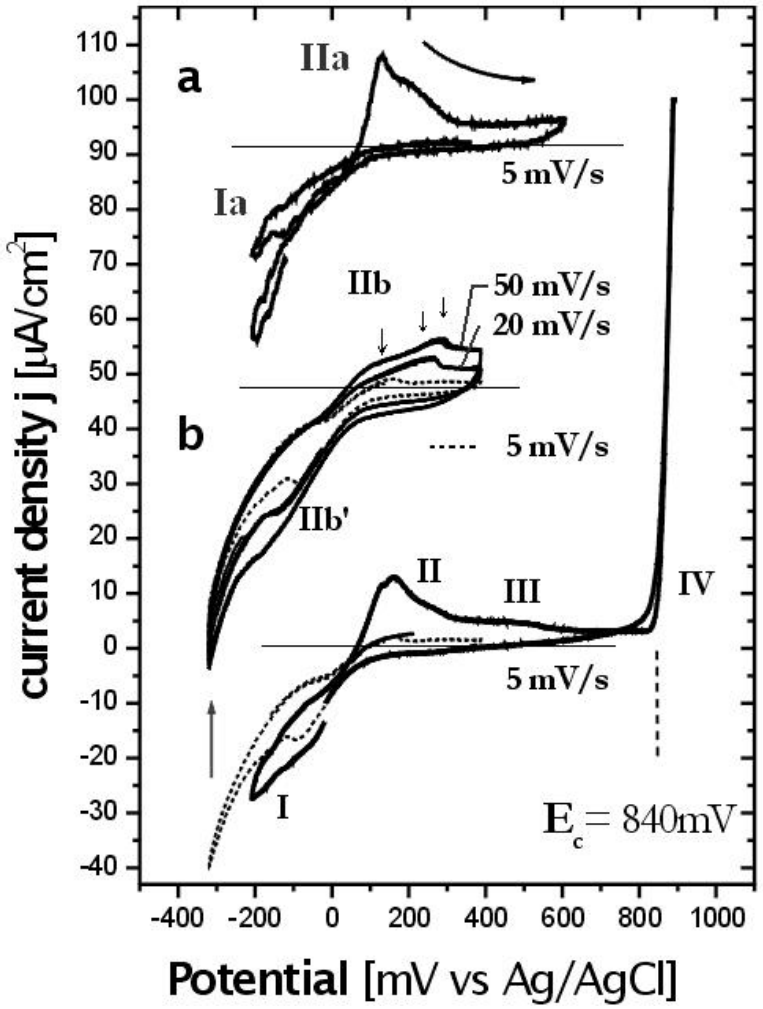

Figure 9.2: The voltammograms (initial and subsequent cycles) in the passive region of Cu_3Au have been obtained with MBE-grown $Cu_3Au(111)$ films for different final potentials. The integration of the peaks IIa and IIb reveals a charge that can be associated with the dissolution of Cu from approximately one monolayer of $Cu_3Au(111)$. The line indicates the zero current. The upper curves are shifted up. For further explanations, see text.

The shape of the measured curves agrees qualitatively with previous data published by Gerischer [ge55], Pickering [pi71] and Kaiser [ka86] for voltammograms including the critical potential and by Moffat [mo91] and Eckstein [ec01] for the sub-critical passive regime. The latter works applied different scan rates and different types of samples, so

that a direct comparison of the current/charge values is not possible. Using much lower scan rates of 0.1 mV/s Moffat obtained for (unpolished) poly-crystalline Cu_3Au samples an integrated oxidation charge (similar to our peak II) of up to 10 layers of Cu_3Au, i.e a value approximately 10 times higher than in our case. In our experiment (single-crystalline $Cu_3Au(111)$), the scan rate of 5 mV/s was most probably too fast for the surface to reach the final passivated surface structure. The peaks IIa/IIb, measured for the samples, suggests, that the initial dissolution/oxidation of Cu takes place in the potential range of +50 mV to +300 mV. The initial peak shape (IIa/IIb) is not uniform and seems to consist of a multi-peak contribution. Several different processes can occur during the dissolution, like dissolution from kink sites, step edges or terrace sites. Also a UPD layer of Cu, which could be present on freshly formed Au islands must be considered [mo91] [ma91]. Cu UPD layers on Au are stable up to 300 mV above the reversible Nernst potential for the bulk deposition and the width of peak II in Figure 9.2 a and b is in that potential range. On Au(111) at slightly higher potentials ($\approx$ 400 mV) the onset of sulfate absorption is observed in H_2SO_4. For the measured sample the value of the critical potential, E_c=0.840 mV is slightly lower than the 900 mV measured by Eckstein in the same electrolyte solution.

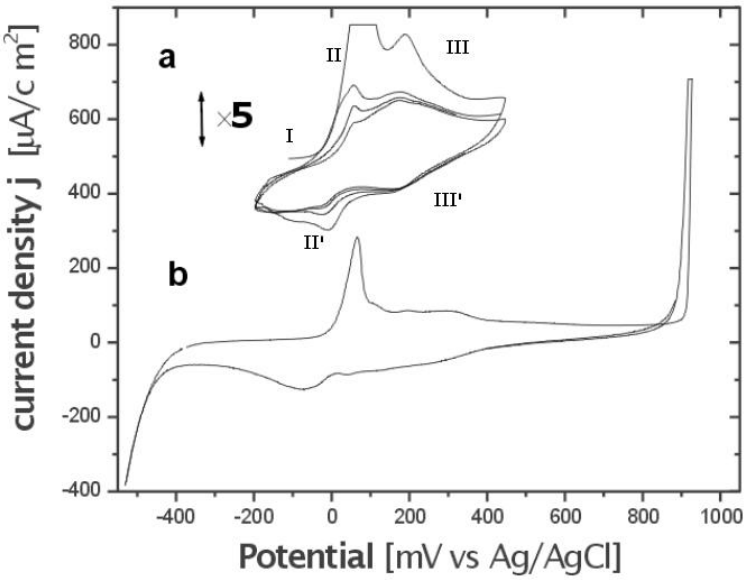

Figure 9.3: Voltammograms in the passive region (a) and after a sweep to values slightly above the critical potential (b) obtained from $Cu_3Au(111)$ single crystal surfaces. For explanations, see text.

A few Current-potential curves (voltammograms) have also been recorded for single-crystal surfaces. The Figure 9.3a shows the initial and the first following cyclic voltammograms of a Cu_3Au crystal (MaTecK 1, X-ray rocking scan shown in Fig. 7.1). The initial scans showed a much higher currents compared to the MBE-grown epitaxial films, which originates probably from a higher defect density on the crystal surface after the mechanical polishing procedure (which often leaves deep scratches or polishing particles between

the high quality flat surface regions). The minor crystalline quality, with the individual grains observed in the X-ray characterization measurements described earlier (Chapter 7), might also contribute to an increased number of defects sites, e.g. at grain boundaries. A contribution of a residual oxygen reduction reaction might also contribute to the slightly 'tilted' shape.

All recorded current-potential curves showed a much smaller current flow in a second and further potential cycles, attributed to a passivation by Au enrichment of the surface. The main peak (II) observed in a first cycle was in the subsequent cycles much smaller or not visible anymore. A broader peak (III) was present in all cases, but with changing ratios on different crystals. With one crystal we included also a sweep into the critical regime, with the result that peak II was very much increased afterwards as shown in Figure 9.3b (IIb, recorded after the same peak has nearly vanished in Fig. 9.3a) and also in region III a broad current contribution is seen. At the critical potential a massive dissolution of Cu occurs, and as the diffusion rate in the liquid electrolyte solution is limited this causes a high concentration of Cu ions at the interface region. With this argument, peak II can be attributed to a Cu dissolution and peak II' with a re-deposition process. To reveal and confirm the origin of the measured current peaks and more careful electrochemical studies have to be performed.

As a conclusion, we could observe passivation behavior during the initial dissolution of Cu from epitaxial $Cu_3Au(111)$ films and from single crystal surfaces. Peaks, representative of Cu dissolution processes, can be observed in the potential range between +50 mV and +300 mV. We did not observe, however, distinct peaks due to a dissolved Cu-UPD layer. Only a broad current distribution in the respective potential region could be noticed (200-300 mV above the Cu Nernst potential). The critical potential had the expected value for both, epitaxial films and single crystals (which is also a confirmation of the right composition of the MBE-grown films).

Chapter 10

Experimental Results: X-Ray Diffraction

In the following we present the results obtained from X-ray diffraction experiments performed at different synchrotron light sources. Cu_3Au has a lattice constant of a_0=0.3753 nm. The reciprocal coordinates we are using are chosen to describe the surface symmetry by two in-plane vectors and one out-of-plane vector, parallel to the surface normal. The in-plane positions H=1 and K=1 of these coordinates correspond to $2\pi/5.308$Å, i.e. the cubic $(1\bar{1}0)$ position. L=1 corresponds to $2\pi/6.5$Å$= 2\pi/3\times2.167$Å, with the bulk Cu_3Au {111} layer spacing of 2.167Å (The coordinates are also described in Appendix B). To distinguish our notation clearly from cubic Miller indices, we use the index 's' for the reciprocal space coordinates.

The usual way to perform the X-ray experiments was, to record the X-ray intensity with a point detector, i.e. collecting the intensity with a scintillation detector, passing a set of slits (detector slits). The movements of the individual motors of the diffractometer were chosen such that the scattering vector $\vec{q}$ moved either along certain straight lines in reciprocal space (e.g. radial scans, H-scans or L-scans) or along a circle around the origin of the reciprocal space (by rotating the sample at fixed detector position, performing a so-called rocking scan). For in-plane scans the incident and exit angles were kept slightly above the critical angle (i.e. at grazing incidence and exit). The intensity distribution of the CTR's, measured in the experiments that will be presented below, were obtained in the common way by performing rocking scans at subsequent L positions along the respective CTR. The individual rocking scans were integrated and corrected according to the different chosen geometries (Appendix D). Diffracted intensity obtained from a $Cu_3Au(111)$ surface can be associated with purely fundamental (i.e. connecting 'fcc-allowed' Bragg peaks;

these rods are not sensitive to elemental order within the cubic $L1_2$ sublattices) and pure ordering or superstructure rods (in-between 'fcc-forbidden' Bragg peaks). For notation of CTR's we use the described surfaces coordinates. The $(02L)_s$ and the $(10L)_s$ rods (and their equivalents) are sensitive to the stacking sequence. The obtained CTR data were compared with model calculations performed by using the program ANAROD [vl00]; this program is fitting the different parameters of a chosen structural model by the Levenberg-Marquard formalism to the data for obtaining the lowest χ^2. The χ^2 characterizes the deviation of the calculated and the measured data points, taking into account the individual error bar (Appendix D).

10.1 Clean Cu_3Au Surface in UHV

The $Cu_3Au(111)$ samples we used for the electrochemical corrosion experiments were prepared in UHV by sputtering and annealing cycles and characterized with LEED and AES. In order to obtain more detailed information about the starting structure we performed a SXRD experiment on the clean single crystal $Cu_3Au(111)$ surface under UHV conditions. We used the crystal delivered by the MPI crystal growth laboratory, which possessed three grains, including a large single crystal grain with a narrow linewidth. The substrate CTR measurements were conducted at the dedicated MPI-MF beamline at ANKA in Karlsruhe, Germany. This beamline was briefly described in chapter 5, including the mobile UHV diffraction chamber we used. The X-ray photon flux at wavelengths in the order of 1Å (0.1nm) is lower at an 2.5 GeV synchrotron light source compared to a 6 GeV source. With the unfocused beam, the photon flux (ph/s/cm^2) at the MPI-MF beamline is approximately 200 times lower, compared to an unfocussed beam at a high energy synchrotron beamline, like e.g. ID32, ESRF. With focusing the flux at the ANKA beamline is increased by a factor of 5 [st]. The measurement of the intensity distribution along the crystal truncation rod of Cu_3Au single crystals was feasible at ANKA. The diffraction intensity from these surfaces benefits from the high number of 79 electrons contributed by the Au atoms. The superstructure ($L1_2$ ordering) peak intensity depends on the difference of the electron number between the two elements Au and Cu, and was sufficient to measure intensity at the minimum of the superstructure CTR. With an energy of 8.8 keV and a maximum exit angle of 54°, imposed by the used mobile diffraction chamber (Fig. 5.1), the maximum L-value that could be reached was L=3.9. After several sputtering and annealing cycles the surface showed, (as seen under an optical microscope), a dense layer of particles (probably polishing particles), that were hidden under the surface before. Although their average

distance was on the μm scale, they contributed to the overall scattering background.

Results for the Clean Surface

In order to obtain structural information of the clean $Cu_3Au(111)$ surface the intensity

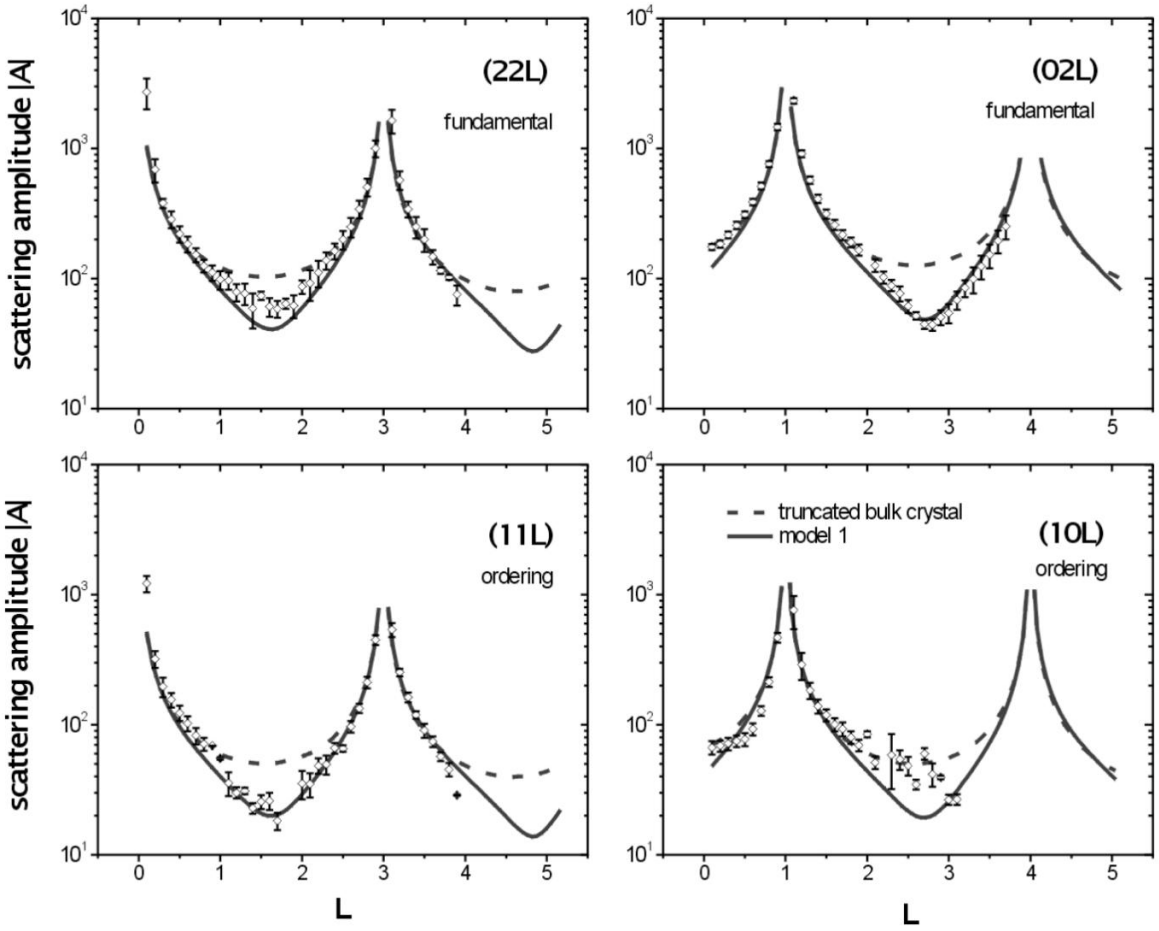

Figure 10.1: The CTR data were obtained from measurements of the clean $Cu_3Au(111)$ surface in UHV at the dedicated MPI-MF beamline at ANKA at an energy of 8.8 keV. For comparison the structure factor calculated for a bulk truncated surface (dashed line) and for a simple model (model 1, continuous line) are shown.

distribution along several CTR's was recorded. We measured the fundamental CTR's denoted $(02L)_s$ and $(22L)_s$ in our surface coordinates, and in addition the $(10L)_s$ and the $(11L)_s$ superstructure rods, together with all their symmetry equivalent rods (and

Element	Δz in pm	Occupancy
Cu, 1.layer	-7.58±1	69.7±1.6%
Au, 1.layer		
Cu, 2.layer	bulk values	bulk values
Au, 2.layer		

Table 10.1: Model 1 is obtained by a fit, in which the first layer relaxation (Cu and Au have the same height) and occupancy are varied. The calculated curve reflects already the main features of the data (continuous line in Figure 10.1).

subsequently averaged the symmetry equivalent data). The corrected data is shown in Figure 10.1, the corresponding error bars are directly the errors obtained from averaging the three symmetry equivalent data points, as this contribution to the error is dominating over the statistical counting error. For the correction of the measured intensity the usual correction factors have been considered, i.e. the footprint area, the exit-angle dependent rod intersection, the polarization factor and the so-called Lorentz correction. In addition the data have been corrected for the exit-angle dependent difference in absorption, due to the different pathway through the 2mm Be cylinder.

The obtained scattering amplitudes A (Intensity I=A^2) for these rods are shown in Figure 10.1. Also shown are simulations for these scattering amplitudes performed with the program ANAROD [vl00]. For all simulations a Debye-Waller factor of 0.7, equal to the value known from the literature for bulk Cu_3Au [xtab], has been used. The dashed line is the A$\propto$1/(1-$e^{2\pi iL}$) behavior following from the summation of unit cell contributions from 0 to $-\infty$ of a truncated crystal ([rob92]). The continuous gray line was obtained by varying the topmost (111) interlayer distance and by allowing for a occupancy of less then unity for the topmost layer of atoms. The values for this simple model (model 1) are listed in detail in Table 10.1. Model 1 includes an inward relaxation of the outer surface layer (of 7.6 pm), as expected from the (simple) argument of missing bonds on the vacuum side of the crystal surface. The $(10L)_s$ CTR is deviating from all simulated rods and was in the following not considered for the fitting procedure. With only the first layer occupancy of 70% χ^2 is 8.1 (atomic roughness) and reaches for model 1 the value 6.03 including in addition the inward relaxation.

The $(22L)_s$, $(02L)_s$ and $(11L)_s$ rods have been first compared to the calculated values on the same scale factor for all three of them. There is observable intensity on the $(11L)_s$ rod, because the contributions of Cu and Au to the scattering do not cancel out, due to the ordering in the Cu_3Au crystal ($L1_2$ structure). As ordered regions can be separated by anti-phase domain walls the ordered domains are in general smaller than the domains or regions, which give rise to the fundamental diffraction peaks. This explains the larger

width of the (fcc-forbidden) $L1_2$ ordering diffraction peaks. The fact that the intensity along the fundamental and the ordering rods can be explained on the same scale by the same model is an indication of the relatively good ordering obtained in the sample. A more detailed analysis, obtained by allowing for a different scaling factor for the ordering scattering amplitudes of the $(11L)_s$ rod together with the fitting of the structural parameters, gave the best results (lowest χ^2) with by approximately 50% increased (compared to the fundamental CTR's) scattering amplitudes for the $(11L)_s$ rod.

Element	Δz in pm	Occupancy
Cu, 1.layer	-1.00±0.3	68.8±3.4%
Au, 1.layer	-0.61±0.15	69.8±0.7%
Cu, 2.layer	0.52±0.04	100±5%
Au, 2.layer	-0.004±0.003	99.98±1.1%

Table 10.2: Results for the parameters of model 2. The (11L) scattering amplitudes are decreased to 57% by using a separate scaling factor. The final χ^2 was 2.30

Although model 1 is reflecting the main features of the experimental data, like the intensity level and the slightly shifted minimum, it is not sufficient to explain the details, e.g. of the shape of the intensity distribution around the minima of the rods. For a further refining, the interlayer spacing and occupancy of the different elements in the first two layers have been varied. The x and y positions have not been considered due to the symmetry of the surface (no observable superstructure). The biggest contribution towards a smaller χ^2 was obtained by releasing the z positions for the Au and the Cu atoms of the first two layers individually. This resulted in a 'rippled' surface, with the center of the Au atoms being 0.4 pm above the center of the Cu atoms in the top layer. The occupancy of the second layer did not differ from unity. The final structure (model 2) with the lowest χ^2 of 2.30 is shown in Figure 10.3 and its parameters are listed in Table 10.2.

Further refinement of the structure was then allowed by taking into account the z-displacement and occupancy parameters of the individual elements for the three topmost layers. The obtained parameters are listed in Table 10.3. The obtained χ^2 was as small as 1.82. In Figure 10.2d, model 1, model 2 and model 3 are included for the $(02L)_s$ CTR. Considering the significantly increased number of parameters, the χ^2 is not too much better for the model 3, and the data is not much better reproduced by taking into account three, instead of only two, top layers in the structural refinement. And considering the limited range of structure factors obtained at $8.8\,keV$ and the rather low signal of the measurement, a more detailed structural analysis is not possible. The result common for all models is an average inward relaxation of the first layer and the fact that the Au in the first (topmost)

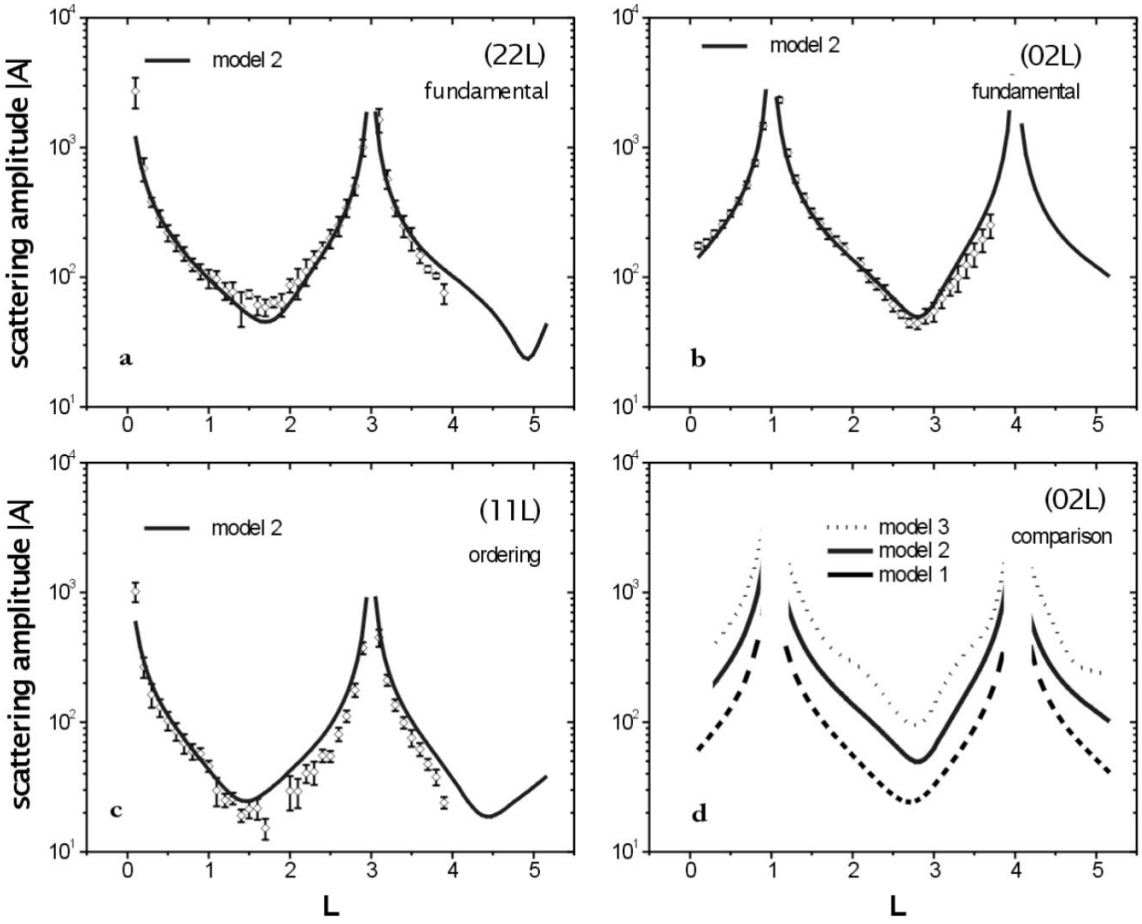

Figure 10.2: The experimental data are shown together with the calculated curves of model 2 (a-c). Model 2 allowed for variation of occupancy and the z-position of Cu and Au atoms in the first two atomic layers. Model 3 considers one more layer, i.e three atomic surface layers. In d a comparison between the three models is shown. The curves are shifted with respect to each other for reason of clarity.

layer is higher (by 0.4±0.33pm) than the Cu atoms (rippled surface). In the second layer the Cu atoms are slightly above the Au atoms (by 0.5 to 0.4pm).

Conclusions for the Clean Surface

We can conclude that we observed an inward relaxation of the outer average surface layer in the order of -0.5% of the $Cu_3Au(111)$ bulk layer spacing (0.2167nm). The Au atoms

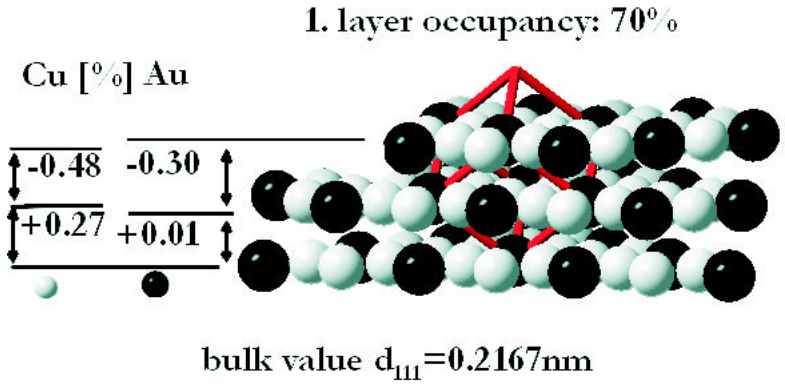

Figure 10.3: Model 2 is obtained by a fit to the data, in which the first two layer relaxation and occupancy are varied (for Cu and Au individually). For the parameters see also Table 10.2.

Table 10.3: Results for the parameters of model 3. The (11L) scattering amplitudes are decreased to 56% by using a proper scaling factor. The final χ^2 was 1.87

Element	Δz in pm	Occupancy
Cu, 1.layer	-1.57±0.16	66.0±1.0%
Au, 1.layer	-1.20±0.07	66.9±0.6%
Cu, 2.layer	-0.10±1.01	97.3±1.1%
Au, 2.layer	-0.55±0.06	95.0±0.7%
Cu, 3.layer	-0.29±0.08	97.9±1.2%
Au, 3.layer	-0.43±0.06	96.3±0.7%
Cu, 4.layer Au, 4.layer	bulk values	bulk values

in this topmost layer are 0.4±0.33pm higher than the Cu atoms in this layer. In the second layer the situation is different: here the Cu atoms are higher by 0.5 to 0.4pm. The surface is smooth on the atomic scale within the coherence length of the probing X-ray beam. The atomic roughness or step structure is accounted for by a 70% occupied first layer. The fact that the scattering factors for the fundamental and the ordering CTR's do not deviate considerably to the calculated values (when fitted on the same intensity scale) indicates a high degree of ordering in the sample. The measured scattering amplitudes can be explained by a fully ordered crystal and crystal surface, but with smaller ordered domain size of the $L1_2$ superstructure, compared to the simple cubic bulk lattice.

10.2 Selective Dissolution: Formation of a Passivation Layer

In Chapter 3.2.4 we described the general (corrosion) behavior of binary alloys in solutions under an applied potential. In the case of the Cu-Au system, with its big difference in the equilibrium potential of the two elements, the less noble element (Cu) will dissolve first. With increasing potential, the Au left behind is expected to protect the surface from further Cu dissolution until the critical potential is reached. As in the case for oxide-covered metal surfaces this behavior is called passivation. At the critical potential E_c a pronounced roughening of the surface is reported at the sharp rise in electrical current and a porous (sponge-like) dealloyed Au layer is finally formed. This thesis work focused on the structural aspects of the passivated region below the critical Potential E_c. Figure 10.4 gives a sketch of the main potential regions that are introduced to describe our observations. We divided the region between the onset of Cu dissolution and the critical potential E_c in an initial region of low overpotential and a region that we call elevated overpotential region. The reasons for this are presented in the following.

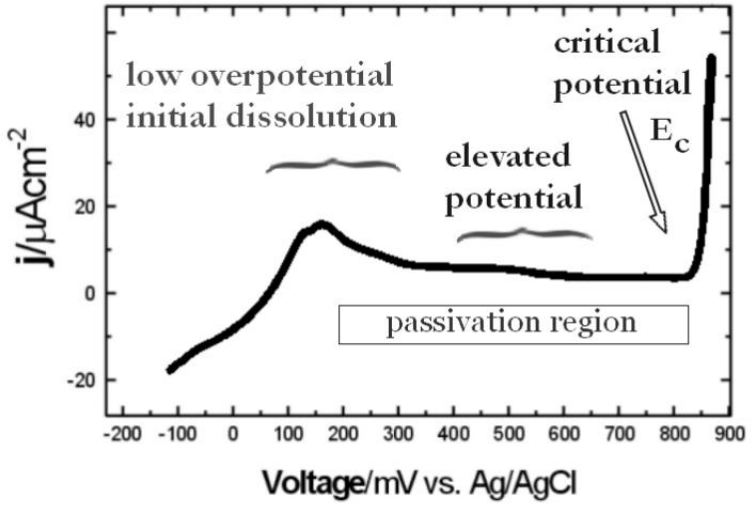

Figure 10.4: Sketch of the main potential regions relevant for selective alloy dissolution. The observations made in the respective potential regions will be presented in the following.

The X-ray experiments presented in the following were carried out in the thin layer in-situ X-ray electrochemical cell described in Chapter 5.4.1. Within this three electrode electrochemical cell, the sample was connected as working electrode (WE) to a potentiostat, which was controlling the applied electrical potential. The counter electrode (CE) in the cell was made from a platinum wire and as reference electrode (REF) we used commercially available ('leak free') Ag/AgCl micro-reference electrodes from different suppliers. The cell

was covered by a 6μm thick mylar foil that could be inflated and deflated by applying a slightly changed electrolyte pressure. Prior to the experiments the cell was cleaned by immersion in a mixture of H_2O_2(30%) and concentrated H_2SO_4 (This strong oxidizing acid is also called "piranha" or Caro's acid) and intensive rinsing with ultra-pure water. Via adapter plates the cell could be mounted to the used RISØ (HASYLAB), and Huber diffractometers (ESRF and ANKA). The used electrolyte solutions were prepared from ultra-pure water (USF, TOC<2 ppb), suprapure (MERCK) concentrated H_2SO_4 and, if used, suprapure HCl acids. The solutions were deaerated by purging the storage bottles with Nitrogen gas for about 1 hour before the experiment.

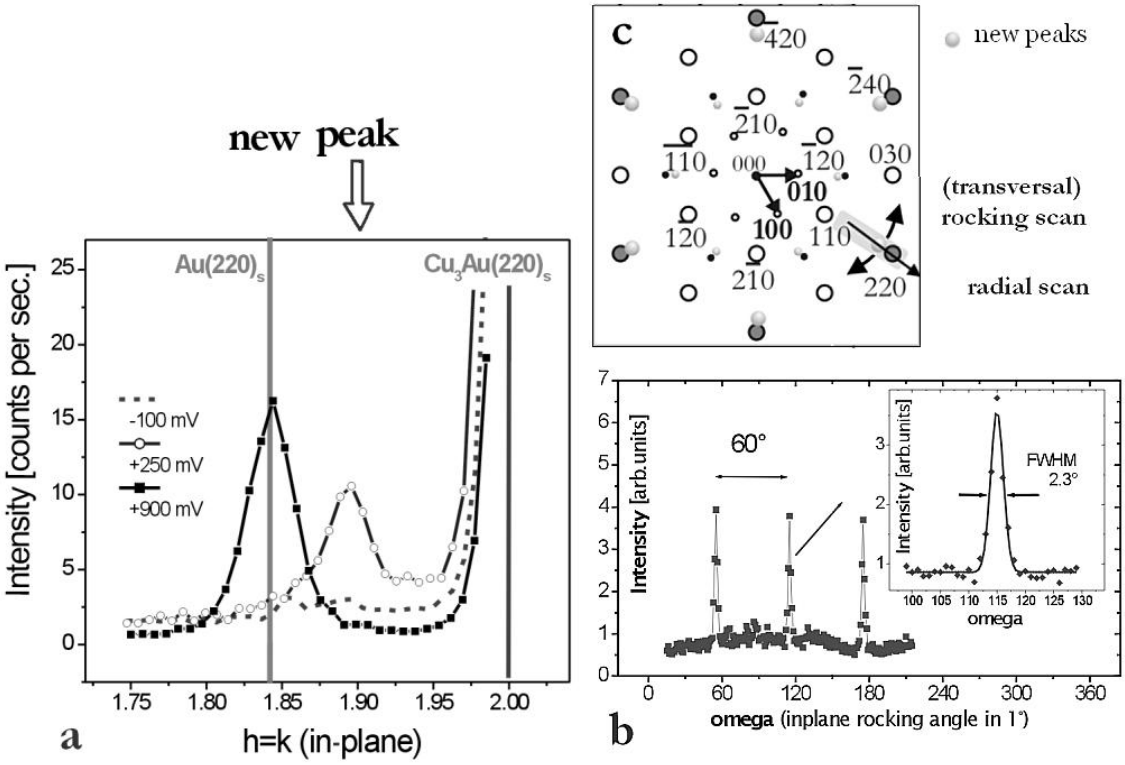

Figure 10.5: (a) In-plane radial scans close to the $(220)_s$ Cu_3Au substrate peak show the formation of a new structure on the surface. At higher potential the position is shifting to the Au bulk value. (b) The new diffraction peaks show in-plane six-fold symmetry and their angular width is typically in the order of 2°, i.e. the corresponding layer is epitaxially oriented. (c) The (111) surface normal ($\langle 001\rangle_s$) of the new structure is aligned with the substrate $\langle 111\rangle$ ($\langle 001\rangle_s$)normal.

At the beginning of the experiment (The UHV sample preparation was described above), and after alignment of the $Cu_3Au(111)$ sample surface to the diffratometer, we

brought the sample into contact with deaerated 0.1 M H_2SO_4 electrolyte solution at a potential of -150 mV (vs. Ag/AgCl). At this potential only Cu_3Au substrate peaks were observed. By increasing the potential, around +200 mV new diffraction peaks were emerging close to the fundamental Cu_3Au substrate in-plane peaks as shown in Figure 10.5 a. The in-plane peaks close to the substrate $(220)_s$-like peaks show the same six-fold symmetry than the substrate (Figs. 10.5 a, b). The angular width of the peaks along an in-plane rocking scan (turning the sample around its surface normal) was around 1-2°, i.e. larger than the 0.1° of the fundamental substrate peaks, but still comparatively sharp. The value of the reciprocal in-plane (H and K) position at this initial stage of the dissolution does not correspond to relaxed pure bulk Au(111). With increasing the applied potential the initially observed diffraction peak is moving in direction of the position expected for pure epitaxial bulk Au(111). At +800 mV (close to E_c) the peak position is very close to this position for epitaxial Au(111). In Figure 10.5 the respective radial scans (a) and rocking scans through the initial peak are shown (b). Figure 10.5 c shows the reciprocal map for the in-plane peaks of Cu_3Au (filled and empty circles) and the observed new peaks.

The formation of epitaxially aligned Au on Cu_3Au was observed by Swann using electron microscopy [sw69]. Intermediate reciprocal peak positions (specular) have been also observed before by Pickering [pi67] and explained by the occurrence of intermediate alloy compositions with the partial dissolution of Cu and was interpreted as a sign of a volume diffusion mechanism. Nevertheless, the properties of surfaces or thin films, including the structure, can deviate considerably from their bulk values. This is well known from many recent studies on heteroepitaxial thin film growth, and as well by the observation of many surface reconstructions. In heteroepitaxial growth, the overlayer often first adopts the lattice constant of the substrate (pseudomorphic growth), before the film relaxes to the bulk lattice constant with increasing thickness. If compressive or tensile stress is present in the film (biaxial strain on e.g. (001) or (111) surfaces), the layer spacing along the direction perpendicular to the surface will increase/decrease according to (bulk) elasticity theory [du97][hor78][st94]. In addition, surfaces, atomic monolayers, or ultra-thin films can have different properties than the respective bulk materials. As an example, for Pb on Cu(111) in electrolyte the in-plane lattice constant is even dependent on the applied potential (electro-compressible)[ch97], and the equilibrium state of the Au(111) surface at room temperature includes one Au atom in addition to every 23 (bulk) atoms along the $< 1\bar{1}0 >$ direction (herringbone reconstruction, Chapter 8.1). Composition and strain can have similar effects on one individual Bragg peak. To clarify the situation here, we have to take the full structural information into account, i.e. in-plane and out-of-plane lattice constants/diffraction peaks. A full analysis of the in-plane and out-of-plane peak positions,

observed during the initial Cu dissolution, will be described in the following section.

10.2.1 Formation of an Ultra-Thin Mono-Crystalline Layer

In order to gain insight into details about the observed new epitaxial structure on the surface the experiment was now performed scanning in-plane and out-of-plane directions at the respective positions in reciprocal space. We increased the potential (stepwise) very slowly, and at the same time we were monitoring the peak position and the intensity as a function of time. The peak intensity emerging from the new epitaxial structure was a function of potential and time. The potential was increased to obtain sufficient intensity to perform the measurement of the CTR from the new structure.

Results and Discussion

After immersing the sample into electrolyte solution at a cathodic potential of -100 mV, we usually observed only Cu_3Au substrate peaks. Only occasionally already a small peak at a position of the new peak, which we described before, was present. However, the rocking scan showed then a rather broad angular distribution of approximately 20°. Stepwise increasing the potential, at +135 mV, a new sharp peak was observed with an angular width of 3°. After keeping the potential at this value for several hours, the intensity of this peak did finally not grow any further. By comparing the diffraction peaks of the substrate and the new epitaxial surface structure, we revealed a defined, inverted stacking of the new structure, as will be described in the following. The ABC-like stacking sequence can be distinguished from a CBA-like stacking, because some of the Bragg peak positions are different. For the (111) surface, these Bragg positions are along the CTR's with no in-plane Bragg peak, e.g. the $(20L)_s$, $(02L)_s$, $(10L)_s$, etc. Each of the possible stacking sequences, ABC or CBA, gives either rise to peaks at L=1, L=4,... or at L=2, L=5,..., i.e. if both twin domains are present, peaks along the respective rods at L=1, L=2, L=4, L=5,... are observed. The crystal substrate is essentially free of domains with faulty stacking. As can be seen in Figure 10.6, the stacking sequence is different for the new layer compared to the substrate. Figure 10.6a shows an in-plane H-scan, i.e. along the $(100)_s$ direction. The peak is due to the $(1.92\ 0\ L)_s$ rod of the observed new layer, i.e. it is observed at the intersection of the $(1.92\ 0\ L)_s$ rod with the surface plane/scan-direction. Figure 10.6b shows scans along the L-direction (L-scans), i.e. perpendicular to the surface plane. Three L-scans are shown. The $(1.97\ 0\ L)_s$ L-scan (3) runs close to the $Cu_3Au(111)$ substrate CTR, which has a Bragg peak at (2 0 2). The sharp intensity peak at L=2 is originating from the close Bragg peak of the substrate with ABC stacking. The $(1.92\ 0\ L)_s$ L-scan (2)

shows intensity emerging from the new epitaxial surface structure. It shows a very broad intensity maximum at approximately L=1. The (1.80 0 L)$_s$ L-scan (1) shows essentially background intensity, which is emerging from both, the close substrate peak and from diffracted intensity from the new structure.

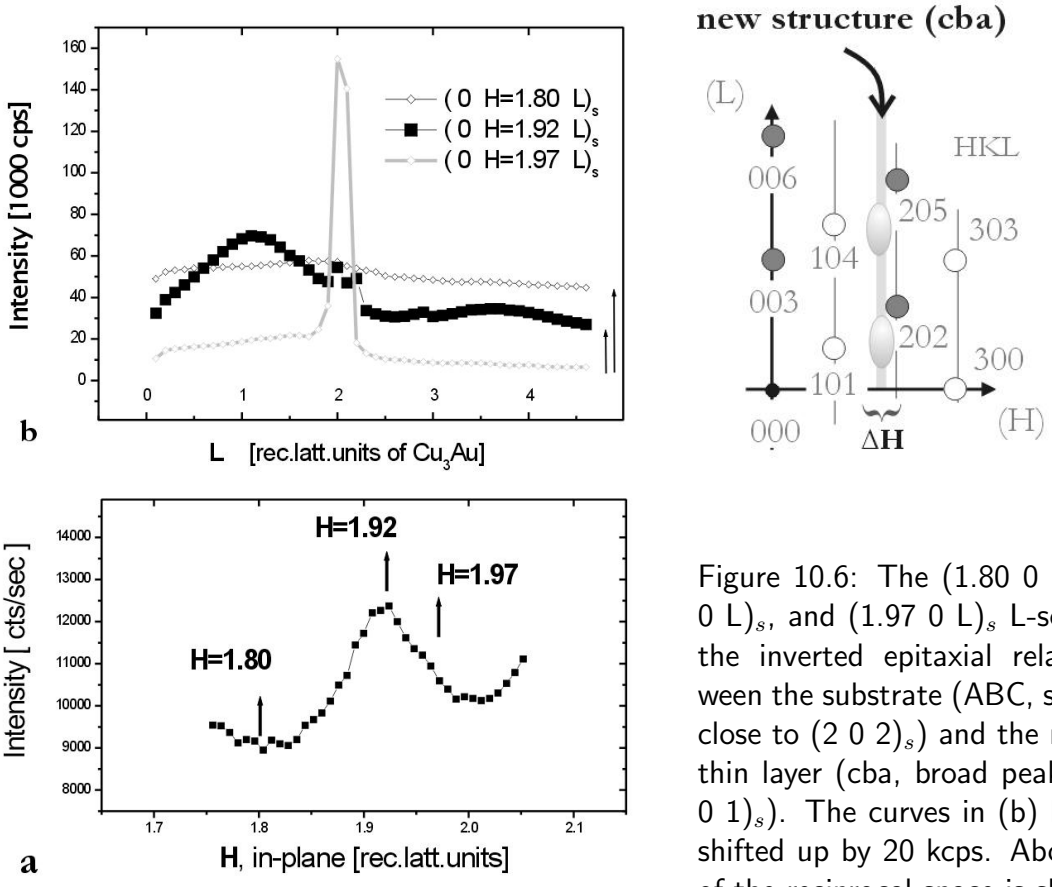

Figure 10.6: The (1.80 0 L)$_s$, (1.92 0 L)$_s$, and (1.97 0 L)$_s$ L-scans show the inverted epitaxial relation between the substrate (ABC, sharp peak close to (2 0 2)$_s$) and the new ultra-thin layer (cba, broad peak at (1.92 0 1)$_s$). The curves in (b) have been shifted up by 20 kcps. Above a part of the reciprocal space is shown.

The L-scans provide detailed structural information about the new surface structure, which emerged with the initial dissolution of Cu. The width of the intensity distribution along the (1.92 0 L)$_s$ L-scan (i.e. at the in-plane position of the observed new epitaxial structure) can be explained as originating from an ultra-thin surface layer (ultra-broad peak in reciprocal space). The width of roughly ΔL=1 points to a thickness in the order of 1×6.5 Å or three monolayers (3ML) in units the $Cu_3Au(111)$ substrate (3×2.167 Å was the chosen unit vector in z-direction in our surface coordinates). The exact width has to be extracted from a model-calculation and fit to a set of CTR data, as will be done later. At L=2 only a sharp contribution to the intensity from the close-by substrate Bragg peak is seen, but in contrast no similar broad contribution. The observed intensity along the (1.92 0 L)$_s$ L-scan is thus as expected from a fcc-like structure with a defined stacking sequence

('cba', written with small letters for the film), which is the faulted sequence with respect to the substrate. The substrate has a ABC sequence and the new ultra-thin film then consequently 'cba', while the 'ABCabc' substrate-film sequence can be excluded, except a fraction not exceeding 3% of the new surface islands, as will be shown later (Fig. 10.24).

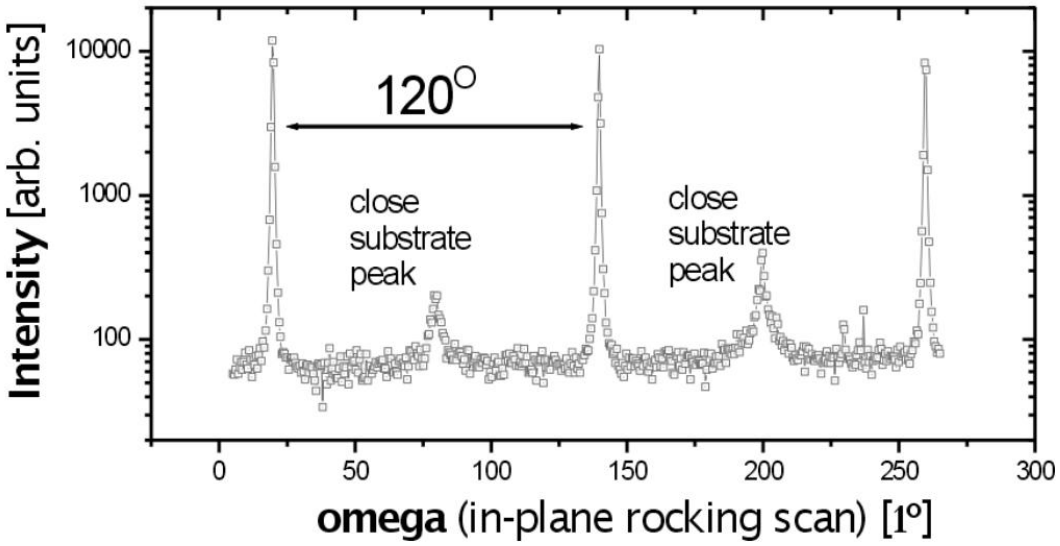

Figure 10.7: On the $(1.92\ 0\ 1)_s$ out-of-plane position an in-plane rocking scan (omega axis parallel to surface normal) shows only one fcc-like stacking, i.e. only ABC and no ACB. The small peaks in between arise due to close $(0\ 2\ 1)_s$-like Cu_3Au peaks

Figure 10.7 shows the three-fold symmetry expected for such a fcc-like crystal structure with one defined stacking sequence 'ABC'. This three-fold symmetry and, equally, the 'exchanged' peak position along the L-scan in Figure 10.6 indicates, therefore, firstly a cubic or pseudo-cubic structure (three-fold symmetry) and secondly an inverted orientational relation (peak positions) between the substrate and the new layer formed with the initial dissolution of Cu. The reason for this behavior is not yet understood. A closer look at the situation at the interface gives an indication of a possible influence of the second nearest neighbor interaction across the interface. The different in-plane atomic distances, which are forming a so-called heterophase interface, are creating energetically 'unfavorable' sites (hcp and on-top) at the interface (Fig. 10.8). By changing the stacking sequence of the (2nd) layer, the distribution of these unfavorable sites can be changed. This is illustrated in Figure 10.9. We write the different atomic sites and stacking positions of the ultra-thin film as 'a', 'b' and 'c'. The first layer of atoms in the film is forming the hexagonal heterophase interface with the ABC stacked substrate, with the fcc-sites ABCa, the hcp-sites ABCb and the on-top sites 'ABCc'. The second layer of film-atoms is then

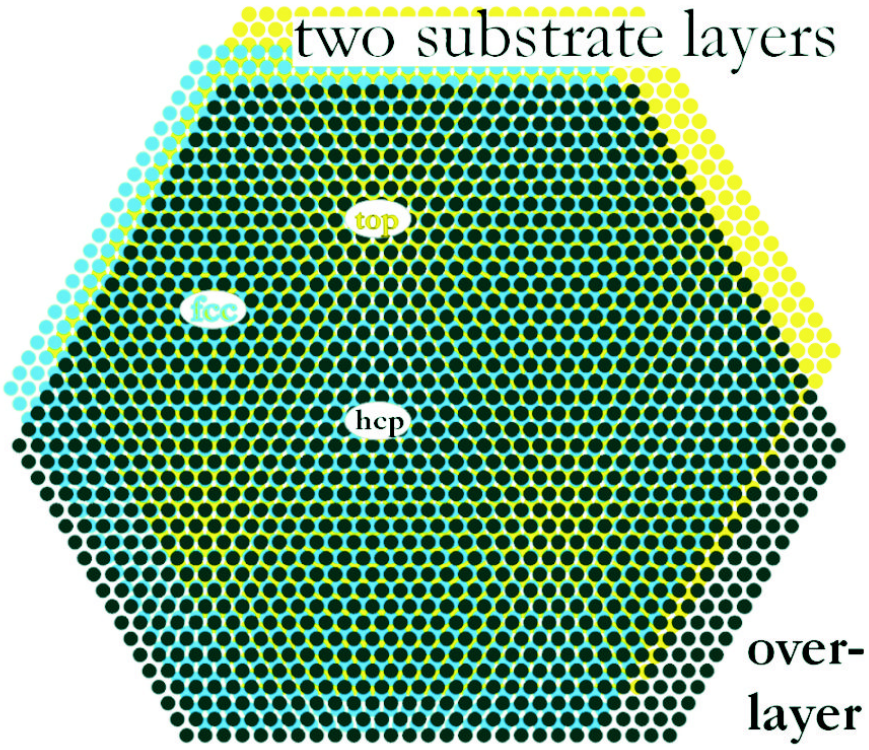

Figure 10.8: If a hexagonal layer with different in-plane lattice spacing (in our case a larger spacing) is placed on-top a fcc-(111) surface, regions of fcc, hexagonal and on-top positions will create a modulation of the height of the surface layer (z direction).

determining the stacking sequence of the fcc-like film. Case I is a inverted stacking with the sequence ABCac(bacb) at the initial ABCa fcc position/region. Case II would be a continued stacking with ABCab(cabc). We observed exclusively case I, where one hcp coordinated atom of the first two layers of the film appears in two regions respectively, and one region of on-top coordinated atoms. For the case II the hcp coordinated atoms of the two first layers are located in the same region, with another region being ideally 'fcc' stacked and an on-top coordinated region. To judge on the validity of the influence of the coordination, calculations are needed, that are up to now, to our knowledge, not existent in the literature.

The occurrence and change of the observed new surface structure is dependent on potential and time. In general for the measurement of a CTR, a sufficient diffracted intensity, from any examined structure is needed, and therefore we increased the potential by small steps to obtain a stronger signal at the initial position of the new peak, i.e. with the peak not yet shifted to the relaxed pure Au position.

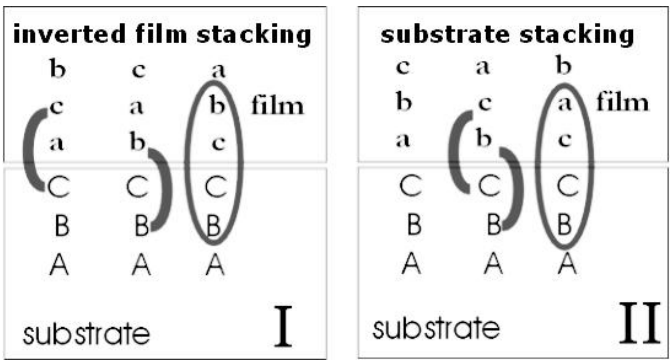

Figure 10.9: Different in-plane atomic distances of two layers are creating 'unfavorable' sites (hcp and on-top) at the interface (Fig.10.8). By changing the stacking sequence of the (2nd) layer the distribution of these unfavorable sites can be changed. We observed case I.

In Figure 10.10 our experimental approach is documented. While increasing the potential we performed radial HK-scans across the new peak at $(0\ 1.9\ \mathrm{L})_s$; the reciprocal position of the radial scan, the corresponding width and the integrated intensity are plotted for the different potentials. During the course of the experiment described in Figure 10.10 the potential has been raised gradually, but never approached the critical potential of ca. 800-900mV (Ag^+/AgCl). The intensity of the new structure peak was monitored by radial HK-scans and at the in Figure 10.10 marked positions (1-5) additional L-scans were measured. Figure 10.11 shows the obtained information. During this experiment the intensity along the new structure rod increased, starting from the first observation at +135mV, by a factor of 4, while the thickness (i.e. the width in L-direction) and the lateral extension (i.e. the width in HK-direction) are not growing considerably. The width in L-direction changes from first 1.04 reciprocal lattice units (rec.latt.units or rlu) to 0.78 rlu, which corresponds to a thickness of d=6.5 Å/ΔL=8.3 Å or 4 monolayers of the Cu_3Au lattice. The lateral extension, as judged by the lateral peak width, was growing from 12.5nm to 15nm.

In Chapter 4 we discussed the diffraction peak for the simple model of a parallelepiped and the peak intensity was growing with N^2 and the width of the diffraction peak decreasing proportional to 0.88/N, with N being the number of atom/scatterers in that direction. A lateral increase of the island dimension from 12.5 to 15 nm is thus not sufficient to explain the increasing intensity. The area covered by the observed islands is thus growing, e.g by nucleation of new ultra-thin islands. At higher potentials neither the intensity nor the lateral or the perpendicular peak width was changing further. The ultra-thin new Au-rich structure then seems to cover the whole surface.

A more detailed analysis of the in-plane and out-of-plane peak positions of the now described experiments, and of others, will be presented later. Here we add the description of one further observation in association with the performed L-scans. The lattice constant of a crystalline structure can usually be derived by determination of the position of Bragg peaks. With our chosen coordinate system the Cu_3Au {111} layers, e.g. give rise to Bragg

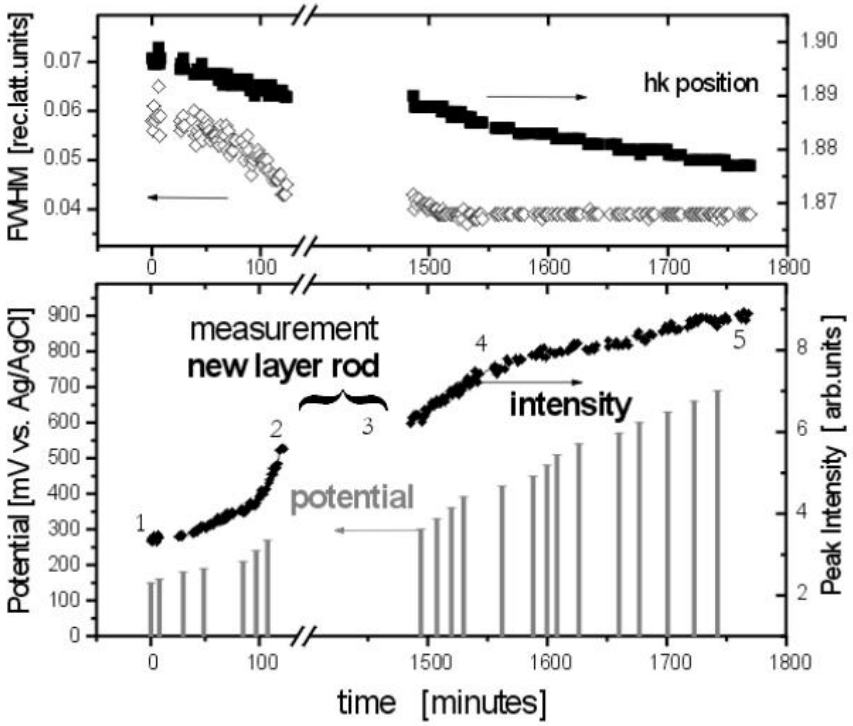

Figure 10.10: After immersing the Cu_3Au sample in deoxygenated 0.1M H2SO4 acid solution a new structure developed on top of the $Cu_3Au(111)$ crystal with Cu dissolution with increasing overpotential. After the intensity obtained for the new peak at (0 1.9 L)$_s$ was a sufficient, a truncation rod of the new structure was measured (2). In this experiment the electrochemical cell was kept always in thin film geometry.

peaks along the specular rod at L=3, L=6,.... Similar, the Cu_3Au Bragg peaks along the (0 2 L)$_s$ rod are at L_1=1, L_2=4,..., i.e. ΔL=3 corresponds to the {111} lattice plane distance of 0.2167 nm and can be calculated from the L-value of each peak position. Interestingly, the two peaks of the L-scan along the new structure rod in Figure 10.11 (0 1.9 L) reveal two different values for the deduced lattice parameter in z-direction, with the value for the lattice constant being smaller for the higher L-value. At some points we recorded in addition to the (0 1.9 L)$_s$-like L-scans also intensity along the 30° rotated rod, i.e. the (1.9 0 L)$_s$-like L-scan. An analysis of this (30°-rotated) rod, gives again two different values, that are both quite different from the values obtained from the (0 1.9 L)$_s$ rod and this time a larger lattice constant for the higher L-value is deduced. This is shown in Figure 10.12.

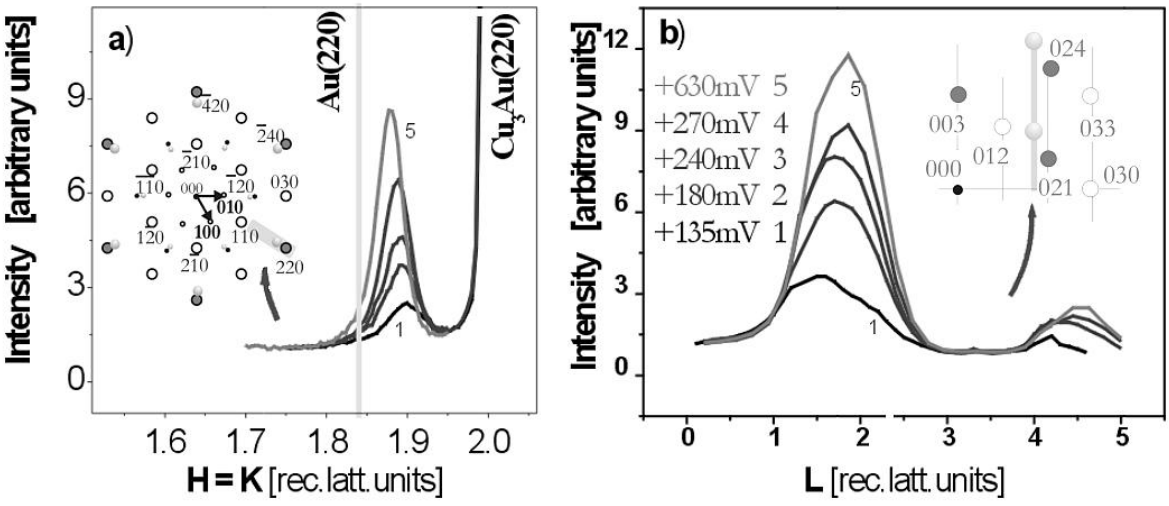

Figure 10.11: We could follow the lateral growth of an ultra-thin layer within the initial dissolution of Cu from Cu_3Au. An estimate of thickness from the width of $\Delta L=1$ gives an value of approximately 3 monolayers.

The fact that the magnitude of the relative deviation of the lattice constant deduced from the different peak positions is systematic in L is shown in Figure 10.12 b. The relative deviation is smaller for higher L-values. It seems that the peaks are shifted relative to an expected position (for an ideal or average fcc layer), and in opposite directions relative to the average position on the $(1.9\ 0\ L)_s$-like and $(0\ 1.9\ L)_s$-like rods. To find an explanation for the relative shift of the peak positions is not straightforward, also because little is known about the detailed atomic structure at interfaces. A relative shift of diffraction peaks is also reported for the martensitic hcp-Co to fcc-Co phase transformation [seb87]. Stacking faults are created during this transformation and are the reason for the shifts of the peaks from the original fcc positions towards the hcp positions. As for many noble metals, the energy of formation of a stacking fault is comparatively low for Au [schw92] [sz02]. A possible contribution from hcp islands within or on-top of the new surface structure therefore has to be considered for the simulation of the scattering data. But also strain, and the release of strain by surface reconstructions, in the ultra-thin film might be the reason for the asymmetric shape we observed.

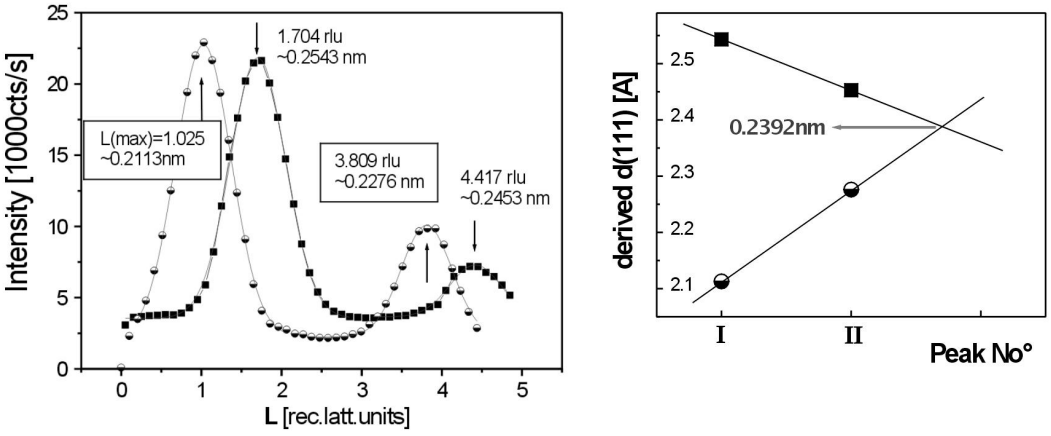

Figure 10.12: A comparison of two L-scans shows a systematic deviation from pure fcc behavior, that is less pronounced at higher L-values. For a homogeneous structure each Bragg peak position would give the same atomic layer spacing.

Conclusion

Therefore we can conclude: at about +135 mV an initial ultra-thin fcc-like Au-rich surface layer is formed but additional structural defects have been detected by a systematic peak shift in L-direction. The layer is epitaxially aligned with the $Cu_3Au(111)$ substrate: The $\langle 111 \rangle$ surface normal of the new layer and the substrate are parallel ($Cu_3Au(111) \| Au_xCu_{1-x}(111)$ in the usual cubic notation) and the in-plane directions are inverted oriented, e.g. $Cu_3Au\ \langle 1\bar{1}0 \rangle \| Au_xCu_{1-x}\ \langle \bar{1}10 \rangle$ in normal cubic notation. The lattice for the new layer is thus rotated compared to the Cu_3Au lattice by 60° or 180°. Because of this rotation of the lattice the epitaxial relation is sometimes also called 'anti-parallel'. The observed layer is growing laterally and by nucleation in new areas, while in thickness only a minor increase could be observed.

10.2.2 Elevated Potential Selective Dissolution

For Cu_3Au, as in general for binary alloys with a rather high melting temperature, the critical potential E_c is an important value to describe the corrosion behavior. The strong rise in dissolution current, is commonly accompanied with a transition in surface morphology from a smooth to a rough or porous type. For the initial subcritical dissolution (low overpotential) we could indeed observe, as described before, a very thin and stable Au-rich

structure developing on the surface of $Cu_3Au(111)$.
Nonetheless, there have been also observations of subcritical occurrence of nano-clusters [mo91] or monolayer-pits [str01], i.e. of non-flat surface morphology below E_c in the literature, but structural studies below the critical potential are scarce. However, the massive rise in current due to enhanced dissolution occurs only at the critical potential.

With the high X-ray flux at the ESRF the mylar foil we used was damaged. During the experiment, that was described before we therefore always kept the in-situ X-ray cell in thin film geometry, i.e. with an electrolyte film of approximatly 10 μm [oc90] since upon inflating (thick layer geometry) the mylar foil was prone to break after a certain beam exposure. In the thin electrolyte layer an enhanced potential drop will occur (IR drop, due to the (dissolution) current I and the enhanced electrolyte resistance R in the thin layer). The actually applied potential can thus deviate on the surface, depending on the actual situation. This leaves some doubt about the exactness of the given values in the experiment. For a better electrochemical control we conducted the experiments, which will be presented in the following, by inflating the mylar foil of the cell to a thick layer during a change of potential. The electrolyte film above the sample was then several mm thick. For the measurement the mylar foil was deflated again. These measurements have been mainly conducted at HASYLAB, where the mylar film of the cell survived for several days, due to a smaller X-ray flux and density (larger spot size). What follows in this section is a description of our observations of a changing surface morphology at elevated overpotentials, but still far below the critical potential.

Formation of Au(111) Islands

At lower overpotentials we had observed new Bragg peaks, indicating a new epitaxial structure formed during the initial dissolution of Cu from Cu_3Au. The in-plane and out-of-plane peak positions and deduced lattice constants were found to deviate from the expected values for bulk Au. A more detailed analysis of this peak positions will follow at the end of this section. We describe now first an experiment at the ESRF (Figure 10.13). In the course of this experiment, the potential was increased by small steps after each hk-scan, which took a few minutes each. No L-scans have been recorded and the cell was kept in thin film geometry, in order to minimize the time between each potential step. Therefore, the shown HK-scans of Figure 10.13 were obtained in less than one hour. With higher applied potentials (above +250 mV), the Bragg peak of the new structure shifted gradually in its in-plane position towards the value for pure bulk Au(111). The full width at half maximum (FWHM) is slightly decreasing, from approximately 0.02 to 0.015 rlu,

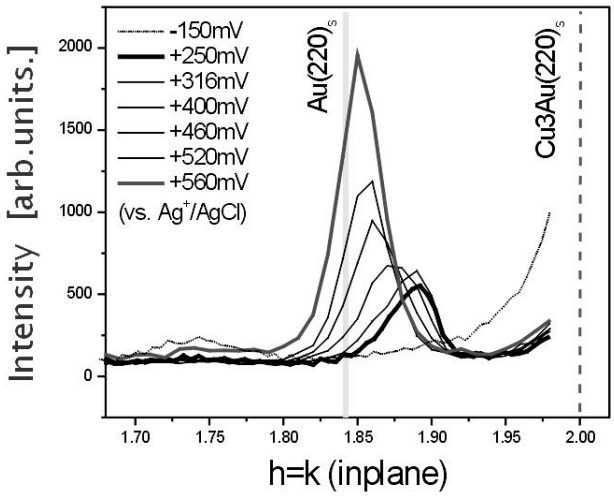

Figure 10.13: The diffraction peak is moving gradually towards the pure Au position. The measurement was completed within one hour.

indicating a coherence length (attributed to an average lateral island dimension) of 14 to 18 nm. At a potential of 560 mV , which is still well below E_c, a position close to the expected pure Au position is reached.

Nevertheless, not only the potential but also the time, are important parameters for the growth. At BW2, HASYLAB the Mylar foil, used to cover the in-situ cell (Chapter 5.4), resisted the X-ray exposure for several days. The beamline has a lower flux of X-ray photons compared to ID32, ESRF, and is causing therefore less beam-induced damage on the foil. This allowed us to inflate the foil above the sample, each time we changed the potential (thus causing an increased electrical current in the cell). Proceeding in this way, we could avoid the large IR potential drop, that occur with a deflated foil in the cell, due to the then increased resistance along the only 10μm-thin electrolyte film. In the next experiments that we describe now, we increased the potential slowly in time. In four runs we could again first observe the initial behavior of the passivation process: A diffraction peak, epitaxially aligned to the $Cu_3Au(111)$ substrate, grew at a reciprocal position close to $H = K = 1.9$ rlu, i.e. between the substrate peak at $H = K = 2$ rlu and the position expected for pure bulk Au(111) at $H = K = 1.84$ rlu. In L-direction the new peak was largely extended, as expected for diffraction from an ultra-thin layer. We recorded only L-scans on-top of the peak, and are therefore not able to correct precisely for background intensity. The width of the L-scan at the initial position gives thus an estimated (coherent) thickness, between 2-5 atomic monolayers. At elevated potentials we now observed an additional diffraction peak emerging exactly at, or in some cases very close to the expected (epitaxial) Au(111) position. This Au peak is much narrower in the L-direction than the initial peak. Figure 10.14 shows the in-plane (radial) HK-scans close to the $(220)_s$ substrate peak, recorded for

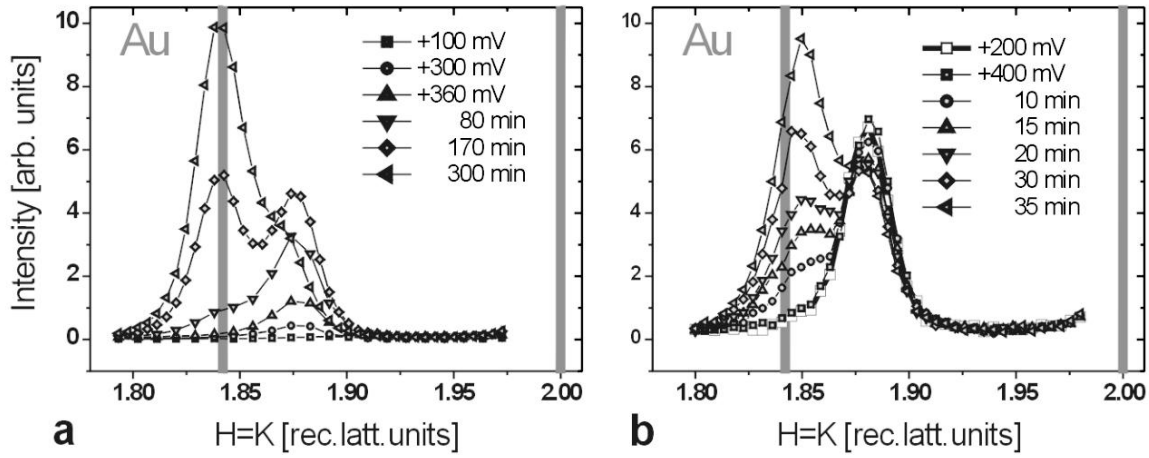

Figure 10.14: For a slow increase of potentials, the ultra-thin layer grows without shifting towards the pure Au position. A second diffraction peak becomes visible. While at 360 mV the new peak is exactly at the pure Au position (a), at 400 mV the peak is growing much faster, but not exactly at the Au position (b).

potentials up to 360 mV and 400 mV, respectively. The additional Au peak was growing faster for the higher potential, and for this faster growth, the Au peak position was not exactly at the bulk Au position. However the sample had been measured already after transfer from UHV in air and the ultra-thin structure with its corresponding peak had been present before immersion into the electrolyte. The peak shown in Figure 10.14 a has been grown in-situ, i.e. there were only Cu_3Au substrate peaks observed after immersion at -100 mV, and the sample was afterwards in electrolyte at potentials above +100 mV (i.e. at potentials, where we observed the growth of the initial passivation film) for 44 hours. Then, at a potential of +360 mV the growth of the additional bulk Au peak was initiated. It is noteworthy that a long growth time at low overpotentials seems to stabilize the ultra-thin structure and, in contrast to the experiment with a much faster increase of the potential presented before (Fig. 10.13), the growth continued with a corresponding peak at exactly or nearly exactly the expected Au position, without an observed shift of the initial peak.

The results for the L-scans are exemplified in Figure 10.15. Directly after immersion into the 0.1M H_2SO_4 electrolyte solution at -128 mV only Cu_3Au substrate peaks could be observed in this experiment. By slowly raising the potential to 290 mV (low overpotentials) we could grow an (initial) ultra-thin passivation layer. The L-scan on this peak $(1.89\ 0\ \mathrm{L})_s$ revealed a broad peak (in the L-direction) with a width of ΔL=0.74 rlu. Approximately,

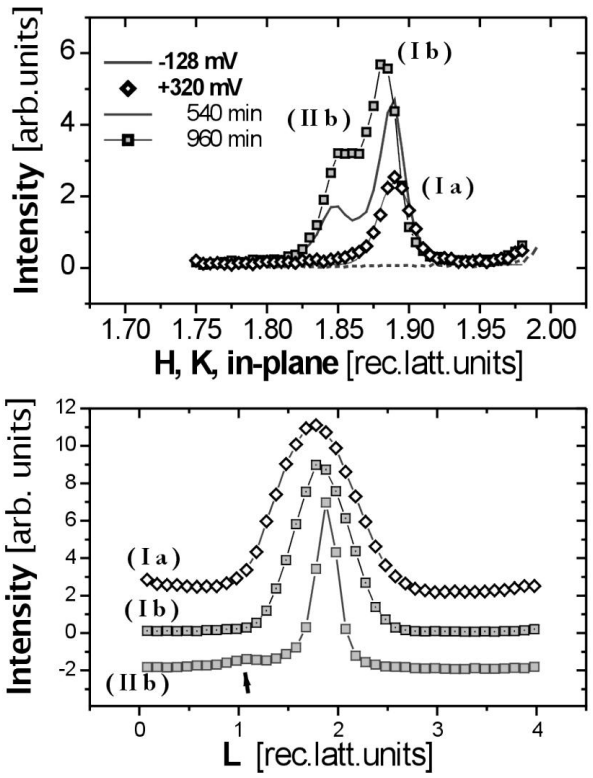

Figure 10.15: The additional peak has always about the same in-plane width (top image) but is now much narrower in L-direction (II b, corresponding to 3nm or approximately 12 atomic layers), while the initial peak is still only a few (3-5) atomic layers thick (I b). The initial peak is labeled I a.

this corresponds to a thickness of d=3/ΔL=4 monolayers of $Cu_3Au(111)$ lattice planes. With the potential at 320 mV we could measure after 540 minutes an additional peak at the expected bulk Au position. The initial peak was still visible. L-scans on both peaks showed that the peak on the bulk Au position had a peak width, much narrower than the initial peak. We measured ΔL=0.55 rlu for the L-scan on the initial peak and ΔL=0.24 rlu for the bulk Au peak, which approximately gives values for the thickness of 5.5 ML for the initial layer and 12.5 ML for the new bulk Au layer, respectively.

The in-plane diffraction peak of the freshly formed bulk Au peak has about the same in-plane width (HK-scan) as the initial peak. In Figure 10.16 the approximately calculated values for the lateral coherence/island size tend to slightly increase for each experimental run. The data-points of the measurement of the initial structure presented in Figure 10.11 and 10.13 are included here. In summary, the peaks show an in-plane width and a corresponding lateral length scale, with the same order of magnitude of 15 to 25 nm for the initial ultra-thin layer and for the thicker bulk Au structures. The thickness of the observed structures is much smaller than the lateral extension (thin islands) and increases from initial values below 1 nm (ultra-thin islands) to values of around 2-3 nm for the structures with

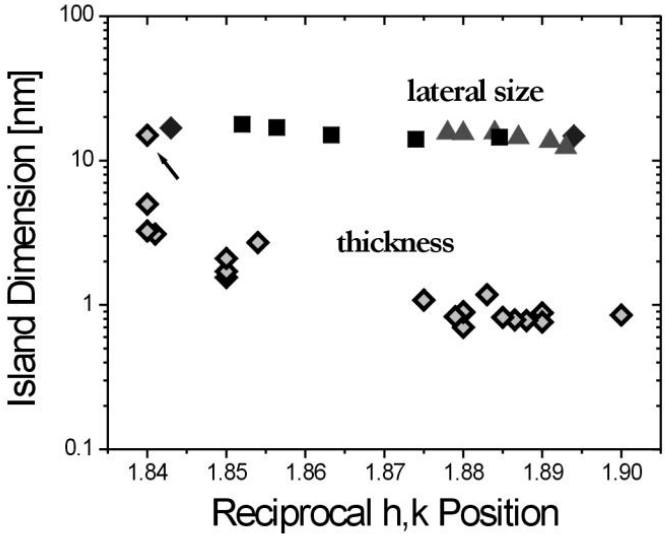

Figure 10.16: The width of the in-plane (HK) diffraction peaks is a measure for the lateral coherently scattering size, which can be associated with an average lateral island size (upper points). The same is true for the thickness (L or z-direction, lower points). During the growth the islands are not essentially increasing in lateral size (15 to 20 nm), but the island thickness is growing. The point indicated by an arrow is associated with a developing porous structure at long time scales (at elevated potentials) and will be presented later in more detail (Chapter 5.3, Fig.11.2).

in-plane peaks close to the pure Au position (thicker islands). In addition one data point is included that was derived from a specular scan (Fig. 11.2) and associated with a porous surface morphology developing for an elevated potential and longer time scales (1-3 days). This was observed with ex-situ AFM images and the thin islands seem to develop then further to a porous structure with an isotrop average shape, i.e. the peak widths or the respective sizes are about the same in all directions. This measurement will be presented later (Chapter 5.3). T

The growth of the passivating layers (below E_c) in our in-situ cell is not homogeneous on the sample. At a point in the experiment, where we observed both the peaks of the two structures occurring during the Cu dissolution, we could measure the respective lateral distribution of their intensity. In Figure 10.17 the sample surface was moved lateral and transversal to the incoming beam, while the detector position and sample orientation were set on the initial peak and on the bulk gold peak positions, respectively. The intensity originating from the illuminated stripe (the footprint of the incoming beam) on the sample, reveals, that the occurrence of both structures is correlated: A maximum of the bulk-Au

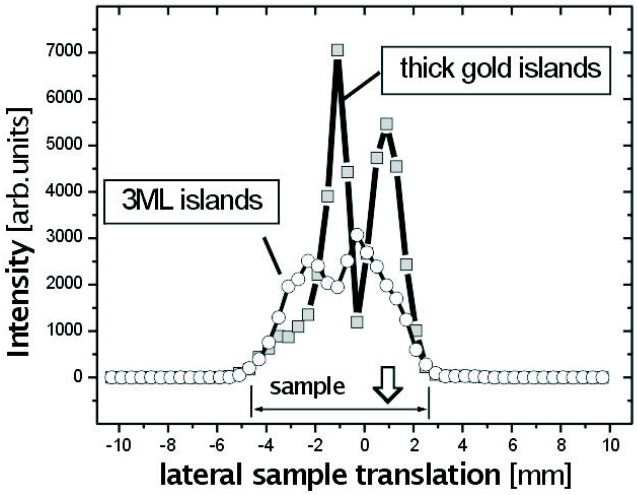

Figure 10.17: X-ray diffraction is averaging over the illuminated area. With both peaks visible a translation of the sample reveals that the maximum of the pure Au peak is correlated with a minimum in the initial peak intensity.

peak intensity is at a point of low intensity from the ultra-thin surface layer, and vice versa. We conclude, that the growth of the passivating layers (below E_c) in our in-situ cell is not homogeneous on the sample. This might be a result of a non-homogeneous electrolyte thickness in the thin-layer X-ray cell or might be influenced by a non-homogeneous defect distribution on the sample, which influences the nucleation of further dissolution.

At the end of this section, we want to discuss now the values of the lattice parameters that can be deduced from the measured Bragg peaks. These values are shown in Figure 10.18 as a plot of the out-of-plane atomic layer distance versus the in-plane atomic layer distance (in our case the $d_{001,s}$ (fcc-d_{111}) vs. $d_{220,s}$ (fcc-$d_{2\bar{2}0}$)). The crystalline structures, formed with the dissolution of Cu during our potential-controlled corrosion experiments, give rise to Bragg peaks and diffracted intensity along surface structure CTR's. Both, the HK-scans across the narrow in-plane Bragg peaks and the L-scans across the broad out-of-plane Bragg peaks can be fitted by a Gaussian peak. As the in-plane Bragg peaks are narrow the in-plane lattice parameter (d_{220}) can be deduced quite accurately. For the out-of-plane parameters deduced from the peaks originating in the observed ultra-thin layers, a large discrepancy for the values deduced from different Bragg peaks was observed (See Figure 10.12). The values deduced from the (1.9 0 L)$_s$-like rod were always lower than the values deduced from the (0 1.9 L)$_s$-like rods and becoming larger for higher L-values. The values deduced from the (0 1.9 L)$_s$-like rods were becoming smaller for higher L-values. Therefore, in the case we measured both rods, we could estimate an extrapolated value as the deviation seemed to vanish for higher L-values. These estimated values for the ultra-thin layer are shown in Figure 10.18 a (open squares), with the error bar determined by the peaks at highest available L-value of the (1.9 0 L)$_s$-like (the lower end) and (0 1.9 L)$_s$-

like rods (the upper end). The black circle indicates the values for the Cu_3Au substrate (a_0=0.375nm) and the filled small squares are obtained from the Au structure that is observed at elevated potentials. All new crystalline structures that were observed after the dissolution of Cu from $Cu_3Au(111)$ show lattice parameters much closer to the expected pure and relaxed (cubic) Au position than to the substrate values. While the parameters deduced from the ultra-thin structures that are observed at lower overpotentials (open squares) are still distinctively away from the cubic bulk Au position, the values obtained at the elevated potentials are essentially like pure or nearly pure bulk Au. From their in-plane position a content of 0-10% of Cu can be estimated.

Also added to the plot is the line for biaxially strained Au(111) overlayers with stain along the (111) plane. Such biaxial stain commonly emerges during the growth of thin layers on a symmetric mono-crystalline substrate, e.g. a (111) or (001) oriented cubic surface. When, like in our case, the overlayer bulk lattice has a larger unit cell, the thin overlayer is often under tensile stress, i.e. the lattice constant along the interface tries to adopt the smaller substrate lattice by an in-plane compression and the distance in the z-direction is then relaxed to larger values. This stress relaxation is governed by the elastic constants of the respective material and is dependent on the orientation of the crystal lattice with respect to the strain directions. A short description is given in Appendix **??**. Another issue is the question, if the values for the (bulk) elastic constants are unaltered (with respect to bulk material) for an ultra-thin film of a thickness of only two or three monolayers, where all the atoms are essentially surface atoms. In the literature often the bulk value is used even for such ultra-thin layers or surfaces [st94]. Although Wolf [wo91] calculated the equilibrium lattice parameter value for ultra-thin free-standing Au layers to be considerably altered , no information of the elastic constant is given. We added the position marked with "w" in Figure 10.18 a, which was taken from his paper for a layer thickness of about 1nm.

Figure 10.18 b shows the values deduced from the diffraction data of mainly (0 1.9 L) L-scans, shown before in Figure 10.11. With ongoing dissolution/higher potential the structure is clearly developing towards a more relaxed state ("cubic line" for relaxed (bulk) Cu-Au alloys with different composition). Here only for the first data point, L-scans along both rods, as described before, have been measured and a extrapolated value could be determined. The data shown in both Figures is in agreement with the interpretation of a strained pure Au layer by using the bulk elastic constants. The exact elucidation of strain/stress is not possible, as no knowledge about the equilibrium state of an ultra-thin Au layer on-top of $Cu_3Au(111)$ is available to our knowledge.

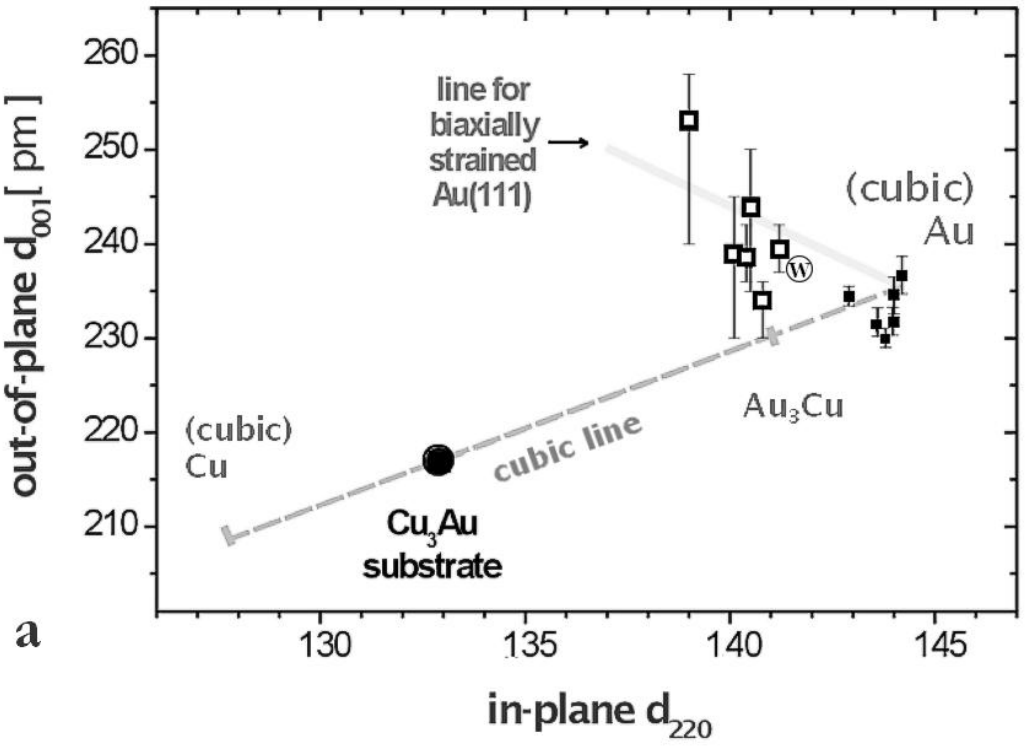

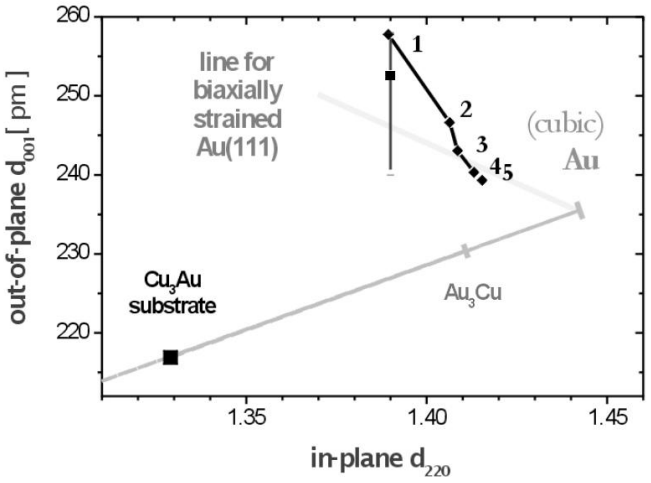

Figure 10.18: In-plane and out-of-plane lattice parameters as deduced from the peaks along the (1.9 0 L)$_s$-like and (0 1.9 L)$_s$-like rods. (a) shows the values as estimated by considering both rods. 'w' marks the equilibrium lattice parameters for an 1nm thick Au(111) film as calculated by Wolf [wo91].(b) shows the values as obtained from the (0 1.9 L)$_s$ L-scans presented in Figure 10.11 and shows the development of one structure with time/potential.

10.2.3 Conclusions for Chapter 10.2

In our observations during the selective dissolution of Cu from $Cu_3Au(111)$ in 0.1 M H_2SO_4 at potentials below the critical potential E_c, we observed two main structures that were developing in two separate potential ranges. Firstly, at low overpotentials an ultra-thin layer covers the surface. The in-plane and out-of-plane lattice constants do not correspond

to the values of bulk Au or bulk Cu-Au alloys. If deviations in composition of the layer, residual strain from the growth process or effects of the very much reduced dimension of this ultra-thin structure are causing this deviation is not finally settled. A fit to CTR data obtained from such an ultra-thin structure revealed a model with two atomic monolayers of Au (while a Cu content in the layers is not excluded) with a partially occupied third and fourth layer. The fit is sensitive to the structural parameters, like the number and occupancy of atomic layers, but less to the composition. L-scans along this ultra-thin structure rods, showing small differences in width, suggested that this layer is growing between approximately 2 and 5 monolayers, if the potential is increased slowly. Secondly, at higher overpotentials (but still well below the critical potential), thicker islands of pure or nearly pure and relaxed Au (bulk lattice parameters) were formed, and at the same time the corresponding peaks for the ultra-thin layer are vanishing. These Au islands are then immediately about 10 ML thick. For a fast increase of potential in the elevated overpotential range we observed a continuous shift of the lattice parameter of the surface structure towards the Au bulk value.

The position (L-value/z-direction) of the recorded out-of-plane diffraction peaks, along the non-equivalent $(1.9\ 0\ \mathrm{L})_s$ and $(0\ 1.9\ \mathrm{L})_s$ rods in reciprocal space, revealed a systematic deviation of the deduced values. With higher L-value the deviation was smaller. The origin of this behavior is not clear yet.

10.3 Surface Structure Rods

The usual way to measure a CTR is by performing (transversal) rocking scans and subsequently integrating the measured intensity. The background and the effect of different peak widths (which results in a smaller relative peak height for the same integrated intensity) are, in this way, correctly taken into account. The technique of CTR measurements has been explained in Chapter 4.7. Recording a CTR is more time consuming than a simple L-scan but the obtained information is more reliable. Data obtained in this way can directly be compared to kinematical calculations and therefore the measurement of CTR's has to be applied when detailed structural information is desired. Nevertheless, in some systems it might be feasible to measure only L-scans [tor04]. We measured CTR intensity distributions of the new surface structure during several beamtimes. Figure 10.10 showed one example for a measurement, where also CTR's were recorded. In this experiment, we we measured at +135 mV a $(1.92\ 0\ \mathrm{L})_s$ rod and Figure 10.19 a shows the obtained data points. As the diffraction peak intensity of the new layer was still low, and the measurement took accordingly a long time, the potential was slowly further increased, trying to obtain a higher peak intensity. Figure 10.10 shows that a big increase in intensity took place when reaching a potential of +270 mV. The in-plane position moved from $(1.92\ 1.92\ 0)_s$ to $(1.89\ 1.89\ 0)_s$. At this stage, the measurement of the $(1.89\ 0\ \mathrm{L})_s$,

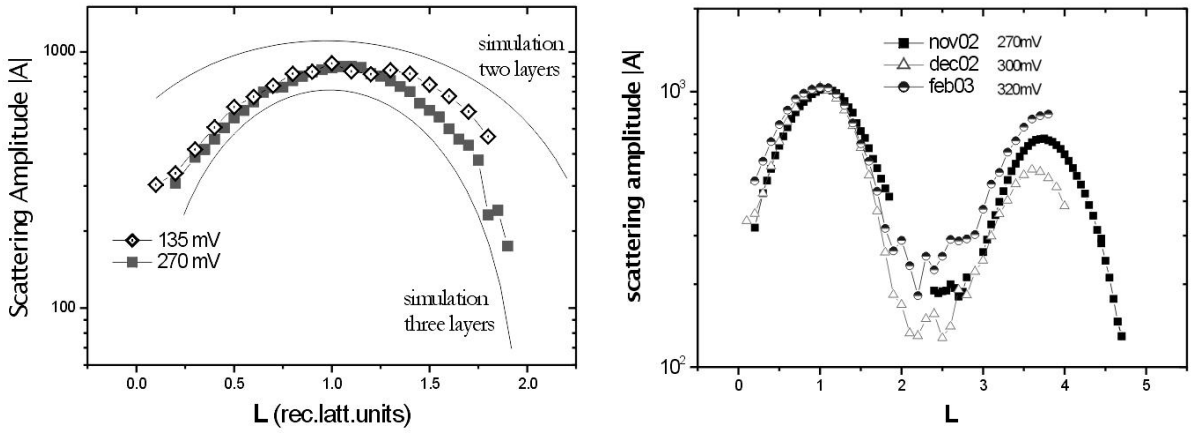

Figure 10.19: The rod at 135mV is wider than the 270mV rod. The center of mass is also shifted. The right graph shows the rods obtained from the new surface layer in three different experiment periods. The data has been corrected also for a 10 μm thick water layer. The data labelled with "dec02" was corrected by the program ANAROD [vl00] and scan by scan using the usual correction factors.

the $(0\ 1.89\ \mathrm{L})_s$, and the $(1.89\ 1.89\ \mathrm{L})_s$ layer rod was completed. Similar rods of the new

epitaxial layer have been recorded during four different experiments at potentials between 270 mV and 350 mV ($Ag^+/AgCl$). In this range of potentials, the new ultra-thin structure develops and is finally stable for a given potential for the timescale of an experimental run. The part of the rod recorded at the lower potential of 135 mV is slightly broader than the rod at 270 mV. These two data sets are compared in the range between L=0 and L=2 in Figure 10.19a, together with two curves obtained from simulations with ANAROD [vl00] for a three and a two mono-layer thick film. For comparison, the scattering amplitudes of the data have been scaled to the same maximum intensity and the calculated curves have been shifted to fit under and above the data points. All the other rods, measured at the potentials between 270 mV and 350 mV, look very similar in their shape with respect to the width of the scattering amplitude distribution. The data for the measured surface structure rods (low overpotential region) is shown in the Figures 10.19b and 10.20. The scattering amplitude or the intensity ($I=A^2$) is a smooth function of the L-position on all rods. This is expected for a homogeneous ultra-thin film and can not be explained, e.g., by an inhomogeneous set of surface regions with a variation of lattice spacings (e.g. with varying composition or different structures).

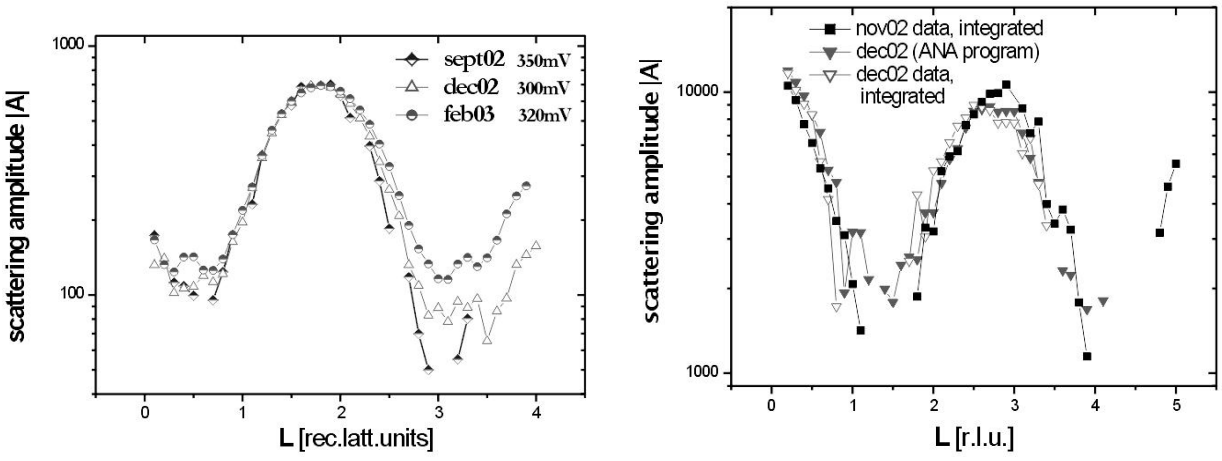

Figure 10.20: The $(20L)_s$ (left) and the $(22L)_s$ rods obtained from the new (ultra-thin) epitaxial layer in three different experimental runs/beamtimes. The data has been corrected also for a 10 μm thick water layer. The potential of each of the rod measurements was in the low overpotential region.

For the measured range, the $(1.9\ 0\ L)_s$ rod includes two maximums at $L \approx 1$ and $L \approx 3.7$. This is remarkable, because for a first peak at L=1, the second peak of an fcc-like structure would be expected at L=4. These deviations were discussed above (Fig. 10.12).

The position of the first and second maximum, respectively, is not exactly the same for the different experiments, but the variations are relative small. Also the ratio of the maximum values on the two peaks is different. A decrease in intensity for Bragg peaks with increasing q-vector (in different runs) can be understood on the basis of a Debye-Waller factor, that can account (besides temperature dependent vibrations) for a static disorder of the structure (atomic displacement parameter; for the nomenclature, see [Tru96]). Static disorder or in other words, statistically distributed strain fields would be expected for a defect rich layer and because of the incoherent interface, due to the different in-plane lattice constants of substrate and the ultra-thin new layer. Figure 10.8 shows that if two hexagonal layers with different in-plane atomic distances form an interface, a modulation (sometimes seen as moirée pattern in STM studies) of z-distances and lateral corrugations is likely to arise, because of the occurrence of different relative positions of the respective atoms. These different coordination positions (e.g. fcc, hexagonal or on-top positions) can have a big energetic difference, especially the on-top position is energetically very unfavorable. One beautiful example for the richness of disorder or reconstruction of such an interface was published at the time of the final writing of this manuscript (STM image of Ag(111)/Ru(0001))[li04]. Stress and modulations might also cause peaks to become asymmetric and can change the relative peak intensities at higher q-value [za].

Simulation of the Surface Layer Rods

As the data for the respective rods, measured in the different experimental runs, were similar, a representative set of all measured data was chosen for the simulation the new surface structure. Here we will discuss the results for the simulation of this set of the CTR scattering data.

Element	Interlayer Spacing	Occupancy
(top) Au, 1.layer	– 242 pm –	5±2%
Au, 2.layer	– 220 pm –	45±3%
Au, 3.layer	– 222 pm –	100±6%
Au, 4.layer		100% (fixed)
Au, bulk	235.4 pm	
Cu_3Au, bulk	216.7 pm	

Table 10.4: Results for the parameters of the simple fcc model for the ultra-thin new structure observed with the initial dissolution of Cu from $Cu_3Au(111)$.

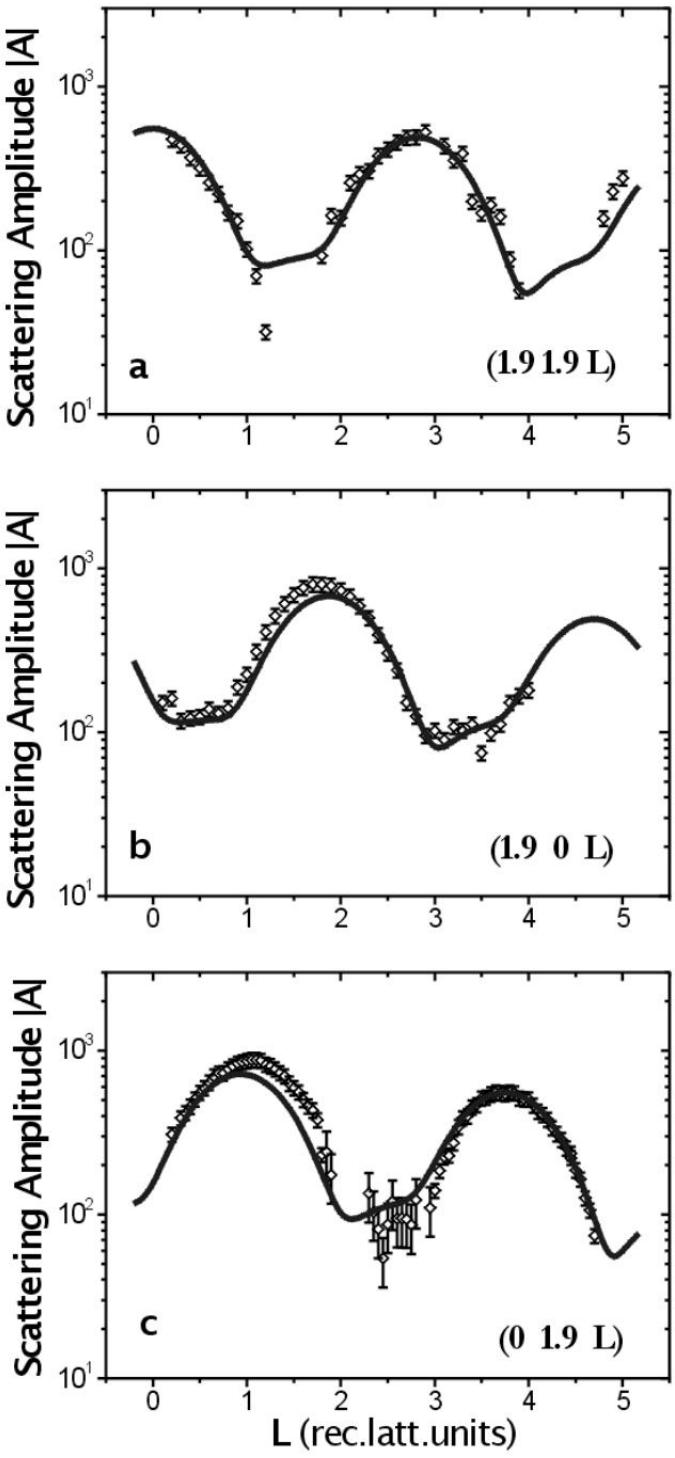

Figure 10.21: The new structure rods have been measured in coordinates of the $Cu_3Au(111)$ surface. The curve is the four-layer fcc model listed in Table 10.4.

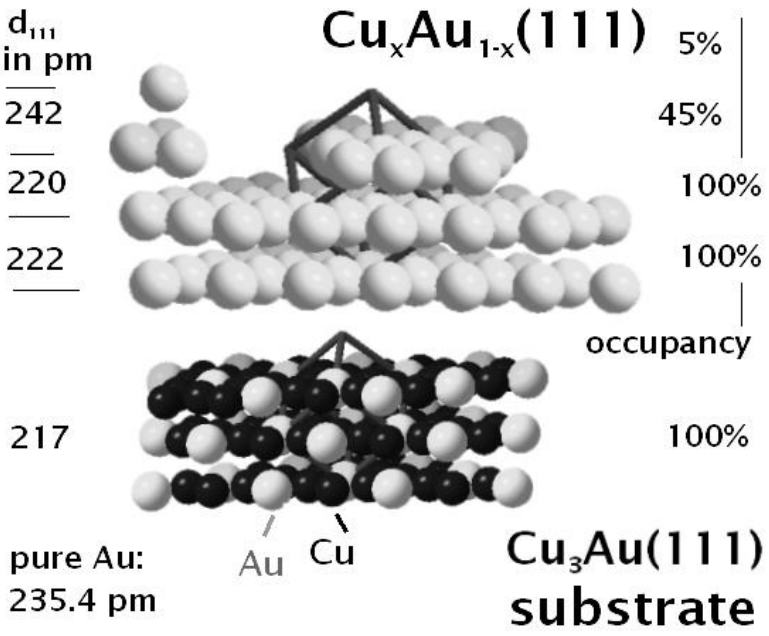

Figure 10.22: Real space model (after model in Table 10.4) with mainly 2 monolayers of pure Au and one partially occupied top layer of Au on-top of the substrate $Cu_3Au(111)$ formed after initial dissolution of Cu at lower overpotentials. Similar fits to the rod data were obtained for a homogenous Cu content.

We started the simulation by fitting the parameters for the layer occupancy and the layer separation for models with several Au layers with a defined fcc stacking (thereafter called "simple fcc model"). Although Cu and Au differ by their number of electrons we were not sensitive to the chemical composition, as we did not obtain the data on an absolute intensity scale and an overall scale factor was used to fit the calculations to the measured intensity level. The small difference in the shape of the atomic form factor (Fig.4.2.1) was outnumbered by the effect of possible different z-displacements for the two elements. For that reason we performed the calculations with Au atoms only, but we note that a certain Cu content in the layer is possible. The width of the CTR peaks where best fitted by 2.5 atomic monolayers, i.e. the third (top) layer occupancy is close to 50%. A fractioned occupancy of an additional fourth layer on-top of the incomplete 3 ML was used to damp out the intermediate maximum of an Laue oscillation occurring for smooth thin layers. For three smooth atomic monolayers we would expect one intermediate Laue oscillation peak on the intensity scale we were able to detect with our signal to noise ratio (Fig. 4.8). We did not observe such an oscillation.

The values for the parameters obtained from fitting the simple fcc model to the data

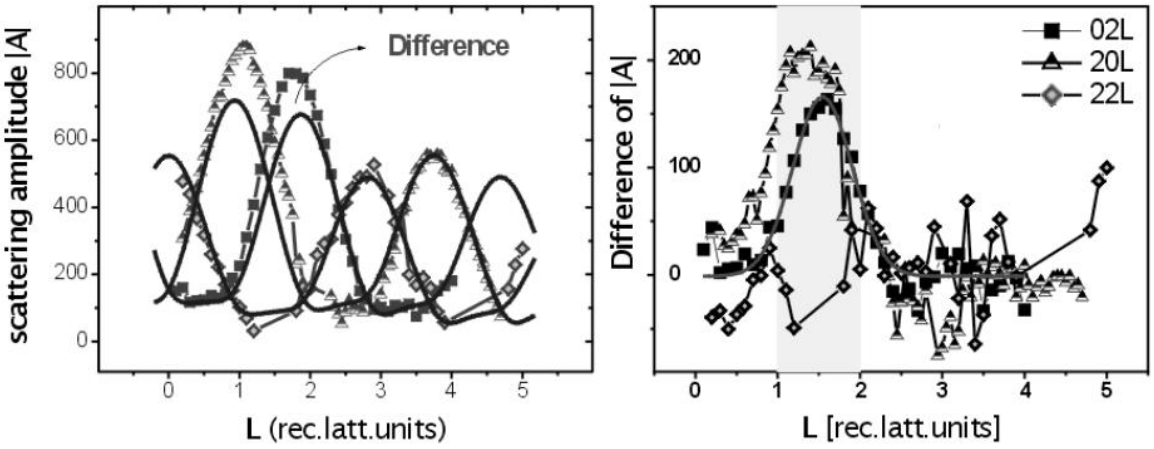

Figure 10.23: The plot shows the calculated difference of the measured CTR data and the calculated curve obtained for the simple fcc model. While the higher peaks are fitted well, a considerable systematic deviation is seen by a peak in the difference at L=1.5 for the $(1.9\ 0\ L)_s$ rod and the $(0\ 1.9\ L)_s$ rod.

are listed in Table 10.4 and a real space model is shown in Figure 10.4. While the maxima at L=3 and L=4 along the $(0\ 1.9\ L)_s$ and the $(1.9\ 1.9\ L)_s$ rods, respectively, are fitted well, the maxima at L=1 and L=2 along the $(0\ 1.9\ L)_s$ and the $(1.9\ 0\ L)_s$ rods, respectively, a considerable systematic deviation is seen. Both peak maxima are moving towards L=1.5. L=1.5 is the L-position were a hexagonal (hcp) structure, with the same lattice plane spacing, would have a Bragg peak along the $(0\ 1.9\ L)_s$ and the $(1.9\ 0\ L)_s$ rod. However, such a hexagonal structure would also contribute at L=3. The difference of the $(1.9\ 1.9\ L)_s$, $(1.9\ 0\ L)_s$ and the $(0\ 1.9\ L)_s$ rod and the simulation for the simple fcc model of the four fcc Au layers (Fig.10.21 d and 10.23) is plotted. The deviation is centered with a peak at L=1.5. This deviation can not be explained by a contribution of domains with a different stacking, i.e. abc instead the acb observed on-top of our ABC substrate. Figure 10.24 shows, that we easily could distinguish such a contribution up to 10%. In addition to the data and the fitted curve of the simple fcc model, presented above, two curves with an additional, incoherent contribution of respectively 10% and 50% of the twin domain are added. Comparing with the data we can exclude the presence of more than about 3% of such twin domains with the parallel epitaxial alignment. In Figure 10.12 we have seen that also for the peak at higher L-value a deviation from a pure fcc model is present, which

can be understood only by a model which includes features that are different from a pure fcc model. The plot in Figure 10.23 shows the difference of the model calculation and the measured CTR data points as a function of L. We have also to consider, that the L-scans that were shown in Figure 10.12, revealed a systematic deviation, present also at the second maximum along each of these two rods. In addition, possible regular interface modulations and/or reconstructions would make it necessary to use a larger unit cell. However, since we do not have CTR data of the second peak along the $(1.9\ 0\ \mathrm{L})_s$ rod, and because of possible complications due to strain in the thin film structure and at the heterophase interface, it is impossible to find a more detailed model with the present, limited dataset. Nevertheless, it became clear that a simple fcc (ultra-thin) model explained the data quite well. A contribution of a fcc-twin domain or of hexagonally coordinated islands/domains could be excluded.

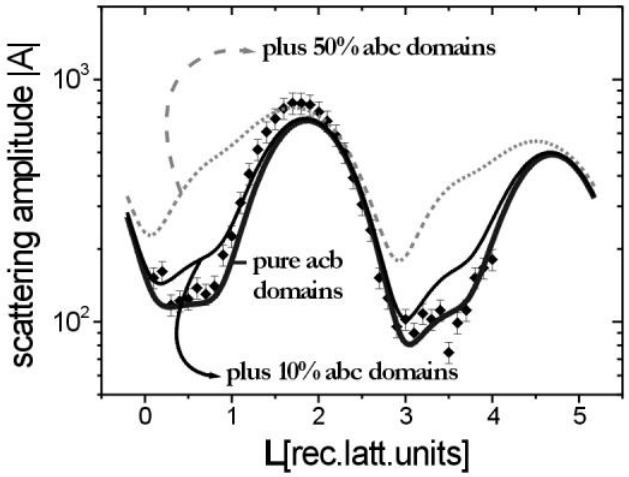

Figure 10.24: The occurring deviation from a pure fcc model can not be explained by adding a contribution from stacking faulted domains.

10.4 Initial Selective Dissolution: Substrate CTR's

The study of the $Cu_3Au(111)$ surface in UHV, which we described above, demonstrated the capabilities of the method of CTR measurements. For a detailed analysis of the structure it is necessary to include the measurement of several non-equivalent rods to obtain a reliable fitting of the parameters of a structural model to the data. A detailed structural analysis requires therefore time consuming measurements and a surface structure, that is stable during this period of time. Nevertheless, by comparing a single CTR, taken at subsequent stages of an experiment, it is possible to discern relative changes in the structure. Especially a roughening of the surface leads to a significant decrease of the intensity compared to the, e.g., $1/(\sin L)^2$-like drop of the CTR for a smooth truncated crystal surface or any other CTR for a structurally different smooth surface. In this way the measurement of one CTR can be used to monitor the actual state of roughness of the surface, compared to an initial surface structure.

Results

With the initial selective dissolution of Cu from Cu_3Au, a new modified surface structure arises, with a lattice constant different from the substrate, as was described in the preceding chapters. In all in-situ electrochemical corrosion experiments we measured also substrate CTR's, which are sensitive to the substrate surfaces, i.e. to the interface structure. The sample for each experiment has been prepared, as described previously in detail, by sputter-annealing cycles in UHV before it was transferred through air and mounted in the in-situ electrochemical X-ray cell. For the measurements of the $L1_2$ superstructure and fundamental rods, the sample had been annealed at a temperature of 360°C, i.e. 30°K below the order phase transition temperature T_c, for periods of typically 12 hours. T_c was in these cases determined in the mobile X-ray diffraction chamber described in Chapter 5.1 by means of X-ray diffraction (of an $L1_2$ superstructure peak). The subsequent ordering was performed and observed in the same chamber. In this way we could control the true value of the temperature and obtain sharp superstructure reflections. Otherwise we obtained $L1_2$ elemental ordering of the Cu_3Au crystal in the UHV chamber at the ESRF, Grenoble without help of X-rays and checked the LEED image and the AES scans after cooling down, which indicated a clean and ordered crystal surface (within the resolution of the LEED image). Since in this case we could not precisely determine T_c the resulting superstructure peaks remained broad (typically in the order of 1° and more for an angular rocking scan).

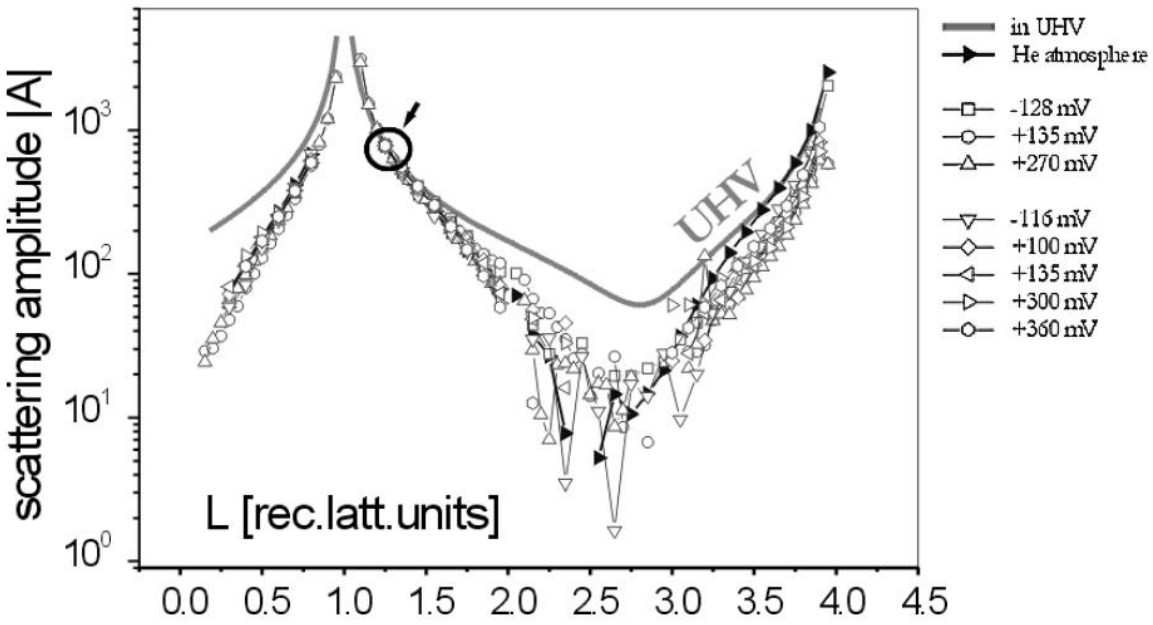

Figure 10.25: The $Cu_3Au(111)$ substrate fundamental $(02L)_s$ CTR's obtained in He atmosphere and after immersion in 0.1 M H_2SO_4 electrolyte solution. The applied potentials were in the range from -128 mV to 360 mV. The curve for model 2 from Figure 10.2 obtained from measurements in UHV is also included (UHV). The samples have been prepared in UHV and transferred through air into the X-ray cell. After transfer no further roughening is observed, even with ongoing Cu dissolution. All curves are scaled to the same scattering amplitude at L=1.25 (marked with arrow).

In some cases, a substrate CTR was measured with the electrochemical cell filled with He gas, before filling it with the electrolyte solution. All data obtained for the case of an He atmosphere and for several applied potentials with the crystal surface immersed in 0.1 M H_2SO_4 solution are included in Figure 10.25 for the fundamental $(02L)_s$ rod and in Figure 10.26 for the $L1_2$ superstructure $(10L)_s$ rod. Similar data have been obtained also for the $(11L)_s$ rod (data not shown). The applied potentials were in-between -128 mV and 360 mV and covered values below the initial Cu dissolution potential (See e.g. the Voltammogram in Figure 9.2) and in the low overpotential region. The data have been corrected for the usual correction factors and in addition for the exit-angle dependent absorption in the 6μm thick mylar foil and an estimated 10μm thick aqueous electrolyte (water) layer. All rods have been scaled to the same intensity/amplitude at one L-point, which is marked by an arrow in the Figures. The absolute intensity can not be directly compared due to possible

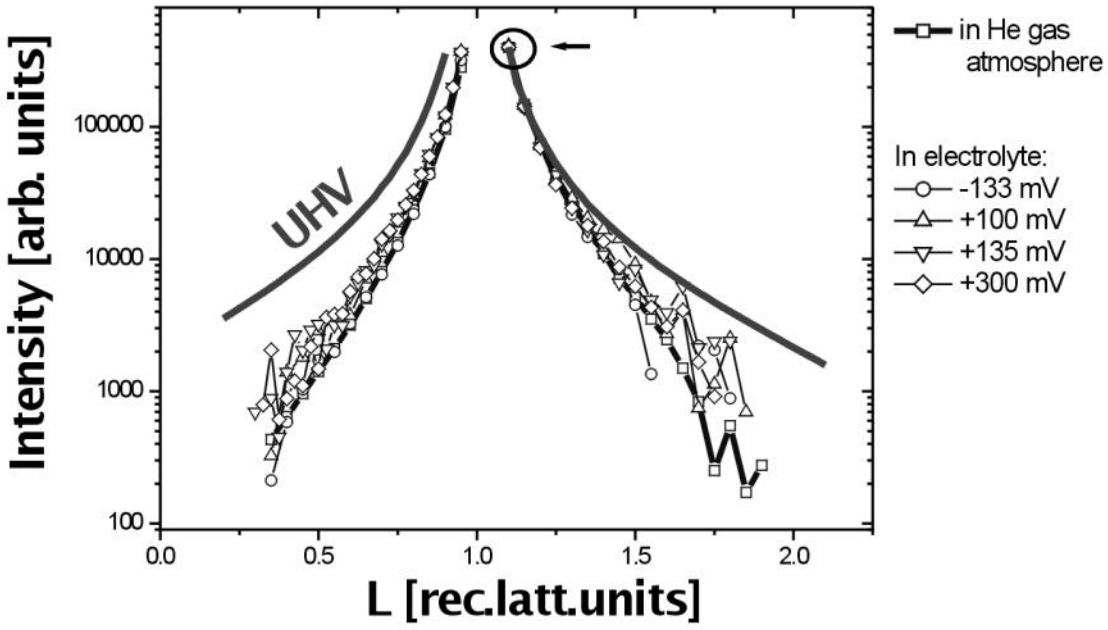

Figure 10.26: The $Cu_3Au(111)$ substrate $(10L)_s$ $L1_2$ ordering CTR's (here intensities are shown) obtained in He atmosphere and after immersion in 0.1 M H_2SO_4 electrolyte solution. All curves are scaled to the same scattering amplitude at L=1.1 (marked with arrow).

changes in the electrolyte thickness and the different incident photon flux at the various beamlines and because of the different X-ray energies used.

Discussion of the CTR data in electrolyte

With the first exposure to ambient air of the UHV prepared Cu_3Au samples, we observed a change in the CTR, compared to the UHV data. This is revealed by the measurement in He atmosphere, after the transfer through air into the X-ray cell. Besides a small change in the shape of the intensity distribution along the CTR an increase in roughness is observed. Due to the contact with ambient air, it is likely that a thin film of water molecules is condensed from the surrounding moist atmosphere on the surface. This might cause, along with a physiosorption of water molecules, small changes in the surface relaxation, i.e. the minimum of the rod is shifting. Furthermore, if the alloy sample is in contact with a liquid film, a first dissolution of Cu might take place, in order to create equilibrium conditions with the initially Cu-free water layer. Another possibility is an initial oxidation processes at room temperature, occurring with the exposure to the oxygen contained in the air.

This initial Cu oxidation and/or Cu dissolution explains the increased roughness after the contact with ambient air. The sample was immersed into electrolyte at potentials below the onset of dissolution, as estimated from the initial peak in the voltammetry (Fig. 9.2). No further increase in roughness is observed at that point, neither along the fundamental CTR, nor along the $L1_2$-ordering CTR. Astonishingly, even with further increased potentials, with values in the range where initial Cu dissolution is taking place, also no further increase of roughness is observed. Note, that during these experiments and at these potentials, the formation of a new, Au-rich surface layer, with a different lattice constant from Cu_3Au, is observed, as will be described in the next Chapter (which is a clear sign, that Cu dissolution indeed takes place). We show in Figure 10.27 also data obtained at an elevated potential, still far below the critical potential E_c.

Despite small variations all measured rods lay essentially on-top of each other. In Figure 10.25 the calculated amplitudes from model 2 for the clean surface in UHV, which was described above, has been added. In comparison to the UHV data, the minimum of the CTR amplitudes is slightly shifted in L (from approximately L=2.8 to 2.7) and the overall intensity/amplitude level is decreased along all the measured rods. Comparable to the faster drop of the specular reflectivity of a surface ($[00L]_s$ rod) in the case of roughness, also the CTR intensity, which has been described above drops off faster if the roughness is increased. For the $Cu_3Au(111)$ surface exposed to electrolyte this is described in Figure 10.27, where the numerical evaluation of the roughness is performed. For comparison the CTR for the UHV prepared/measured surface is shown (I). Using the numerical β-model of the ROD software [vl00] to account for the roughness, we can approximately reproduce the measured data by the model 2 for the UHV surface, which has been described above, plus a β factor, which is for the electrolyte and the He exposed surfaces in the order of =0.56 (II). The dramatic increase of roughness if progressing to further more positive potentials is also exemplified (III). In this case the potential was increased to a value of 400 mV and a much increased pure Au peak was observed afterwards. Because of the limited amount of samples and beamtime we could not confirm the behavior of the CTR at these elevated potentials. A fit to these data points revealed a β-factor of 0.95, which is very rough.

We see clearly, that ongoing corrosion leads to a major increase in roughness. The fact, that there is no increase in roughness with the ongoing initial selective Cu dissolution at relatively low dissolution potentials, indicates that the dissolution itself does not further increase the roughness and leaves a smooth surface. This could be understood by a dissolution process, which resembles a (negative) step-flow process, which is well known to occur on surfaces treated in UHV. This conclusion is similar to the results of an in-situ electrochemical STM study recently published [ec01] [str01]. This observation is for the

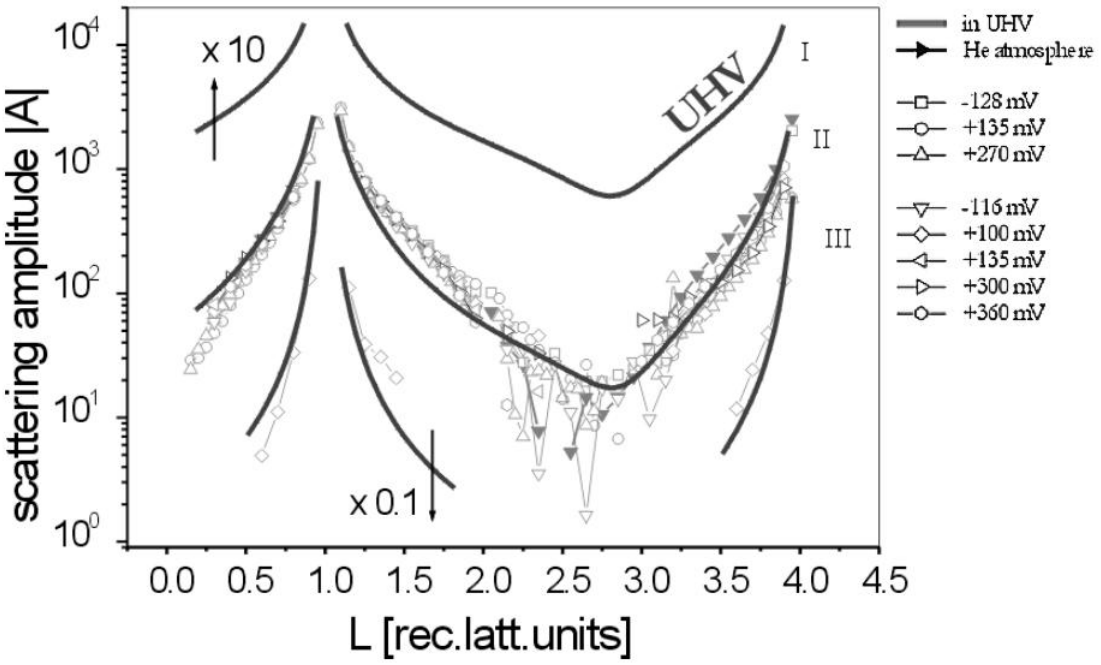

Figure 10.27: After UHV preparation and transfer through ambient air an increased roughness is observed in comparison to UHV data. The fit for model 2 from Figure 10.2 obtained from measurements in UHV is shown (UHV) and shifted upwards for clarity.

fundamental and the $L1_2$-ordering CTR the same. In addition, we observe the build-up of a new Au-rich structure along with the initial Cu dissolution. Surface diffusion must therefore play a major role in the dissolution process.

We have to consider here that the thickness of the electrolyte layer could not be exactly controlled, and small changes in intensity with different measurements might occur. Nevertheless, with the very rough surface at this stage changes of the rod profile due to structural differences are less easy to observe. This is illustrated in Figure 10.28, where 30% (a rather high number) of the Cu atoms have been removed from the top three layers of the $Cu_3Au(111)$ model (model 2) of Chapter 10.1. The curves calculated for this depletion of Cu is shown in addition to the curves with the fully occupied layers. While for the surface without roughness the occurring oscillations are clearly distinguished, the rough curves shows pronounced differences only close to the minimum. At the position of the minimum our measurements are showing no clear intensity peak anymore and the measured integrated intensity is thus inaccurate or missing. We obtain from these measurements the general increase in roughness, but no further structural information.

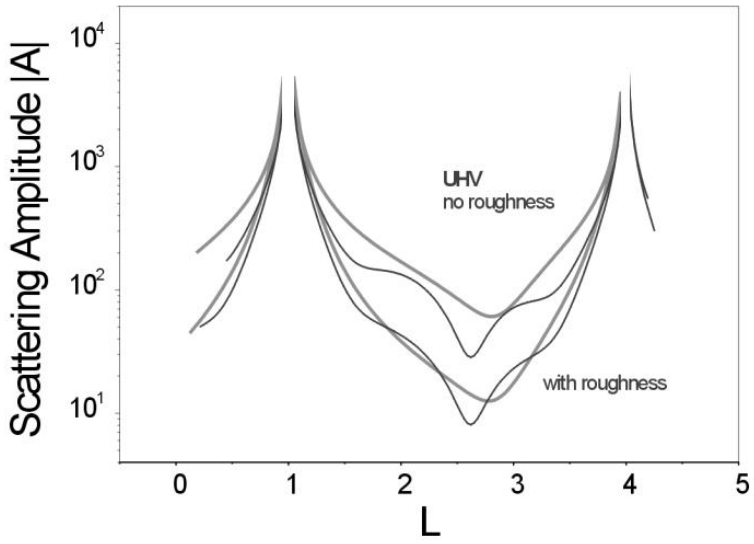

Figure 10.28: A calculation of the respective CTR for 30% of the Cu atoms removed from the first three layers. The curve for model 2 from Figure 10.2 is also shown. In the case of large roughness the curves are difficult to distinguish in a measurement.

Conclusion for Chapter 10.4

After the transfer through air the roughness of the surface was already much increased compared with the surface in UHV. The CTR data did show no further increase of the surface roughness with the initial dissolution process at lower overpotentials. Only at higher potentials a large increase in roughness is observed. As we described before, thicker almost pure Au islands are formed in this potential region. For the detection of further structural details by measuring CTR intensity, like e.g. an increase of defects in the substrate lattice due to Cu dissolution, the surface/interface was too rough to obtain conclusive data.

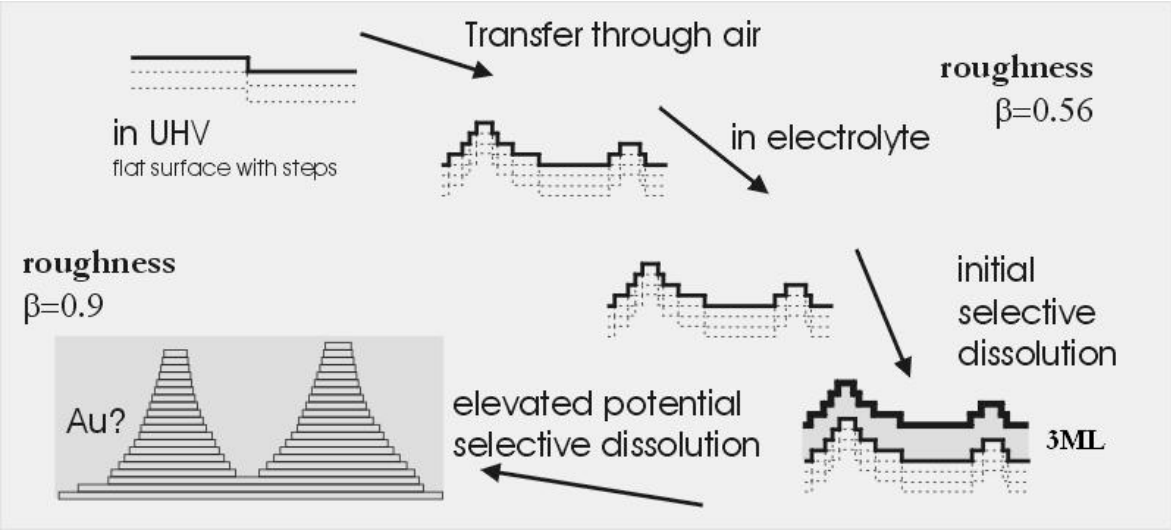

Figure 10.29: The fact that the substrate CTR data does not considerably change during the initial dissolution process at lower overpotentials indicates that the roughness is not changing, i.e. the surface morphology is essentially not altered. Only with higher potentials (close to the critical potential E_c) a large increase in roughness is observed.

10.5 Energy Dependent X-ray Scattering at the Cu K-edge

With the method of X-ray diffraction we could observe structural details on the $Cu_3Au(111)$ surface during the selective dissolution of Cu at potentials below the critical potential E_c. Some questions remain. Why is the ultra-thin structure only stable at lower overpotentials? Does the ultra-thin film contain still Cu? Diffraction is primarily a method to examine structural features, especially (but not only) for crystalline materials and phases. Nevertheless, utilizing the adsorption edge/edges of the elements that built up the structure, also chemical information is accessible. The combination of both is called Dispersion Anomalous Fine Structure (DAFS).

In Chapter 4.2.3 we discussed the scattering behavior close to adsorption edges of the scattering elements. The atomic form factor can be written $f(E) = f_0 + f'(E) + if''(E)$ with the so-called real and imaginary dispersion corrections f' and f''. The value for f' is negative. Both correction factors are tabulated and are related to each other by a Kramers-Kronig transformation. In the corresponding formulas, the electron number of the atoms, when present, has to be replaced by an effective Z_{eff}, with $Z_{eff} = Z_0 + f'$. As a consequence, the scattering close to the edge gets weaker.

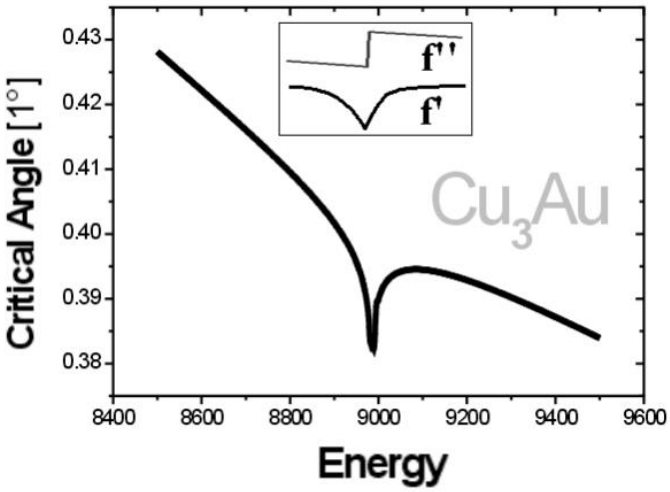

Figure 10.30: The critical angle α_c is becoming smaller with higher energy. At an adsorption edge of the material (f' and f'' are shown in the inset), α_c shows in addition a dip, caused by the dip in f' at the adsorption edge.

The energy dependent measurements, described in the following, were performed at grazing incident and exit angle above the critical angle and by recording an in-plane diffraction peak at different energies. We will first discuss the peculiarities of this chosen geometry, i.e. the refractive effects at shallow angles, exemplified for the case of a clean

Cu_3Au surface. With Z_{eff}, also the critical angle α_c is in general dependent on f'(E), and will show a distinct change close to the adsorption edge. For the case of Cu_3Au this is shown in Figure 10.30. By increasing the energy, the critical angle is becoming smaller with the smaller photon wavelength ($\alpha_c \propto \lambda$). If an absorption edge lies within the considered range of energies (f' and f" is sketched in the inset of Figure 10.30), α_c shows in addition a corresponding dip. For a smooth surface, with a pronounced peak in the transmission function T at α_c, this has consequences for the measured energy-dependent or anomalous diffraction intensity, as is exemplified in Figure 10.31 for our experimental conditions. The

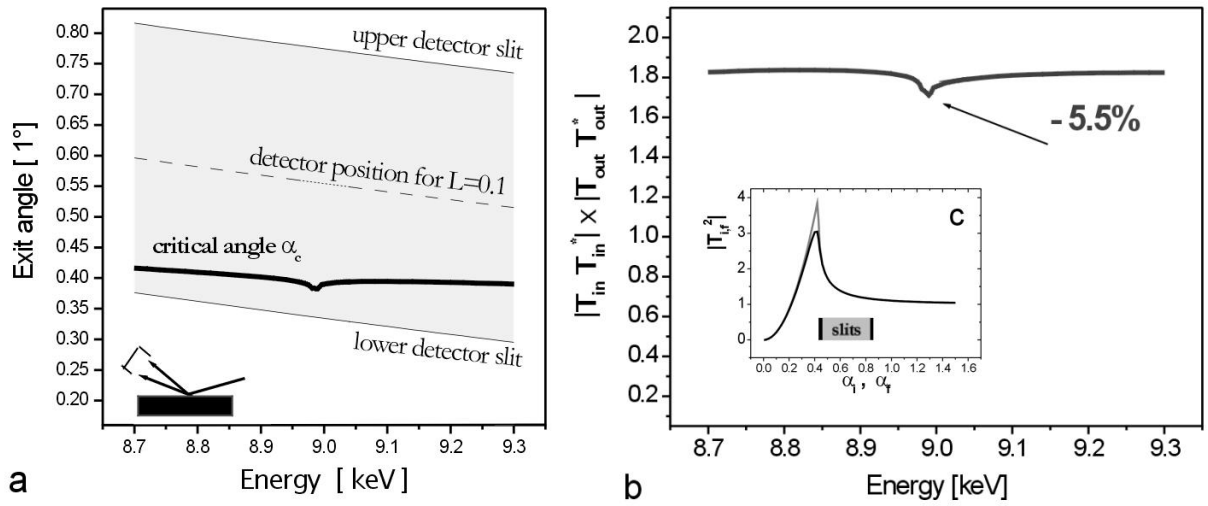

Figure 10.31: If the energy-dependance of an in-plane peak of an ideal Cu_3Au surface is measured with an incident and an exit angle close to the critical angle, the transmission function T shows also an energy dependance, which the data has to be corrected for.

intensity of the respective in-plane diffraction peaks is measured in our experiment at a fixed L-value of L=0.1. With higher energy, the exit angle for this special case (with fixed incident angle), as well as the critical angle, are becoming smaller. The angles covered by the grey area in Figure 10.31 a shows the range of exit angles, that is collected by the detector aperture (defined by the upper and lower detector slits) at the respective energy. In Chapter 4.3 we introduced the transmission function T (DWBA theory), and with the scheme, described above, we can calculate an effective transmission function for Cu_3Au by integrating the transmission factors for the exit angles collected in the detector over the ideal transmission curve (T for Cu_3Au is shown in the inset of Figure 10.31 b for E=8.5 keV (β=1.532×10^{-6}), together with the detector slit positions). For the incoming beam it is

sufficient to consider only the value of the transmission function at the incident angle, as the divergence of the synchrotron beam is small. The result for this ideal case is shown in Figure 10.31 b. The transmission, in this case, already exhibits a small dip of about 5%. Shown is the product of the incoming (in) and exit (out) squared transmission function ($T_{in}T^{\star}_{in} \times T_{out}T^{\star}_{out}$), which has to be multiplied by the respective scattering function (e.g. the square of the scattering amplitude) to obtain the diffracted intensity for a real case of diffraction from an atomic structure.

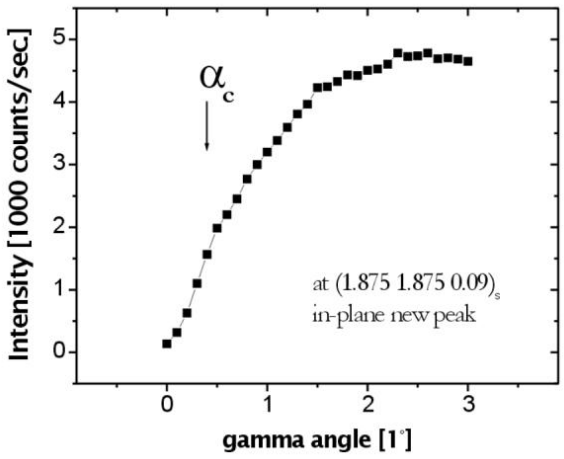

Figure 10.32: The scan of the exit-angle (gamma-scan)..

The previous consideration was based on an ideally flat and clean surface. However, the mosaic spread of the used crystal, or a present thin film or islands of a different material, roughness of the surface and, eventually, a disordered surface layer or defects within the surface region will cause deviations from the ideal transmission curve. For our experiment we could not observe a peak at α_c in an exit-angle scan of the ultra-thin overlayer, as it would be expected from an ideal surface as is shown in Figure 10.32. Therefore we will not correct for refractive effects. Nevertheless, we will include this effects in the error estimation in the discussion of the experimental results.

Experimental Results

The samples used for the experiments, which are described now, where prepared in UHV as described previously. The ordering, which was not monitored with X-rays, resulted in broad superstructure reflections. Typical measured energy-dependent curves are shown in Figure 10.33. The data were obtained from two samples. On the first sample, a peak at the expected pure Au position indicated, that a 3nm thick, pure or nearly pure, Au film was present on the surface directly after immersion to the electrolyte at -100 mV. With

this sample the energy dependence of the present peak at the expected Au-position at $(1.84\ 1.84\ 0.1)_s$ (curve A in Figure 10.33), and of a substrate peak at $(2\ 2\ 0.1)_s$ (B) have been measured with the potential still at -100 mV. The measured intensity is typically

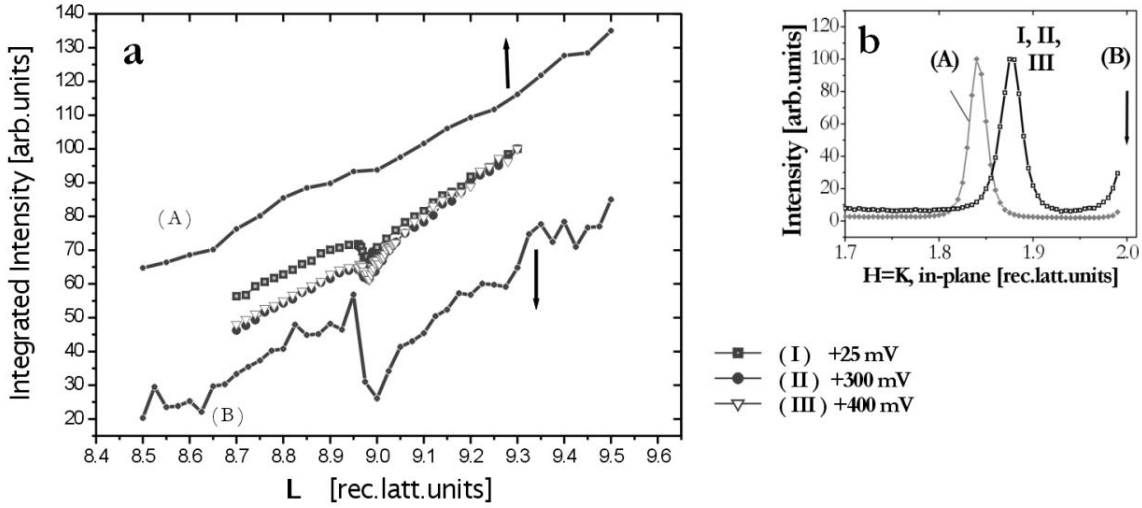

Figure 10.33: (a) The data were obtained by integration of rocking scans at different energies from two samples with different surface layers present. The curves A and B were measured at $(1.84\ 1.84\ 0.1)_s$ (peak A in (b) and $(2\ 2\ 0.1)_s$) (position B in (b)) with thick Au-rich islands present. The curves I, II, III were measured at different potentials on a sample with an ultra-thin Au-rich layer present. The overall inclination of the data originates in the energy dependent transmission of X-ray photons in different materials and is explained in more detail in the text.

increasing with higher energy due to then lower absorption along the pathway of the X-ray beam. Curve A was measured by using the mirror of the beamline to suppress photons with higher harmonic energies. The obtained curve showed variations from point to point of the measurement, that could not be attributed to the energy dependent form-factor of Cu as the expected shape e.g. at the start or the end of the curve was expected to be much smoother. Curve B was then measured without the mirror in place, but the variations in intensity were still large. The curves A and B represent the best data obtained during this first part of the measurement (first sample). Nevertheless, the data shows a clear dip for the Cu_3Au substrate peak at the Cu adsorption edge (E=8979 eV), while for the $(1.84\ 1.84\ 0.1)_s$ peak no such dip is observed at all (within the resolution of the dataset). For the second sample (Fig. 10.33, curves I, II, III; and Fig.10.34 b), we had moved the monochromator crystals relative to the beam, so that the X-ray beam was impinging on a different spot of the monochromator crystal surface. The intensity showed now a smoother course with changing the energy. After immersion of the new sample at -100 mV, a peak

at $(1.88\ 1.88\ 0.09)_s$ was already showing the presence of an ultra-thin epitaxial layer. At a potential of -100 mV also a peak at an expected Cu position was observed (close to $(2.08\ 2.08\ 0.1)_s$). As also the ultra-thin Au-rich layer was present, an Cu dissolution must have already taken place with the immersion into the electrolyte (for unknown reasons, but possibly due to an unstable potential during the immersion) and the dissolved Cu was then probably re-deposited onto the sample. We were increasing the potential to +25 mV in order to dissolve the respective Cu. At +25 mV the Cu-peak intensity decreased, and no Cu peak was finally observed. The energy dependence of the peak at $(1.88\ 1.88\ 0.1)_s$ was then measured on this sample at subsequent potentials of +25 mV, +300 mV and +400 mV. The data of these measurements are shown in Figure 10.33 I, II and III, respectively and clearly exhibits a present dip, located exactly at the energy of the Cu absorption edge of 8.979 keV and being smaller in magnitude compared to the effect for the Cu_3Au substrate peak (curve B). After correction for the absorption in the thin electrolyte film all three measured curves (I-III) were lying essentially on-top of each other. The in-plane peak emerging from the ultra-thin structure (Fig. 10.33 b) did also not change for the different potentials up to 400 mV. At 450 mV we then observed, by HK- and L-scans, the growth of an additional peak at the expected pure Au position (data not shown). This behavior was described in the previous section. However, the growth of this Au peak was not homogenous over the sample surface, as was revealed by scanning the sample laterally. We repeated the energy dependent measurement also for the new emerging peak, but we did not succeed to obtain a reliable data set . This might have been caused by the inhomogeneous growth and the fact, that the beam position is moving with different energies due to the monochromator movement). AFM images of the surface after the experiment will be shown in Figure 11.3.

Discussion

As already mentioned, the measured intensity is typically increasing with higher energy. This increase is determined by the energy dependent transmission of the X-ray beam through the materials in the path-way of the beam. An additional contribution comes from the monitor that we used to normalize to the incident beam intensity, i.e. the monitor signal (gas counter). Such a gas counter is utilizing an electrical current produced by the ionization of the gas atoms in the counter, which is also energy dependent, i.e. proportional to the (photoelectric) absorption. The monitor gas was in our case ambient air and the path inside the monitor was 0.18 m long. In detail, the corrections we applied to the measured intensities considered the path through 1 m of air, 0.5 mm of Kapton foil, and

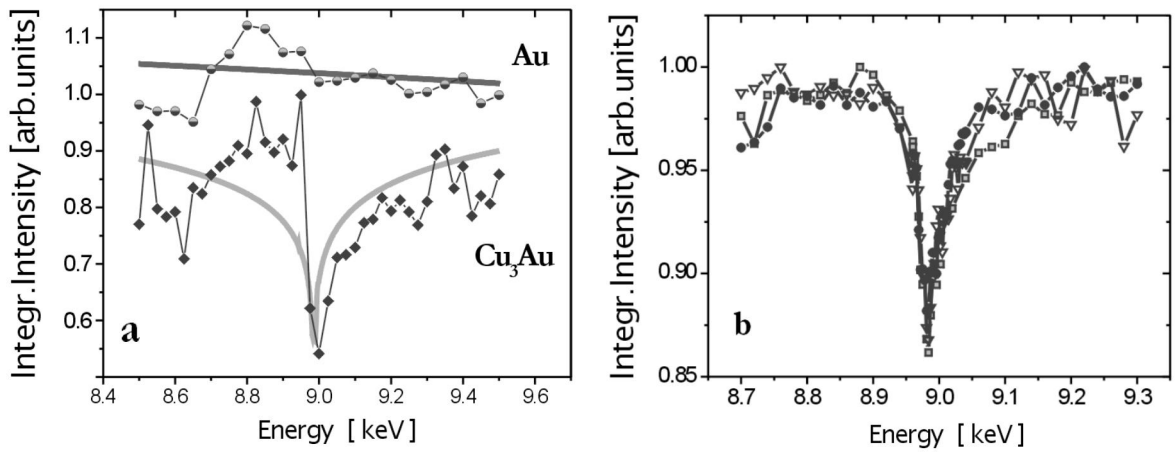

Figure 10.34: The data for the first sample (a) and the second sample (b) after correction. The basic tilt, i.e. the ratio of the intensity at lower and higher energy can be adjusted by assuming different thicknesses of the electrolyte layer above the sample surface. Values between 3μm and 20μm have been used.

the incident and exit-angle dependent pathway through the 6 μm thick Mylar foil and the dilute aqueous electrolyte layer on-top of the sample surface (which we approximately treated as pure water). The (assumed) thickness of the electrolyte layer was varied in the calculations in order to obtain the same level of corrected intensity at the beginning and at the end of the measured range of energy, which was chosen symmetrically to the energy of the Cu-edge.

The corrected curves for the data (curves A, B, I, II and III of Figure 10.33) are shown in Figure 10.34 a and b. While the curve B, measured for an in-plane peak of Cu_3Au, shows a large dip at the adsorption edge of Cu, for the curve A, measured for the peak at H=K=1.84, no such dip is observed, within the resolution of the measurement. For the curves I, II and III also a clear dip at the absorption edge of Cu is present, but with a magnitude smaller than for the case of the Cu_3Au substrate peak. The curves I, II and III are, after correction and the application of an scaling factor to match the intensity levels, basically identical within the resolution of the measurement. Also the in-plane peak at $(1.9\ 1.9\ 0.1)_s$ was not changing for the different potentials. We had observed this peak already directly after immersion and the structure is thus characteristic for a potential of 400 mV as it did not change before reaching potentials higher than 400 mV. In 10.34 a the curves calculated for pure Au and Cu_3Au, and in Figure 10.35 the curves calculated for CuAu and Au_2Cu are added. For Cu we obtained a measurement of the absorption edge

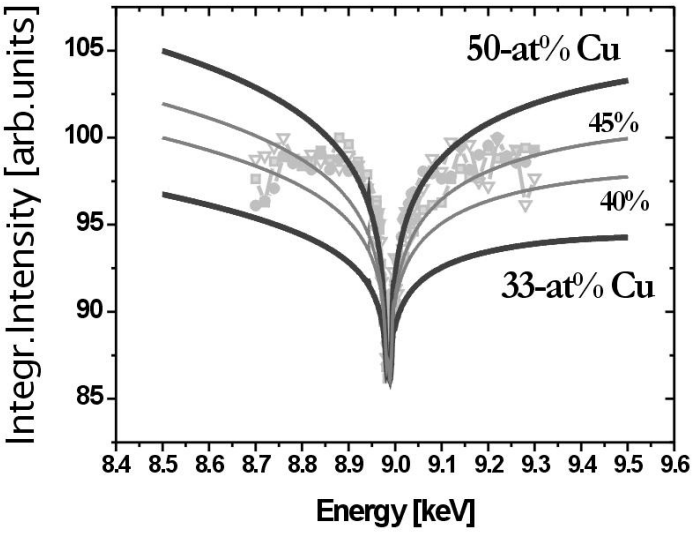

Figure 10.35: Corrected anomalous diffraction intensity of the $(1.9\ 1.9\ 0.1)_s$ reflexof the ultra-thin surface islands and some calculated curves. The measurement suggests a Cu content of approximately 45%.

by monitoring the rise of the background intensity (diffuse scattering). We replaced in the tabulated values for f" of Cu the region of the absorption edge by this measured values and obtained f' by a Kramers-Kronig transformation of these f" values. We obtained in this way a curve for f' that was not exhibiting the very sharp and deep dip of the calculated f' values but was otherwise identical to the theoretical curves from the literature. For the f^0(E,q), f'(E) and f"(E) of Au we used the tabulated values. The calculation is based on Equation 10.1.

$$I(E,q) \propto (f^0_{Au}(E,q) + f'_{Au}(E) + 3 * (f^0_{Cu}(E,q) + f'_{Cu}(E)))^2 + (f''_{Au} + 3 * f''_{Cu}))^2 \quad (10.1)$$

Equation 10.1 holds for the fundamental fcc reflections of a thin film, where the atoms of the unit cell scatter in phase and the scattering amplitudes from all atoms add up constructively.

During the measurements we encountered some problems with the reliability of the monitor signal, which were arising from the beamline optics at ID32, ESRF. The beamline ID32(ESRF) was described in Chapter 5.2. The energy of the photons of the X-ray beam is changed by moving the monochromator crystals to the respective Bragg angle. This results in a lateral movement of the beam on the surface of the monochromator crystals and results

in a different height of the exit beam, and further down-stream of the beamline, also on the mirror surface, if the mirror is used. However, the crystal surface of the monochromator and the mirror surface turned out to be laterally inhomogeneous in respect to the direction and intensity of the reflected X-ray beam. We attributed the large observed variations of the curves A and B (when changing the energy by a small step and even far away from the Cu adsorption edge) to these inhomogeneities. These variations occur mainly, because by the moving X-ray beam position the efficiency of the monitor signal seemed to be influenced in an unpredictable way. Nevertheless we obtained reliable data for the ultra-thin film by searching a good position of the monochromator.

Because of the quality of the data obtained for the Cu_3Au peak, we did not apply any correction in Figure 10.34 a. The data is in agreement with a Cu content of 75%. As was discussed above, the corrections for the refractive effects are in the order of 5% for an ideally flat and clean surface of Cu_3Au and the geometry chosen for our experiments. We undertook up to date no detailed analysis of the situation that arises, when a defect rich film of approximately three atomic monolayers of unknown Cu content, lies on-top of a Cu_3Au substrate. For an estimation of the effect of the refractive correction we applied the corrected transmission function for Cu_3Au to the data obtained for the ultra-thin film. The result is shown in Figure 10.36. Whereas without any correction the best fit of the

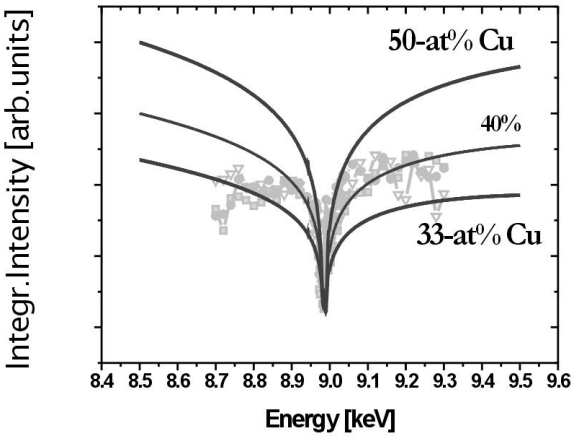

Figure 10.36: The corrections in the case of an ideally smooth surface slightly lower the obtained value for the Cu content in the ultra-thin islands to a value slightly below 40%.

theoretical curve to the data suggests a Cu content of approximately 45% (Fig. 10.35), the application of the Cu_3Au correction is giving a data set, which is explained by a Cu content slill as high as 38%. However, we estimate the real effect for the three monolayer thick structure to be much smaller, as we did not observe the maximum of the exit angle scan in Figure 10.32. For the data obtained for the peak at $H = K = 1.84$, i.e. the expected pure Au

position, we observed no dip within the resolution of the experiment. This is in agreement with a pure Au structure, as it is also expected from the (in-plane and out-of-plane) peak position.

Our anomalous measurements therefore suggest that an ultra-thin film is formed with the initial dissolution of Cu from $Cu_3Au(111)$, with a Cu content of approximately 40%. The thicker islands formed at elevated, but still sub-critical potentials, are then composed of pure Au, as is indicated by the lattice constants of the Au structure and the anomalous measurements, presented here.

Conclusions

We performed anomalous scattering of surface structure Bragg peaks. A sample with a Bragg peak corresonding to the thin pure gold layers present at elevated overpotentials did not show a dip at the Cu absorption edge at 8.975 keV. The anomalous measurement of a substrate peak was in agreement with a Cu content of 75%. For a sample with an ultra-thin layer present on the surface the corresponding Bragg peak intensity showed a clear dip at The Cu absorption edge. The analysis revealed a major contribution of 40% Cu in the ultra-thin structure.

10.6 An experiment with Cl^--containing Electrolyte

The results of this work, as reported so far, support the general opinion, that surface diffusion plays a major part in the initial corrosion of Cu-Au alloys. From this point of view it is important to have the possibility to change the surface mobility of adatoms, to reveal the influence on the observed phenomena. In an electrochemical environment this is possible by additives to the electrolyte. Additives can either enhance or diminish the surface mobility or, in general, any other electrochemical reaction. Well known from the economically very important processes of metal deposition is the role of brighteners, that help to obtain smoother surfaces of the deposit. Also often studied because of their immense importance are corrosion inhibitors. With this background, it is clear that it will be of great interest to study the influence of different additives on the formation of the surface structures that we observed during our experiments in pure 0.1 M H_2SO_4 electrolyte solutions. Well known is the enhanced surface mobility of Au surfaces in Cl^--containing solutions[[gi01][ma90]]. We will report here on a first experiment of the initial corrosion of $Cu_3Au(111)$ in Cl^--containing diluted H_2SO_4 electrolyte solutions (5 mM HCl + 0.1 M H_2SO_4).

Experimental Results

The same as the pure 0.1 M H_2SO_4 solutions, also the Cl^--containing diluted H_2SO_4 electrolyte solutions have been prepared from high-purity (suprapure, Merck) concentrated acids and ultra-clean water (TOC < 2 ppb). The usage of the electrochemical in-situ X-ray cell and the experimental procedure was the same as in the experiments described above. As always in this work we report the applied potentials with respect to a saturated Ag/AgCl reference electrode. The results for this one experiment are shown in Figure 10.37 a-c. Directly after immersion of the sample into the Cl^--containing diluted H_2SO_4 electrolyte solution at -138 mV we observed, besides the Cu_3Au substrate peaks, a small in-plane peak at $(1.89\ 1.89\ 0.1)_s$, i.e. at the position, where the peak corresponding to the ultra-thin layer had been observed before. The in-plane diffraction scans are shown in Figure 10.37 a. The corresponding L-scan (Fig. 10.37 b and c) showed a very broad peak, as observed in pure diluted H_2SO_4 electrolyte. The potential was increased, starting at -100 mV, by steps of 50 mV up to to a value of +350 mV. The curves for less than +200 mV have been omitted in Figure 10.37, because there was no significant change in the peak position. The intensity was growing from +100 mV onwards, until reaching a potential of +200 mV. At each potential we performed HK-scans and L-scans at the respective positions, i.e. a

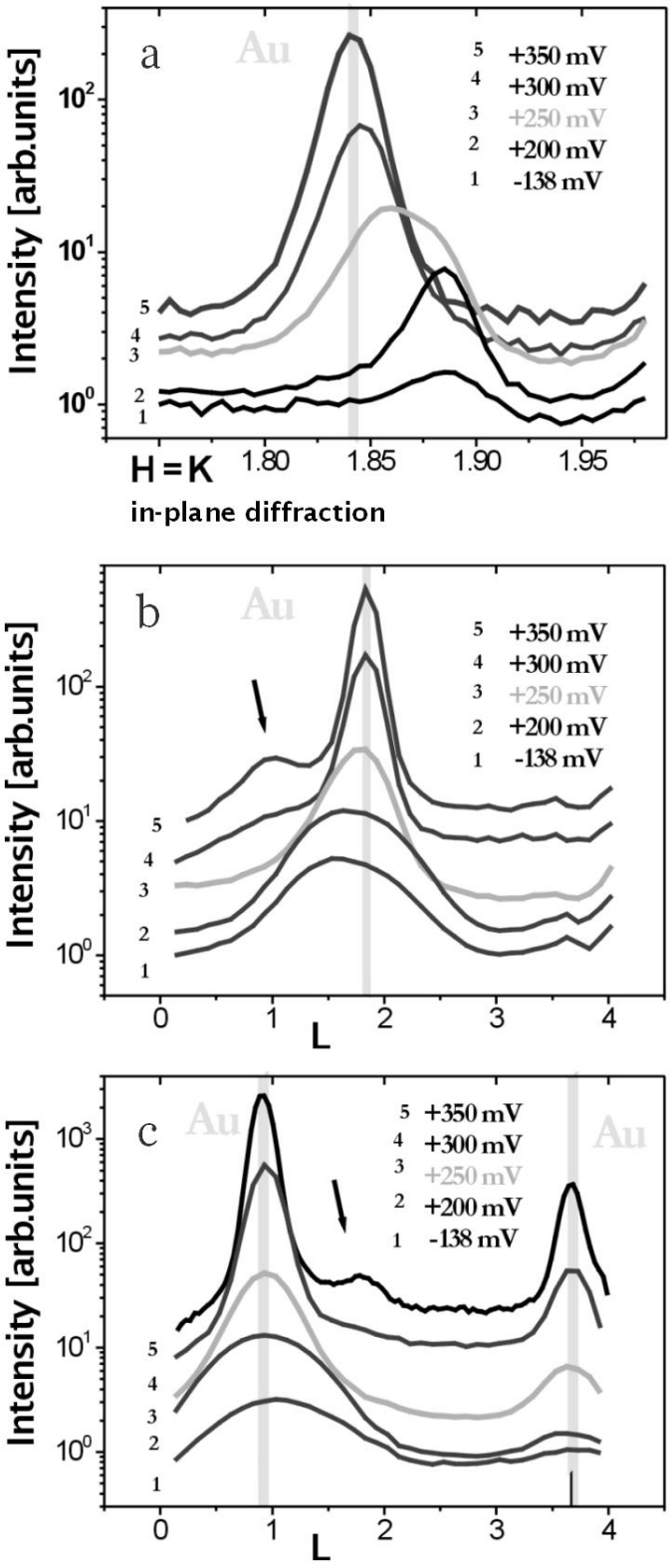

Figure 10.37: A first experiment of the initial corrosion of $Cu_3Au(111)$ in Cl^--containing diluted H_2SO_4 electrolyte solutions (5 mM HCl + 0.1 M H_2SO_4). In (a) the radial in-plane diffraction peaks are shown. A small peak was visible after immersion into the electrolyte at negative potentials. Already at +250 mV the position was shifting towards the expected pure Au position. The position for an epitaxial (anti-parallel) and relaxed structure of pure Au is marked by the vertical grey line in the Figures.

(b and c) The shown L-scans along the (0 K L)$_s$ and the (H 0 L)$_s$ rod were recorded at the H and K value corresponding to the peak of the in-plane diffraction peak shown in (a). The width is changing from an initially broad value to the much sharper peak width of the final peak. At elevated potentials also the twin domain is visibly growing, while at 250 mV only the anti-parallel domain is observed.

radial in-plane scan close to $(1.89\ 1.89\ 0.1)_s$ and the L-scans along the rod corresponding to the observed in-plane peak at the respective peak position, e.g. the $(1.89\ 0\ \mathrm{L})_s$ and $(0\ 1.89\ \mathrm{L})_s$ L-scans. The time interval between each change of potential was approximately 1 hour, at the potential of +150 mV, we waited 2 hours before changing to +200 mV. Up to a potential of +200 mV we basically observed a growing intensity from an ultra-thin layer at the in-plane $(1.89\ 1.89\ 0.1)_s$ position and the respective L-scans, similar to the results in pure 0.1 M H_2SO_4 electrolyte. With the growth of the diffracted intensity the (in-plane) peak position was not shifting at these lower potentials, until, with changing the potential to +250 mV, we observed a much broader in-plane peak (the shape is indicating a contribution of two components, as will be discussed later) at $(1.86\ 1.86\ 0.1)_s$, i.e. closer to the expected epitaxial Au position. The L-scans at this position revealed narrower, but still broad, peaks (in the L-direction) compared to the width at lower potentials. With a further increase to +300 mV the in-plane diffraction peak shifted further in direction to the expected pure Au position and the corresponding peak-width was smaller than observed at +250 mV and of the same order than e.g. at +200 mV. At +350 mV the in-plane peak was then at exactly at the pure Au position and further increased in intensity. The corresponding L-scans at +300 mV and +350 mV revealed now ticker islands, similar to the observations in pure 0.1 M H_2SO_4 electrolyte. The corresponding thickness, as estimated from the width of the peaks in the L-scans, is approximately 3 nm at +300 mV and approximately 4nm at +350 mV. Interesting is the development of the stacking faulted domain, that is observed at +300 mV and +350 mV. While at potentials lower than +300 mV no intensity is observed at the position along the L-direction, which corresponds to the occurrence of faulted domains (as described in Chapter 10.2.1), at +300 mV and clearer at +350 mV, a small contribution is present (indicated by the arrow in Fig. 10.37 b and c). Note the logarithmic scale in the Figures.

Discussion

The observations of the structural changes on the $Cu_3Au(111)$ surface with the initial selective dissolution of Cu in Cl^--containing diluted H_2SO_4 electrolyte solution with low, i.e. sub-critical, potentials are similar to the results obtained in pure 0.1 M H_2SO_4 solutions, but show differences in the details of the results. Firstly, at lower overpotentials (for the Cu dissolution), we observed, like in pure 0.1 M H_2SO_4 solution, the formation of an ultra-thin epitaxial Au-enriched layer, as can be deduced from the observed peak positions and corresponding peak widths. However, already at 250 mV, the initially observed peak position clearly started to shift in direction of a pure Au position. At this potential also

a intermediate thickness is observed, the deduced thickness of 1.4 nm, being between the 3-5 monolayers (below 1 nm), observed for the initial peak, and the 3 nm for the thicker Au layers. Such an intermediate thickness has not been observed before. For the case of the pure 0.1 M H_2SO_4 solution in the previous experiments, we observed the onset of a similar growth of a pure or nearly-pure Au structure at potentials between 350 mV and 450 mV, depending on the different experiments with different time-potential histories before. The intermediate thickness of 1.4 nm for the growing layer was observed here for the first time. For the previous experiments in pure 0.1 M H_2SO_4 solution, the growth started firstly already much closer to the Au position and secondly the thickness was always immediately in the order of 3 nm. The time interval of usually one or two hours, between each change of potential, was much longer than for the experiment in pure 0.1 M H_2SO_4 solutions, presented above in Figure 10.13, where a continuous shift towards the Au lattice constant was observed (but at comparatively higher potentials) with changing the potential in time intervals of ten minutes. For this experiment we do not have the information of the out-of-plane diffraction, i.e. the corresponding L-scans are missing. Otherwise the performed experiments in pure 0.1 M H_2SO_4 solutions were conducted with even longer time intervals, due to the time-consuming measurement of integrated CTR intensity at the different potential values.

Conclusions

In this Chapter we presented the data obtained for the initial selective dissolution of Cu from $Cu_3Au(111)$ in Cl^--containing diluted H_2SO_4 electrolyte solution. Like in pure diluted H_2SO_4 electrolyte, we observed the growth of firstly an ultra-thin Au-rich layer and secondly the emergence of thicker, nearly pure, Au islands at higher (but below E_c) potentials, with the ultra-thin layer vanishing. We can conclude that the presence of the halide ion Cl^- causes the structural change of the ultra-thin Au-rich layer towards nearly pure Au islands, to occur at lower potential values compared to pure diluted H_2SO_4 electrolyte, i.e. at already +250 mV (Ag/AgCl), in contrast to the otherwise observed onset potentials for the structural change of +350 mV and larger. This result fits to the observation of a lower critical potential in Cl^--containing electrolyte [mo91].The observation of a continuous increase in thickness of the associated islands, suggests an altered dynamic behavior with the presence of Cl^- in the electrolyte.

10.7 Observations after Lost Potential Control

For the in-situ experiments the application of a controlled potential during the entire experiment is a prerequisite. When one suddenly interrupts an electrical circuit/current, an overshoot of potential might occur , i.e. in our case potentials well above the critical potential might be present for a short time interval. Also we observed sometimes an unstable potential with the first immersion of the sample into the electrolyte solution. It was also not possible to predict the exact potential values at the sample in the case when the connection to the reference electrode was lost. The potentiostat reacted then by applying high, either cathodic or anodic, potentials. There were several possible reasons that caused or could have caused a loss of potential control. The X-ray beam could e.g. produce holes in the mylar foil that was covering the electrochemical in-situ cell and a subsequent loss of the electrolyte could interrupt the signal of the reference electrode causing the potentiostat to apply undefined potentials. Similarly, the moving diffractometer could cause an interruption of one of the connections or accumulated gas/air could block the reference electrode. At some occasions we could spend some time on characterizing crystal surfaces, after we lost potential control at some moment. A few interesting observations made, are presented here.

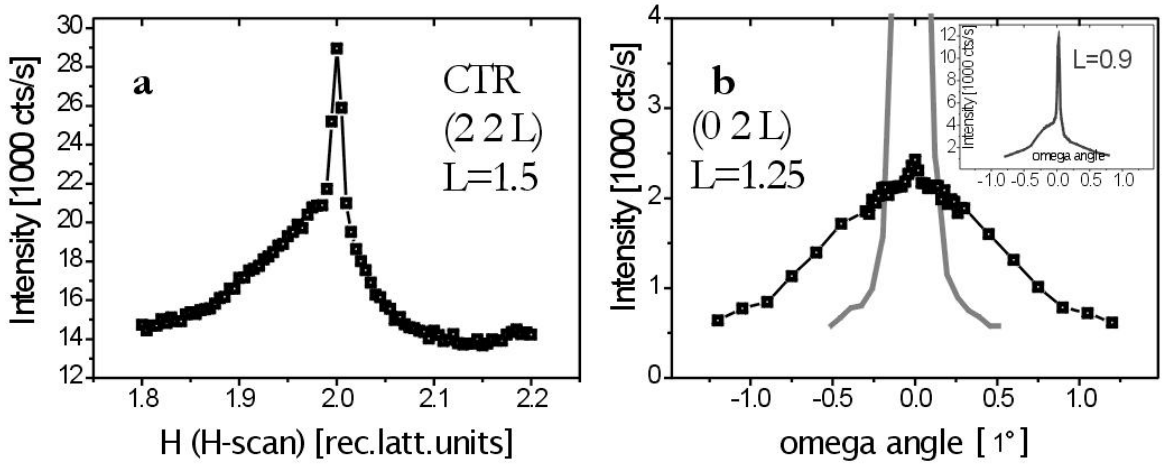

Figure 10.38: An H-scan (a) and rocking scans (b) at different positions of Cu_3Au substrate CTR's. The origin of the broad component is not yet clear.

Figure 10.38 shows the shape of the intensity distribution at points along the Cu_3Au substrate CTR. In (a) a large Au peak was present, directly after immersion into the electrolyte, and the Cu_3Au substrate CTR at $(2\ 2\ 1.5)_s$ showed a broad asymmetric component

in an H-scan (equally in the K-scan through the CTR). In Figure 10.38 (b) a rocking scan at L=1.25 on the $(0\ 2\ L)_s$ rod is shown, measured after the loss of potential control and with an associated large Au peak present. For comparison the lower part of the peak at the same position, before the loss of potential control is included in the Figure with the same scale (gray line). The Inset shows the rocking scan at L=0.9, i.e. slightly below the Cu_3Au substrate Bragg peak at $(0\ 2\ 1)_s$, where the broad component is not centered with the main CTR peak. Otherwise, we measured the rocking scans at the $(0\ 2\ L)_s$ CTR positions L=1.1, L=1.2, L=1.3 and L=1.4 (and the same positions on the symmetry equivalent CTR's), where the broad component was centered (relative to the sharp CTR peak) and its width was increasing from approximately 1° for L=1.1 and 2° for L=1.2 to 4° at L=1.4.

In Figure 10.39 we present two reciprocal maps of an initial peak at $(1.89\ 1.89\ 0.1)_s$ and a larger peak at the pure Au position $(1.84\ 1.84\ 0.1)_s$ that was present on the same sample after the potential control was lost, directly after the mapping of the first peak was completed. The initial peak at H=K=1.89 rlu (Fig. 10.39 a) showed already a slight asymmetric peak shape of the corresponding radial HK-scan with higher intensity on the side towards the pure Au position at H=K=1.84 rlu , i.e. a pure Au peak was starting to grow (See also the inset of Figure 10.39 d (arrow)). The expected position for the bulk (pure) Au peak is marked in the maps (a) and (b), with a cross at H=K=1.84 rlu. After the loss of potential control for this sample, a pure Au peak was observed at H=K=1.84 rlu (Fig. 10.39 b and d), with approximately 10 times higher intensity, compared to the peak at H=K=1.89 rlu before. The width of the peak decreased from 0.038 rlu to 0.024 rlu, indicating an increased lateral coherent extension of the associated structures/islands, from an estimated value of 7 nm to 11 nm. In Figure 10.39 c both maps, (a) and (b), are scaled to the same peak height and added for a better comparison. The shown peaks have different peak widths in radial and in transversal direction. The width in radial direction (arrow in Figure b) is in general determined by the coherent size of the scattering objects, while the width of the transversal direction (i.e. the direction perpendicular to the radial direction) can be additionally broadened by a spread of orientation, e.g. a mosaic spread. A rocking scan (which moves the scattering vector $\mathbf{q}$, e.g. along the dashed curve in Figure b) follows essentially the transversal direction. The shown peaks in Figure (a) and (b) are broader in this direction, and its peak width, of in our case typically 1.5°-2° in the corresponding rocking scans, is therefore, determined by the orientational distribution of the scattering Au or Au-rich islands around the exact epitaxial orientation (The substrate peak is, with typically 0.1°, much narrower).

A last interesting detail of the growth behavior of the Au or Au-rich islands, revealed by the characterization of samples after the loss of potential control, is presented in

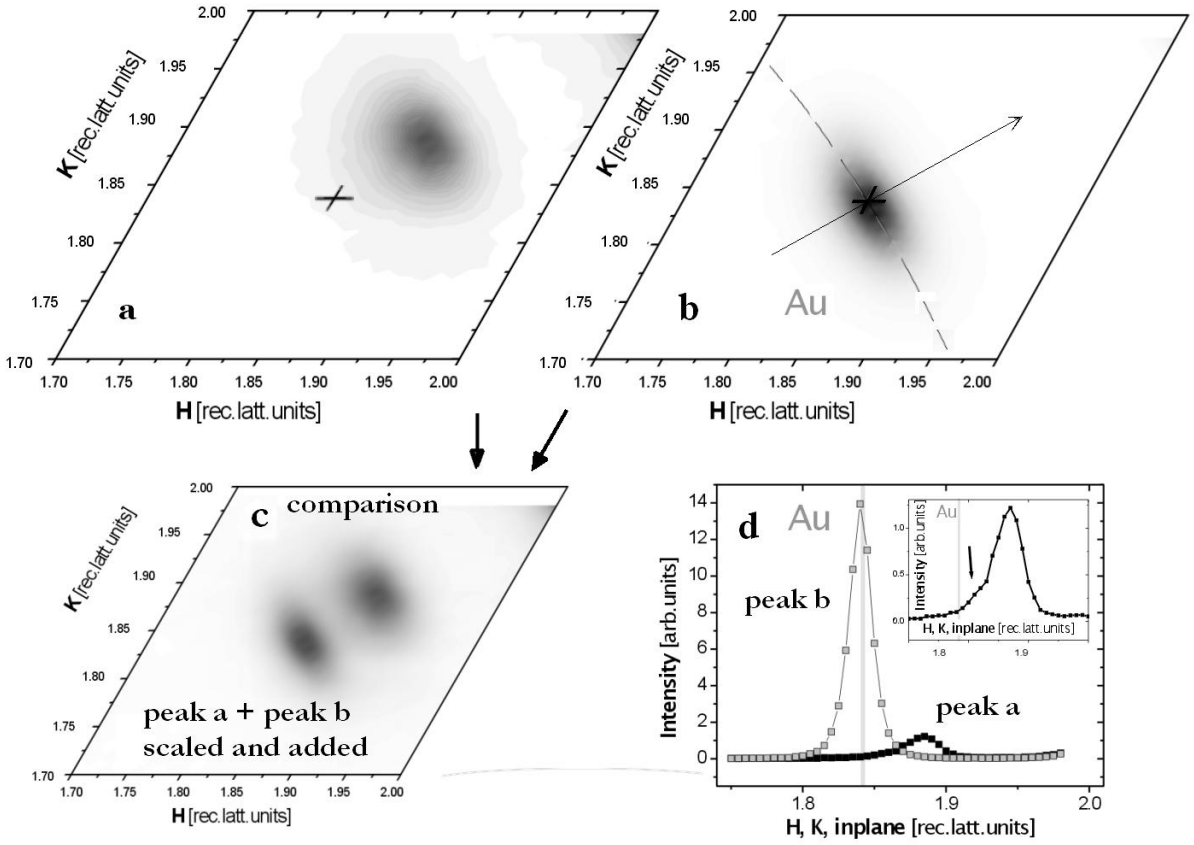

Figure 10.39: Reciprocal maps of an initial ultra-thin layer with a peak at (1.89 1.89 0.1)$_s$ (a) and a larger peak at the pure Au position (1.84 1.84 0.1)$_s$ that was present on the same sample after the potential control was lost. In (c), both datasets are scaled to the same peak height and added for better comparison. (d) shows the corresponding radial HK-scans through the two peaks. (The direction is indicated in (b) by an arrow). Their angular width (along the circular line in (b)) is typically in the order of 1-2°

Figure 10.40. The shown (0 1.90/1.84 L)$_s$ L-scans reveal details about the layer/island thickness and about the stacking sequence (as was described in Chapter 10.2.1). If the potentiostat applied a cathodic potential, we observed the same ultra-thin layer as in the case of controlled, potential dependent dissolution at lower overpotentials (Fig. 10.40 a). For comparison, (Fig. 10.40 b) shows a thicker pure Au structure obtained at a (controled) potential of 320 mV (taken from Fig. 10.15), with predominantly the 'acb' stacking present (with respect to the 'ABC' substrate stacking). In several cases the sample was found with

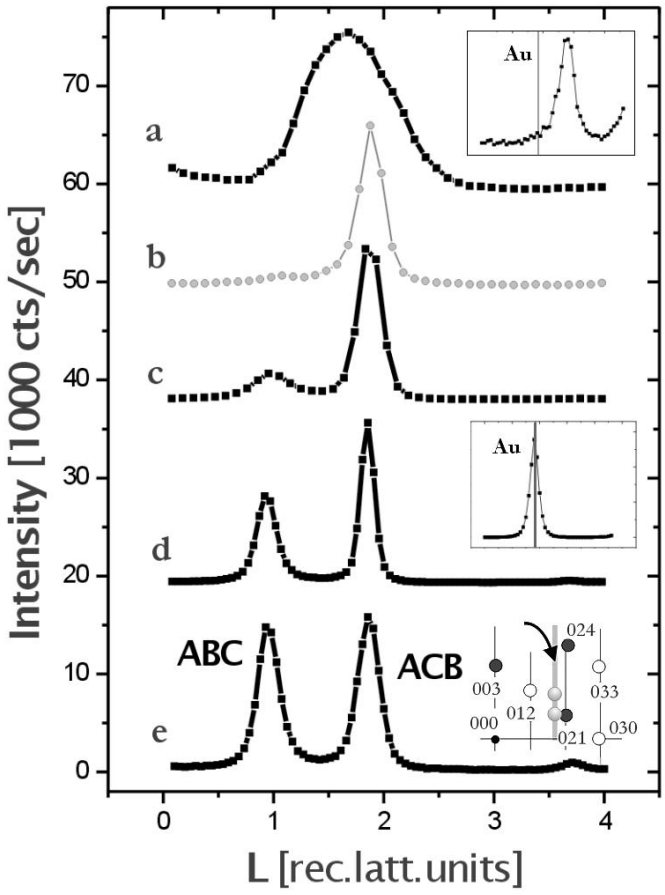

Figure 10.40: With the loss of potential control of the Cu_3Au sample in electrolyte a certain amount of current can pass at an undefined potential. In several cases the sample was found with a layer of thicker pure Au or with an ultrathin Au-rich layer after the loss of potential control (a,c-d).For comparison, (b) shows a pure Au structure obtained at 320 mV (taken from Fig. 10.15) with predominantly the acb stacking present (with respect to the ABC substrate stacking). In all cases the peaks indicating the presence of stacking faulted domains (close to L=1) are relatively stronger than in the case of the formation at controlled, sub-critical potentials.

a thick layer of pure Au after the loss of potential control (the potentiostat applied a anodic potential). Figure 10.40(c-d) shows the corresponding L-scans and the inset of curve (d) gives an example for a corresponding HK-scan. The in-plane and out-of-plane peak positions correspond to the expected value for pure Au, and gives values for the estimated thickness between 2 and 5 nm, and of 10-15 nm for the lateral size, for the shown peaks. In all cases for the thicker pure Au layers being present, the diffraction peaks caused by the stacking faulted domains (At L=1 for the shown (0 1.9 L)$_s$ L-scans) are relatively stronger than in the case of the formation with controlled, sub-critical potentials (shown in b). The different peak heights are indicating a presence of both stacking domains. The ratio of the twin domains on the surface is up to 50% at most (Fig 10.40) c-d).

10.8 Final Discussion and Conclusions: X-Ray Diffraction

By X-ray diffraction we could follow the growth and change of passivating Au-rich islands on the surface. Starting with only a few monolayers thick but about 20 nm wide islands, the thickness reached at the very end (i.e. with the formation of a porous Au network) values equal to the lateral extension, being still in the order of 20 nm. With a very slow increase of potential (i.e. the forming structure could grow during many hours) an ultra-thin island was forming that did only considerably grow further at elevated potentials by forming directly much thicker structures. For a faster potential increase (within 1 hour) a continuous shift of the in-plane peak position was observed. Time plays thus a major role in the stability of the passivation layers, possibly by a decrease of defects that were present with the initial formation of the passivation layer (aging effect). The details of the growth are dependent on the potential and the time. Interesting was also the observation that with the loss of potential control, like it occurred due to the failure of one of the components of the set-up, we could observe different ratio's of normal (abc) and of the inverted stacking (cba) of the formed islands. Otherwise, i.e. with a slow and controlled increase of potential, we observed nearly 100% inverted epitaxial islands.

The thickness of the ultra-thin layer was estimated from L-scans along reciprocal space intensity rods to be only a few atomic monolayers (between 2 and 6 ML). The actual thickness was depending on the exact value of the applied potential and the time we stayed at a certain potential before. At certain values of the potential we recorded a CTR of the formed ultra-thin layer by measuring integrated intensities, i.e. performing rocking scans (in transversal direction, i.e. rotating the sample around its surface normal). Although, in general, CTR data recorded in this way from well ordered structures offers a possibility to obtain detailed structural information (as was explained in Chapter 4.7), in our case of dissolution at room temperature it is not evident to observe such well ordered structures. The interface of ultra-thin overlayers of elements with different bulk lattice constant compared to the substrate, as we observed it in our case for the lower overpotentials of the Cu dissolution, is known to exhibit various defects and reconstructions or strain relief patterns [li04] [gu95] [br94]. Nevertheless, we were able to follow the intensity along the ultra-thin layer rod and with a simple fcc model of two continuous and one with 50% occupied third layer of Au atoms, we could nearly reproduce the data. The data was, as in most cases of diffraction studies, not recorded on an absolute intensity scale, i.e. a scale factor was used to fit the data on the level of the calculated intensity/scattering

amplitudes. The fitting was not sensitive on a content of Cu in the ultra-thin layer, supposingly because the expected defects present, will dominate over the slight differences in the shape of the respective atomic form factors for Cu and Au (Chapter 4). For different Cu and Au compositions of the film we thus obtained fits of similar quality by using the scale factor to compensate for the reduced scattering due to the reduced electron density with more Cu intermixed. Also a Cu adlayer on-top of two atomic layers of Au can thus explain the CTR data (a possible Cu UPD layers on Au in this potential range).

Further to discuss in this respect, are the performed L-scans, i.e. the line scans along the respective ultra-thin layer rods, that were performed occasionally up to higher L-values, including the second thin overlayer Bragg peak. A comparison of the deduced lattice constants (calculated via the peak position) revealed a systematic deviation of the (from all positions calculated) average, on the two kind of rods (i.e. the $(1.9\ 0\ L)_s$ with a Bragg peak close to L=1 and the $(0\ 1.9\ L)_s$ with a Bragg peak close to L=2). The values deduced from the $(0\ 1.9\ L)_s$ rod were always smaller than the average (and vice versa). With this knowledge it is clear that, in addition to the CTR data we obtained, a wider range in L for the measured integrated CTR intensity is desired.

The lattice constants derived for the ultra-thin structure were already close to the bulk Au position but were shifted as expected for an biaxially strained layer (tensile stress) and bulk elastic constants, with a resulting enhanced z-distance. A calculation by Wolf [wo91] revealed an equilibrium structure with lattice constants close to the values we observed for the ultra-thin islands. However, such ultra-thin structures are rarely studied. The thicker islands growing at elevated potentials were nearly at the exact position for bulk Au (0-10% Cu). The observed lattice constants seem to be in agreement with nearly pure Au structures formed on the $Cu_3Au(111)$ surface after selective dissolution of Cu. This is in contrast to a value of approximately 40% of Cu determined for the ultra-thin layer with the anomalous diffraction measurements. Here a clear dip in the diffraction intensity of the studied sample at the Cu-edge was observed. Note that with the formation of 10 ML pure Au about 24 ML pure Cu are dissolved into the electrolyte. Even in thin film geometry of the in-situ cell, where the electrolyte film is about 10μm thick and the atoms are trapped within this layer, the absorption effect can be neglected. The observed anomalous diffraction intensity is thus a clear sign of a major contribution of Cu in the ultra-thin layer.

In the case with Cl^--ions present in the electrolyte solution, the rapid transition of the ultra-thin structure to the thicker layers occurred at lower potentials (≈200-250 mV) compared to experiments in pure 0.1 M H_2SO_4 solution (≈400-450 mV). Although, with experiments on longer time scales in pure 0.1 M H_2SO_4 solution we also observed the

occurrence of the pure gold structure at slightly lower potentials (e.g. after 9 hours at 320 mV). Nevertheless, the formation of the pure gold islands with a similar rate as in the experiment with the Cl^--containing H_2SO_4 electrolyte, was observed at 150-200 mV higher potentials. Interestingly, this observed shift in potential is of the same order than the corresponding shift in the critical potential E_c, for this system, as it was measured by Gerischer [ge55] or later by Moffat [mo91]. The presence of Cl^--ions is known to increase the Au surface mobility on Au surfaces [gi01]. On the contrary it would be interesting to study in further experiments the influence of corrosion inhibitors on the structural changes during the Cu dissolution.

Chapter 11

Experimental Results: Ex-Situ AFM

Atomic force microscopy is an easy to use technique, capable to image the topography of surfaces up to a lateral resolution of interatomic distances. The AFM, in comparison to the STM, is less disturbed by surface roughening and is therefore the imaging technique of our choice. The technique was described in Chapter 5.3. The main part of the AFM images were performed at the ESRF in Grenoble, using a commercially available in-air AFM (Molecular Imaging (MI) Dimension 3100). As a tip for the AFM we used the commercially available tip NSC12/15 from Silicon-MDT Ltd, Moscow, Russia. This tip has a specified radius of curvature of less than 10 nm and a resonance frequency of typically 315 kHz.

After some of the in-situ X-ray measurements of the corrosion of $Cu_3Au(111)$ that were presented before, we recorded AFM images in air. After the X-ray measurements, we drained the electrolyte inside the electrochemical X-ray cell with the applied final potential of typically 400 mV (In this work always vs. Ag/AgCl), and cleaned the samples with ultra-pure water. The crystals were subsequently stored in dry atmosphere and we conducted the ex-situ AFM studies usually some days afterwards, when the AFM set-up was available. In addition to these post-X-ray images, we were performing a dedicated ex-situ AFM study. For this study the crystal surfaces were prepared in UHV, as described above, and subsequently immersed in 0.1 M H_2SO_4 electrolyte solution in a standard three electrode glass cell. This glass cell was described in Chapter 5.5. No X-ray beam was used in this dedicated ex-situ AFM study.

By analyzing diffraction patterns of crystals (reciprocal space), averaged direct-space values of structural parameters of the crystals or crystal surfaces are obtained. A regular lattice plane distance or periodicity in real space produces e.g. a Bragg peak in direction of the periodicity. The periodicity can also be due to a regular arrangement of islands

on the surface or of the ligaments of a porous structure. Small angle X-ray scattering (SAXS) is then possible. In contrast, the AFM reveals directly an image of a real space surface. Provided that the image size is sufficient, statistical analysis from these AFM images can be obtained. An AFM image consists of a set of height values z($\vec{r}$) at specific surface points. These surface points are given in coordinates of two in-plane unit vectors, $\vec{e}_x$ and $\vec{e}_y$, i.e. $\vec{r}$=x·$\vec{e}_x$+y·$\vec{e}_y$. Frequently the AFM image consists of 512×512 of such height values, arranged in a squared lattice. This dataset can then be analyzed. One important function for the statistical analysis of such AFM images is the height-height correlation or autocorrelation function (HHCF) C($\vec{r}$):

$$C(\vec{r}) =< [z(\vec{r_0}+\vec{r})- < z >][z(\vec{r_0})- < z >] > . \tag{11.1}$$

The brackets $< >$ denote the averaging procedure over all pairs of surface points of the image lattice (x, y) which are separated by the vector $\vec{r_0}$. If the correlation is performed between all pairs of the 2D AFM images, the function is also called 2D autocorrelation function. Side peaks that occur in the HHCF can be interpreted by an average island distance, while the central peak is a function of the detailed shape and distance of the islands. Another used function is the height-difference correlation function (HDCF) H(r). For large $|r|$ the HDCF usually saturates at a value of H(r)=$2\sigma^2$, where σ is the root mean squared (rms) roughness parameter. σ is a measure for the average deviation of the height values from the average height $< z >$. For more details the reader is referred to the literature [ton94][te02]. The 2D autocorrelation functions (HHCF) H($\vec{r}$) and 2D power spectral densities (PSD) have been deduced with the help of the (public domain) software WSxM [wsxm]. For spatially averaged height-difference correlation functions (HDCF) and power spectral densities (PSD) also the programm DATAPLOT was used [ri00].

$$H(\vec{r}) =< [z(\vec{r_0}+\vec{r}-z(\vec{r_0}))) >]^2 > . \tag{11.2}$$

The modulus of the Fourier transformation of the autocorrelation function is called power spectral density (PSD) S($\vec{k}$).

$$S(\vec{k}) = |F\{C(\vec{r})\}| \tag{11.3}$$

11.1 Images after X-ray Experiments

Typically, the highest potential applied during the X-ray measurements was not more than +500 mV. The reason for this was that we recovered the clean $Cu_3Au(111)$ crystal surface for subsequent experiments, by a few sputter-annealing cycles in UHV. Therefore we

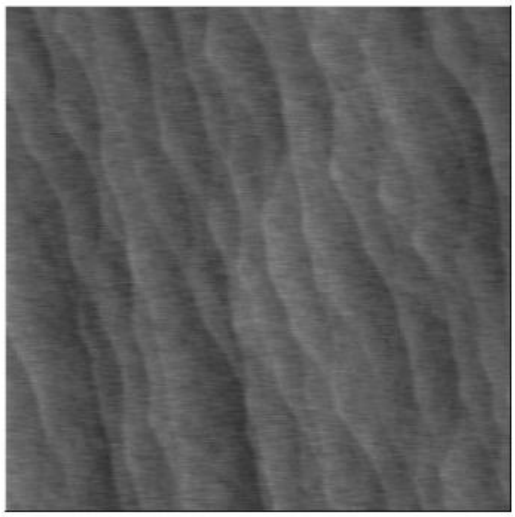

a) z_{max}= 5nm, 1μm x 1μm

Figure 11.1: (a) AFM image (1μm $\times$ 1μm) of a clean $Cu_3Au(111)$ surface directly after preparation by sputtering and annealing cycles in UHV. Steps are clearly visible. Their height corresponds to a Cu_3Au $\{111\}$ inter-layer distance of 0.2167nm.

(b and c) Two AFM images (1μ m $\times$ 1μm) at two different spots on the sample of a $Cu_3Au(111)$ surface after an in-situ X-ray study. The two different spots on the sample show differences in the imaged island size and in the distance of the islands.
The color code below will be used for all AFM images in this chapter.

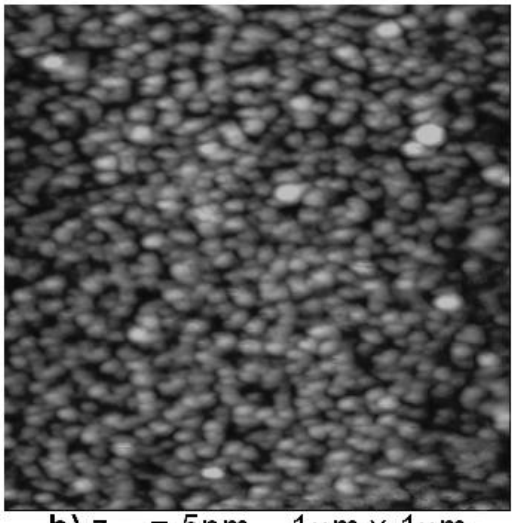

b) z_{max}= 5nm, 1μm x 1μm

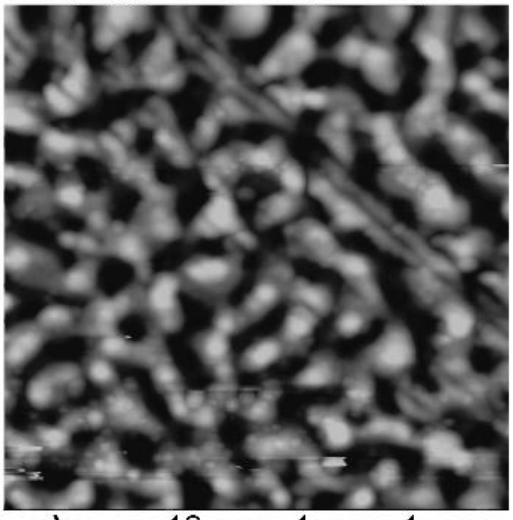

c) z_{max}= 10nm, 1μm x 1μm

avoided potentials close to the critical potential E_c, where the formation of a porous Au-rich layer and a pronounced roughening are reported. The critical potential is approximately at a potential of 900 mV (vs. Ag/AgCl) for Cl^--free 0.1 M H_2SO_4 or 700 mV for Cl^--containing 0.1 M H_2SO_4 electrolyte solution. The time interval in which the sample was kept in electrolyte at the specific potentials of the performed measurements was ranging from a few hours up to 48 hours.

A first example for AFM images after corrosion experiments is given in Figure 11.1. For comparisons a clean $Cu_3Au(111)$ surface is shown in Figure 11.1 (a), as imaged directly after preparation by sputtering and annealing cycles in UHV. Steps are clearly visible in Figure 11.1 (a), and the step height corresponds well to the Cu_3Au {111} inter-layer distance of 0.2167 nm, as was shown above (Fig. 7.4). The images 11.1 b and c, taken after X-ray measurements and selective dissolution of Cu, were obtained from the same sample surface (MaTecK crystals). The sample was immersed in electrolyte for 200 min at a potential of 450 mV and only Bragg peaks corresponding to pure Au have been observed at this potential. The sample was then dried and imaged in air with the AFM. The two images shown in Figure 11.1 b and c were taken at two different areas on the surface. The corresponding images show in one case a surface that is densely packed with islands (Fig. 11.1 b). In the other case a more open (porous) surface morphology is observed. The islands have then a slightly larger size and the average distance between them has approximately doubled (Fig. 11.1 c). For both spots also $10\mu m \times 10\mu m$ large images were taken and show that the structures are at least uniform on this lateral scale of 10 μm at the imaged areas.

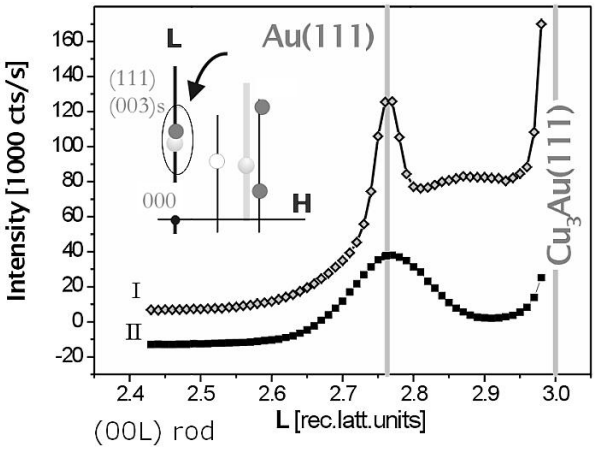

Figure 11.2: The specular Au peaks are recorded on different lateral positions of the sample surface presented in Figure 11.1 b and c. Two kinds of peak shapes were observed. The sharp peak can be associated with a coherent width of approximately 15nm (equal to the lateral size) and seems to emerge from the surface area with the porous morphology. The lower curve is shifted down by 20000 cts/s.

After these AFM measurements, we checked the in-plane and specular X-ray diffraction

peaks on the same surface. These ex-situ X-ray diffraction measurements are related directly to these AFM images and are thus presented here. We observed, as in electrolyte before the AFM measurements, only peaks very close to the positions expected for pure and relaxed (bulk) Au islands, and no peaks for an ultra-thin layer. The in-plane radial scans at different lateral sample positions at the reciprocal $(1.84\ 1.84\ 0.1)_s$ (Au) position showed only small variations in peak position and peak width (This data is not shown). The specular $(0\ 0\ 2.76)_s$ peak (Au-position), on the other side, was changing considerably when changing the lateral position of the sample and illuminating different areas. These areas have a typical average size of about 1×0.5 mm as the incoming beam is typically 0.2 mm high and 0.5 mm wide (incoming beam slits) and the (111) Bragg reflex is, for the used energy of 12.5 keV, at an incident angle ϑ of about 13°. Two different kinds of peak shape have been observed (Fig. 11.2). In some areas, a double peak structure, consisting of a sharp component exactly at the Au position and a broader component, with a maximum in between the Au and the Cu_3Au position is observed. The width of the sharp peak of 0.05 rlu corresponds to a coherent thickness of approximately 15 nm and is thus of the same size than the lateral extension. In other areas, a single broad peak was observed, with a width of 0.12 rlu, corresponding to a coherent thickness of approximately 5 nm.

Another example is shown in Figure 11.3 a-d. Here the sample has been immersed in electrolyte at a potential of 450 mV for 36 hours, before the AFM images were taken in air. All four images were recorded in the same region on the sample (Other regions ($10\,\mu$m$\times10\,\mu$m) showed only the porous surface morphology or only the surface covered with densely packed islands). The images show a surface covered with a layer of densely packed islands, and in addition, patches of a more open or porous surface morphology. These porous areas seem to have mainly a homogeneous area/size. In Figure 11.3 d two scratches or defect lines are decorated with this porous surface areas.

All other samples showed only a dense layer of islands after the performed in-situ X-ray measurements, although the island size and distance was slightly varying, from case to case (30-80 nm). Figure 11.4 shows as an example the sample after the measurement in Cl^- containing 0.1 M H_2SO_4 electrolyte solution (other images in pure 0.1 M H_2SO_4 solution were similar). The maximum potential of 350 mV was applied during approximately 1 hour. The average island size for the sample of Figure 11.4 is approximately 40 nm and the average island distance is around 80 nm, as was determined from an autocorrelation-function treatment of the image. The image appears not very clear and the island size might be over-estimated due to tip size effects.

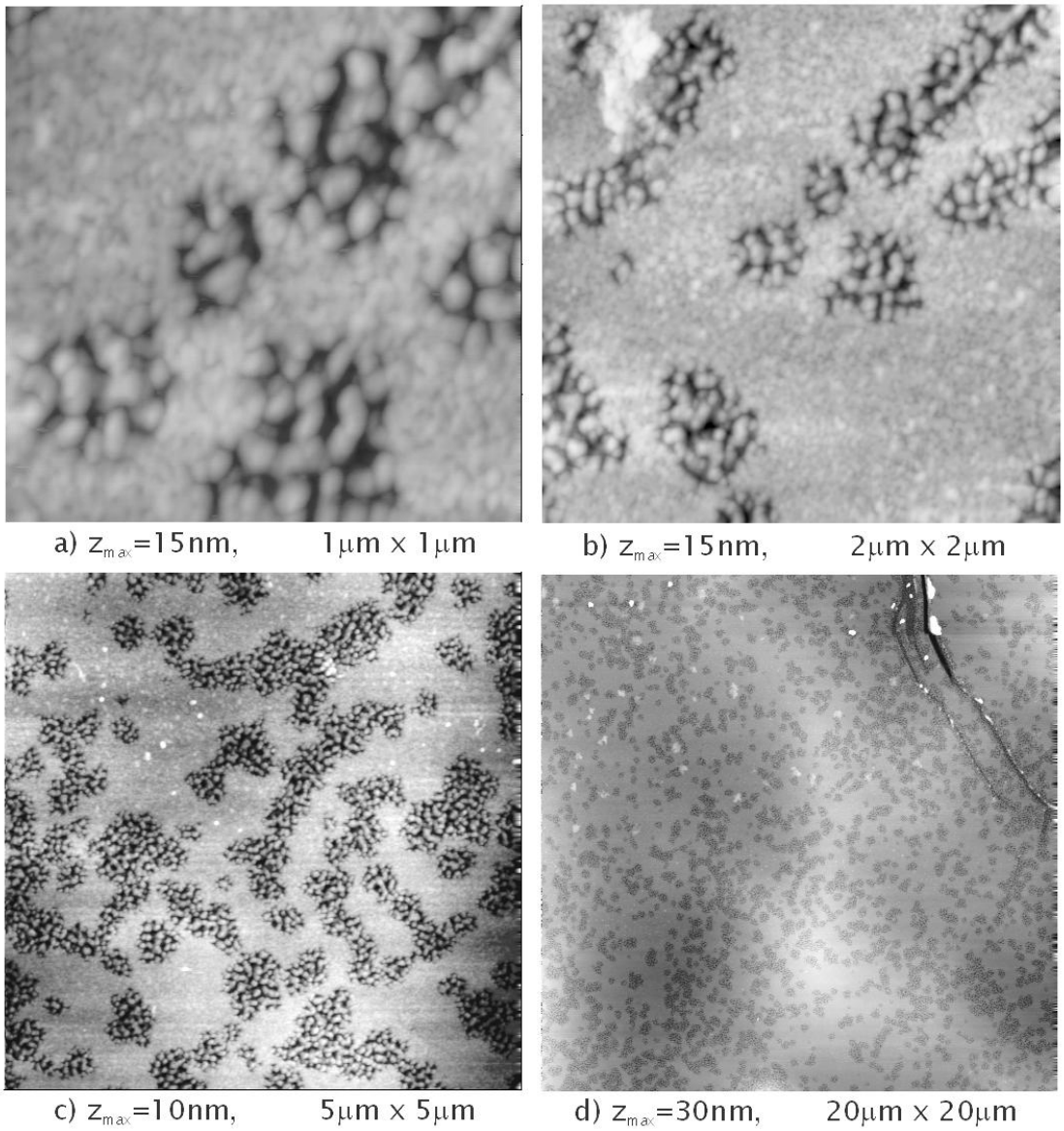

Figure 11.3: In-air AFM images, after in-situ X-ray measurements, of a $Cu_3Au(111)$ sample immersed in electrolyte at 450 mV for 36 hours.

11.2 Ex-Situ Study

During the performed X-ray measurements the sample was usually held at the respective applied potentials for many hours. In contrast, a cyclic voltammogram is performed with a typical potential-sweep rate of e.g. 10 mV/s, i.e. the whole range of potential for the electrochemical experiment is applied within a short time. Typical potential ranges for voltammetry are around 500 mV and one potential cycle is thus completed within a usual

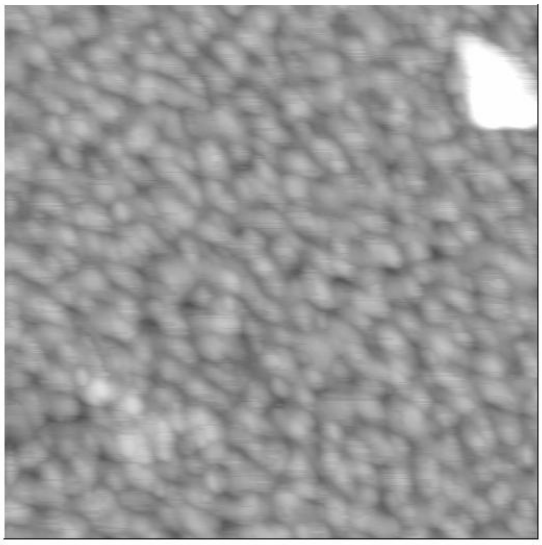

Figure 11.4: AFM image after the measurement in Cl^- containing 0.1 M H_2SO_4. The maximum potential of 350 mV was applied during approximately 1 hour. The average island size is approximately 40 nm and the average island distance is around 80 nm.

time of 2 minutes. The aim the ex-situ AFM study was to compare the surface topography, obtained after the X-ray experiments in our in-situ X-ray cell, with surfaces treated in a standard electrochemical glass cell without X-ray exposure.

The Cu_3Au samples were prepared in UHV in the usual way (as described above). A first AFM image was taken from the clean surface, before the sample was immersed in 0.1 M H_2SO_4 electrolyte solution at a potential of -100 mV. Subsequently, either a cyclic voltammogram (CV) was recorded, or a fixed potential was applied for several minutes. Afterwards the sample was taken out of the electrolyte solution, rinsed with ultra-pure water and dried shortly in a stream of nitrogen gas. If several different potentials or potential cycles were conducted, this procedure was repeated after the AFM images were completed.

An example for such an ex-situ AFM series is given in Figure 11.5. Figure 11.5 a and shows an AFM image of the $Cu_3Au(111)$ surface directly after preparation in UHV. Although the surface is still covered with a few thick islands, which are most probably residues from a former corrosion experiment, i.e. thick Au islands, LEED and AES indicated a clean and ordered $Cu_3Au(111)$ surface. The visible steps are approximately 2Å or multiples of 2Å high and correspond thus well to the {111} distance of Cu_3Au (2.167Å). The plot below the AFM image shows the surface height along the white line in the image. On the terraces a roughness with an amplitude of approximately 1Å (smaller than the {111} distance of Cu_3Au) is observed. The inset shows a part of the image that was con-

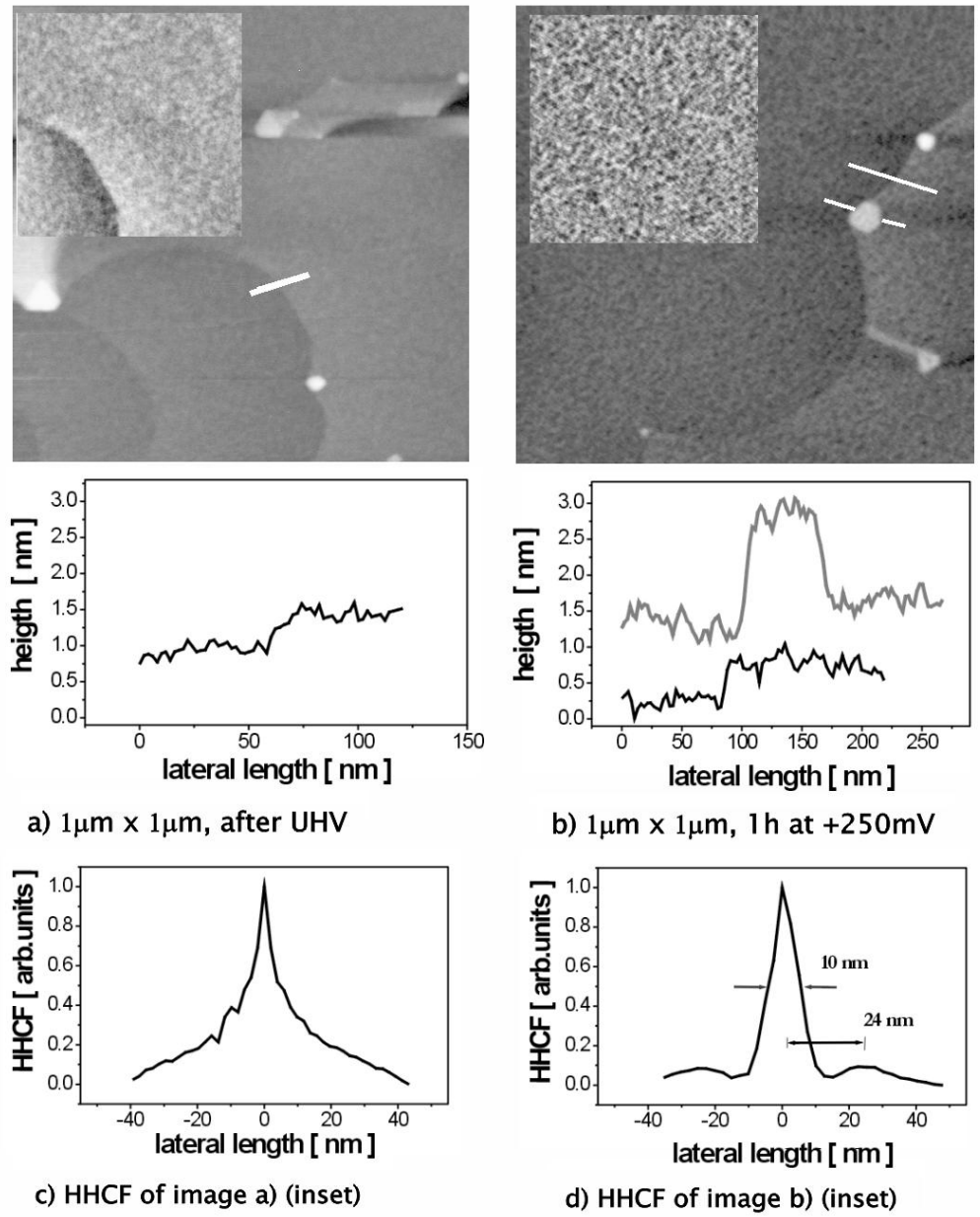

Figure 11.5: (a) AFM image and a typical line scan of a $Cu_3Au(111)$ surface after UHV preparation. The bright islands are probably residing Au islands of preceding corrosion experiments. (b)AFM image and typical line scans the surface after 1 hour of immersion in 0.1 M H_2SO_4 electrolyte solution at a potential of +250 mV(Ag/AgCl). (c) and (d) show the respective HHCF along the fast scan line. (d) shows correlation side peaks, (c) not. The inset shows a part of the image that was contrast enhanced.

trast enhanced for a clearer visibility. The HHCF (Fig. 11.5 c), calculated along the fast (horizontal) scan line, from this part, shows no distinctive correlation that could be associated with a homogeneous island size. The image in Figure 11.5 b shows the same surface, directly after the sample was immersed in 0.1 M H_2SO_4 electrolyte solution and held at a potential of +250 mV for 1 hour. This potential is well below the observed transition of a surface covered with the ultra-thin layer to the thicker Au islands (This transition potential was observed to be at 350-450 mV in our thin-film X-ray cell, see Chapter 10.2.2) and we therefore assume that we imaged ultra-thin islands. The height variations of the surface have clearly increased in comparison to the AFM image taken directly after the UHV preparation. The inset shows again a contrast enhanced part of the AFM image and the plot below the image includes the surface profile along the two white lines. The thick island is likely to be a residing Au island of a preceding corrosion experiment (before the sputter-annealing cycles in UHV). At this stage, the HHCF $C(\vec{r})$ in Figure 11.5 d clearly shows features due to a regular island distribution, which was not observed in the HHCF for Figure 11.5 a (Fig. 11.5 c). Two side peaks on either side of the central peak indicate an average island size and distance. The central peak has a FWHM of approximately 10 nm and the side peak appears at a distance of 24 nm, i.e. the average island distance is 24 nm. Note that the AFM tip specification for the tip curvature is 10nm and the images have not been corrected for tip curvature effects.

A second example for a series of AFM images is shown in Figure 11.6. The first image (a) was taken of the $Cu_3Au(111)$ surface directly after the preparation in UHV, where Auger Electron Spectroscopy (AES) and a LEED image indicated a clean and ordered surface. The visible steps are approximately 0.2nm high, which corresponds well to the Cu_3Au {111} layer distance of 0.217nm. Directly afterwards the sample was fixed to the clean standard electrochemical glass cell and immersed in 0.1 M H_2SO_4 electrolyte solution at a potential of -100 mV. Then several cycles of a cyclic voltammogram (CV) between -100 mV and +400 mV (Ag/AgCl) have been recorded. The CV was shown above (Fig. 9.3). Figure 11.6 b shows one of the AFM images that were recorded after the sample was taken out of the electrolyte. The surface is now densely packed with islands. The corresponding height-height autocorrelation function (HHCF) $C(\vec{r})$ along the horizontal (fast) AFM image line is shown in Figure 11.6 (d). Its central peak possesses a width of 13.5 nm for the image (b) and the maximums of the side peaks appear at a displacement of 38 nm. The distance of the side peaks corresponds to an average island-island distance. We will present below also Fourier transformed images, where a ring around the origin emerges, due to the average nearest-neighbor distance of the islands. The root mean square (rms) roughness for Figure 11.6 b is calculated with the help of the WSxM software

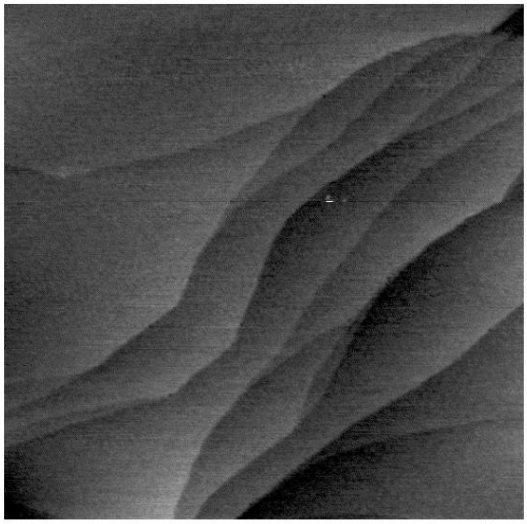

a) 1μm x 1μm, step heigth ~2Å

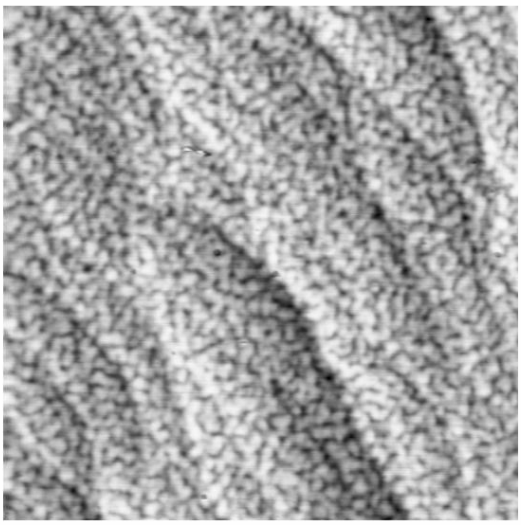

b) 1μm x 1μm, z_{max}= 5 nm

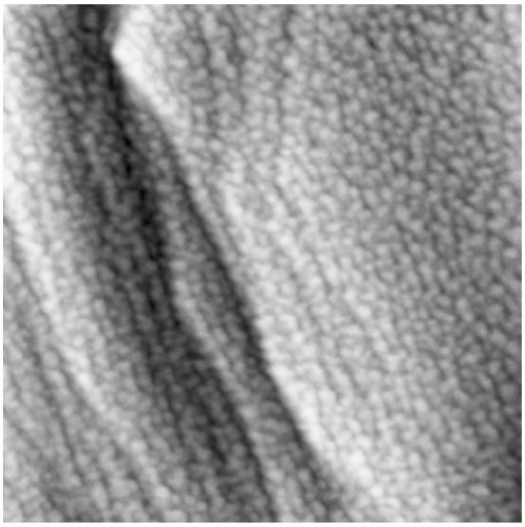

c) 1μm x 1μm, z_{max}= 10 nm

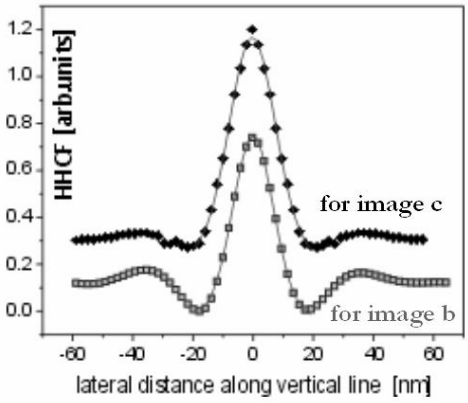

d) Autocorrelation Function for images b) and c)

Figure 11.6: (a) AFM image after UHV preparation. (b) Image of the same surface after performing several cycles of a CV between -100 mV and +400 mV (Ag/AgCl). (c) The same surface after a subsequent potential cycle to values slightly above the critical potential E_c. The CV's were shown in Figure 9.3. (d) The height-height autocorrelation function (HHCF) along the horizontal (fast) AFM image line.

to be 4 Å. In a second potential cycle, performed after the completion of the preceding AFM images, the potential was swept to values slightly above the critical potential with sweep rate of 5 mV/s. The corresponding CV curve was shown in Figure 9.3. The AFM image taken after this second potential cycle does not show a major change in the surface morphology. Nevertheless, an increased central peak width in the corresponding HHCF in Figure 11.6 (d) reveals a slightly enhanced island size. The FWHM of the central peak of the HHCF is in this case 15.4 nm. The root mean square (rms) roughness for Figure 11.6 c is 6 Å.

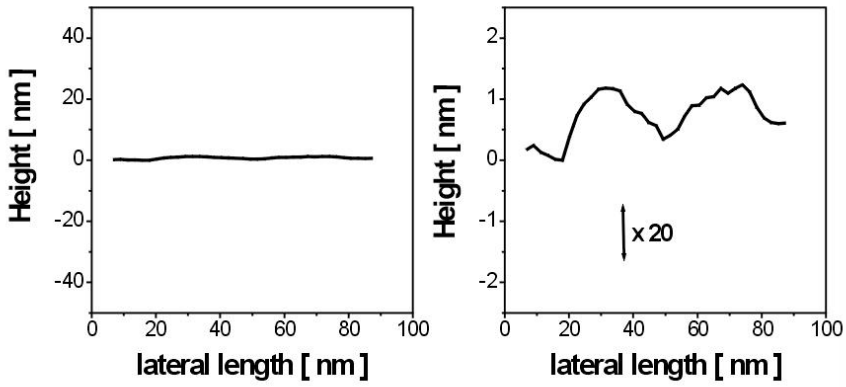

Figure 11.7: A typical line scan of an AFM image after corrosion at a potential of +400 mV. The lateral and the height scale of the left image are the same.

Figure 11.7 shows a typical linescan (taken from Fig. 11.6 (b)). The left image is ploted with equal scales for the lateral lenght and the height to show the real proportions. In the right image the height is enhanced by a factor of 20. Along the shown line an island height of about 1-1.5 nm can be seen. The result for the X-ray measurements of the thicker islands formed in the elevated potential region was a thickness of 1.5-3 nm. We still have to consider a possible tip size effect (the tip curvature is specified to be 10 nm), and also the islands might already merge. Therefore the AFM result for the island thickness has to be taken as a lower border of the true value and fits thus well to the X-ray diffraction result.

11.3 Discussion of AFM Images

Some of the in air AFM images of clean $Cu_3Au(111)$ surfaces directly after UHV preparation show a roughness of the surface on the scale of 1 Å, while others did not. As we measured the AFM images in air an initial oxidation might occur and produce the perceived roughness. Nevertheless, no clearly distinctive island structure could be observed after the UHV sputter-annealing cycles and the HHCF C(r) for the rough surfaces was essentially without features, showing only a broad central peak. Most of the imaged surfaces taken directly after the UHV preparation show only flat terraces and steps that correspond in height to the {111} distance of Cu_3Au. Only with a first dissolution of Cu in 0.1 M H_2SO_4 electrolyte solution at +250 mV (in the low overpotential range) the picture changes. Now the AFM images show clearly thin islands covering the surface (seen as an increased roughness and in the distinctive change of the height-height correlation function, showing now a side peak, Fig. 11.5). The average island distance of 24nm is the smallest value observed during our study, compared to about 40 nm for the dense islands and up to 140 nm for the porous surface morphologies. The enhanced height variation in the AFM image after the dissolution of Cu at +250 mV is of the order of 4 Å, but might well be limited due to the finite tip size (10 nm). During the X-ray measurements in this potential range, presented in the preceding chapter, we observed a growing ultra-thin Au-rich film of a thickness of 2-4 atomic layers, i.e. the values agree reasonably well.

With the corrosion at slightly higher potentials (around +400 mV and more), the islands become much clearer in the AFM images. All AFM images taken, either after a potential cycle (voltammogram) to 400 mV (with a sweep rate of 5 mV/s) or after applying directly a potential of 400 mV for 3 minutes, show surfaces densely covered with islands of a typical distance of around 40 nm. Figure 11.6 (b) shows an example for a corresponding AFM image and Figure 11.7 a typical linescan (taken from Fig. 11.6 (b)). The island height is around 1-1.5 nm according to the linescan in Figure 11.7, and corresponds well to the estimated island height from the respective X-ray L-scans presented above. Applying even higher potentials does not change the AFM image considerably, although for the example of Figure 11.6 (c) the rms roughness deduced from the images has increased from 4 Å(for the image 11.6 b) to 6 Å. This suggests that with ongoing Cu dissolution at this stage, the Au islands covering the surface grow in thickness. During this ex-situ AFM study of the initial corrosion of $Cu_3Au(111)$ we applied potentials up to values slightly above the critical potential E_c for short periods of time, and in no case we observed the open or porous surface morphology that we observed for the samples immersed in electrolyte for longer times during the X-ray measurements (as described above).

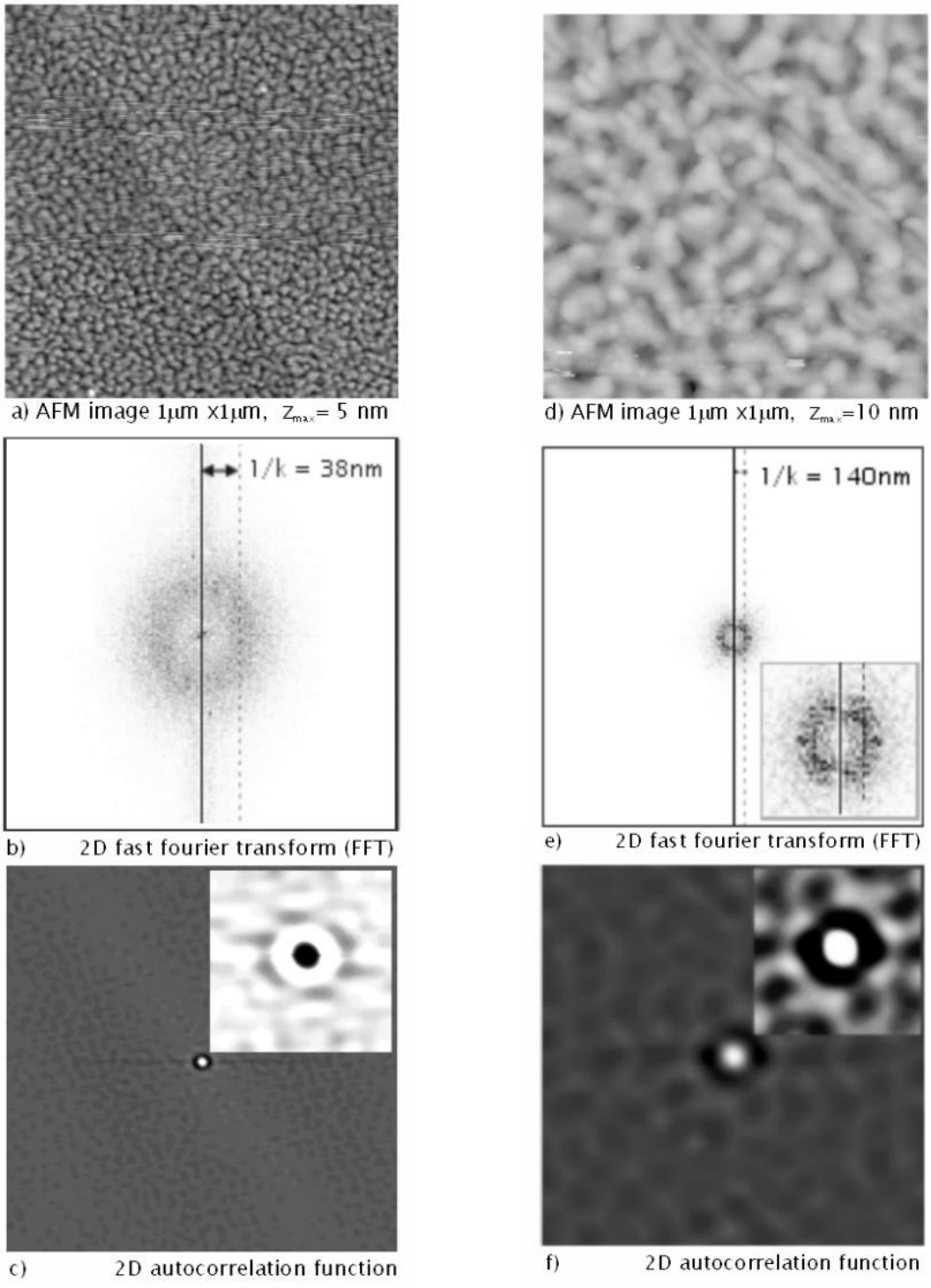

Figure 11.8: Two typical AFM images. One shows islands densely covering the surface (a), the other image reveals an open or porous surface structure (d). The derived 2D FFT shows the average island distance as a ring around the center (b and e). The 2D autocorrelation image reveals that the islands posses in average an ordered structure between nearest neighbors (c and f).

We have already presented some correlation functions above. All AFM images recorded after the dissolution of Cu from a $Cu_3Au(111)$ surface posses a distinctive ring in the 2D PSD plot and hexagonally arranged side peaks in the 2D HHCF. This is shown for two representative examples in Figure 11.8. The AFM images are both $1\mu m \times 1\mu m$ large. Figure 11.8a was recorded together with the image, shown in Figure 11.6 b, and Figure 11.8d was already shown before. The ring around the center in the 2D PSD plots reveals an average island distance of 38 nm for the densely packed surface (b) and 140 nm for the porous surface (e). The distance of the maximum of the PSD is marked as a vertical line in the plots. Similar formation and coarsening of a porous Au structure with selective electrochemical dissolution has been reported for a small angle neutron diffraction experiment at potentials above E_c for a Ag-Au alloy [ne94]. The 2D HHCF plots show a size of $1\mu m \times 1\mu m$ as the original AFM images. Six side peaks, which are hexagonally arranged around the central peaks, are clearly visible in both plots (c and f). The inset shows an enlarged region of the respective plots around the central peak. In some cases the hexagonal peak structure in the corresponding 2D HHCF is clearer when a smaller sized image is cut from a larger image, which might be associated with a missing clear long-range order of the islands.

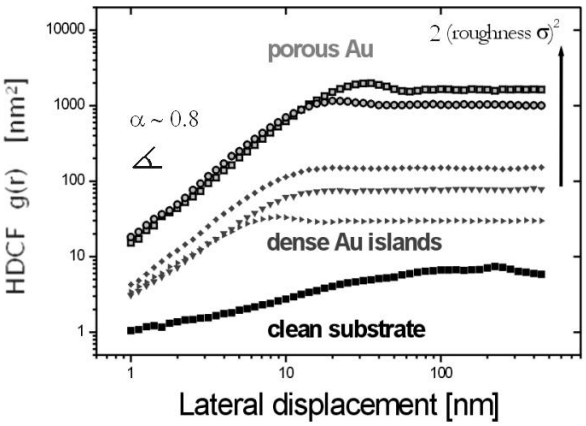

Figure 11.9: The HHCF for a selection of AFM images of the clean $Cu_3Au(111)$ surface (lowest curve) and after dissolution of Cu. The curves for the clean surface shows the smallest saturation value of the HDCF at large displacements, i.e. the smallest roughness. All curves after a dissolution of Cu show an initial increase of the HDCF value with a similar slope and saturate at displacements of about 10 to 30 nm.

The morphology of the $Cu_3Au(111)$ surfaces, after the dissolution of Cu, is dominated by the observed islands. The roughness that can be deduced using the standard AFM software, is thus strongly influenced by the island thickness. For the open or porous morphology that has been observed only with the long time scales of the X-ray measurements, the visible pores are also contributing to an increased rms roughness parameter. This can be seen in Figure 11.9, where the HDCF curves are shown for a selection of AFM images. The exact values show some variation for the different experiments, but a clear tendency

is that the roughness increases from the clean surface to the porous surfaces.

Many physical processes give rise to an ordered surface with patterns similar to our case. Examples are island formation during deposition (nucleation and growth) [sp98], mound formation with ion bombardment [ag01] of surfaces (interplay of different diffusion rates, e.g. at step edges) or spinodal decomposition [her98]. Many examples can be found in the literature. For more conclusive results further analysis and eventually further studies (e.g. in-situ electrochemical AFM with long time scales) are needed.

11.4 Conclusion for the AFM images

The change of surface morphology with the selective dissolution at potentials below E_c has been imaged with ex-situ in-air AFM. Clearly visible in the images are the islands that can be correlated with the thicker pure Au islands observed for the elevated sub-critical potentials with X-ray diffraction (as presented in the previous chapter). The lateral size, as well as the observed island thickness, fit well to the results of the X-ray diffraction, presented above. An interesting detail is the observed lateral correlation (HHCF or C(r)) of the formed islands that persist also for the porous morphology formed at longer time scales at sub-critical potentials. The average island distance that can be associated with the side peak of the HHCF reveals values of 24 nm for the first observation of (ultra-thin) islands at +250 mV, about 40 nm for the thicker islands at elevated potentials and up to 140 nm for the observed porous structures.

Chapter 12

Summary and Perspectives

It is now well established that detailed structural knowledge on the atomic scale is necessary to fundamentally understand materials and related processes and to tailor new modern materials and applications. This is also true for the economically very important process of electrochemical corrosion. With the performance of the first in-situ X-ray diffraction experiments for the selective electrochemical dissolution of Cu from $Cu_3Au(111)$ in pure and in Cl^- containing 0.1 M H_2SO_4 electrolyte solution we revealed a multitude of structural details. We used monocrystalline Cu_3Au alloy samples with well-defined low-index (111) surfaces and studied the dissolution below the critical potential E_c. The corrosion and related passivation is a non-reversible process that depends strongly on different parameters like time, potential, and e.g. electrolyte composition. This spans a multidimensional space of experimental parameters that can only be fully explored with a multitude of single experiments, and would be more efficiently achieved by exploiting a larger number of samples. We summarize here the main results of this work and give some perspectives that follow from our experience and results.

Summary of the Main Results

A schematic plot of the main results is shown in Figure 12.1. During the selective dissolution of Cu from $Cu_3Au(111)$ below the critical potential E_c we could observe the formation and structural changes of an epitaxial passivation layer. Above or at values positive of the equilibrium or Nernst potential of Cu (overpotentials) the dissolution of Cu starts. Two separated potential regimes below E_c were identified in pure 0.1 M H_2SO_4 solution, with a regime below a potential of about 350 mV (low overpotentials) and above 350 mV (elevated overpotentials).

Low Overpotentials

At low overpotentials (lower than about 350 mV vs. Ag/AgCl) we could observe the formation of an ultra-thin epitaxial (monocrystalline) passivation layer. The positions and widths of the according reciprocal Bragg reflections indicate islands of an lateral size of about 15 nm and a thickness of about 3 atomic monolayers (≈0.6 nm). The structure is Au-rich (Au_xCu_{1-x}) in comparison to Cu_3Au as can be clearly seen from the observed lattice constants. The anomalous diffraction measurements suggested a Cu content of 40% in the ultra-thin surface layer. The epitaxial relation of this ultra-thin layer to the substrate is $Au_xCu_{1-x}(111)\|Cu_3Au(111)$ for the surface/layer normal and $Au_xCu_{1-x}(1\bar{1}0)\|Cu_3Au(\bar{1}10)$) for the in-plane orientations, i.e. an inverted stacking of the {111}-planes of the surface structure. The second nearest neighbor coordination and their energetic differences have been suggested to determine this defined orientation. For the potential-controlled slow dissolution solely this inverted ultra-thin domains/islands have been observed for low overpotentials. At low overpotentials we could obtain ultra-thin islands that were stable in time. The analysis of the surface rod intensity from a stable ultra-thin layer revealed a structure consisting of two continuous atomic layers and one discontinuous third layer (50% occupancy) with an only by 5% occupied forth layer (ultra-thin layer). The data could essentially be understood with a fcc-like (slightly rhombohedrally distorted) structure of inverted stacking (i.e. a epitaxial orientation that is rotated by 60° or 180° with respect to the substrate stacking) on the $Cu_3Au(111)$ substrate.

Nevertheless, some deviations were observed. Especially the peaks on the $(0\ 1.9\ L)_s$ rod were shifted to lower values, while the peaks along the $(1.9\ 0\ L)_s$ rod were shifted to higher values. We related these deviations to defects that are present in the formed ultra-thin passivation layer (at room temperature an annealing of defects takes a comparatively long time due to low diffusion rates). For the composition we did, up to now, not obtain a conclusive result. While the deduced lattice parameters of some samples suggest a strained Au layer with very low Cu content, anomalous diffraction of other samples indicates a Cu content as high as 40%. The stable ultra-thin layer has values for its in-plane and out-of-plane lattice constants that are close to values calculated for freestanding ultra-thin (about 1 nm) Au layers by Wolf [wo91]. However, calculations for supported ultra-thin $Au(111)/Cu_3Au(111)$ layers are to our knowledge not in the literature.

Similar to the case of pure 0.1 M H_2SO_4 solutions, ultra-thin epitaxial islands are observed with 5 mM Cl^--ions present in the electrolyte. However, the regime of stability for this case ends already at about 200 mV, in agreement with a similar shift of the critical potential E_c in Cl^--containing electrolyte [mo91].

Ex-situ AFM images taken in the regime of low overpotentials indicate a regular formation of islands that give rise to a side peak at a distance of about 24 nm (average island distance) in the autocorrelation function (HHCF).

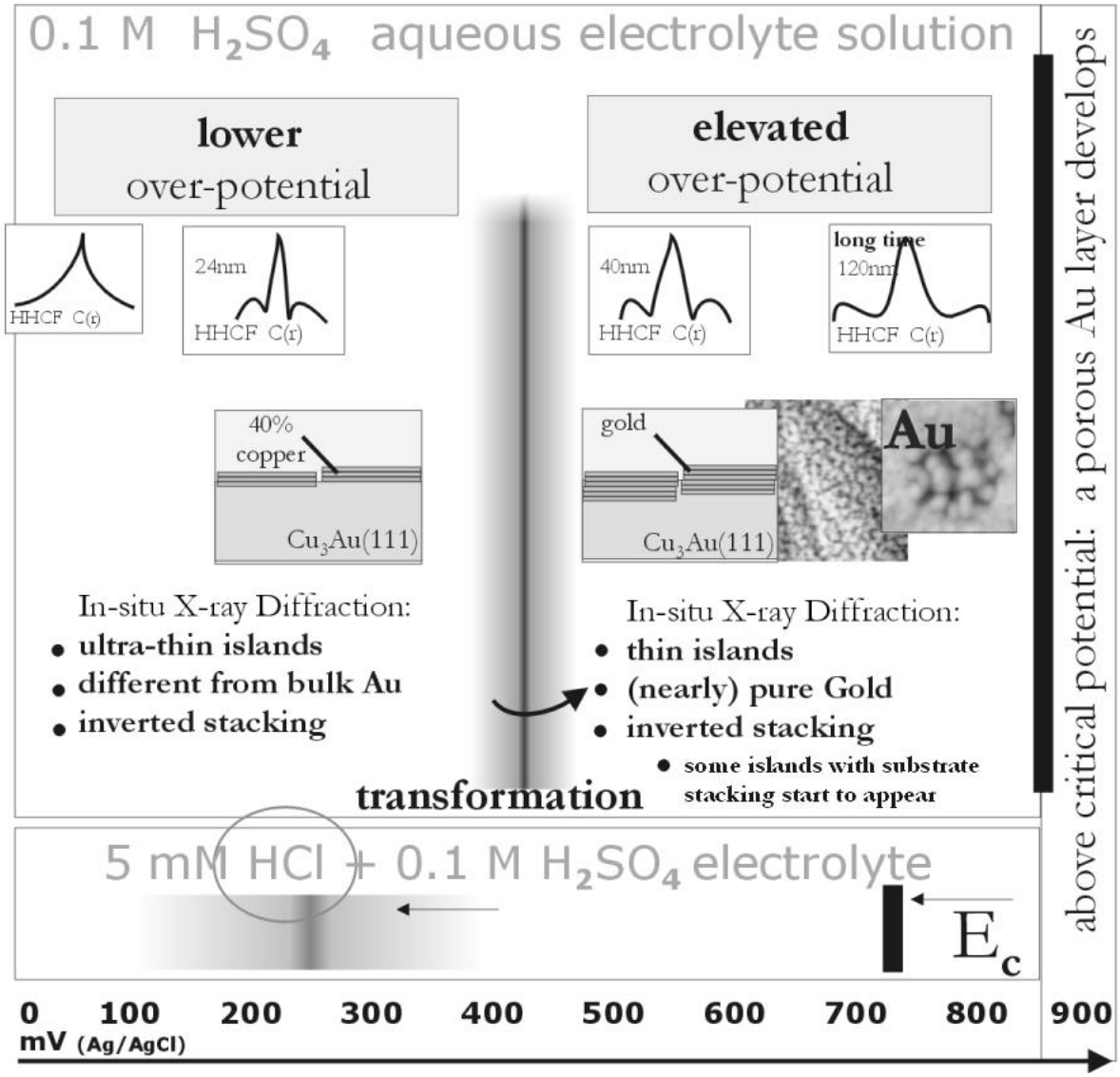

Figure 12.1: A schematic plot of the main results.

Elevated Overpotentials

At more anodic potentials (elevated overpotentials) the formation of thin Au islands with bulk Au structure is observed. The initially present ultra-thin islands vanished. X-ray diffraction, in agreement with ex-situ AFM images, indicate the formation of islands with

a thickness of about 3 nm and a lateral island size of about 20 nm. The AFM images reveal surfaces densely packed with islands of an average distance of about 40 nm. However, after X-ray experiments with the sample immersed in electrolyte at elevated potentials for more than one day, some regions on the sample showed a porous surface morphology with a distance between the observed islands or legaments of up to 140 nm. Both, images of large continuous porous areas, as well as images where the porous regions were distributed homogeniously as small patches of about 200 nm in diameter. Defect lines were decorated densely with these patches. Ex-situ specular X-ray diffraction obtained from samples that showed the surface densely packed with islands, as well as large porous areas, showed two distinctive lineshapes. A broad Au peak with a width corresponding to a layer thickness of about 5 nm was associated with the densely packed islands, while a sharper peak revealed an island thickness of about 15 nm (equal to the lateral size) and was associated with the porous areas. this suggests that the porous structure consists of Au legaments of an isotropic average diameter.

For a more rapid increase of potential in pure and in Cl^--containing 0.1 M H_2SO_4 solutions, we observed a continuous shift of the in-plane lattice constant in the elevated regime from the position for the ultra-thin layer to the epitaxial bulk Au position.

The growth of the thin pure Au layer at elevated potentials resulted in an equal epitaxial orientation as the ultra-thin islands at lower overpotential, i.e. in anti-parallel epitaxial pure or nearly pure Au islands. Nevertheless, a small contribution of the twin island/domain (i.e. the parallel orientation on the substrate) is observed for the elevated potential regime. At higher potential the contribution gets more pronounced. With the loss of potential control (i.e. a very high dissolution rate for a short time at very anodic potentials) we observed layers with up to a 50% contribution of the parallel oriented islands.

Future Perspectives

Further important experiments that are suggested here are addressing the time dependence at different potentials of the epitaxial growth of the passivation layer on $Cu_3Au(111)$:

- Potential steps from below the Cu Nernst potential to defined potentials in the low and the elevated potential regime might reveal potential dependent differences e.g. in the partial occurrence of the anti-parallel and the parallel aligned islands. Also the occurrence of strain in the substrate surface at certain potentials (as observed on the samples after loss of potential) might give information on the formation mechanisms.

- Using higher X-ray energies we started already to follow the in-plane peaks at H=K=1.84 (Au) and H=K=1.9 with the help of a position sensitive detector (PSD) at an intermediate incident angle, but nevertheless exciting both Bragg peaks simultaneously, and thus recording data without moving detector or sample and obtaining a much better time resolution. We showed the feasibility of such an experiment at 17 keV. Transmission cells should be further developed.

- Similar experiments might reveal different results for present additives in the electrolyte. Besides the experiments with Cl^--ions (which are known to enhance surface diffusion) also the presence of corrosion inhibitors, like e.g. Thiol molecules, are promising candidates.

- Similar studies on $Cu_3Au(001)$ (and other surface orientations) might give interesting additional insights. On Au(001) a hexagonal reconstruction is reported. A comparison of the behavior of $Cu_3Au(001)$ and $Cu_3Au(111)$ is thus promising.

In addition to X-ray measurements at synchrotron radiation facilities we suggest other experiments that might give important insight in revealing the mechanisms of corrosion and passive layer formation of alloys:

- In-situ AFM studies might reveal important knowledge of the formation of the island structures and there time dependence.

- Cross-sectional atomic resolution transmission electron microscopy (HRTEM) might reveal important information for the structure of the interface between the substrate and the Au-rich islands.

- In-situ FTIR in electrolyte might reveal information of adsorption of sulfate (SO_4^{2+}) on the different structures.

- For Ag-Au alloy single crystals (Ag and Au have nearly identical lattice constants) CTR measurements or high-resolution reflectivity might reveal a Au enrichment of the surface. The system Cu^{2+}/modified-Ag_xAu_{1-x} might give important results, also for the behavior of Cu-Au alloys, e.g. by exploring Cu UPD layers.

Chapter 13

Acknowledgements

This thesis would not have been possible without the many people, colleagues and friends, who taught me, helped me, advised me, and encouraged me during the last years.

I would like to express my deepest gratitude to my thesis adviser, Professor Dr. Helmut Dosch, for his support. He assured a constant backup for my work. I am thankful for having had the chance to be a member of his group and share its many ups and few downs during the last years.

I am grateful to Professor Dr. Clemens Bechinger for having accepted the duties of the second referee. I hope I could offer him some new insights in an interesting field of research.

Privat Dozent Dr. Jörg Zegenhagen suggested the subject and always supported its progress. He never imposed his ideas and encouraged me to follow my own way. The door to his office was always open -and not only when I had problems with the english language. Thank you.

I am thankful to Dr. Andreas Stierle for his constant interest in my work. I learned a lot from him, during many discussions about crystal truncation rods and synchrotron radiation. Some important experiments, performed during this thesis, are based on his suggestions.

I acknowledge Professor Dr. Dieter M. Kolb for welcoming me at his Institute in Ulm. I learned what Electrochemistry is nowadays, by discussing with the members of his group, and especially with his students Alexander Reizle and Michael Schweizer I could collaborate later on.

I owe my thanks to many members of the Department Dosch at the Max-Planck-Institut

für Metallforschung in Stuttgart. I was relying on the support and help of many people during the preparation and performance of beamtimes and during my visits in Stuttgart. I owe a lot to Herrn Kammerlander from the glassblower workshop, Herrn Henes and Herrn Keppler from the Crystal Growth Laboratory, Ioan Costina, Arndt Dürr, Nikolai Kasper, Bärbel Krause, S.Kumaragurubaran, Harald Reichert, Alexander Reicho, Kenneth Ritley, Reinhard Streitel, Carsten Tieg, Ralf Weigel, Annette Weißhardt and Hubert Zajons. And I owe my thanks to all colleagues in Stuttgart for creating a pleasant atmosphere during my stays in Stuttgart.

I am grateful for the cooperative atmosphere at the ESRF that made my stay in France so special. Lionel André, Bruce C.C. Cowie, Helena Isern, Tien-Lin Lee, Christian Rettig, Manuel Perez, Thomas Schröder, Sebastian Thiess and Samantha Warren helped me with technical support and to conduct the measurements at ID32 and HASYLAB, Hamburg. Irina Snigireva provided some SEM images and Au contacts. Tobias Schülli treated my Cu absorption edge with his program for Kramers-Kronig transformations. The mechanical workshops manufactured my in-situ cells and Faraday cages. The staff of the detector pool provided excellent service and the safety group was always cooperative. Thank you all.

I am happy for having been given the opportunity to work in the Electrochemistry Laboratory, which is a collaboration of Roberto Felici from the INFM-OGG in Grenoble and ID32, ESRF. The expertise of Fabio d'Anca for the design of my in-situ electrochemical cell has essentially contributed to the success of my experiments.

Furthermore I want to thank Prof. M.Asta and Prof. J.Krug for discussion and for sharing their knowledge.

I also want to acknowledge the staff of HASYLAB, Hamburg for the professional support during my measurements at the beamline BW2.

Many of the mentioned people were not only professionally working colleagues, but became friends in the many necessary coffee breaks during the long working days and many night shifts. Thank you for your friendship.

Last but not least, all members of my family, especially my parents, were always there in the background. The farm holidays (Ferien auf dem Bauernhof) were always a relaxing alternative to the academic world.

I want to thank Alina for her love and understanding.

Appendix A

List of Acronyms

AES	Auger Electron Spectroscopy
ANKA	Ångstømquelle Karlsruhe
AFM	Atomic Force Microscope
CE	Counter Electrode
CTR	Crystal Truncation ROD
DAFS	Diffraction Anomalous Fine Structure
DWBA	Distorted Wave Born Approximation
EC-AFM	In-situ Electrochemical AFM
EC-STM	In-situ Electrochemical STM
ESRF	European Synchrotron Radiation Facility
FT	Fourier Transformation F
FTIR	Fourier Transform Infrared Spectroscopy
FWHM	Full Width at Half Maximum
GID	Grazing Incidence Diffraction
HASYLAB	Hamburg Synchrotron Laboratory
HDCF	Height-Difference Correlation Function (H(r) or g(R))
HHCF	Height-Height Correlation Function C(r)
LEED	Low Energy Electron Diffraction
MBE	Molecular Beam Epitaxy
ML	Monolayer

NC-AFM	Non-Contact Atomic Force Microscopy
RE / Ref	Reference Electrode
SCE	Saturated Calomel Electrode
SHE	Standard Hydrogen Electrode
SPM	Scanning Probe Microscope
STM	Scanning Tunnelling Microscope
SXRD	Surface Sensitive X-Ray Diffraction
UHV	Ultra High Vacuum
WE	Working Electrode
XRD	X-Ray Diffraction
XSW	X-ray Standing Wave Technique

Appendix B

Adopted Surface Coordinates

The reciprocal space is defined by the vectors a*, b*, and c*. They depend directly on the chosen real space unit cell.

$$\vec{a}^\star = 2\pi \times \frac{\vec{b} \times \vec{c}}{\vec{a} \cdot (\vec{b} \times \vec{c})} \tag{B.1}$$

Usually the common (bulk) unit cells are chosen. For the fcc metals like Au, Cu, Cu_3Au this is the well known cubic cell, with four atoms in the basis. The unit vectors are the same than for a simple cubic one, i.e. all vectors are perpendicular. For surface science experiments an adopted unit cell is chosen, so that the z-axis of the real space unit cell corresponds directly to the L-axis of the reciprocal space. With such an adopted unit cell it is easy to distinguish between in-plane and out-of-plane components of the scattering vector. A CTR can be labeled with two in-plane components (e.g. 10L, 22L, ...). In LEED images it has been established to take the points closest to the origin to define the in-plane components. For the out-of-plane vector there are two possibilities: the first one takes the first reflection on the 00L Rod to be the c* axis, and the second one is to chose the length of c*, so that all Bragg reflections can be labeled with integer L. We label all Bragg reflections with integer L, i.e. the first specular Bragg peak of $Cu_3Au(111)$ is $(003)_s$, which is equal to the $(111)_{cubic}$ reflection.

$$\begin{pmatrix} a \\ b \\ c \end{pmatrix}_{bulk} = \begin{pmatrix} x_{11} & x_{12} & x_{13} \\ x_{11} & x_{12} & x_{13} \\ x_{11} & x_{12} & x_{13} \end{pmatrix} \times \begin{pmatrix} a \\ b \\ c \end{pmatrix}_{surface} \tag{B.2}$$

In general a coordinate transformation can be performed by multiplication of the original coordinate vector with a transformation matrix.

We used for our measurements the following matrix for the transformation from our

hexagonal coordinates $(HKL)_s$ to the fcc coordinates (HKL):

$$\begin{pmatrix} a \\ b \\ c \end{pmatrix}_{cubic} = \begin{pmatrix} 2/3 & 1/3 & 1/3 \\ -1/3 & 1/3 & 1/3 \\ -1/3 & -2/3 & 1/3 \end{pmatrix} \times \begin{pmatrix} a \\ b \\ c \end{pmatrix}_{hexagonal} \tag{B.3}$$

Figure B.1 shows the fully ordered surface of $Cu_3Au(111)$. The dark circles are the Au atoms. The surface unit vectors of the adopted surface coordinates are also shown. In Figure B the reciprocal space is shown with both nomenclatures, the fcc indices in the top row and the surface indices at the bottom.

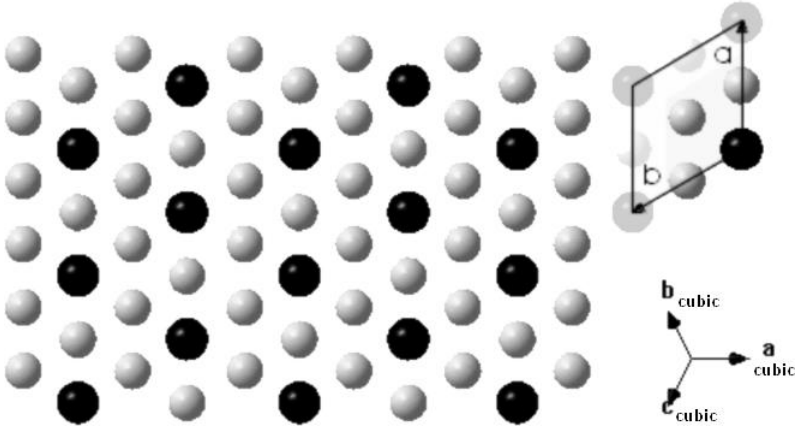

Figure B.1: The fully ordered top layer of the (111) surface of Cu_3Au. Dark circles are Au atoms. The cubic unit vectors are shown.

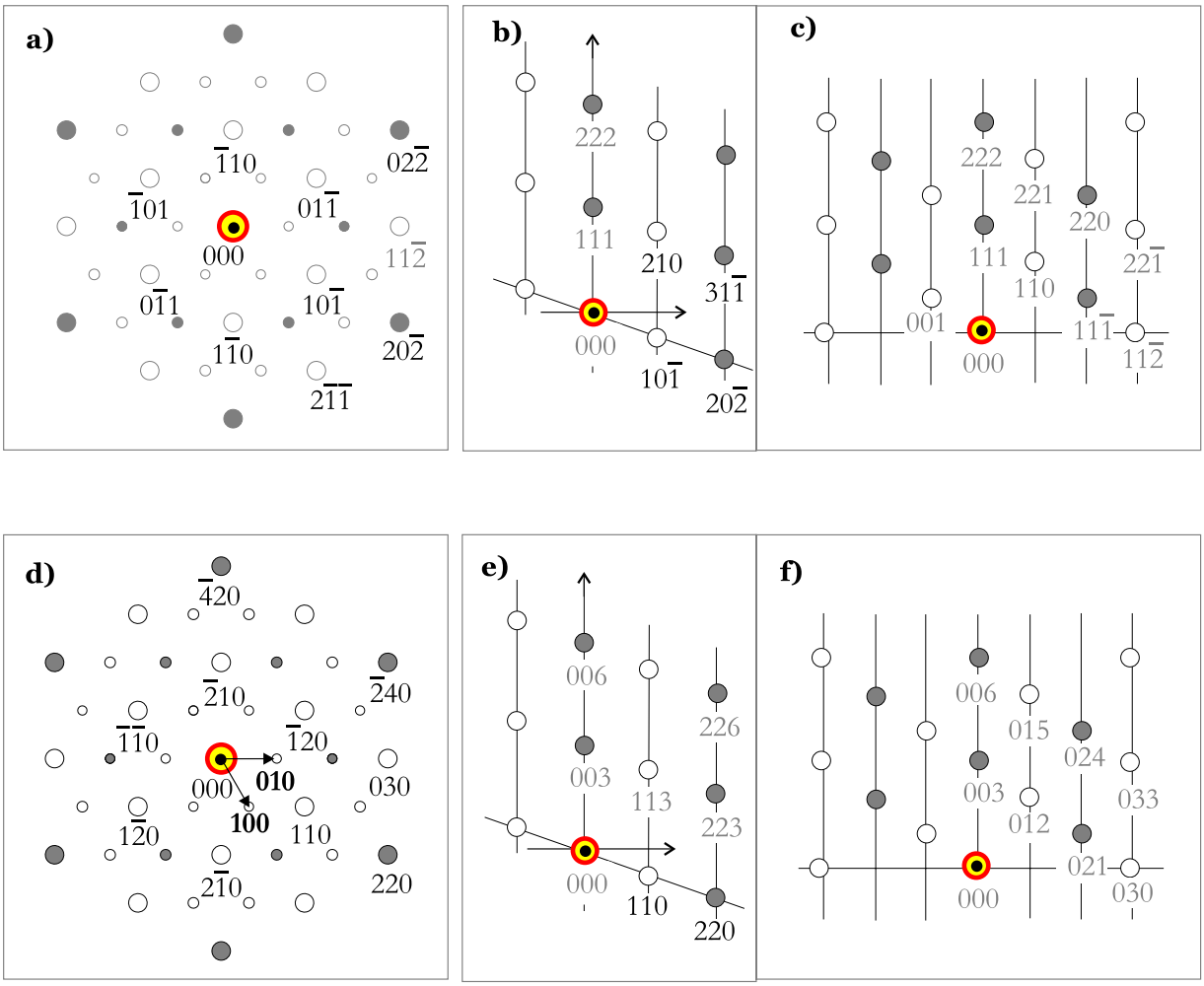

Figure B.2: Reciprocal map in usual bulk coordinates (a-c) and in surface adapted coordinates used in this work(d-f). In-plane maps are shown in a and b. Big circles correspond to Bragg reflections, small circles in the in-plane maps indicate intensity due to a intersected CTR. Filled circles represent fundamental (allowed reflections in a fcc lattice) and open circles are due to superstructure reflections or CTR's.

Appendix C

Strains in Pseudomorphic Heterolayers of Cubic Materials

Based on Hook's law, the relationship between the stress (σ) and strain (ε) in a solid can be described by

$$\sigma_{ij} = C_{ijkl}\varepsilon_{kl} \qquad i, j, kandl = 1, 2, or3, \tag{C.1}$$

where the four-rank tensor C_{ijkl} contains the 81 stiffness constants (also called elastic constants) of the respective solid. σ and
varepsilon are both second-rank tensors with there first index representing the directions of the stress and strain fields and their second index the normal directions of the surfaces that the fields are applied to. Due to symmetry of C_{ijkl}, equation C.1 can be simplified to a matrix form:

$$\sigma_i = C_{ij}\varepsilon_j \qquad iandj = 1, 2 \ldots, 6. \tag{C.2}$$

In this notation i or j (1, ..., 6) denote the former 11, 22, 33, 23/32, 31/13 and 12/21 of the original matrix notation of Equation C.1.

It can be shown that for cubic crystals, with the axis (**a** , **b** and **c**) of the cubic unit cell, most of the matrix elements C_{ij} vanish and C_{11}=C_{22}=C_{33}, $C_{12} = C_{13} = C_{23}$ and $C_{44} = C_{55} = C_{66}$:

$$\begin{pmatrix} \sigma_1 \\ \sigma_2 \\ \sigma_3 \\ \sigma_4 \\ \sigma_5 \\ \sigma_6 \end{pmatrix} = \begin{pmatrix} C_{11} & C_{12} & C_{12} & 0 & 0 & 0 \\ C_{12} & C_{11} & x_{12} & 0 & 0 & 0 \\ C_{12} & C_{12} & x_{11} & 0 & 0 & 0 \\ 0 & 0 & 0 & C_{44} & 0 & 0 \\ 0 & 0 & 0 & 0 & C_{44} & 0 \\ 0 & 0 & 0 & 0 & 0 & C_{44} \end{pmatrix} \times \begin{pmatrix} \varepsilon_1 \\ \varepsilon_2 \\ \varepsilon_3 \\ \varepsilon_4 \\ \varepsilon_5 \\ \varepsilon_6 \end{pmatrix} \tag{C.3}$$

Element	C_{11}	C_{12}	C_{44}
Cu	168	121	75
Cu_3Au	191	138	66
Au	186	157	42

Table C.1: Values for the stiffness or elastic constants (GPa) of Cu and Au. Taken from [sim].

Often observed for the growth of a thin cubic (001) heteroepitaxial layer on a substrate is a pseudomorphic growth mode, where the growing layer adopts to the lattice of the substrate in direction of **a** and **b** (i.e. $\varepsilon_1 = \varepsilon_2 = \varepsilon_\parallel$in the surface plane) and grows in thickness (**c**-direction). The film is then constrained to have the same in-plane lattice parameters as the substrate, while it is free to relax in the growth direction **c**. This means that the strain in **c** direction is zero (σ_3=0, no constraint). From Equation C.5 we can thus deduce for the case of (001)‖(001) interfaces:

$$\sigma_3 = C_{12}(\varepsilon_1 + \varepsilon_1) + C_{11}\varepsilon_3 \qquad \longrightarrow \qquad \varepsilon_\perp = \varepsilon_3 = -2 \quad \frac{C_{12}}{C_{11}} \quad \varepsilon_\parallel. \tag{C.4}$$

The situation for an (111)‖(111) film-substrate interface can be derived in a similar way, if the used coordinate system is transformed from the normal cubic coordinates **r**(**a**, **b**, **c**) to the new adopted coordinates **r'**(**a'**, **b'**, **c'**) with the c'-axis parallel to the (111) film/substrate normal. This can be achieved with applying the following transformation matrix, which contains an azimuthal angle ϑ that can be arbitrarily chosen:

$$a_{ij} = \begin{pmatrix} \cos\vartheta - 1/\sqrt{2}\cdot\sin\vartheta & \cos\vartheta + 1/\sqrt{2}\cdot\sin\vartheta & -2\cos\vartheta \\ -\sin\vartheta - 1/\sqrt{2}\cdot\cos\vartheta & -\sin\vartheta + 1/\sqrt{2}\cdot\cos\vartheta & 2\sin\vartheta \\ 1/\sqrt{2} & 1/\sqrt{2} & 1/\sqrt{2} \end{pmatrix} \tag{C.5}$$

This matrix transforms the coordinates ($\mathbf{r'}_j$=$a_{ij}\cdot\mathbf{r}_j$) and the tensors (C'_{ijkl}=$a_{im}a_{jn}a_{kp}a_{lq}C_{mnpq}$ and σ'_{ijkl}=$a_{im}a_{jn}a_{kp}a_{lq}C_{mnpq}\sigma'_{kl}$). Similar to Equation C.4 it follows:

$$\sigma'_3 = \frac{1}{2}\left((c_{11} + 2c_{12} - 2c_{44}\varepsilon'_1) + (c_{11} + 2c_{12} - 2c_{44})\varepsilon'_2 + (c_{11} + 2c_{12} + 4c_{44})\varepsilon'_3\right) \tag{C.6}$$

and finally for the (111)‖(111) film-substrate interface:

$$\varepsilon_{\mathrm{cot}} = -\left(\frac{2C_{11} + 4C_{12} - 4C_{44}}{C_{11} + 2C_{12} + C_{44}}\right)\varepsilon_\parallel \tag{C.7}$$

For the materials Cu, Cu_3Au and Au the values for the stiffness constants [sim] are given in Table C.1.

Appendix D

ANAROD and Correction Factors

ANAROD is a computer program initially written by Elias Vlieg [vl00]. The program package has essentially two parts: ROD for fitting structural models to the data, and ANA for extracting integrated intensities and apply correction factors to the data from the usually performed angular rocking scans.

Integrated Intensities and Correction Factors

X-ray Diffraction data is usually collected by diffractometers of different types. The measured diffraction data has to be corrected by geometrical correction factors before any quantitative analysis. The use of different diffractometers results in different correction factors. For further details and for different diffractometer types, the reader is referred to the literature [vl87][vl97][vl98][ro00] [ev95]. This section follows basically the description given by Vlieg [vl97], and the respective 6-circle diffractometer, with its definition of the angles, was shown in Figure 5.2. The measurements at different points in reciprocal space imply different angles of the used detector towards the sample and towards the incoming beam. The used slits are usually fixed during the entire measurements. For a measurement performed by angular rocking scans at the respective L-value and including the main correction factors, the measured (integrated) intensity $I_{int,\omega}$ can be related to the respective calculated intensity I_{calc} by:

$$I_{calc} = I_{int,\omega} \cdot L_{\varphi} \cdot P \cdot C_{rod} \cdot C_{area} \tag{D.1}$$

with the polarization factors P, the Lorentz factor for an angular ω-scan L_{φ}, the correction for the angle-dependent active area C_{area} and the correction for the rod interception. The respective correction factors for the case of the 6-circle diffractometer are shortly described in the following.

The Polarization Factor

As all our X-ray measurements were performed with synchrotron radiation, we only consider horizontal polarization. The intensity for an observation at an angle α_{pol} to the direction of the polarization is given by $\cos^2\alpha_{pol}$. Expressed in the angular coordinates of the 6-circle diffractometer considered here, we obtain:

$$P_{hor} = 1 - (\sin\alpha\cos\delta\cos\gamma + \sin\gamma\cos\alpha)^2 \tag{D.2}$$

The Lorentz Factor for the 6-circle Diffractometer

The measurements with the diffractometer are performed in real space, i.e. limited by detector acceptance angles, which are determined by the detector slits. As the integration is performed in reciprocal space, the necessary transformation of the angular integration variables to reciprocal space variables, includes a geometrical correction in integration volume and is usually called the Lorentz factor L_φ:

$$L_\varphi = 1/\sin\delta\cos\beta_{in}\cos\gamma \tag{D.3}$$

The definition of the angles can be found in Figure 5.2.

The Rod Interception for the 6-circle Diffractometer

The projection of the detector aperture along the rod is changing with different L-positions due to the altered angular positions of detector and sample. This implies that the performed angular rocking scan cuts a different part of the rod and the measured intensities have to be corrected for this effect. This is done by the rod intersection correction C_rod. For the 6-circle diffractometer we obtain a lengthy expression:

$$C_{rod} = \frac{2\,\cos\beta_{in}\cos\gamma}{\cos\alpha\cos(\alpha - 2\,\beta_{in}) + \sin(2\,\alpha - 2\,\beta_{in})\sin\gamma + 2\sin(\alpha - \beta_{in})^2\cos\delta\cos\gamma} \tag{D.4}$$

The Active Area for the 6-circle Diffractometer

The incoming beam of lateral size s_1 and the detector slit width along the sample surface s_2 are defining the active area of the sample surface, i.e. not the entire surface contributes to the intensity measured with the detector. In addition the detector acceptance has to be projected on the surface. The correction for the active area is then determined by:

$$C_{area} = 1/\sin\delta\cos\alpha - \beta_{in} \tag{D.5}$$

Definition of χ^2

For the comparison of calculated intensities $|A_{hkl}^{calc}|^2$ and the measured data $|A_{hkl}^{exp}|^2$, ROD uses the usual definition of χ^2:

$$\chi^2 = \frac{1}{N-P} \sum \left(\frac{|A_{hkl}^{calc}|^2 - |A_{hkl}^{exp}|^2}{\sigma_{hkl}} \right) \tag{D.6}$$

where N is the number of measured data points of integrated intensity, P is the number of parameters, and σ_{hkl} the respective error bars of the data. For a comparison of different models with different number of parameters, the parameters were fixed after each fit and only one parameter for the intensity scale was subsequently used to obtain comparable numbers with equal P.

The β-Model for Surface Roughness

In general, surface roughness always leads to a decrease in diffracted intensity. This fact can be expressed with a single roughness factor R_β: I_{corr}=$R_\beta \times I_{calc}$. A very simple model is used by ROD, which is called the β-model and in which the surface levels n have an occupancy of β^n. Although the calculation might be complicated, a formula that is often valid is:

$$R_\beta = (1-\beta)\left((1-\beta)^2 + 4\beta \sin \pi (l - l_{Bragg})/N_{layers}{}^2\right]. \tag{D.7}$$

N_{layers} is the number of layers in the unit cell and l_{Bragg} is the L-value of the nearest Bragg peak.

Bibliography

[ab] Handbook of Mathmatical Functions, ed. M. Abramovitz and I.A. Stegun, National Bureau of Standarts, Washington, 1972

[ach93] H. Niehus, C. Achete, Surf.Sci.**289**, 19-29 (1993)

[ag01] M. Aguilar, E. Anguiano, J. A. Aznarez, J. L. Sacedon, Rough Growth Fronts of Evaporated Gold Films, Compared With Self-Affine and Mound Growth Models, Surf.Sci.**482** 935 (2001)

[al86] J. Als-Nielsen, Physica 140A(1986) 376-389

[al00] Jens Als-Nielsen, Des McMorrow, Elements of Modern X-ray Physics, John Wiley & Sons Ltd., Chichester , England 2000.

[at83b] B.G. Ateya, H.W. Pickering, The Effects of Potential and Kinetic Parameters on the Formation of Passivating Noble Metal Rich Surface Layers During the Selective Dissolution of Binary Alloys, Corr.Sci. **23** (1983) 1107

[at85] A. Atkinson, Reviews of Modern Physics **57** (1985) 437.

[aug] L.E. Davis, M.C.MacDonnald, P.W. Palmberg, G.E. Riach, R.E. Weber, Handbook of Auger Electron Spectroskopy, 2.Edition., Eden Prairie: Perkin-Elmer Corp. 1978

[aug26] P. Auger, Compt. Rend. (Paris) 177, (1923) 169; Ann.Phys.(Paris) 6,(1926), 183; historic review: Surf.Sci. 48 (1975) 1

[ba90] J. V. Barth et al., Phys.Rev.B **42**, 9307 (1990)

[ba96] H. Niehus, Th. Baumann, M. Voetz, K. Morgenstern, Surf.Rev.Lett.**3**, 1899 (1996)

[bi82] G. Binnig, H. Rohrer, Ch. Gerber, E. Weibel, PRL **49**(1982)

[bi99] G. Binnig, H. Rohrer, In Touch with Atoms, Rev.Mod.Phys.**71**, 324(1999)

[bo96] S.W. Bonham, C.W. Flynn, Resonant RHEED Study of $Cu_3Au(001)$Surface Order, Surf.Sci.**380**(1996) L760

[bw] Born and Wolf, Principles of Optics, Pergamon Press, Oxford, 1970

[br94] H. Brune, H. Röder, C. Boragno, K. Kern, Strain Relief at Hexagonal-Close-Packed Interfaces, Phys.Rev.B **49**, 2997 (1994)

[bu82] T.M. Buck, G. H. Wheatley, and L. Marchut, Phys.Rev.Lett.**51**, 43 (1983)

[ca02] E. Casero, C. Alonso, J.A. Martin-Gago, F.Borgatti, R.Felici, F. Renner, T.L.Lee, J.Zegenhagen, Nitric-oxide adsorption and oxidation on Pt(111) in electrolyte solution under potential control, Surf.Sci. 507 (2002), 688-694

[ch97] Y. S. Chu, I. K. Robinson, A. A. Gewirth, Properties of an electrochemically deposited Pb monolayer on Cu(111), Phys.Rev.B.**55**, 7945 (1997)

[chj93] J. S. Chen, M. Salmeron and T. M. Devine, Intergranular and Transgranular Stress Corrosion Cracking of Cu-30Au, Corr.Sci.**34**, 2071 (1993)

[chs93] S.J. Chen et al., Selective Dissolution of Copper from Au-rich Cu-Au Alloys: An Electro-Chemical STM Study, Surf.Sci.**292**, 289 (1993)

[cl80] J. Clavilier, R. Faure, G. Guinet, R. Durand, Preparation of Monocrystalline Pt Microelectrodes and Electrochemical Study of the Plane Surfaces Cut in the Direction of the {111} and {110} Planes, J.Electroanal.Chem. **107**, 205 (1980)

[co95] F. Comin, A cryogenically cooled, sagital focusing scanning monochromator for ESRF, Rev.Sci.Instr. **66**, 2082 (1995)

[cou90] D.J. Coulman, J. Wintterlin, R.J. Behm, G. Ertl, Phys.Rev.Lett. **64**, 1761 (1990)

[corr] Corrosion Cost and Preventive Strategies in the United States, NACE Publication No. FHWA-RD-01-156, 2002 (Web site: www.nace.org)

[cow50] J.M. Cowley, Phys.Rev.**77**, 667 (1950)

[cow95] J.Cowley, Diffraction Physics, Elsevier Science B.V., 3rd edition (1995)

[cu78] Cullity, B.D., Elements of x-ray diffraction, Addison-Wesley, Reading (1978)

[dat] Arthur L. Robinson, in: X-ray Data Booklet, Chapter 2.2, LBNL, Berkeley. This chapter with more details: http://xdb.lbl.gov

[de96] M. C. Desjonqueres and D. Spanjaard, Concepts in Surface Physics, Springer, 1996

[du97] D. J. Dunstan, Review: Strain and Strain Relaxation in Semiconductors, J.Mat.Sci.**8**, 337-375 (1997)

[do86] H. Dosch, B. W. Batterman, and D. C. Wack, Depth Controlled Grazing-Inzidence Diffraction of Synchrotron X Radiation, Phys.Rev.Lett. **56, 1144 (1986**

[do87] H. Dosch, Evanescent Absorption in Kinematic Surface Bragg Diffraction, Phys.Rev.B **35, 2137 (1987**

[do91] H. Dosch, L. Mailänder, H. Reichert, J. Peisl, Long Range Order Near the $Cu_3Au(001)$ Surface by Evanescent X-ray Scattering, Phys.Rev.B **43, 13172 (1991**

[do92] H. Dosch, Critical Phenomena at Surfaces and Interfaces, Springer Tracts in Modern Physics **126**, (1992)

[do00] H. Dosch, H. Reichert, Ordering, Disordering and Segregation at Binary Interfaces: Model System $Cu_3Au(001)$, Acta.mater.**48** , 4387 (2000)

[ec01] Gerald A. Eckstein, In-situ Rastertunnelmikroskopische Untersuchungen zur selektiven Korrosion von niedrigindizierten $Au_3Cu(hkl)$ und $Cu_3Au(hkl)$ Legierungseinkristallen, Dissertation, Erlangen 2001

[ed94] G. J. Edens, X. Gao, and M. Weaver, J.Electroanal.Chem **375**, 357 (1994)

[er01] J. Erlebacher, M. J. Aziz, A. Karma, M. Dimitrov, K. Sieradzky, Evolution of Nanoporosity in Dealloying, Nature **410**, 450 (2001)

[ern00] C. Ern et al., Phys.Rev.Lett.**85**, 1926 (2000)

[ern01] C. Ern, Dissertation, University of Stuttgart (2001)

[ert85] G. Ertl, J. Küppers, Low Energy Electrons and Surface Chemistry, VCH Weinheim (1985)

[et] V.H. Etgens, Experimental Report, ESRF.

[et97] F. Brossard, V.H. Etgens, A. Taddjedine, In-situ surface X-ray diffraction usinng a new electrochemical cell optimised for third generation synchrotron light sources, Nucl.Inst.Methods B **129, 419 (1997)**

[et99] V.H. Etgens, M.C. Martins Alves, A. Taddjedine, Electrochimica Acta **45**, 591 (1999)

[evn60] Ulrick R. Evans, The corrosion and oxidation of metals, (1960)

[ev95] K. W. Evans-Lutterodt, Mau-Tsu Tang, Angle Calculations for a 2+2 Surface Diffractometer, J.Appl.Cryst. **28**, 318 (1995)

[ew36] P. Ewald, Zeit f. Krist., 93 (1936) 396

[fe85] R. Feidenhans'l, J. Bohr, M. Nielsen, M. Toney, R.L. Johnson, F. Grey and I.K. Robinson, in Festkörperprobleme XXV, (1985) 545

[fl87] M. Fleischmann and B.W. Mao, J.Electroanal.Chem.**229**,125 (1987)

[fo79] A. J. Forty, Corrosion Micromorphology of Noble Metal Alloys and Depletion Gilding, Nature **282**, 597 (1979)

[fo80a] A. J. Forty, P. Durkin, A Micromorphological Study of the Dissolution of Silver-Gold Alloys in Nitric Acid, Phil.Mag.A **42**, 171-188 (1980)

[fo80b] A. J. Forty, G. Rowlands, A possible Model for Corrosion Pitting and Tunneling in Noble Metal Alloys, Phil.Mag.A **43**, 171-188 (1980)

[fr99] H. J. Freund and M. Bäumer, Metal Deposits on Well Ordered Oxide Films, Surf.Sci.**61**, 127 (1999)

[fri13] W. Friedrich, P. Knipping und M. v. Laue, Ann.d.Physik, (4), **61**, 971 (1913)

[fro76] A.T.Fromhold, Jr.,Theory of Metal Oxidation, in: Defects in Crystalline Solids Vol.9 and 12, ed. S.Amelinckx, R. Gevers, J. Nihoul, North Holland Publishing Company, Amsterdam, 1976

[ge55] H. Gerischer, H. Rickert, ber das electrochemische Verhalten von Kupfer-Gold-Legierungen und den Mechanismus der Spannungskorrosion, Zeitschrift fr Metalkunde **46**(1955) 681

[ge58] R.P. Tischer und H. Gerischer, Z.Elektochem.**62**, 50 (1958)

[gew97] A.A. Gewirth and B.K. Niece, Chem.Rev. **97**, 1129 (1997)

[gi01] M. Giesen, Step and Island Dynamics at Solid/Vacuum and Solid/Liquid Interfaces, Prog.Surf.Sci.**68**, 1 (2001)

[gu95] C. Günther, J. Vrijmoeth, R. Q. Hwang, R. J. Behm, Strain Relaxation in Hexagonally Close-Packed Metal-Metal Interfaces, Phys.Rev.Lett. **74**, 754 (1995)

[gr32] L. Graf, Metallwirtschaft **11**, 77 (1932)

[gr47] L. Graf, Die Ursachen der Spannungskorrosionsemppfindlichkeit homogener Legierungen, Zeitschrift fr Metallkunde **38**(1947) 193

[gr55] L. Graf, Die Ursachen der Spannungskorrosionsemppfindlichkeit homogener Legierungen, Zeitschrift fr Metallkunde **46**(1955) 378

[gu94] A. Guinier, X-ray Diffraction, Dover Publications, New York, 1994

[ha98] Carl .H. Hamann, Andrew Hamnett, Wolf Vielstich, Electrochemistry, Wiley-VCH, 1998

[har85] U. Harten, A. M. Lahee, J. Peter Toennies, Ch. Wöll, Observation of a Soliton Reconstruction of Au(111) by High-Resolution Helium-Atom Diffraction, Phys.Rev.Lett.**54**, 2619 (1985)

[he94] M. Henzler, W. Göebel, Oberfläechenphysik des Festköerpers, Teubner Stuttgart (1994)

[hen] R. Henes, Max-Planck Institute for Metal Research, Stuttgart, private communication.

[her98] Stephan Herminghaus, Karin Jacobs, Klaus Mecke, Jörg Bischof, Andreas Fery, Mohammed Ibn-Elhaj, Stefan Schlagowski, Spinoidal Dewetting in Liquid Crystal and Liquid Metal Films, Science **282**, 916 (1998)

[herr51] C. Herring, in: The Physics of Powder Metallurgy, ed. W. E. Kingston, McGraw-Hill, New York (1951)

[ho99] Holy, Pietsch, Baumbach, High-Resolution X-Ray Scattering from Thin Films and Multilayers, Springer Tracts in Modern Physics, Volume 149 (1999)

[hor78] J. Hornstra and W. J. Bartels, Determination of the Lattice Constant of Epitaxial Layers of III-IV Compounds, J.Cryst.Growth **44**, 513 (1978)

[it98] Kingo Itaya, In-Situ Scanning Tunneling Microscopy in Electrolyte Solutions, Prog.Surf.Sci. **58**, 121-248 (1998)

[it98] K. Itaya, In-Situ Scanning Tunneling Microscopy in Electrolyte Solutions (Review), Prog.Surf.Sci. **58**, 121 (1998)

[jack] J.D. Jackson, Classical Electrodynamics

[jam] R.W. James, The Optical Principles of the Diffraction of X-Rays, Cornell University Press, Ithaca, New York

[ka86] Alloy Dissolution, in Corrosion Mechanisms, Marcel Dekker Verlag, New York (1986)

[ka89] H. Kaiser, Werk. Korros.Sci. **40**, 1 (1989)

[ka93] H. Kaiser, Selective Dissolution of High and Low Diffusivity Alloys - A Comparison of Kinetical and Micromorphological Aspects, Corr.Sci. **34**, 683 (1993)

[ka03] H. Kaiser, G.A. Eckstein, Corrosion of Alloys, in Encyclopedia of Electrochemistry, eds. Allen J.Bard and M.Stratmann, Wiley-VCH 2003

[ke51] D.T. Keating and B.E. Warren, J.Appl.Phys. **22**, 286 (1951)

[kl] M. Kleinert, D.M. Kolb, University of Ulm, unpublished EC-STM images.

[ko78] D.M. Kolb, in Advances in Electrochemistry and Electrochemical Engineering, edited by H. Gerischer and C. W. Tobias (Wiley, New York, 1978), Vol.11, p.125

[ko96] D.M. Kolb, Reconstruction Phenomena at Metal/Electrolyte Interfaces, Prog.Surf.Sci.**51** (1996) 109

[la91] J.Laurent, D. Landolt, Anodic Dissolution of Binary Single Phase Alloys at Subcritical Potential, Electrochim.Acta **36**(1991) 49

[la92] Z.W. Lai, Theory of Ordering Dynamics for Cu_3Au, Phys.Rev.B **41**, 9239 (1992)

[la36] Die außere Form der Kristalle in ihrem Einfluß auf die Interferenzerscheinungen an Raumgittern, M. v. Laue, Annalen d. Physik 26,(1936) 55

[lb] Landolt-Börnstein, Numerical Data and Functional Relationships in Science and Technology, Springer Verlag Berlin 1975

[la36] Die außere Form der Kristalle in ihrem Einfluß auf die Interferenzerscheinungen an Raumgittern, M. v. Laue, Annalen d. Physik 26,(1936) 55

[lb] Landolt-Börnstein, Numerical Data and Functional Relationships in Science and Technology, Springer Verlag Berlin 1975

[le84] Heather Lechtman, Pre-Columbian Surface Metallurgy, Sci.Am.**250**, 38 (1984), and: Andean Value Systems and the Development of Prehistoric Metallurgy, *in:* Technology and Culture, **25**, 1-36 (January, 1984)

[li04] W.L. Ling, J. de la Figuera, N.C. Bartelt, R.Q. Hwang, A.K. Schmid, G.E. Thayer, and J.C. Hamilton, Strain Relief through Heterophase Interphase Reconstruction: Ag(111)/Ru(0001), Phys.Rev.Lett.**92**, 116102 (2004)

[luth] H. Lüth, Surfaces and Interfaces of Solid Materials, Springer, Berlin

[ma90] O. M. Magnussen, J. Hotlos, R. J. Nichols, D. M. Kolb, R. J. Behm, Phys.Rev.Lett. **64**, 2929 (1990)

[ma91] O. M. Magnussen, J. Hotlos, G. Beitel, D. M. Kolb, R. J. Behm, Atomic Structure of Ordered Adlayers on Single-Crystalline Gold Electrodes, J.Vac.Sci.Technol.**B9**, 969 (1991)

[ma92] O. M. Magnussen, J. Hagebock, J. Hotlos, R. J. Behm, Faraday Discussion **94**, 329 (1992)

[ma90] Binary Alloy Phase Diagramms, Editor in Chief: T. B. Massalski (1990)

[ma00] O. M. Magnussen, M. R. Vogt, Phys.Rev.Lett.**85**, 357 (2000)

[mar01] F. Maroun, F. Ozanam, O. M. Magnussen, R. J. Behm, The Role of Atomic Ensembles in the Reactivity of Bimetallic Electrocatalysts, Science **293**, 1811 (2001)

[mat87] G. Materlik, M. Schmäh, J. Zegenhagen, and W. Kelkoff, Ber.Bunsengesellschaft Phys. Chem.**91**, 292 (1987)

[mc90] E.G. McRae, T.M. Buck, Surface Compositional Ordering and Domain Walls in Cu_3AU, Surf. Sci.**227**,67-72 (1990)

[mi79] A.R.Miedema, Z.Meallk. **69**, 455 (1979) cited in H.Over et al.[ov97]

[mo91] T. P. Moffat, F-R. F. Fan, and A. J. Bard, Electrochemical and Scanning Tunneling Microscopic Study of Dealloying of Cu_3Au, J.Electrochem.Soc.**138** 3224 (1991)

[nag62] E. Nagy and I. Nagy, J.Phys.Chem.Solids **23**, 1605 (1962), cited in [bo96]

[na02] Zoltan Nagy, Hoydoo Yoo, Applications of surface scattering to electrochemistry problems, Electrochim.Acta **47**3037-3055 (2002)

[ne94] R.C.Newman, K.Sieradzki, Metallic Corrosion, Science **263**, 1708 (1994)

[new95] R.C. Newman, Stress Corrosion Cracking Mechanisms, in: Corrosion Mechanisms in Theory and Praxis, eds. P. Marcus and J. Oudar, Marcel Dekker, New York 1995

[nev80] L. Névot,P. Croce, Revue Phys.Appl. 15 (1980) 761

[ni02] H. Niehus, Surface and Sub-surface Alloy Formation Connected with Ordered Superstructures, in: The Chemical Physics of Solid Surfaces, ed. D.P. Woodruff, Vol.10,p.346-403, Surface Alloys and Alloy Surfaces, ELSEVIER 2002

[oc90] B. M. Ocko, J. Wang, A. Davenport, H. Isaacs, In-Situ X-ray Reflectivity and Diffraction Studies of the Au(001) Reconstruction in an Electrochemical Cell, Phys.Rev.Lett.**65**, 1466 (1990)

[op91] I.C. Oppenheim, D.J.Trevor, Ch.E.D.Chidsey, P.L. Trevor, K. Sieradzki, Science **254**, 687 (1991).

[ov97] H. Over, G.Gilarowski, H. Niehus, Surf.Sci. **381**, L619 (1997)

[ov98] H. Over, Prog.Surf.Sci.**58**, 249 (1998)

[pa68] P.W.Palmberg, Appl.Phys.Lett. **13**, 183 (1968)

[pa89] B.W. Parks, J.D. Fritz, and H.W. Pickering, The Difference in The Electrochemical Behavior of the Ordered and Disordered Phases of Cu_3Au, Scripta Metallurgica **23**, 951 (1989)

[par55] L.G. Parratt, Phys.Rev. 95 , 359 (1955)

[pi63] H.W. Pickering and P.R. Swann, Corrosion **19**, 369t (1963)

[pi67] H.W. Pickering, C. Wagner, Electrolytic Dissolution of Binary Alloys Containing a Noble Metal, J.Electrochem.Soc. **114**(1967) 698

[pi71] H.W. Pickering, P.J. Byrne, On Preferential Anodic Dissolution of Alloys in the Low Current Region and the Nature of the Critical Potential, J.Electrochem.Soc. **118**, 209 (1971)

[pi83] H.W. Pickering, Characteristic Features of Alloy Polarization Curves, Corr.Sci. **23**, 1107 (1983)

[pi91] J.D. Fritz, H.W. Pickering, Selective Anodic Dissolution of Cu-Au Alloys: TEM and Current Transient Study, J.Echem.Soc. **138**(1991) 3209

[po63] M. Pourbaix, Atlas d'Equilibres Electrochemique, Gauthier Villars, Paris, 1963

[re96] H. Reichert, S.C. Moss, K.S. Liang, Phys.Rev.Lett. **77**, 4382 (1996)

[rei92] R. Reining and K.G. Weil, J.Electrochem.Soc.**139**, L93 (1992)

[ri00] DATAPLOT, written by Dr.Kenneth Ritley, can be obtained from www.mf.mpg.de/en/abteilungen/dosch/index en.html; K. A. Ritley, M. Schlestein, H. Dosch, Datascan: An extensible program for image analysis in Java, Computer Physics Communications **137**, 300-311 (2001)

[ro00] O. Robach, Y. Garreau, K. Aid and M. B. Veron-Jolliot, J.Appl.Cryst. **33**, 1006 (2000)

[rob86] I.K. Robinson, Phys. Rev. B 33, 3830 (1986)

[rob92] I.K. Robinson and D.J. Tweet, Surface X-ray Diffraction, Rep.Prog.Phys.**55**, 599-651(1992)

[ros71] G. Rosenbaum, K.C. Holmes, J. Witz, Synchrotron Radiation as a source for X-ray Diffraction, Nature **230**, 474 (1971)

[sa91] A. R. Sandy, S. G. Mochrie, D. M. Zehner, K. G. Huang, D. Gibbs, Structure and Phases of the Au(111) Surface: X-ray-Scattering Measurements Phys.Rev.B**43**, 4667 (1991)

[sc03] Tobias Schulli, Dissertation, Linz 2003

[sch96] W. Schweika, et al., Phys.Rev.B **53**, 8937 (1996)

[schw49] J. Schwinger, Phys. Rev. 75, 1912 (1949)

[seb87] M.T. Sebastian and P. Krishna, Diffraction Effects from H.C.P. Crystals with Random Growth Faults Undergoing Transformation to the F.C.C. Phase by the Deformation Mechanism, phys.stat.sol.(a) **101**, 329 (1987)

[schw92] S. Schweizer, C. Elsässer, K.Hummler, and M. Fähnle, Ab initio calculation of stacking-fault energies in noble metals, Phys.Rev.B **46**, 14270 (1992)

[si89] K. Sieradzki, R.R. Corderman, K. Shukla, R.C. Newman, Computer Simulation of Corrosion: Selective Dissolution of Binary Alloys, Phil.Mag.A **59**(1989) 713

[si93] K.Sieradzki, Curvature Effects in Alloy Dissolution, J.Echem.Soc. **140**(1993) 2868

[sim] Gene Simmons and Herbert Wang, Single Crystal Elastic Constants and Calculated Aggregate Properties: A HANDBOOK, 2nd ed., The M.I.T. Press, Cambridge, Massachusetts (1971).

[sh03] The More Elements, the Merrier; G. Shiflet, Science **300**, 443(2003).

[shi73] D. Shirley, Phys.Rev.A **7**, 1520(1973)

[so86] R. Sonnenfeld, P.K. Hansma, Atomic Resolution Microscopy in Water, Science **232** (1986) 211

[so86b] B. Drake, R. Sonnenfeld, J. Schneir, P.K. Hansma, G.Slough, R.V. Coleman, Rev.Sci.Instr. **57**(1986) 441

[sp98] G. Springholz, V. Holy, M. Pinczolits, G. Bauer, Science **282**, 734 (1998)

[st] Dr. A. Stierle, Max-Planck Institute for Metal Research, Stuttgart, private communication.

[st94] F. H. Streitz, R. C. Cammarata, K. Sieradzki, Surface-Stress Effects on Elastic Properties. I.Thin Metal Films, Phys.Rev.B, **49**, 10699 (1994)

[str01] M.Stratmann and M. Rohwerder, A Pore View of Corrosion, Nature **410**, 420 (2001)

[sw69] P. R. Swann, Mechanism of Corrosion Tunneling With Special Reference to Cu_3Au, Corrosion **25**, 147 (1969)

[sz02] P. Szelestey, M. Patriarca, L. F. Perondi and K. Kaski, Modified EAM Potentials for Modeling Stacking-Fault Behaviour in Cu, Al, Au, and Ni, Int.J.Mod.Phys. B, **16**, 2823 (2002)

[tam19] G. Tammann, Z.anorg.allg.Chem.**107**, 1 (1919) cited in [ge58]

[tan81] Y. Tanishiro et al., Surf.Sci.**111** 395 (1981)

[tar02] U. Tartaglino et al., Bending Strain-Driven Modification of Surface Reconstruction: Au(111), Phys.Rev.B**65**, 241406(R) (2002)

[te02] C. Teichert, Self-Organisation of Nanostructures in Semiconductor Heteroepitxaxy, Phys.Rep. **365**, 335-432 (2002)

[tha67] L. N. Tharp, E. J. Scheibner, J.Appl.Phys.**38**, 4355 (1967)

[to95] Micheal F. Toney et al., Electrochemical Deposition of Copper on a Gold Electrode in Sulfuric Acid: Resolution of the Interfacial Structure, Phys.Rev.Lett.**75**, 4472 (1995)

[ton94] W. M. Tong and R. S. Williams, Kinetics of Surface Growth: Phenomenology, Scaling, and Mechanisms of Smoothening and Roughening, Annu.Rev.Phys.Chem **45**, 401 (1994)

[tor04] X. Torrelles and J. Rius, Faster Aquisition of Structure-Factor Amplitudes in Surface X-ray Diffraction Experiments, J.Appl.Cryst.**37**, 395 (2004)

[Tru96] K.N. Trueblood (Chairman) et al., Atomic Displacement Parameter Nomenclature, Report of a Subcommittee on Atomic Displacement Parameter Nomenclature, Acta Cryst. A**52**, 770 (1996)

[ve03] C. Vericat, M.E.Vela, G.A.Andreasen, R.C.Salvarezza, F.Borgatti, R.Felici, T.L. Lee, F.Renner, J.Zegenhagen, J.A.Martin-Gago, Following adsorption kinetics at electrolyte/metal interfaces through crystal truncation scattering: Sulfur on Au(111), Phys Rev.Lett. 90 (2003) 75505

[vin82] G.H. Vineyard, Phys. Rev. B 50 (1982) 4146

[vl87] E. Vlieg, J. F. Van der Veen, J. E. Macdonald and M. Miller, J.Appl.Cryst. **20** (1987), 330

[vl97] E. Vlieg, J.Appl.Cryst. **30** (1997), 532

[vl98] E. Vlieg, J.Appl.Cryst. **31** (1998), 198

[vl00] E. Vlieg, A Concise ROD Manual, University of Nijmegen. The software is available from the ESRF webpage www.esrf.fr/computing. A short publication appeared in: E. Vlieg, ROD: a program for surface X-ray crystallography, J.Appl.Cryst.**33**, 401 (2000)

[wa33] C. Wagner, Z.Phys.Chem. **B 21**(1933)25
C. Wagner, Z.Phys.Chem. **B**(1938) 455.

[war] B.E. Warren, X-Ray Diffraction, Dover Publications.Inc., New York

[we86] J.M. West, Basic Corrosion and Oxidation, 2nd. edition Ellis Horwood, Chichester, 1986

[wo91] D. Wolf, Surface Stress Induced Structure and Elastic Behaviour of Thin Films, Appl.Phys.Lett.**58**, 2081 (1991)

[wsxm] WSxM, AFM/STM software (www.nanotec.es)

[xtab] International Tables of X-Ray Crystallography, J.A. Ibers and W.C. Hamilton eds. Kynoch Press, Birmingham, 1974; atomic scattering factors are in Vol.IV, chapter 2.2, by D.T. Cromer and J.T. Waber.

[za] H. Zajonz, Max-Planck Institute for Metal Research, Stuttgart, private communication.

[ze98] G. Scherb, A. Kazimirov, and J. Zegenhagen, A novel thick-layer electrochemical cell for in-situ x-ray surface diffraction, Rev.Sci.Instr.**69**, 512 (1998)

[ze98b] Th. Koop, W. Schindler, A. Kazimirov, G. Scherb, J. Zegenhagen, Th. Schulz, R. Feidenhansl, J. Kirschner Rev.Sci.Instr.**69**, 1840 (1998)

[zhu88] X.-M. Zhu et al., Phys.Rev.B **37**, 7157 (1988)